Modelling and Simulation of Air and SF_6 Switching Arcs in High Voltage Circuit Breakers

Thesis submitted in accordance with the requirements of the University of Liverpool for the degree of Doctor in Philosophy by

Jian Liu

May 2016

Department of Electrical Engineering and Electronics

The University of Liverpool

Acknowledgement

I deeply appreciate the support from my supervisor, Dr. J. D. Yan during the period of my postgraduate study.

My deepest thanks go to Prof. Michael T. C. Fang for his kind help and encouragement. Without his sincerely help, the work could not have been successfully conducted. I wish to thank my best friend, Dr. Quan Zhang, for all the valuable discussion, friendliness and kind help.

I would like to thank my friend, Dr. Yuqing Pei, for her friendliness. My special appreciation would go to Linda Boyne from Royal Liverpool Hospital for her kind taking care since the unexpected change of my life.

Last but not least, I wish to thank my girlfriend Rosita Y. H. Wei for all her love and encouragement over the time.

Abstract

This thesis is concerned with the modelling of switching arcs in air in high voltage circuit breakers and with a comparative study of interruption capability of air and SF_6 switching arcs. Emphasis is given to the identification of dominant energy transport processes for arc interruption and the material properties associated these processes.

There have been renewed interests in air arcs because of its possible use in a mixture with other gases as a replacement for SF_6 in circuit breakers for environment protection. Computer simulation of the switching air arc has been carried out using arc models based on laminar flow and on turbulent flow for the experimental set up of Fang et al [41] under DC current and that of Frind and Rich [66] for the current zero period. DC arc voltages predicted by arc model assuming laminar flow (LAM) are much lower than those measured. Thus, turbulence is introduced to account for additional power loss mechanism not included in the laminar flow model.

Two turbulence models have been used to take into account of turbulence enhanced momentum and energy transport: the Prandtl mixing length model (PML) and the standard k-epsilon model or its modified version. For the DC air nozzle arc of Fang et al [41] the value of the turbulence parameter, c= 0.06, in PML has been chosen to match the predicted arc voltage with that measured at 1 kA DC and a stagnation pressure of 10 bar. PML can give satisfactory agreement with experiments over a DC current range from 250 A to 3 kA. When the standard k-epsilon model is used, the predict arc voltage is much higher than that measured indicating that turbulence cooling is too strong. One of the turbulence parameters of the standard k-epsilon model which controls the dissipation rate of turbulent kinetic energy is adjusted to match the predicted arc voltage with the experimentally measured arc voltage under the same discharge conditions as those for finding the value of c in PML. With this chosen value of $C_{1\varepsilon}$= 1.62, the modified k-epsilon model (MKE) gives similar results to those of PML.

Three arc models (LAM, PML and MKE) are used to compute the critical rate of rise of recovery voltage (RRRV) for the air nozzle arc of Frind and Rich [66]. The presence of the shock inside the nozzle in the presence of the arc prevents the optimisation of the value of turbulence parameter for PML due to numerical convergence problems. RRRV predicted by PML and LAM are much lower than the experimental value. MKE with $C_{1\varepsilon}$= 1.65 is successful in predicting satisfactorily the RRRV at di/dt= 13.5 A/μs for several stagnation pressures. However, it has been found that a single value of $C_{1\varepsilon}$ chosen for one value of di/dt cannot give satisfactory prediction of RRRV for other values of di/dt.

A comparative computational study of SF_6 and air switching arcs based on MKE has been carried out for the experimental conditions of Frind and Rich [66] for di/dt= 13.5A/μs at several stagnation pressures. Under the same discharge conditions RRRV of SF_6 switching arc is one order of magnitude higher than that of air switching arc. Such large difference in the interruption capabilities of SF_6 and air is due to the different dominant energy transport processes responsible for the arc cooling during current zero period. Two material properties of the arc plasma, the product of density and specific heat at constant pressure (ρC_P) and that of density and enthalpy (ρh) are responsible for the distinctive arc features for SF_6 and air. SF_6 switching arc has a distinctive arc core surrounded by a thin region with steep temperature gradient. Under the same discharge conditions as those of SF_6 air switching arc has no distinctive core structure. Its radial temperature profile is very broad and arc radius is much bigger than that of SF_6. Such broad radial temperature profile of air arc is due to the peaks of turbulent thermal conductivity at 4,000 K and 7,000 K produced by the corresponding peaks of the material property of ρC_P of air. For SF_6 ρC_P has a peak just below 4,000 K, which ensures rapid temperature decay above 4,000 K and a gentle temperature tail below 4,000 K. In comparison with SF_6 under the same pressure difference across the nozzle the velocity inside air arc is much higher than that of SF_6. With ρh of air being greater than that of SF_6 for temperature higher than 7,000 K together with higher velocity enthalpy transport capability of air arc is much higher than that of SF_6. Energy balance calculation for the current carrying core indicates that after the breakdown of quasi-steady state turbulent thermal conduction is the dominant energy

transport process for SF_6 while for air arc axial convection is dominant. As a consequence the rates of decay of arc temperature and arc radius for air arc a few microseconds before current zero are much slower than those of SF_6, thus resulting in a large difference between RRRVs for the two gases under the same discharge conditions. To find an alternative arc quenching gas with similar interruption capability to that of SF_6 one should aim at ρC_P and ρh of the alternative gas with similar features to those of SF_6.

Table of the Contents

List of Figures

List of Tables

List of Symbols and Abbreviation

B	Magnetic field
B_ν	Planck function
c	Parameter in mixing length model
c_{light}	Speed of light
$C_{1\varepsilon}$	One of the turbulence parameters in k-e model
$C_{2\varepsilon}$	One of the turbulence parameters in k-e model
C_u	One of the turbulence parameters in k-e model
C_p	Specific heat capacity at constant pressure
E	Electrical field
E_0	Electrical field in steady state
$E_{r,s}$	Energy of species r at an excited state s
F	radiation flux
$g_{r,s}$	Statistical weight of the state s
G_{ke}	Generation of the turbulence kinetic energy
h	Enthalpy
h_p	Planck's constant
h'	Fluctuation of enthalpy
I	Current
I_t	Turbulent intensity
I_ν	Spectral radiation intensity
$\bar{\bar{I}}$	Unity tensor
J	Current density
k_b	Boltzmann constant
ke	Turbulent kinetic energy per unit mass
k_l	molecular thermal conductivity
k_t	Turbulent thermal conductivity

k_ν	Spectral absorption coefficient
k'_ν	Effective spectral absorption coefficient
LAM	Laminar flow model
m_r	Mass per particle
MKE	Modified k-epsilon model
n_r	Number density of species r
$n_{r,s}$	Number of particles of species r at an excited state s
p	Pressure
p_i	Instant pressure
P_0	Power loss per unit length
Pr_t	Turbulent Prandtl number
PML	Prandtl mixing length model
q	Net radiation loss per unit time and volume
q_a	Radiation absorption
q_e	Radiation loss
Q_j^R	Turbulence enhanced heat transfer
r	radial direction
r_δ	Arc's thermal radius
R	Radius
R_Ω	Resistance
SKE	Standard k-epsilon model
T	Temperature
u_i and u_j	Velocity fluctuations
v	Radial velocity
v_r	The magnitude of the velocity vector
V	Voltage
$\vec{V}$	Velocity vector
V_c	Velocity scale

$\vec{V_i}$	Instant velocity vector
w	Axial velocity
z	Axial direction
Z_r	Partition function of species r
λ_c	Length scale
μ_{ab}	Dissociation energy
μ_m	Permeability
μ_l	Molecular viscosity
μ_t	Eddy viscosity
ε	Turbulence dissipation rate
ε_q	Net emission coefficient (NEC)
ϵ_ν	Emission of radiation
$\in_i$	Instant energy in energy conservation equation
$\in$	Energy in time averaged energy conservation equation
θ_δ	Arc's thermal area
ν	Frequency
ρ	Density
ρ_i	Instant density
σ	Electrical conductivity
σ_{ke}	Turbulent Prandtl number for ke
σ_ε	Turbulent Prandtl number for ε
τ	Arc's time constant
$\bar{\bar{\tau}}$	Stress tensor
$\bar{\bar{\tau}}_i$	Instant stress tensor
$\bar{\bar{\tau}}_{ij}^R$	$Reynolds\ stress$
φ	Electrical potential
Ω	Solid angle

Chapter 1. Introduction

1.1. Brief Review of the Development of High Voltage Circuit Breakers

Circuit breakers are an essential part of a power system and important apparatus for safety and reliable operation of a power system. A typical power system consists of several generation stations and consumers interconnected by transmission and distribution networks [1], as shown in Figure 1-1. The objective of any power system is to generate electric energy in sufficient quantities, to transmit it to various load centres and then distribute it to various consumers, and also to maintain quality and reliability of transmission (i.e. frequency and voltage are constantly maintained at specified values) at an economic price [1]. Circuit breakers are used in transmission and distribution substations (Figure 1-1) for protection and control of power flow. They are required to de-energize a load or to isolate a faulty part of the system so that the equipment or the line can be repaired or protected from high short circuit current. The operation of a circuit breaker involves the separation of two metallic contacts inside an interrupter of a circuit breaker. Upon contact separation an arc is formed. The task of a circuit breaker is to change an arc with high electrical conductivity at contact separation to an insulator soon after an AC current zero within the time duration allowed by power system stability [2, 3].

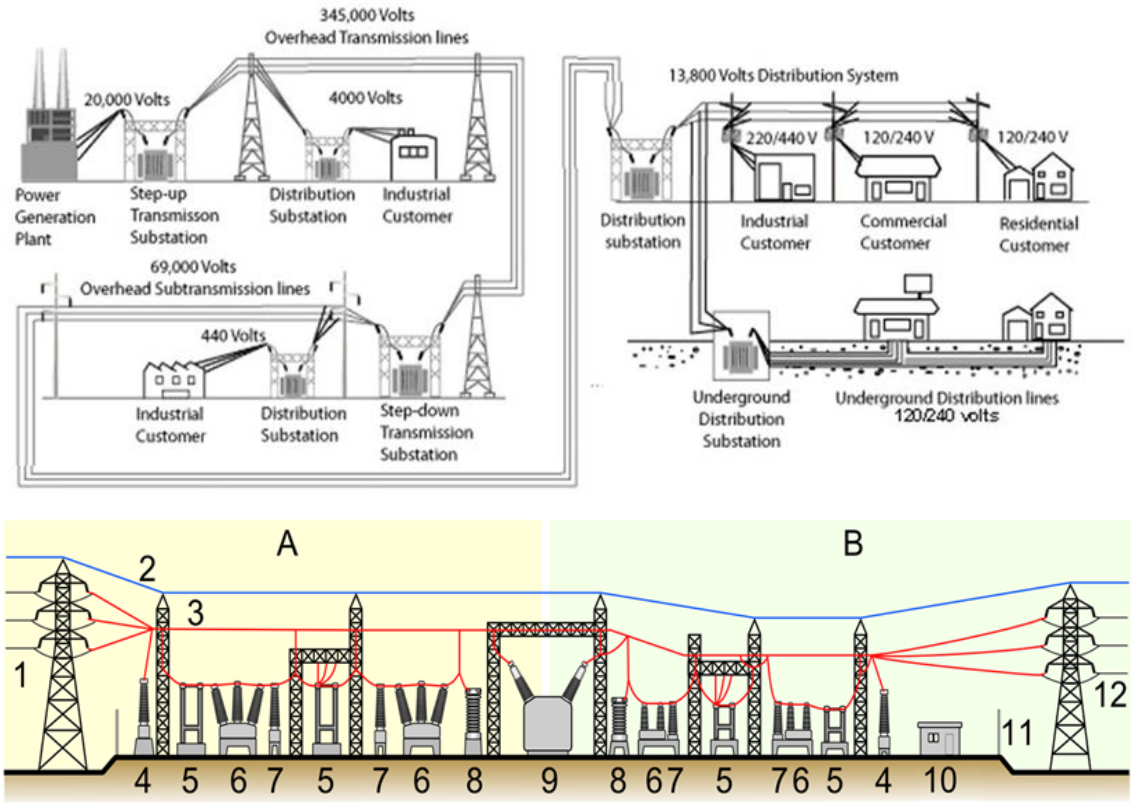

Figure 1-1 Diagram showing the typical constituting components of a generation, transmission and distribution network [4]. A: Primary power lines' side, B: Secondary power lines' side, 1. Primary power lines 2. Ground wire 3. Overhead lines 4. Transformer for measurement of electric voltage 5. Disconnect switch 6. Circuit breaker 7. Current transformer 8. Lighting arrester 9. Main transformer 10. Control building 11. Security fence 12. Secondary power lines

In early days of electrical power systems, the transmission voltage level was low (typically in the order of 10 kV in 1890s and 100 kV in 1910s [5], and fault currents were small which could be easily interrupted by the separation of two contacts in air. The distance between the two contacts was set at such a length that the arc in between could no longer be maintained by the system voltage. From 1950s to now, with an increasing demand of power consumption and the resulting growth of power generation, and also the requirement of reducing power loss during transmission (especially when long distance transmission becomes necessary, e.g. in China, United States and Russia), the transmission voltage level of power systems has been dramatically increased. For example, the transmission voltage level of power systems is typically 400 kV and 275 kV in the UK

nowadays [6]. In China, the requirements on power transmission is even higher due to necessarily of long distance power transmission, and thus the voltage level is above 500 kV, e.g. three Gorge project [4]. With even more demands in need of electric power for both industry side and domestic use, the transmission lines with ultra-high voltage levels (>1000 kV) is now developing in China [7]. The continuous increase of transmission voltage levels inevitably results in ever increasing capacity of power system, and more importantly it gives rise to increasing fault current levels. As a result, the aforementioned simple way of current interruption became inadequate and special devices (i.e. circuit breakers, especially those which can withstand high transmission voltages, known as high voltage circuit breakers) had to be developed. Various types of circuit breakers were developed using different switching media which included oil, vacuum, air, sulfur hexafluoride (SF_6) and gas mixtures [2-3, 8-10].

This thesis is solely concerned with the processes occurring in an arc inside a high voltage circuit breaker, the voltage of which is usually above 110 kV. Although vacuum breakers at 110 kV and above have recently been developed [11] its wide adoption has not been reported. At voltage 110 kV and above gases are still exclusively used as a switching media. Before the invention of SF_6 circuit breaker [8] compressed air from a high pressure reservoir was used to control and extinguish the arc in a supersonic nozzle interrupter. Such breakers were known as gas blast circuit breakers [2, 8].

The superior dielectric strength of SF_6 (3 times higher than that of air at room temperature and atmospheric pressure) [10] and the discovery of its superior arc quenching capability [12] ushered in an era of active development SF_6 breakers from late nineteen fifties of the last century to the present day. SF_6 breakers gradually evolved from a two-pressure breaker [13] to puffer type breaker [14] and, finally, self-blast (or auto-expansion) breaker [15, 16].

The effects of wide use of SF_6 in electrical power equipment on environment have attracted much attention as SF_6 has been shown to be a greenhouse gas [17]. In its normal state SF_6 is chemically inert, non-toxic, non-flammable, non-explosive, and thermally stable up to a temperature 500 °C [17]. However, some of byproducts due to arcing and partial discharge of SF_6 contaminated by air, water vapour and contact metal vapour are toxic [17, 18]. SF_6 is also an efficient absorber of infrared radiation. Because SF_6 is largely immune to chemical and photolytic degradation, its contribution to global warming is accumulative and virtually permanent. Its warming potential per unit mass is estimated on a 100-year basis to be approximately 24,000 times greater than that of CO_2. In recent years, much research has therefore been done to find an alternative insulation and switching medium to SF_6. A number of gas mixtures have been tried [19] but so far no gases/gas mixtures have been found which have equal to SF_6 arc quenching capability [19]. The search for a replacement gas to SF_6 is hindered by a lack of knowledge as regards the gas property which determines the arc interruption capability.

1.2. Review of Switching Arc Modelling

The arc was discovered by Davy and Rutter in 1808 [20], which has been used for illumination for over two hundred years. Arc has also been used for current interruption, as a heat source (e.g. arc heaters, waste disposal), for material cutting, joining, surface treatment and material processing [21]. The review of arc modelling is restricted to the modelling of switching arcs, which forms the subject of matter of this thesis.

1.2.1. Black Box Arc Models

Investigation into switching arc modelling began early in the 20th century with Slepian's race theory for arc interruption [22]. In this theory arc interruption is considered as a race between dielectric recovery of the gas in between the contacts and the rise of the transient voltage across them. This theory fails to recognize that the first phase of arc interruption is thermal recovery, which is followed by dielectric recovery.

In thermal recovery of the arc current interruption depends on a race between power loss of the arc and power input due to the imposed transient voltage. Based on this concept, Cassie [23] proposed an arc model assuming that the arc is cylindrical with uniform temperature of resistance per unit length given by R. The time variation of Resistance is given by

$$R_\Omega \frac{d}{dt}\left(\frac{1}{R_\Omega}\right) = \frac{1}{\tau}\left[\left(\frac{E}{E_0}\right)^2 - 1\right] \qquad (1\text{-}1)$$

where t is the time, τ arc's time constant, E the electrical field and E_0 the electrical field in steady state.

Note that time constant, the steady state electrical field and the initial value of arc resistance will have to be derived from experimental results. Equation (1-1) is known as Cassie's equation. It was claimed [24] that Cassie's model was applicable before current zero.

In 1943 Mayr [25] proposed a cylindrical arc model in which the temperature was allowed to vary but power loss per unit arc length was constant. This led to Mayr's equation:

$$R_\Omega \frac{d}{dt}\left(\frac{1}{R}\right) = \frac{1}{\tau}\left[\left(\frac{EI}{P_0}\right)^2 - 1\right] \qquad (1\text{-}2)$$

where P_0 is the power loss per unit length and other symbols have the same meaning as in Cassie's equation.

Mayr's model was found to be more applicable after current zero [24]. This prompted Browne to propose a composite model [24] which combined Cassie's equation for the period before current zero and Mayr's equation after current zero.

Cassie's and Mayr's equations cannot be derived from arc conservation equations. They were based on ad hoc assumptions which introduced free parameters, such as arc time constant and steady electric field in Cassie's equation and power loss per unit arc length and arc time constant in Mayr's equation. Their use is limited to where test results are available for a particular type of interrupter from which the values of the free parameters can be derived. Because of its mathematical simplicity black box arc models are still used [26].

1.2.2. Integral Arc Models for Axial Flow

It was recognized by Swanson and his co-workers [27-32] and by Topham [33] around 1970 that an arc burning in a supersonic nozzle was similar to a boundary layer in that the axial diffusion of momentum and heat inside the arc can be neglected in comparison with their radial counterparts and the pressure imposed upon the arc is the same as the cold flow surrounding the arc. Since at the time computer power was still very limited and numerical algorithms for the solution of boundary layer type of arc conservation equations were not robust, boundary layer integral method was used to derive radially integrated arc conservation equations. The closure of these radially integrated equations requires knowledge of radial profiles of axial velocity and temperature [27, 34]. However, fixed shapes of velocity and temperature profiles make poor prediction of arc behaviour during current zero period [35].

Investigations into arcs in axial gas flow were carried out at Brown Berveri [34, 36].A two-zone model assuming constant temperature in each zone was used to investigate a 2 kA DC nitrogen arc [36]. Lowke, Ludwig and Tuma [37, 38] introduced a channel model in which arc temperature and velocity are uniform across arc conducting area.

In 1974 Cowley [39] took an important step in that the arc conservation equations in integral form together with the external flow equations were rigorously formulated. Chan

et al [40] extended the formulation to include an energy integral equation for the arc conducting core. The previously mentioned integral models are special cases of this general formulation and the differences between them lie in the assumption for the closure of integral equations. This integral model has achieved considerable success at high currents [41].

1.2.3. Differential Arc Models and the Use of Commercial Computational Fluid Dynamic (CFD) Packages

By the beginning of nineteen eighties computing technology advanced at a rapid speed and our understanding of basic arc physics, especially with regard to radiation transport in high pressure arcs [42, 43] has been much improved. At the same time, robust algorithms for numerical solutions of highly nonlinear partial differential equations became well established [44]. Arc modelling based on arc conservation equations in full differential form (commonly known as differential arc models) began to emerge [43]. Fang and his co-workers [43, 45-47] investigated the physical processes of arcs burning in a supersonic flow in nitrogen and SF_6 assuming that the arc can be treated as a boundary layer and the pressure imposed on the arc can be calculated by those one- dimensional equations of external flow. Their work on nitrogen nozzle arc of the BBC Group [36] shows that arc theory based on laminar flow [43] can predict satisfactorily the thermal (arc temperature), aerodynamic (pressure and velocity) and electrical behaviour of the nozzle arc. However, when laminar arc theory was applied to SF_6 nozzle arcs there was a large discrepancy between the predicted and measured critical rate of rise of recovery voltage (RRRV) [46]. It was concluded that for SF_6 arcs it is necessary to introduce turbulence enhanced momentum and energy transport [47].

The rapid advancement of computing power at an affordable price in the form of personal computers and the availability of general purpose CFD packages prompted research activities in adapting commercial CFD packages to simulate the whole arcing period

inside circuit breakers. Of commercial CFD packages PHOENICS has the longest history [48]. Around 1990 PHOENICS was the only commercial CFD package which was capable of simulating compressible flow. The first published attempt in this area is that of Rutten [49], who simulated a DC arc at 1 kA. The use of commercial CFD package for the simulation of circuit breaker arcs has proven not an easy task [50]. Correct arc physics and boundary conditions must be incorporated and solutions verified by experimental results.

Fang and his co-workers successfully simulated using PHONICS an arc interacting with a shock wave in a supersonic nozzle [51, 52] , a puffer breaker [53] and the operation of an auto-expansion breaker [16, 54, 55]. Since PHOENICS is not very user friendly, Gleizes and his co-workers in France started using Fluent [56, 57] to simulate the arc. Fluent has gradually become the dominant CFD package for arc simulation [58-61].

1.3. **Objective of the Thesis**

A satisfactory switching arc model is the key to achieve predictive design of high voltage circuit breakers. The design of such breakers still relies upon costly short circuit tests although, with the aid of CAD design tools, it is believed that the number of short circuit tests required for the development of a new breaker has been reduced. The difficulty in achieving predictive design lies with a lack of reliable test data for the verification of computer simulated results and with the deficiencies in the modelling of the effects of turbulence on switching arc behaviour. It is in a way not surprising as even for the simplest fluid, incompressible fluid with constant properties, there is no universal turbulence model applicable for all fluid dynamic situations [62]. Turbulence models are designed for particular flow situations. There are a number of turbulent models the choice of which mainly depends on the experience of the user.

The closure of the governing equations describing turbulent flow inevitably introduces free parameters, commonly known as turbulent parameters, the values of which will have to be found by matching the predicted results with test data. The success of a particular turbulence model is measured by the range of applicability of the chosen values of turbulence parameters. The availability of reliable test data is therefore of critical importance in establishing a satisfactory turbulence model for switching arcs.

Much work has been done on the modelling of turbulent SF_6 arcs [46, 63-65]. However, there is very little work on air arcs in gas flow. It is not known if turbulence is important for such arcs in air. It appears that for arcs in nitrogen good agreement between prediction and experimental results was achieved without resorting to turbulence [41, 45].

Extensive test results in the form of DC arc voltage [41] and in the form of RRRV [66] have been reported for an air arc in a supersonic nozzle interrupter with fixed upstream and downstream pressures. Such a two-pressure system eliminates pressure transients caused by reflections within a circuit breaker which inevitably affect the arc in the nozzle interrupter. Thus, the test results given in [41, 66] are well suited for the verifications of arc models for air.

The thesis aims at establishing a satisfactory arc model to predict arcs in air under DC and transient conditions. Through the comparison between experimental results and the results predicted by an arc model assuming laminar flow the role of turbulence in air arcs can be determined.

It is not known what material properties determine the characteristics of arcs in different gases especially if turbulence is important. The identification of such material properties is important in the search of a replacement switching gas for SF_6 as this is urgently required for environment protection. In the thesis a comparative study of air and SF_6 arcs

under identical test conditions will be conducted and the material properties responsible for the vastly different interruption capabilities of these two gases identified.

1.4. **Main Contribution**

In order to achieve the objectives presented in Section 1.2, a detailed computational investigation has been carried out to study the behaviour of the air switching arc under both steady state (with direct currents) and transient (with a current waveform consisting of a DC plateau and a subsequent current ramp with a fixed rate of current decay) conditions. The main contribution of the present work is summarized as follows:

(a) The mathematical model for air switching arcs has been established;
(b) The importance of turbulence in determining the behaviour of air switching arcs has been confirmed;
(c) The material properties which are mainly responsible in the determination of the air arc behaviour have been identified;
(d) Through a detailed comparative study of air and SF6 arcs, the material properties responsible for the vastly different interruption capacities of these two gases have been found. Based in this finding, a general guidance concerning how to search for a replacement of SF6 has been suggested.

The organization of the thesis, with details in the contents of each chapter, is given in Section 1.4. In addition, a number of publications relevant to the present work have been produced which are listed in Appendix.

1.5. **Organization of the Thesis**

The thesis is organized as follows:

Chapter 2 gives a detailed discussion on the basic arc physics based on which the mathematical model of the nozzle arc is derived. A detailed description is then given for

the model of switching arcs assuming turbulent flow, which includes the time averaged arc conservation equation and the governing equations of the turbulence models applied in this thesis. A critical review has been given regarding the thermodynamic and transport property data of air published by different authors, based on which the data used for the arc modelling of the present work has been determined. The principle of radiation transfer for high pressure arcs has been discussed, and the radiation model used in the present investigation, which is based on net emission coefficient (NEC), is then given. The data of NEC reported by different authors, obtained from both experiments and calculations, has been critically reviewed, after which the NEC data used in this thesis is selected.

Chapter 3 describes the computational fluid dynamics (CFD) solver, ANSYS Fluent, together with pre-processing tools (ANSYS DesignModeler, for creating geometry and, ANSYS Meshing, for generating mesh) and post-processing tool (ANSYS CFD-post, for data analysis). The implementation of the arc model in ANSYS Fluent, which is based on parallel computing, has been described.

Chapter 4 reports the investigation of a DC air arc burning in the supersonic nozzle used in the experiments of Fang et al [41]. Computations are carried out using the arc model based on both the laminar flow (referred to as laminar flow model) and turbulent flow described by two turbulence models (the Prandtl mixing length model and the standard k-epsilon model or its modified version). The role of turbulence is established by comparison between experimental results and those predicted by laminar flow model. The dominant energy transport processes and the associated material properties in determining the behaviour of air switching arcs are identified.

Chapter 5 is concerned with the transient behaviour of an air nozzle arc, which is subjected to a current ramp with a rate of current decay, di/dt, towards current zero and a voltage ramp with the rate of increasing, dV/dt, after current zero. The investigation is based on the experimental conditions of [66] typical of the current zero period of arcing. The role

of turbulence and the material properties determining the interruption capability of air as a switching medium are further investigated for a rapidly changing arc during current zero period. The same turbulence models as in Chapter 4 are be used to study the transient air arc behaviour, together with inclusion of the laminar flow model for demonstration of the role of turbulence. The computed values of RRRV are compared with those reported in [66]. Based on such comparison, together with the investigation of Chapter 4, the role of turbulence and material properties in determining the behaviour of air switching arcs are identified. A discussion on the relative merits of the turbulence models employed are also given.

Chapter 6 gives a detailed comparative study on the behaviour of the switching arcs in air and SF_6. The investigation is based on the experimental conditions of Frind and Rich [66] which has reported the RRRV for a nozzle arc in both air and SF6. The effects of turbulence for both the air and the SF_6 arcs are accounted for by the standard k-epsilon model with one of its turbulence parameter ($C_{1\varepsilon}$) adjusted to match the experimental results. The computational results together with the measured RRRV are used to analyse the differences of the arc behaviour in air and SF_6 and the dominant energy transport processes with associated material properties responsible for such differences. Through the investigation, a general guidance, which is concerned with how to search for a replacement of SF_6 as a switching medium for gas-blast circuit breakers, has been suggested.

Chapter 7 gives appropriate conclusions drawn from the all investigations presented in this thesis. Suggestions are also given for the future work.

Chapter 2. Basic Arc Physics and the Governing Equation of Switching Arcs

2.1. Basic Arc Physics

Arcs in high voltage circuit breakers are usually at atmospheric pressure or above. At such pressures collisional processes between particles inside an arc are dominant in that the processes associated with photons (e.g. photon ionization, photon excitation) are negligible in comparison with their collisional counterparts (e.g. impact ionization and excitation) provided that electron number density is sufficiently high ([67]). For a switching SF_6 nozzle arc at an upstream pressure of 7.8 bar and an exit pressure of 1 bar electron number density at current zero is above the threshold electron number density required to ensure collisional processes dominant ([68]). Since switching arc is maintained by a current, the average energy of an electron gained from electric field in between two successive collisions is much smaller than its random thermal energy at the pressures normally encountered in circuit breakers ([69]). Thus, all species within an arc attain the same temperature. Such an arc is known as in local thermal equilibrium (LTE) [67]. Because the escape of photons to the surroundings of an arc, radiation field within the arc is no longer that of black body. Thus radiation intensity within an LTE arc departs from Planck's law [67]. The other properties of an LTE arc are identical to an arc in complete thermal equilibrium. These properties are summarised below:

(1) The velocity distribution of all particle species can be described by Maxwell's velocity distribution function with a single temperature:

$$dn_r = n_r f(v_r) dv_r \tag{2-1}$$

$$\mathrm{f}(v_r) = \frac{4v_r^2}{\sqrt{\pi(2k_bT/m_r)^3}} exp^{-\frac{m_r v_r^2}{2k_bT}} \tag{2-2}$$

where v_r is the magnitude of the velocity vector, n_r the number density of species r, m_r the mass per particle, T the common temperature for all particle species and k_b is the Boltzmann constant.

(2) The population density of excited states for each particle species follows the Boltzmann distribution:

$$n_{r,s} = n_r \frac{g_{r,s}}{Z_r} exp^{-\frac{E_{r,s}}{k_b T}} \tag{2-3}$$

where $n_{r,s}$ is the number of particles of species r at an excited state s. $g_{r,s}$ is the statistical weight of the state s, $E_{r,s}$ its energy and Z_r is the partition function of species r.

(3) The number densities of charged particle species are related through the Saha equation:

$$\frac{n_{r+1} n_e}{n_r} = \frac{2Z_{r+1}}{Z_r} \frac{(2\pi m_e k_b T)^{\frac{3}{2}}}{h^3} exp^{-\frac{\chi_{r+1}}{k_b T}} \tag{2-4}$$

where n_r and n_{r+1} are the number density of ion species in the (r)th and (r+1)th ionisation state respectively. n_e is the electron number density, χ_{r+1} the ionisation energy which is required to produce an ion in the (r+1)th state from the (r)th state, m_e the electronic mass and h the Planck constant.

(4) For chemical reactions the forward reaction is always balanced its reverse reaction, which is known as the principle of detailed balancing. The mathematical description of this principle is commonly known as mass action law or Eggert Equation. For example, the number densities of species involved a dissociation chemical reaction are given by

$$[ab] \Leftrightarrow [a] + [b]$$

$$\frac{n_a n_b}{n_{ab}} = \frac{Z_a Z_b}{Z_{ab}} \left(\frac{m_a m_b}{m_a + m_b}\right)^{3/2} \left(\frac{2\pi k T}{h^2}\right)^{3/2} \exp\left(-\frac{\mu_{ab}}{k_b T}\right) \tag{2-5}$$

where μ_{ab} is the dissociation energy.

Total pressure of the arc is equal to the sum of species pressures.

$$p = k_b T \sum_s n_i \tag{2-6}$$

where s is the total number of species.

The equilibrium composition of an arc in LTE at a given pressure and temperature can be calculated using the above properties together with conservation of mass and charge quasi-neutrality ([70]). With the aid of equilibrium composition thermodynamic quantities, such as density and enthalpy, can be tabulated as a function of temperature and pressure (e.g. [70, 71]).

2.2. **The Governing Equations of a Switching Arc in LTE**

The conservation equations of a switching arc in LTE are similar to an ordinary fluid but modified to include the Lorentz force in momentum conservation equation and Ohmic input and radiation transport in the energy conservation equation. These equations are given below in conservation form:

The mass conservation is given by

$$\frac{\partial \rho_i}{\partial t} + \nabla \cdot \left(\rho_i \vec{V_i}\right) = 0 \tag{2-7}$$

where t is time, ρ the instant density, and $\vec{V}$ the instant velocity vector. Subscript "i" denotes that it is an instant variable.

The momentum conservation equation reads:

$$\frac{\partial}{\partial t}\left(\rho_i \vec{V_i}\right) + \nabla \cdot \left(\rho_i \vec{V_i}\,\vec{V_i}\right) = -\nabla \mathrm{p}_i + \nabla \cdot \bar{\bar{\tau}}_i + \vec{J} \times \vec{B} \tag{2-8}$$

where p is the pressure, $\bar{\bar{\tau}}$ the stress tensor, $\vec{J}$ the current density and $\vec{B}$ the magnetic flux density. The last term in the momentum equation is the Lorentz force which is generated by the interaction between the current passing through the arc and the magnetic field generated by the arcing current itself.

The stress tensor $\bar{\bar{\tau}}_l$ is given by

$$\bar{\bar{\tau}}_l = \mu_l \left[\left(\nabla \vec{V}_l + \nabla \vec{V}_l^{\,T} \right) - \frac{2}{3} \nabla \cdot \vec{V}_l \bar{\bar{I}} \right] \qquad (2\text{-}9)$$

(Note: Two bars on the top of a letter or symbol indicate a tensor in this thesis.)

where μ_l is the laminar viscosity and $\bar{\bar{I}}$ the unity tensor. Superscript "T" denotes the transpose of a vector tensor.

The energy conservation equation can be written as:

$$\frac{\partial}{\partial t}(\rho_i \in_i) + \nabla \cdot \left(\vec{V}_l (\rho_i \in_i + p_i) \right) = \nabla \cdot \left(\mathrm{k}_l \nabla T_i + \bar{\bar{\tau}}_l \cdot \vec{V}_l \right) + \sigma \vec{E}^2 - q \qquad (2\text{-}10)$$

where k the thermal conductivity, T the temperature, σ the electrical conductivity, $\vec{E}$ the electrical field, q is the net radiation loss per unit time and volume, and $\in$ is given by

$$\in_i = h_i - \frac{p_i}{\rho_i} + \frac{\left| \vec{V}_l \right|^2}{2} \qquad (2\text{-}11)$$

where h is the enthalpy. h for air is determined by T and p in tabulated form by Yos [71].

Since circuit breakers are operated at either 50 Hz or 60 Hz, low frequency approximation can be introduced to simplify the electromagnetic fields associated with a switching arc [72]. Displacement current generated by the changing electric field and the electric field induced by the changing magnetic flux can be neglected in comparison respectively with the arcing current and the electrical field generated by the arcing current. Thus, current density is linked to electrical field by a simplified Ohm's law and Maxwell's equations for electromagnetic field are reduced to charge conservation and Ampere's law:

Ohm's law links current density to electrical field

$$\vec{\mathrm{J}} = \sigma\vec{E} \tag{2-12}$$

Charge conservation gives an additional equation to calculate $\vec{E}$.

$$\nabla \cdot \left(\sigma\vec{E}\right) = 0 \; or \; \nabla \cdot (-\sigma\nabla\varphi) = 0 \tag{2-13}$$

where φ is electrical potential and $\vec{E} = -\nabla\varphi$

Magnetic flux density is linked to current density through Ampere's law:

$$\nabla \times \vec{B} = \mu_m\vec{\mathrm{J}} \tag{2-14}$$

where μ_m is permeability and the Lorentz force can be expressed in terms of magnetic flux density,

$$\vec{J} \times \vec{B} = \frac{1}{\mu_m}\left(\nabla \times \vec{B}\right) \times \vec{B} = -\nabla\left(\frac{\vec{B}^2}{2\mu_m}\right) + \frac{1}{\mu_m}\left(\vec{B} \cdot \nabla\right)\vec{B} \tag{2-15}$$

The determination of net radiation loss, q, requires a consideration of radiation transport inside the arc. The discussion is given in Section 0.

The above equations are supplemented by the equation of state, which is usually expressed as

$$\rho = f(\mathrm{p}, \mathrm{T}) \tag{2-16}$$

and the transport properties, μ, *k*, and σ, which are functions of temperature and pressure given in tabular form [e.g. [71]].

The above equations together with the supplementary relations fully determine the dynamics of a switching arc in LTE once the boundary and initial conditions are specified.

2.3. The Governing Equations for a Turbulent Switching Arc

2.3.1. The Effects of Turbulence on Arc Behaviour

It has been mentioned previously that it is necessary to introduce turbulence in order to achieve agreement between the predicted and experimentally measured RRRV for SF_6. However, it has been noted that there are other factors which may account for the discrepancy between measured RRRV and that predicted by an LTE arc model based on laminar flow. These factors are concerned with the departure of a switching arc from LTE, which is caused by the rapid variation of gas discharge conditions around current zero [73-75]. The temperature of an SF_6 gas blast arc changes rapidly with a characteristic time of a microsecond [68]. The rates of some chemical reactions inside an SF_6 arc, especially those involving molecules, are not fast enough to follow the change of temperature [73, 75]. Thus, the composition of an SF_6 arc departs from that of LTE, which directly affects electrical conductivity. Electron velocity distribution function in the direction of electric field can depart from Maxwellian velocity distribution function due to the rapid rise of recovery voltage across two contacts after current zero [74]. Electron temperature can also be higher than that of heavy particles after current zero because of high electric field [73]. When these factors are taken into account in an arc model based on non-thermal (two-temperature model) and non-chemical equilibrium assuming laminar flow the predicted electron number density is always higher than that of LTE at the same electron temperature. Thus, RRRV predicted by a non-LTE arc model under laminar flow is much lower than that predicted by LTE model under laminar flow [73].

It is well known that chemical reaction rates can be increased by a few orders of magnitude under turbulent conditions [76]. It is therefore more likely that a turbulent arc is in LTE. Turbulent arc modelling in SF_6 to date is based on the assumption that the arc is in LTE.

Such LTE turbulent arc models have achieved considerable success in predicting the RRRV of SF_6 switching arcs [16, 46, 65].

For gases other than SF_6 very little experimental and theoretical investigation on switching arcs has been reported. The exception is the extensive experimental work on a nitrogen arc burning in a supersonic nozzle at a stagnation pressure of 23 bar by the BBC group [34, 36, 69, 77] and the theoretical investigation of the same arc by Zhang et al [43]. The transient behaviour of this nitrogen nozzle arc is investigated by linearly ramping down the current to zero from 2 kA DC at a rate of -39 A/μs. High speed streak records of the transient arc clearly demonstrate that the arc downstream of nozzle throat is turbulent [77]. However, arc model based on laminar flow can give excellent agreement with the measured temperature and electrical field for a DC 2 kA nitrogen arc [43] as well as the RRRV within the experimental uncertainty [45]. Thus, it appears that turbulence is not necessary for a satisfactory prediction of arc behaviour in nitrogen. However, caution must be exercised in that the effects of turbulence will be more pronounced at low currents [77], hence during current zero period. There appears to be very few reliable RRRV test results on nitrogen. The conclusion on the effects of turbulence given in [45] was based on a single RRRV measurement. Further verification with reliable test results will be required in order to ascertain the role of turbulence in arc interruption in nitrogen.

Experimental work on DC characteristics of air nozzle arc has been reported by Fang el al [41] and on RRRV by Frind and Rich [66]. No rigorous theoretical work on air arcs has so far been reported. Since air is an important industrial gas and is often mixed with other gases in the pursuit of finding a replacement gas for SF_6, the establishment of a satisfactory arc model for air therefore forms part of this thesis. For the same pressure difference across a nozzle the velocity in an air arc can be much higher than that of SF_6 because air density is lower than that of SF_6. Air arc can therefore become more unstable than SF_6 if arc instability is driven by shear layer instability [78]. We therefore discuss in the next section the relevant turbulence models and the governing equations for arcs in turbulent flow.

2.3.2. Turbulence Models

It is believed that the basic equations presented in Section 2.2 can fully determine the characteristics of turbulent flow [78]. However, even with the most powerful computer to date direct numerical solution (DNS) of flow conservation equations is not practical in that the grid size and time step required to resolve the smallest eddies and the highest frequency fluctuations will result in prohibitive computation cost. Modern computers still cannot meet the storage requirement demanded by the spatial resolution of turbulent flows of industrial importance. So far DNS has only been applied to very simple flows [78].

The resemblance between a free jet and a nozzle arc suggests that we follow the same approach for the turbulent free jet to account for enhanced momentum and energy transfer inside a turbulent arc. Although turbulent flow is chaotic, turbulent flow does exhibit certain statistical features. For example, for a number of turbulent flows the time averaged quantities characterising the flow (e.g. velocity) have definite patterns. Of the statistical analysis of turbulent flows time average is the simplest, which was first used by Reynolds over 150 years ago [79]. However, the time averaged flow conservation equations always contain more unknowns than the number of equations available. This is commonly known as the closure problem for turbulent flow [78]. In order to make the number of unknowns equal to the number of equations assumptions will have to be introduced, which results in many turbulence models [78, 80]. There is no theoretical guidance on what closure assumptions should be made. Thus, turbulence models are designed for special applications.

2.3.3. The Governing Equations of Turbulence Models Based on Effective Eddy Viscosity

There are a large number of turbulence models [62, 78, 80]. However, there is no general theoretical guidance regarding the choice of turbulence models for turbulent arcs in supersonic flow. Our choice of turbulence models is restricted to those which have been

applied with success to similar flow conditions as those of an arc burning in a supersonic flow as well as their suitability for engineering application (low computational cost). Thus, we choose those turbulence models which are based on time averaged conservation equations. In the time average momentum equation there is a term given by the time average of the product of fluctuations of velocity components.

$$\bar{\bar{\tau}}_{ij}^{R} = -\rho\langle u_i u_j\rangle = Reynolds\ stress \tag{2-17}$$

where $\langle\ \ \rangle$ represents time average, u_i and u_j are the velocity fluctuations. The above term is equivalent to a stress which is commonly known as Reynolds stress. In order to close the time averaged equations we need to link Reynolds stress with time averaged velocity. There are various ways of doing this, which gives rise to a number of turbulence models [62]. We choose turbulence models which belong to the category of effective eddy viscosity. For these turbulence models Reynolds stresses are linearly linked to the main strain via eddy viscosity by means of Boussinesq hypothesis [78]. Thus, Reynolds stress tensor is given by

$$\bar{\bar{\tau}}^{R} = \mu_t\left[\left(\nabla\vec{V} + \nabla\vec{V}^{T}\right) - \frac{2}{3}\nabla\cdot\vec{V}I\right] \tag{2-18}$$

where $\vec{V}$ is the time averaged velocity vector and μ_t is the eddy viscosity which is related to the length (λ_c) and velocity (V_c) scales characterising the turbulence.

$$\mu_t = \rho\lambda_c V_c \tag{2-19}$$

The closure of time averaged momentum equation needs to find extra relationships to compute the turbulence length and velocity scales. A similar term to Reynolds stress appears in the time averaged energy conservation equations, which represents the enhanced heat transfer by turbulence.

$$Q_j^{R} = \rho\langle u_i h'\rangle = -\frac{k_t}{C_p}\frac{\partial h}{\partial x_i} = -\frac{\mu_t}{Pr_t}\frac{\partial h}{\partial x_i} \tag{2-20}$$

where h' is the fluctuation of enthalpy, h the time averaged enthalpy and k_t the turbulent thermal conductivity. Pr_t is the turbulent Prandtl number.

If the influence of density fluctuation can be neglected the mathematical form of the time averaged conservation equations are almost identical to those given in section 2.2 but with the following modifications to momentum and energy conservation equations:

Time averaged mass conservation:

$$\frac{\partial \rho}{\partial t} + \nabla \cdot \left(\rho \vec{V}\right) = 0 \tag{2-21}$$

Time averaged momentum conservation:

$$\frac{\partial}{\partial t}\left(\rho \vec{V}\right) + \nabla \cdot \left(\rho \vec{V}\,\vec{V}\right) = -\nabla \mathrm{p} + \nabla \cdot \bar{\bar{\tau}} + \vec{J} \times \vec{B} \tag{2-22}$$

$$\bar{\bar{\tau}} = \mu\left[\left(\nabla \vec{V} + \nabla \vec{V}^{T}\right) - \frac{2}{3}\nabla \cdot \vec{V}\bar{\bar{I}}\right] \tag{2-23}$$

where $\mu = \mu_l + \mu_t$, μ_l is the molecular viscosity for laminar flow and μ_t is the turbulence viscosity.

Time averaged energy conservation equation:

$$\frac{\partial}{\partial t}(\rho \in) + \nabla \cdot \left(\vec{V}(\rho \in + p)\right) = \nabla \cdot \left((k_l + k_t)\nabla T + \bar{\bar{\tau}} \cdot \vec{V}\right) + \sigma E^2 - q \tag{2-24}$$

where thermal conductivity consists of molecular (k_l) and turbulent (k_t) thermal conductivity.

There are a number of turbulence models based on eddy viscosity [62, 80]. Of these models Prandtl mixing length model has been shown to be most successful for the modelling of turbulent SF_6 switching arc [64, 65]. The standard k-epsilon model [62, 80] is almost the industrial standard for the modelling of turbulent shear flow. An arc burning in a supersonic nozzle belongs to shear flow. We will apply these two turbulence models

to air switching arc in case laminar flow arc model fails to give satisfactory agreement with experimental results of [41, 66].

2.3.3.1. Prandtl Mixing Length Model

This is the simplest and oldest turbulence model devised by Prandtl in 1925 [79]. In analogy with a round fluid jet, the turbulence length for an axisymmetrical switching arc is chosen as a fraction of the length scale characterizing the arc thermal influence region, which is given by arc's thermal radius [47]:

$$\mathrm{r}_\delta = \left(\frac{\theta_\delta}{\pi}\right)^{0.5} \tag{2-25}$$

where θ_δ the thermal area of the arc defined by

$$\theta_\delta = \int_0^\infty \left(1 - \frac{T_\infty}{T}\right) 2\pi r dr \tag{2-26}$$

where r is the radius and T_∞ is the temperature near the nozzle wall at which the radial gradient is negligible.

The turbulence length scale is given by

$$\lambda_c = c\mathrm{r}_\delta \tag{2-27}$$

where c is a turbulence parameter the value of which is to be adjusted to fit the experimental results.

The velocity scale of turbulence is a function of the length scale and the mean velocity gradient. For an axisymmetrical arc this is given by

$$V_c = \lambda_c \left(\left|\frac{\partial w}{\partial r}\right| + \left|\frac{\partial v}{\partial z}\right|\right) \tag{2-28}$$

where w and v are respectively the axial and radial velocity components. Thus eddy viscosity can be calculated and turbulent thermal conductivity is also determined by usually assuming Pr_t=1.

2.3.3.2. Standard k-epsilon Model

The standard k-epsilon model introduces two additional equations to the time averaged conservation equations: one describes the conservation of turbulent kinetic energy per unit mass and the other turbulence dissipation rate:

$$\frac{\partial}{\partial t}(\rho ke) + \nabla \cdot \left(\rho ke \vec{V}\right) = \nabla \cdot \left(\left(\mu_l + \frac{\mu_t}{\sigma_{ke}}\right)\nabla ke\right) + G_{ke} - \rho\varepsilon \tag{2-29}$$

$$\frac{\partial}{\partial t}(\rho\varepsilon) + \nabla \cdot \left(\rho\varepsilon \vec{V}\right) = \nabla \cdot \left(\left(\mu_l + \frac{\mu_t}{\sigma_\varepsilon}\right)\nabla\varepsilon\right) + C_{1\varepsilon}G_{ke}\frac{\varepsilon}{ke} + C_{2\varepsilon}\rho\frac{\varepsilon^2}{ke} \tag{2-30}$$

where

$$\mu_t = \rho C_u \frac{ke^2}{\varepsilon} \tag{2-31}$$

The generation of the turbulence kinetic energy G_k is related to the rate of strain, which is given by Equation (2-32) below for an axisymmetrical arc

$$G_{ke} = \mu_t \left[2\left(\frac{\partial w}{\partial z}\right)^2 + 2\left(\frac{\partial v}{\partial r}\right)^2 + 2\left(\frac{v}{r}\right)^2 + \left(\frac{\partial w}{\partial r} + \frac{\partial v}{\partial z}\right)^2\right] \tag{2-32}$$

2.4. Approximate Radiation Transport Model and Review of Radiation Data

2.4.1. Radiation Transport in High Pressure Arc

It is now well established that in high pressure arcs radiation transport is an important energy transport mechanism (Hermann [69], Shayler and Fang [81] and Zhang [43]). The calculation of net radiation loss in the energy conservation equation requires the calculation of the divergence of the radiation flux vector:

$$\mathrm{q} = \nabla \cdot \vec{\mathrm{F}} = \int_0^{\infty} \int_0^{4\pi} I_\nu \vec{n} d\nu \, d\Omega \tag{2-33}$$

where I_ν is the spectral radiation intensity, $\vec{n}$ is unit vector in the direction of the ray, ν the frequency and Ω the solid angle and $\vec{\mathrm{F}}$ the radiation flux vector.

The spectral radiation intensity I_ν is found by integrating the radiate energy conservation equation

$$\frac{\partial I_\nu}{\partial n} = \epsilon_\nu - k'_\nu I_\nu \tag{2-34}$$

along the ray path $\vec{n}$ using the boundary condition that no radiation enter the arc (Figure 2-1).

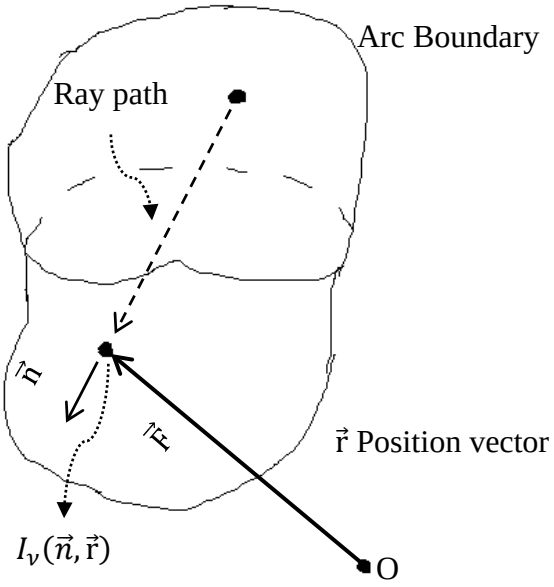

Figure 2-1 Spectral radiation intensity starting from the arc boundary

In Equation (2-34) ϵ_ν is the emission of radiation which for arcs in LTE is given by

$$\epsilon_\nu = k'_\nu B_\nu \tag{2-35}$$

where B_ν is the Planck function:

$$B_\nu(T) = \frac{2h_p\nu^3}{c_{light}^2}\frac{1}{e^{\frac{h_p\nu}{k_bT}}-1} \tag{2-36}$$

where h_p is the Planck's constant, c the speed of light in vacuum and k_b the Boltzmann's constant.

k'_ν in Equation (2-35) is the effective spectral absorption coefficient which includes stimulated emission. It is given by

$$k'_\nu = k_\nu\left(1 - e^{-\frac{h_p\nu}{kT}}\right) \tag{2-37}$$

where k_ν is the spectral absorption coefficient. The calculation of k_ν requires a knowledge of arc plasma composition at the given temperature and pressure and the

spectral data in terms of line profile, molecular band structure and continuum radiation. For high pressure arcs, the frequency range for the calculation of k_ν spans from infrared to vacuum ultra violet [81]. Typical spectra distribution of k_ν at a fixed temperature and pressure for air is given in Figure 2-2 [82].

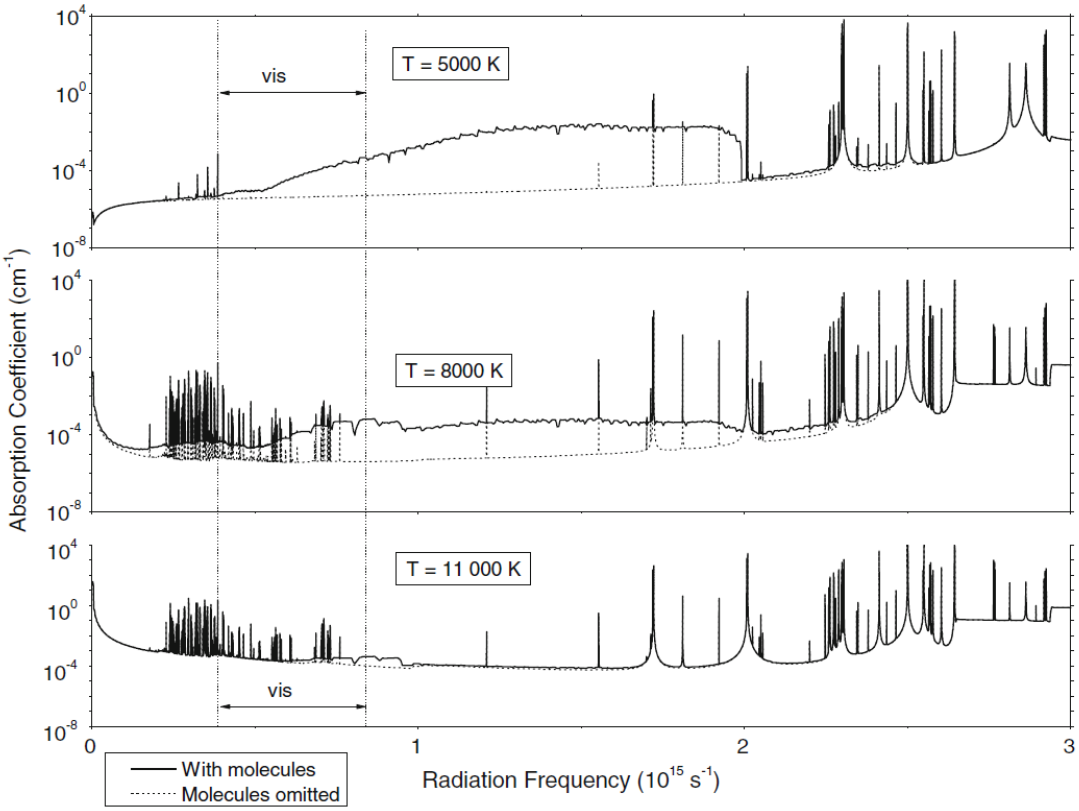

Figure 2-2 Contribution of molecular species to the spectral absorption coefficients of radiation in air plasma at various temperatures as a function of the radiation frequency at the plasma pressure of 0.1 MPa. The figure is taken from Aubrecht [82].

In order to compute the radiation flux vector at a given point inside the arc it requires:

(1) The solution of radiant energy conservation equation at a given frequency along a ray path defined by a unit vector n from the arc boundary to the point of interest (Figure 2-1). In order to compute K_ν at a point along the ray one needs to compute the plasma composition for the given temperature and pressure as well as the relevant photo absorption cross sections.

(2) The direction of the ray path needs to cover a solid angle of 4π for the chosen frequency at a given point. Thus it requires the solution of the said equation in 3-dimension

(3) The solution of radiant energy conservation equation needs to cover the whole arc spectra.

(4) In order to resolve the rapid variation of k_ν (similar to a delta function, Figure 2-2) the frequency intervals need to be very small in order to calculate radiation flux vector sufficiently accurately (see the integration with respect to frequency in Equation (2-33)). The computation cost is therefore prohibitively high. In addition, such an approach is perhaps not worth pursuing as the arc in a circuit breaker is often contaminated by electrode and nozzle vapour the distribution of which cannot be predicted with high accuracy due to the uncertainty in the calculation of the erosion rate of electrode and nozzle wall. If turbulence is important the turbulent diffusion coefficients of electrode and nozzle wall vapour in the arcing gas are difficult to estimate. A simplified radiation transport model needs to be found for arc simulation.

The usual simplification for radiation transport is to assume radiation either optically thin or thick. Such simplification is not valid in the arc context as arc radiation is dominated by the lines which are neither optically thin nor thick. In recent years P1 model [83] and partial characteristics (a simplified 3-D calculation, [84]) have been applied to arc without much success [85]. Since the semi-empirical radiation transport model of [43] has been successfully applied to nitrogen [43] and SF_6 [64, 85], we use the same approach for the computation of net radiation loss in arc energy conservation equation for air.

2.4.2. **Approximate Radiation Transport Model**

The radiation transport model of [43] is based on the detailed calculation of radiation transport within a wall stabilized arc [69, 81] and [42] and the experimental results of [69] on a nitrogen nozzle arc. At a given arc cross section, radiation transport is divided into an arc core region and a radiation absorption region as shown in Figure 2-3.

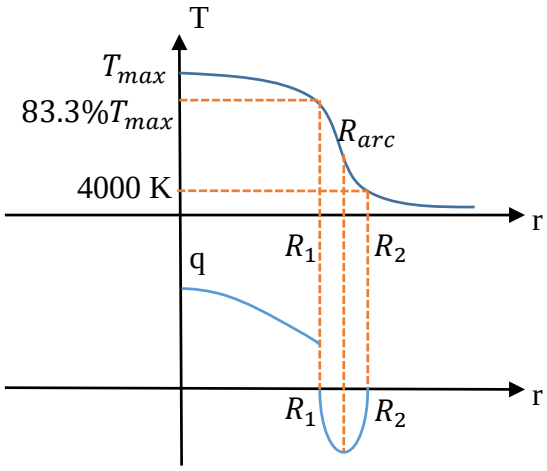

Figure 2-3 Schematic diagram showing the approximate radiation model.

(1) Arc Core Region:

The arc core region is defined as from the axis to the arc core boundary, R_1, which is defined as the position at which the temperature is 83.3% of the axis temperature. The net radiation loss per unit volume and second, q, inside this core is assumed to be related to the net emission coefficient, ε_q, (NEC) for a given arc radius, temperature and pressure by:

$$q_e = 4\pi\varepsilon_q(p, T, R_{arc}) \tag{2-38}$$

where radiation arc radius R_{arc} is defined by

$$R_{arc} = \frac{R_1 + R_2}{2} \tag{2-39}$$

where, R_1 and R_2 are the arc core boundary and the arc electrical boundary, respectively. The arc electrical boundary is defined as the radial position at the temperature is 4,000 K. The radiation flux, Q, at the core boundary is given by:

$$Q = \int_0^{R_1} q_e 2\pi r dr \tag{2-40}$$

(2) Radiation Re-absorption Region:

The radiation absorption region is defined as the region between the arc core boundary and the arc electrical boundary. In Figure 2-3, the absorption region is bounded by R_1 and R_2. The distribution of radiation absorbed per unit volumn and time in this region is given by

$$\frac{q_a(r)}{q_0} = 1.1 - \left(\frac{R_1 + R_2 - 2r}{R_2 - R_1}\right)^2 \tag{2-41}$$

where

$$q_0 = \frac{Q \times PCT}{A_{eq}} \tag{2-42}$$

where PCT is the percentage of the radiation energy flux at the arc core boundary, Q, absorbed in this region. A_{eq} is the equivalent area within which the amount of radiation, $Q \times PCT$, is absorbed. This area is defined by

$$A_{eq} = \int_{R_1}^{R_2} \left[1.1 - \left(\frac{R_1 + R_2 - 2r}{R_2 - R_1}\right)^2\right] 2\pi r dr \tag{2-43}$$

For the whole arc region, we can define q is positive indicating radiation loss (q_e). Then, we have

$$q = \begin{cases} q_e, & r \le R_1 \\ -q_a, & R_1 < r \le R_2 \end{cases} \tag{2-44}$$

2.4.3. Critical Review of Air Net Emission Coefficients by Different Authors

2.4.3.1. Net Emission Coefficient for Air

The concept of net radiation emission coefficient was first introduced by Liebermann and Lowke [42]. It is assumed to be a function of pressure, temperature and arc radius. Net emission coefficient is calculated and given in tabular form by computing the net emission coefficient on the axis of an infinitely long, isothermal cylindrical arc confined by a solid wall at room temperature. As indicated in the discussions on air transport properties (section 2.5), net emission coefficients also differ widely depending on the authors. Since net emission coefficient is an important parameter for radiation transport a critical review of air net emission coefficients is given below.

Since dry air contains about 78% of nitrogen, the NEC for air can be close to nitrogen. For nitrogen, there are experimentally derived NEC (Ernst et al [86]) for comparison with those derived theoretically. This provides a check on the reliability of spectral data associated with nitrogen by different authors (Shayler and Fang [81], Aubrecht et al [82] [87], Gleizes et al [88] [89], Billoux et al [90], Naaghizadeh et al [91] and Peyrou et al [92]).

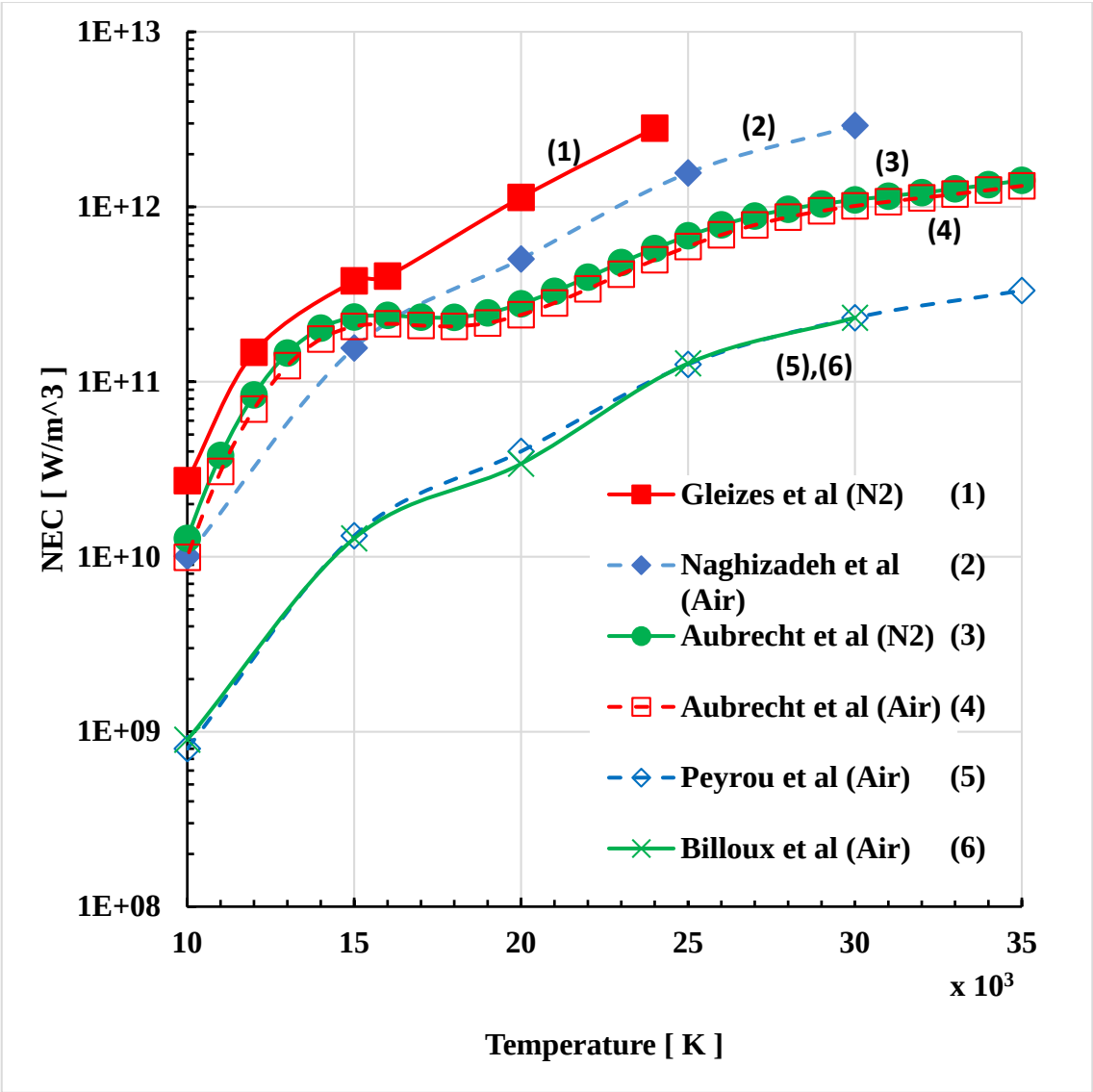

Figure 2-4 Comparison of NEC for N_2 and Air for R = 0 (no radiation absorption) and P =1 atm taken from various authors: (1) [88], (2) [91], (3) [87], (4) [82], (5) [92], (6) [90]

Figure 2-4 gives the NEC for an infinitely thin arc (zero arc radius). Thus, there is no radiation absorption. The differences in NEC between different authors are therefore entirely due to the differences in spectra data used for the calculation of k'_ν and atomic and molecular data required for the computation of plasma composition. Much of the spectral data is calculated by different authors, the details of which are not given in the published literature. It is therefore not possible to judge the relative merits of the spectral data used by different authors. However, for nitrogen we will use the experimental results

of Ernst et al as a judge for the accuracy of nitrogen NEC. It should be noted that net emission coefficient is given by the integration of $B_\nu k'_\nu$ over arc spectra. Higher emission means a higher average absorption coefficient. Therefore, it is expected that higher emission will result in higher absorption when arc is of a certain size.

Of the data given in Figure 2-4 the emission coefficient for air at zero arc radius calculated by Naghizadeh et al [91] is the highest for T>15,000 K, which is an order of magnitude higher than those of Peyrou et al [92] and Billoux et al [90]. The net emission coefficient of Aubrecht et al [82] is above that of Naghizadeh et.al [91] for T < 15,000 K. Also plotted in Figure 2-4 is the net emission coefficient by Gleizes et al [88] at zero arc radius for Nitrogen. On the whole radiation of nitrogen is stronger than that of air.

Net emissions coefficients from different authors for a 1 mm radius arc are given in Figure 2-5. Compared with emission at zero arc radius (Figure 2-4), the differences between net emission coefficients by different authors for the 1 mm radius arc are reduced because of radiation absorption. This is expected as the average absorption coefficient for the whole spectra for higher emission is also higher. The net emission coefficients for nitrogen with the same arc radius from different authors (Aubrecht et al [87], Gleizes et.al [88] and Shayler and Fang [81]) together with the experimental results of Ernst et al [86] are given in Figure 2-5. The net emission coefficient of Shayler and Fang for nitrogen is closest to the experimental results of Ernst et.al. Net emission coefficient of Shayler and Fang is still on average lower than that of Ernst el.al by a factor of 2. Thus, for radiation transport calculation in nitrogen arc it is recommended that a factor of 2 be multiplied to the emission coefficient of Shayler and Fang.

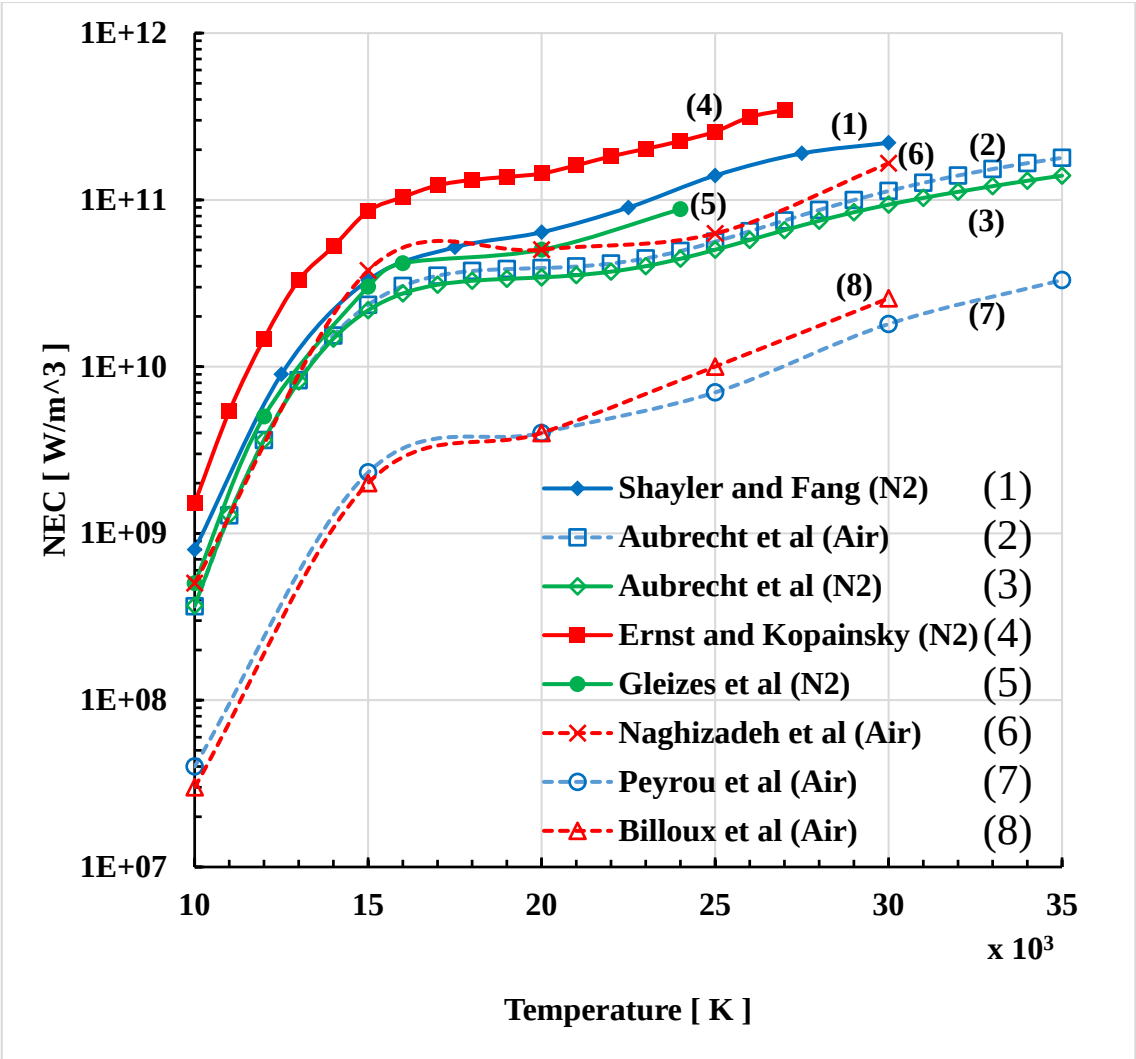

Figure 2-5 Comparison of NEC computed by different authors for N_2 and Air with an arc radius of 1 mm at P =1 atm. Curves: (1) [81] ,(2) [82], (3) [87], (4) [86], (5) [88], (6) [91], (7) [92] and (8) [90].

2.4.3.2. Comparison between NEC Data of N_2 and Air

Results of emission of radiation at 1 atm for nitrogen and air computed by different authors are plotted in Figure 2-4 for comparison. Radiation emission of nitrogen is higher than that of air. The differences between nitrogen and air for a 1 mm radius arc are not significant for the results of Aubrecht et.al [82], but quite appreciable for Gleizes et.al [88] and Naghizadeh et al [91]. It indicates that the average absorption coefficient over the whole arc spectra for nitrogen is higher than that of air. When radiation absorption is important one would expect that the differences between the net emission coefficients for

nitrogen and air would become smaller than that shown in the emission for these two gases (Figure 2-4) as more radiation will be absorbed by nitrogen due to higher average absorption coefficient. This is shown in Figure 2-5, where the net emission coefficients for nitrogen and air are plotted for an arc with a radius of 1 mm. The results of Aubrecht et al [87] for air are slightly higher than those for nitrogen indicating that radiation due to species associated with oxygen is less absorbed. The results of Gleizes et al [88] and Naghizadeh et al [91] show no systematic trend but the net emission coefficients for nitrogen and that for air are very close for arc with 1 mm radius. It should also be noted that the differences between the results of Aubrecht et al [87] and those of Gleizes et al [88] are greatly reduced in comparison with the emission results with absorption. When radiation absorption is important, the differences between the calculated net emission coefficients by different authors ([87, 88, 90-92]) for nitrogen and air can be considered negligible due to the uncertainty of the atomic and molecular data for photon absorption. It is not known why the net emission coefficients of Billoux et al [90] and Peyrou et.al [92] are an order of magnitude lower than others.

There are no experimentally derived net emission coefficients for air. Since net emission coefficients for air and nitrogen can be considered virtually the same for arcs of finite dimension, the experimental results for a 1 mm radius nitrogen arc of Ernst et al [86] should be taken as the true net emission coefficients for air arc of the same radius. As previously indicated, the net emission coefficients of Ernst et al are close to twice of those of Shayler and Fang. Therefore, for computing the net radiation loss in air arcs within the air arc core we multiply the net emission coefficients of Shayler and Fang given at 1 atm and 10 atm by a factor of 2. Interpolation or extrapolation of the results of [81] is used to calculate the net emission coefficient at pressures other than 1 atm and 10 atm.

2.5. **Review of Transport Properties**

Material properties (thermodynamic and transport properties) together with radiation characteristics of high temperature gas determine the features of arc discharge at high

pressure. For arcs burning in a nozzle at a current of a few hundred amperes or above electrical power input into the arc is balanced by enthalpy transport and radiation loss. Enthalpy transport depends on the product of density and enthalpy. Electrical input depends on the temperature distribution inside the arc as electrical conductivity is determined by temperature at a given pressure. This close link between electrical conductivity and arc temperature determines the electrical behaviour of the arc. Of the other transport properties viscosity is usually not important as viscous stress can be neglected for convection dominated arc such as that in a supersonic nozzle (Zhang et al [43]). However, if the cause of turbulence in arc discharges is hydrodynamic in nature, viscosity is important in determining the onset of instability [79]. For high pressure arc discharges thermal conduction is negligible in comparison with radiation loss. Thus, in our search for an alternative arcing gas to SF_6 we need to compare the capability of enthalpy transport, radiation characteristics and viscosity of a potential replacement gas with those of SF_6. We therefore need to have reliable sources of material properties for computer simulation.

For high pressure arc discharges temperature can reach 25,000 K. It is therefore necessary, for computer simulation of arc discharges, to provide thermodynamic properties (density and enthalpy), electrical conductivity and viscosity for a temperature range from ambient to 30,000 K at a given pressure. It is not possible to provide this information by experimental measurements at such high temperature. Thermodynamic and transport properties are obtained by computation assuming that the high temperature gas is at LTE. The properties of high temperature air were first given by Yos in 1963 [71], which were revised in 1967 [93]. Devoto [94] computed air electrical conductivity, which was found to be higher than that of Yos [93]. There were little activities in this area following the publication of the paper of Devoto [94]. However, there seemed to be a surge of activities in the calculation of high temperature gas properties in 1995 firstly by Murphy [95], which was then followed by Capitelli [96], D'Angola [97] and by Wang [98]. This surge of activities is due to the use of high temperature gas for material processing, environment related studies and the search of a replacement gas for SF_6 in circuit breakers.

There are appreciable differences between computed properties of high temperature air given by different authors. The differences in electrical conductivity can reach a factor of 2 at 30,000 K (Figure 2-6). Such differences are due to the different electron momentum collision cross sections with heavy particles and different gas compositions used by different authors. It is difficult for a user of the material properties to make a judgment regarding the reliability and accuracy of collision cross section data and atomic and molecular data employed by different authors. It is fortunate that experimentally derived electrical conductivity for nitrogen (Morris et al 1970 [99]) and air (Devoto et al 1978 [100]) is available for comparison with the computed electrical conductivity for a temperature range up to 14,000 K. For nitrogen, electrical conductivity given by Yos is in good agreement with experimental results (Fig. 3 of Morris [99]). Since nitrogen is a major component of air, the good agreement between Yos data and experimental results indicates that electron momentum collision cross sections with nitrogen ions, atoms and molecules and the nitrogen composition in this temperature range are close to reality. Since the same data necessary for the computation of air composition and electrical conductivity related to the contribution due to nitrogen will be used for the computation of air composition and electrical conductivity, this implies that Yos data for air is perhaps more reliable as far as nitrogen related processes are concerned. This is proven by a direct comparison of Yos electrical conductivity for air with the experimental results at 1 atm as shown in Figure 2-6. The good agreement of Yos air electrical conductivity with experimental results shows that the air composition of Yos is also computed properly, which results in the right values for thermodynamic and transport properties. Thus, Yos data will be adopted for the simulation of air arcs.

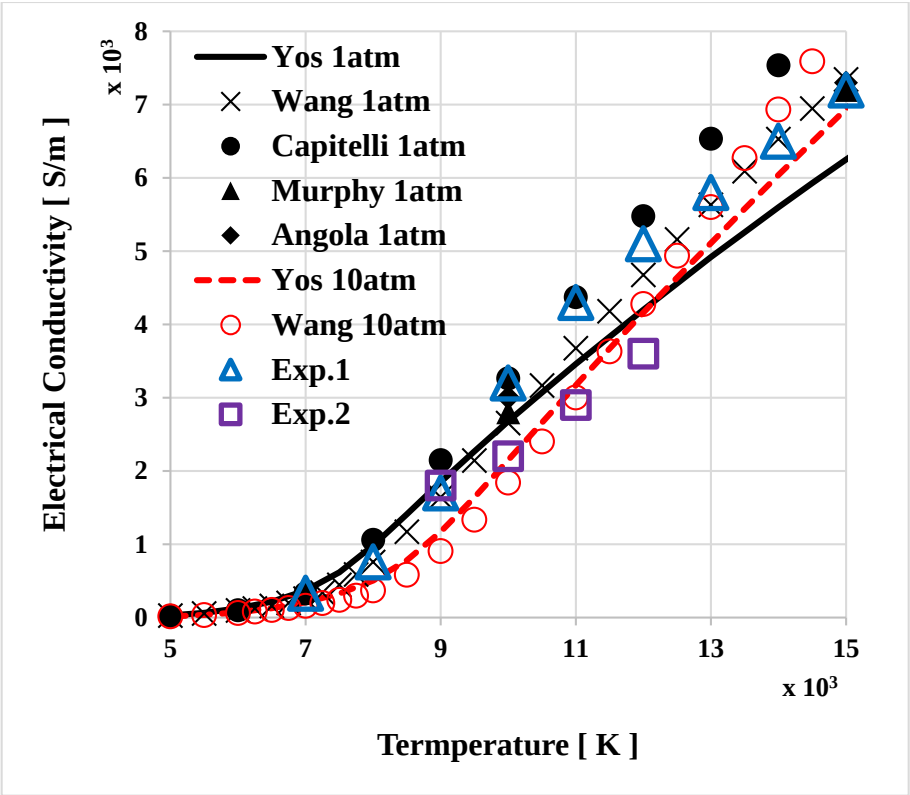

Figure 2-6 Air electrical conductivity from different sources and pressure levels. Exp.1 and Exp.2 refer to experiment measurements of Asinovsky et al [101] and Schreiber et al [102], respectively.

The product of density (ρ) and enthalpy (h) and kinematic viscosity for air are given in Figure 2-7 and Figure 2-8 respectively, where the corresponding values of SF_6 are also given for comparison. It should be noted that below 7,000 K ρh of SF_6 is higher than that of air and above this temperature this trend is reversed. In fact, ρh of air is on average 50% larger than that of SF_6 in the temperature range from 7,000 K to 20,000 K and there is little difference between these two gases for temperature above 20,000 K. Since air density is small than that of SF_6, air velocity could be much larger than that of SF_6 under the same pressure difference across the nozzle. This implies that enthalpy transport as an energy removal process could be more important in air arcs than in SF_6 in the high temperature region of the arc.

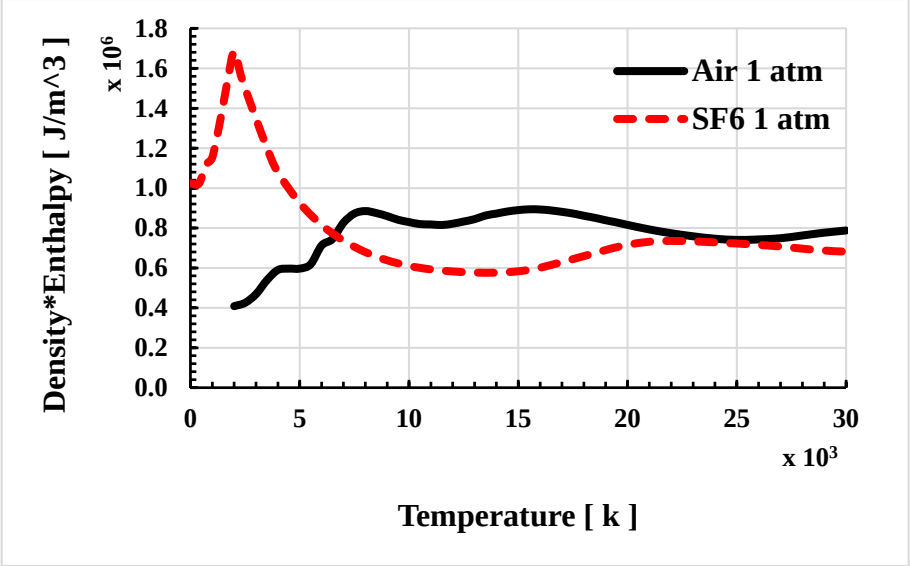

Figure 2-7 The product of density and enthalpy of air and SF_6 at 1atm

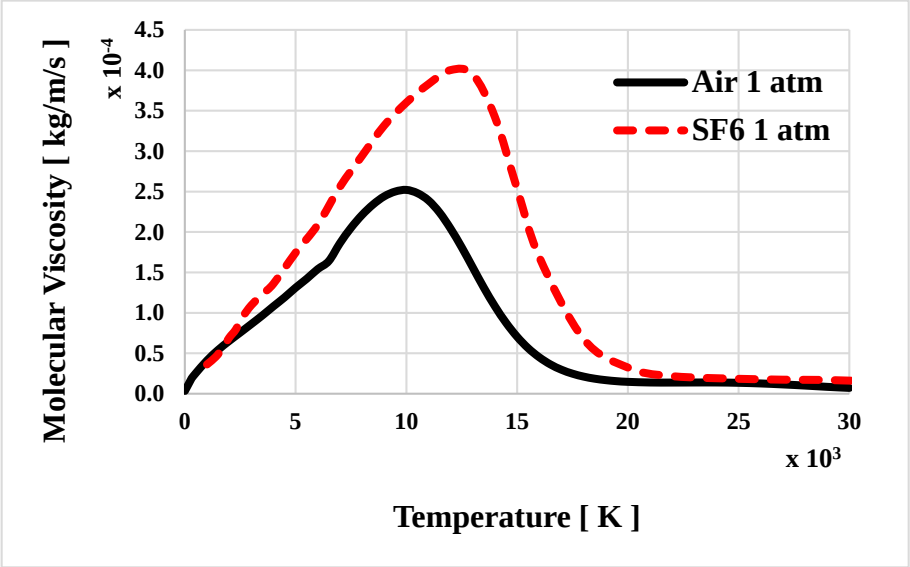

Figure 2-8 The molecular viscosity of air and SF_6 at 1atm

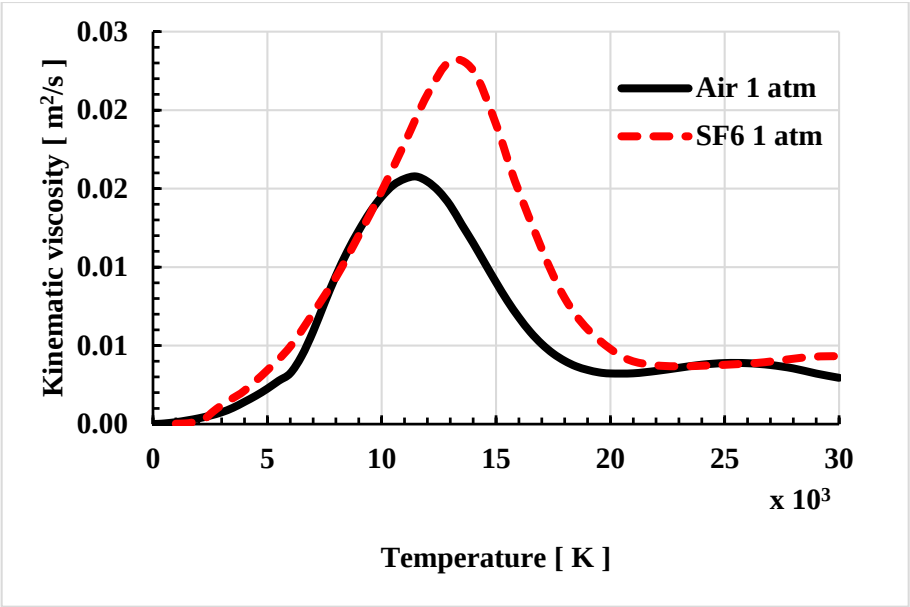

Figure 2-9 Kinematic viscosity of air and SF_6 at 1atm

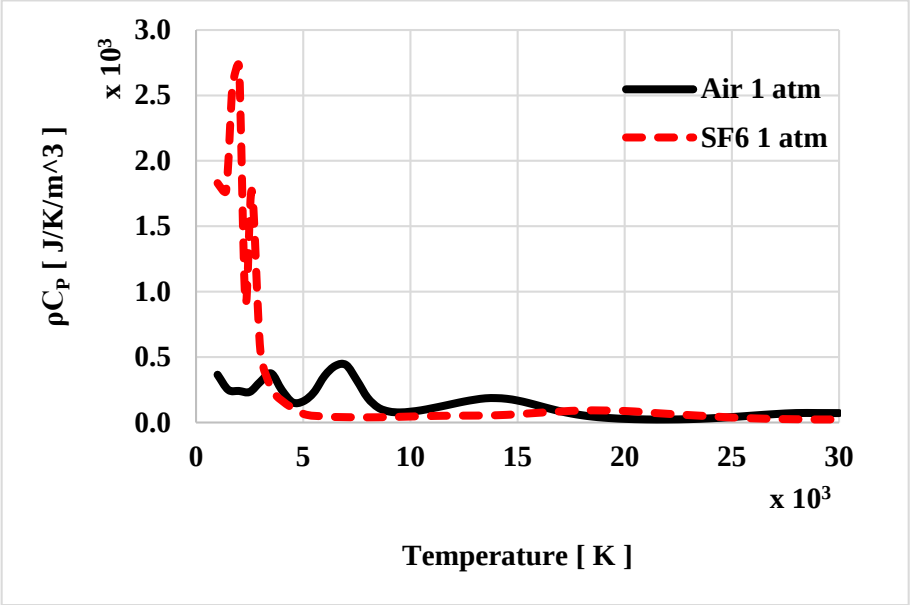

Figure 2-10 The product of density and specific heat capacity at constant pressure of air and SF_6 at 1atm

Table 2-1 Kinematic viscosity for air (Unit: m^2/s) at lower temperature range

	300 K	500 K	1,000 K
AIR	1.64E-6	3.86E-5	1.26E-4
SF_6	2.60E-6	4.90E-6	2.32E-5

Kinematic viscosity (Figure 2-9) is an important quantity in the determination of the stability of a flow. Since nozzle arc is similar to a round fluid jet, the stability of the jet flow depends on the critical Reynolds number. Kinematic viscosities for air and SF_6 for temperature up to 1,000 K are tabulated in Table 2-1. Although in a small range of temperature (approximately 400 K - 1,000 K) kinematic viscosity of SF_6 is lower, kinematic viscosity for air in the temperature range encountered from 1,000 K to 25,000 K encountered in nozzle arcs is on the whole lower than that of SF_6. For the same pressure difference across a nozzle velocity in air arc will be higher than that of SF_6 because of air density is much lower. Thus, critical Reynolds number for air nozzle arc with the same pressure difference as that of SF_6 nozzle arc will be higher than that of SF_6 nozzle arc. Air nozzle arc is therefore to be more unstable than SF_6 nozzle arc.

Other thermodynamic (enthalpy, density, and specific heat at a constant pressure) and transport properties (electrical conductivity, viscosity and thermal conductivity) of air from Yos [71] at 1 atm and 10 atm are given respectively in Figure 2-11 to Figure 2-16. Numerical experiments show that the difference in the computed arc voltage using pressure dependent thermodynamic and transport properties and that using those fixed at 10 atm is less than 15%. Since for switching arc applications the pressure within the nozzle would be close to 10 atm the aforementioned properties for air at 10 atm will be used to obtain computational results. In addition, error in arc voltage measurement would be no less than 15% due to short to short variation. Thus, the use of air gas properties at 10 atm is considered acceptable.

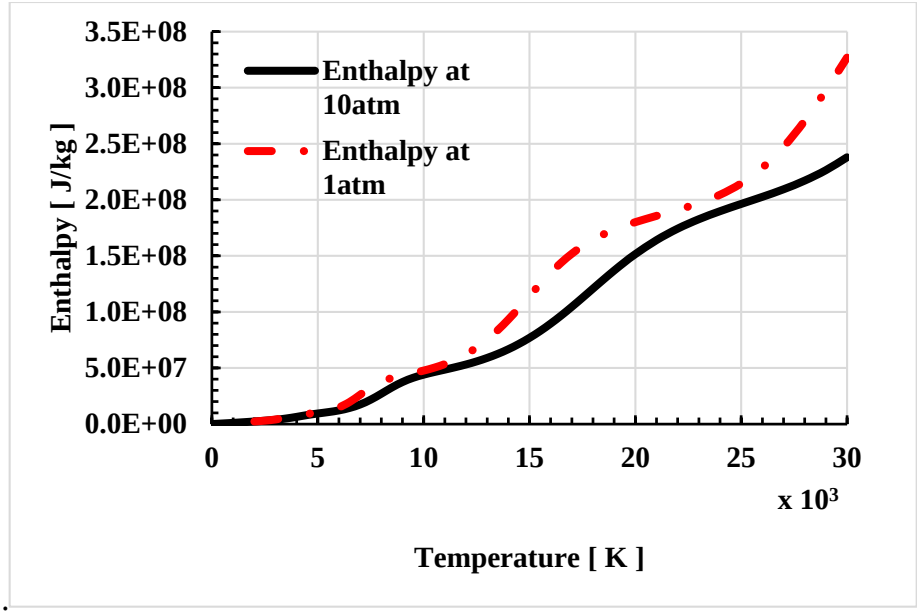

Figure 2-11 Enthalpy per unit mass of air plasma as a function of temperature for pressure at 10 atm and 1 atm taken from [71].

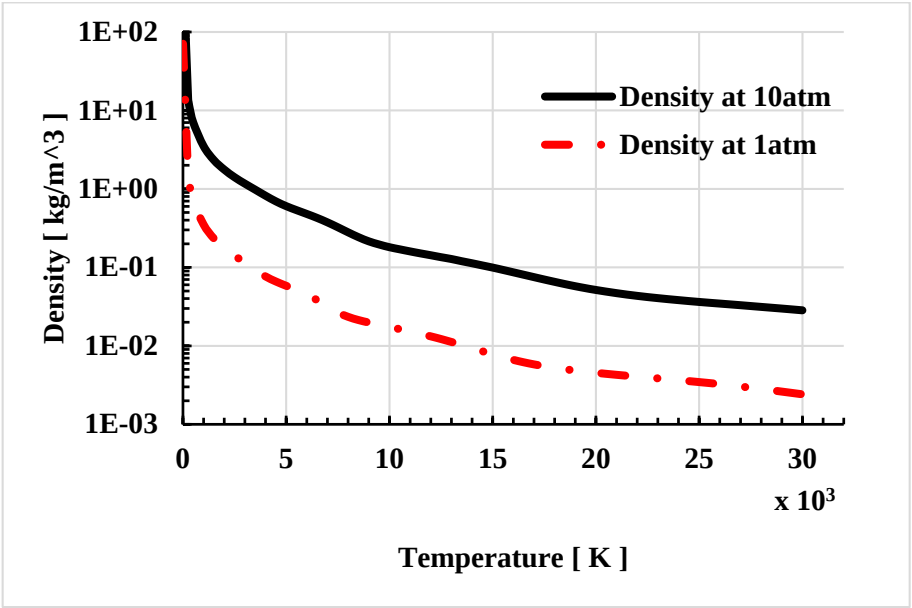

Figure 2-12 Density of air plasma as a function of temperature for pressure at 10 atm and 1 atm taken from [71].

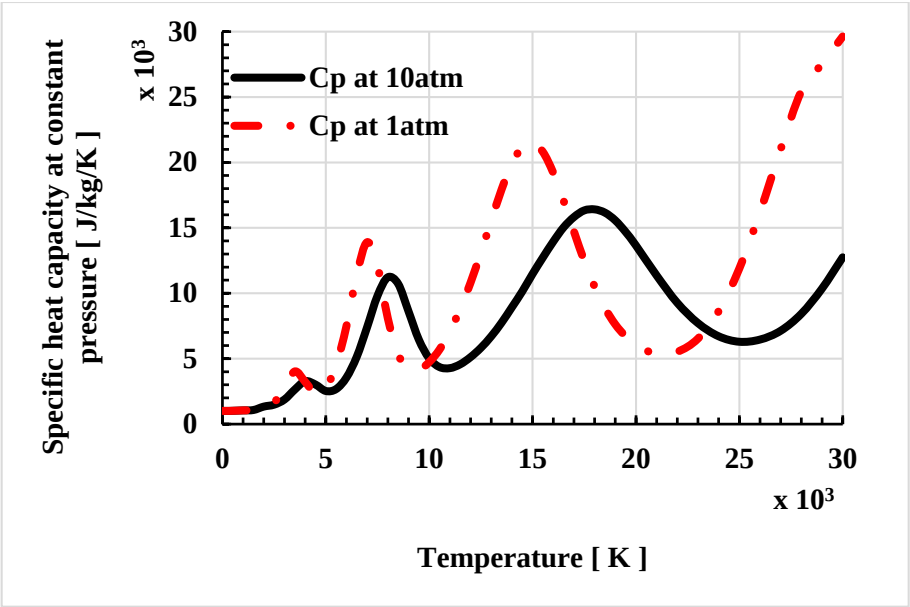

Figure 2-13 Specific heat capacity at constant pressure of air plasma as a function of temperature for pressure at 10 atm and 1 atm taken from [71].

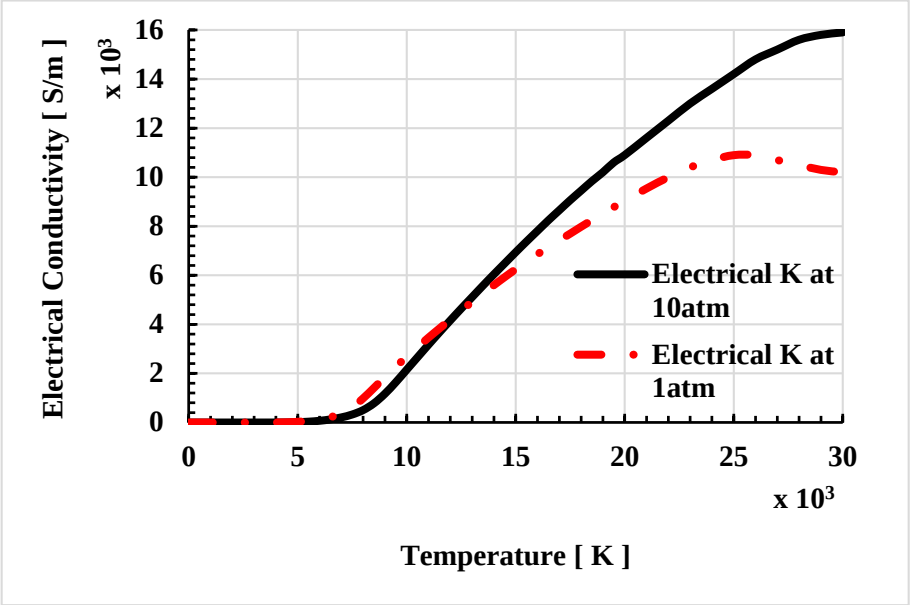

Figure 2-14 Electrical conductivity of air plasma as a function of temperature for pressure at 10 atm and 1 atm taken from [71].

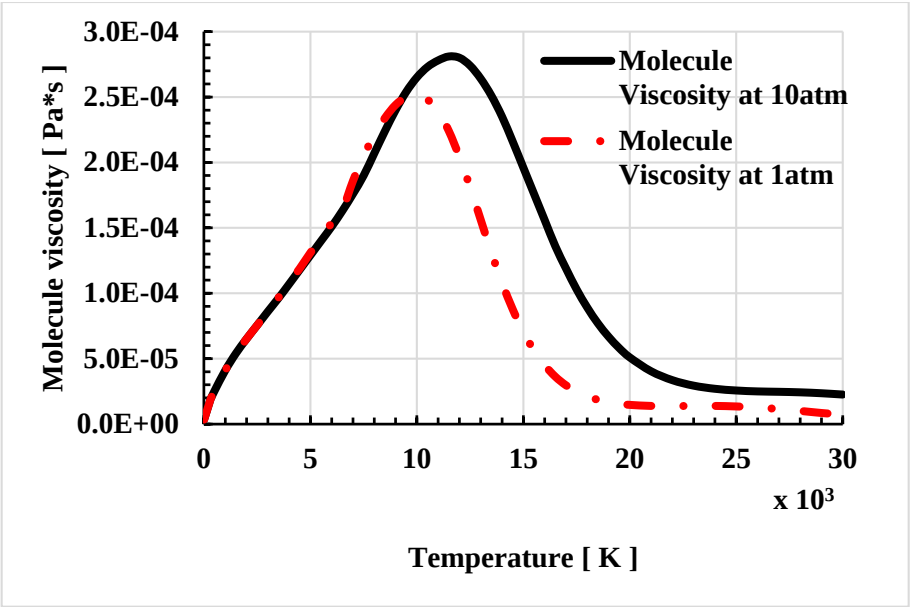

Figure 2-15 Molecule viscosity of air plasma as a function of temperature for pressure at 10 atm and 1 atm taken from [71].

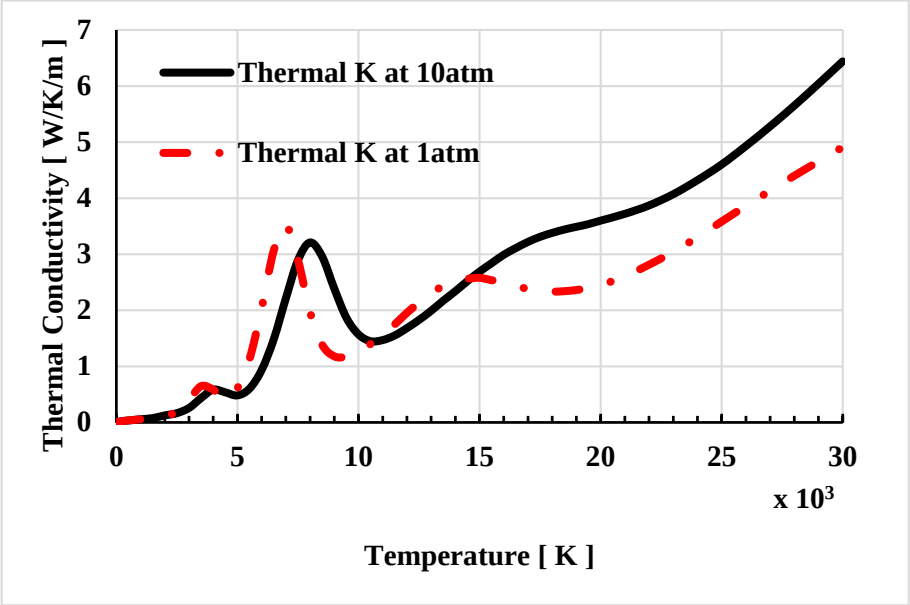

Figure 2-16 Thermal conductivity of air plasma as a function of temperature for pressure at 10 atm and 1 atm taken from [71].

ρC_p for air and SF_6 at 1 atm is shown in Figure 2-10. It should be noted that that the peaks of ρC_p for these two gases occur at different temperatures. If turbulent effects are

important these peaks can influence the temperature profile through turbulent hear conductivity, which directly affects the arc conductance.

2.6. Experimental Results used for Verification of the Arc Model

The verification of the arc model requires extensive reproducible experimental results covering a wide range of test conditions. Such experimental data is very scarce for air switching arcs. Of the very limited test results, Fang et al [41] have reported the voltage measurements of a DC air arc in a supersonic nozzle, and Frind and Rich [66] have reported RRRV measurements for a nozzle interrupter. These experimental conditions have been chosen for the study of this thesis.

The experimental investigations of [41, 66] are based on a two-pressure nozzle-electrode configuration as shown in Figure 2-17. Such a two-pressure system eliminates pressure transients caused by wave reflections within a circuit breaker which inevitably affects the arc in the nozzle interrupter. The reason for choosing such two-pressure system, instead of a full scale circuit breaker, for our investigation is that, in a full scale circuit breaker, e.g. a puffer type circuit breaker and/or an auto-expansion circuit breaker, the arc in the nozzle interrupter is often subject to pressure waves generated in other parts of the breaker due to interaction between the nozzle interrupter and the rest of the breaker. Under such circumstances, it is difficult to analyse the behaviour of the arc itself and the dominant energy transport processes due to the aforementioned interaction. To avoid such complications and focus our attention on the dominant energy transport processes inside the arc, especially on analysing the role of turbulence, we study the nozzle arc in a two pressure system.

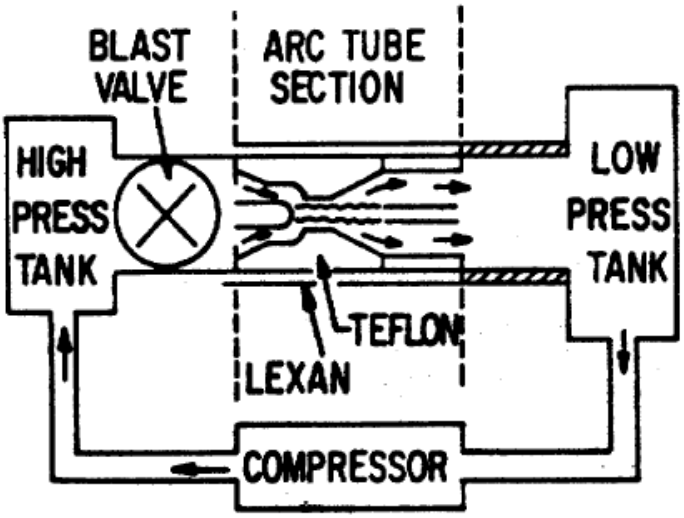

Figure 2-17 Schematic diagram of two pressure system used in the experiments of [41, 66].

Altogether, arcs in two nozzles, i.e. the nozzle of Fang et al [41] (Figure 2-18 (a)) and the nozzle of Frind and Rich [66] (Figure 2-19 (a)), will be computationally studied in the present investigation. For the nozzle of Fang et al [41], measured DC arc voltages are obtained for a range of currents and at 3 stagnation pressures. Typical results of measured DC arc voltages are plotted in Figure 2-18 (b) for P_0 = 10 bar.

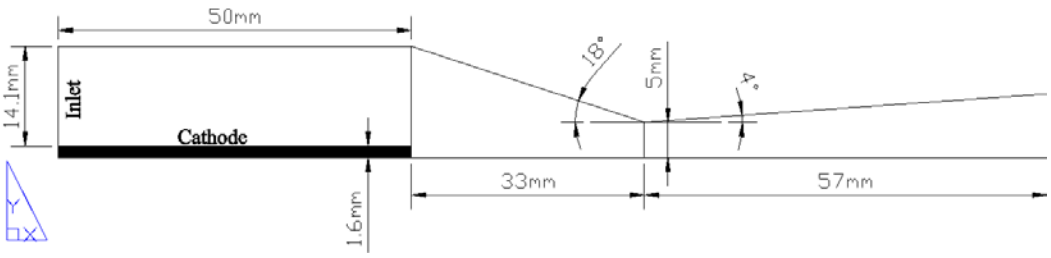

(a)

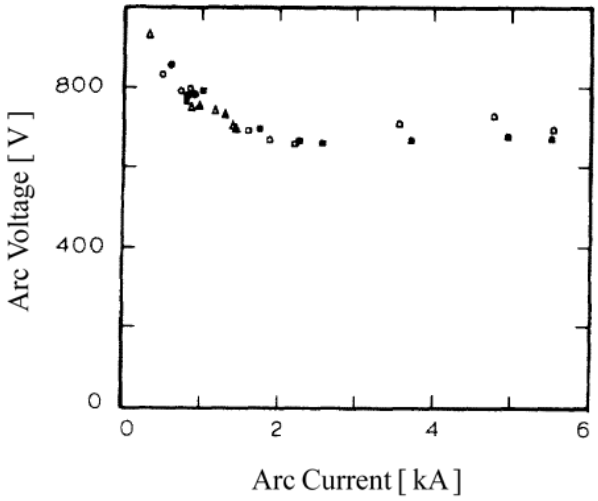

(b)

Figure 2-18 (a) Nozzle geometry used in the experimental investigation of Fang et al [41] and (b) the measured DC arc voltages at P_0 = 10 bar.

For the nozzle of Frind and Rich, measured values of RRRV of the nozzle interrupter are obtained for stagnation pressures ranging from 7.8 atm to 37.5 atm and the rate of current decay, di/dt, ranging from 6 A/μs to 27 A/μs, with both air and SF_6 as interruption media. The experimental results of Frind and Rich enables the comparative study of the arc behaviour in both air and SF_6, the details of which will be presented in Chapter 6.

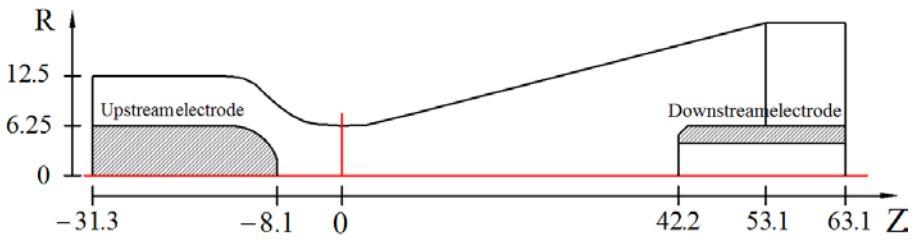

(a)

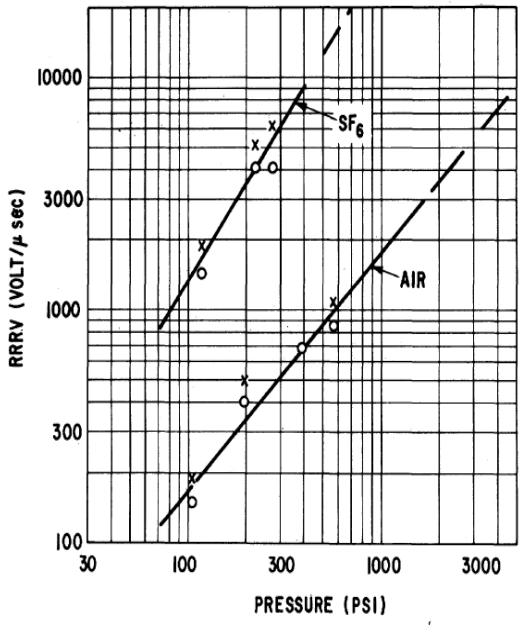

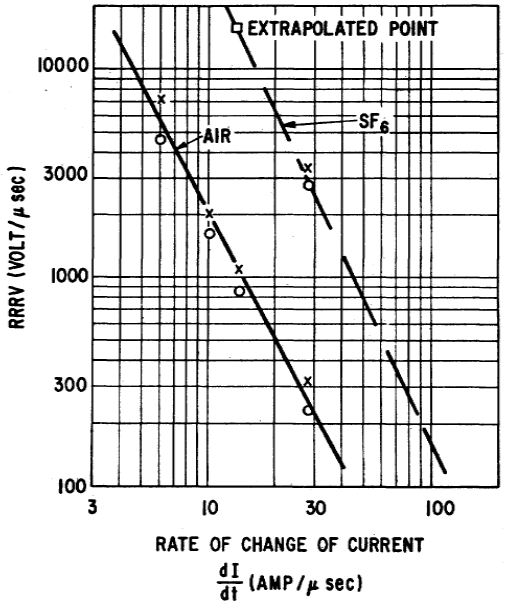

(b) (c)

Figure 2-19 (a) Nozzle geometry used in the experimental investigation of Frind and Rich [66] and (b) the measured RRRV of the nozzle interrupter as a function of stagnation pressure at di/dt =13.5 A/μs with both air and SF6 and (c) the measured RRRV of the nozzle interrupter as a function of di/dt at P_0=37.5 atm with both air and SF_6.

The scatter of experimentally measured RRRV is not mentioned in [66]. We therefore evaluate the experimental scatter for the measured RRRV (in terms of percentage difference) at a particular set of discharge conditions by using the following relation:

$$\text{Experimental scatter} = \frac{\left|RRRV_{ignite} - RRRV_{clear}\right|}{\left(RRRV_{ignite} + RRRV_{clear}\right)/2} \qquad (2\text{-}45)$$

where $RRRV_{clear}$ is the measured RRRV for thermal clearance, and $RRRV_{ignite}$ is the that for thermal reignition. After obtaining the experimental scatters for individual measurements using the above relation, we can then evaluate the average experimental scatter of the measured RRRV for the range of discharge conditions which is around 40%

2.7. **Summary**

The basic properties of an arc in LTE are discussed and the conditions necessary for an arc to attain LTE are given. Arc conservation equations based on LTE together with the relevant Maxwell's equations for electromagnetic fields associated with the arc under low frequency approximation are presented. The effects of turbulence on SF_6 switching arcs are reviewed. Since velocity inside an air nozzle arc will be higher than that inside an SF_6 nozzle arc with the same pressure difference at the nozzle inlet and exit, turbulence effects on air arcs need to be considered. Thus, the governing equations for turbulent switching arcs based on the Prandtl mixing length model and the standard k-epsilon model are given and the reasons for choosing these two turbulence models are discussed.

Radiation loss is an important energy loss mechanism in high pressure arcs. It is shown that it is not practical to undertake a detailed radiation transport calculation based on the solution of radiation transport equation. An approximate radiation transport model based on net emission coefficient is given. Net radiation emission coefficients for air differ widely depending on the authors. The available radiation data has been critically reviewed and the justifications for using the net emission coefficient of Shayler and Fang [81] in the current investigation are given.

Similarly, it has been found that there are large discrepancies in air transport properties, especially electrical conductivity, among the published literature. A critical review of the

available data has been conducted and the reasons for adopting Yos 1967 data [71] for our investigation are discussed.

The arc model described in this chapter needs to be verified by extensive reproducible test results which are however very limited. Of the limited test results for air switching arcs, we choose those of Fang [41] and Frind and Rich [66] for our investigation, the details of which are described in this chapter.

Chapter 3. The Implementation of Arc Model in ANSYS Fluent Solver

3.1. Introduction

The conservation equations governing the behaviour of the switching arc and its surrounding gas flow given in Chapter 2 (hereafter referred to as the arc model) are similar to the Navier-Stokes equations for ordinary fluid flow. Therefore, computer simulations on the behaviour of switching arcs, i.e. solution of the arc model, can be done by using numerical methods based on computational fluid dynamics (CFD) [44, 103]. Nowadays, there are commercially available software CFD packages with PHOENICS [48] and ANSYS Fluent [56] being extensively used for switching arc simulations, both of which use the finite volume method to solve numerically the fluid conservation equations [44, 103]. PHOENICS is the first general purpose CFD software package developed by CHAM [48]. This software has been used at the University of Liverpool for nearly 25 years for switching arc simulations with results extensively verified by experiments [53, 54, 104]. However, PHOENICS is not user friendly which requires the user to be highly experienced in CFD [104]. ANSYS Fluent, on the other hand, is a CFD solver integrated in ANSYS software package developed by ANSYS Inc. [105]. ANSYS Fluent includes a modern Graphic User Interface (GUI) [106] which is very easy to use. Due to its user friendliness, ANSYS Fluent is more extensively used than PHOENICS in recent years for computer simulations of switching arcs [58-61]. We therefore choose ANSYS Fluent to implement the arc model, perform computer simulations and obtain computational results of the air and SF_6 switching arcs for the present work.

This chapter is concerned with the implementation of the arc model in ANSYS Fluent with parallel processing solver. The chapter is organized as follows A brief description on the general procedure of the implementation of the arc model is given in Section 3.2. The ANSYS Fluent solver is briefly introduced in Section 3.3. The details regarding the setting up of the arc model with the solver is described in Section 3.4. The procedure of the

parallel processing for the switching arc simulation is discussed in Section 3.5. Finally, concluding remarks of this chapter are given.

3.2. **Methodology Regarding to the General Procedure on the Implementation of the Arc Model**

The implementation of the mathematical model for switching arcs can be done by setting up a CFD problem in any of the main stream general purpose CFD software packages, e.g. ANSYS Fluent and PHOENICS, etc. The general procedure for the setup of a CFD problem/implementing the arc model, involves the following aspects:

(1) Create the geometry of computational domain and generate mesh.

(2) Choose numerical method: most of the commercially available CFD packages, including ANSYS Fluent, solve the fluid governing equations using finite volume method [107].

(3) Set up physical model: in this step, one needs to specify the governing equations of the arc model, i.e. time-averaged Navier-Stokes equations describing the gas flow, the governing equations describing the electric field, the governing equations for the radiation model, and the governing equations for turbulence models, etc. For most of the commercially available CFD packages, including ANSYS Fluent, this can be done by using the GUI of a particular software, and by using a User Defined Scalar (UDS) if an equation is not available for selection but one needs to create the equation.

(4) Set up gas properties: in this step, one needs to specify the thermodynamic and transport properties of the gas to be computationally investigated. For high temperature air, these properties are tabulated by Yos [71] which are described in Chapter 2.

(5) Set up boundary conditions: numerical solution of the governing equations for the arc model based on finite volume method requires appropriate boundary conditions.

(6) Set up input data: necessary input data is required for solving the arc model, including NEC for the radiation model, electric current and user defined initial conditions for numerical solution, etc.

(7) Initialize fields: numerical solution of the governing equations for the arc model based on finite volume method requires specification of the initial state of the system, i.e. initial condition. This can be done by using either the default way of initialization provided by a particular CFD software or user defined initial conditions provided as an input file.

(8) Solution control and start computing: for most of the commercially available CFD packages, including ANSYS Fluent, the most commonly used solution control methods include linear relaxation control and false (pseudo) time step relaxation control. For the solution of the arc model in the present work, both the two methods are used which depends on the complexity of the problem.

(9) Result analysis: after the numerical solution of the arc model is obtained, one needs to view, analyse and export the computational results by using certain post-processors provided by a particular CFD software package.

A flow chart of the aforementioned procedure is given in Figure 3-1 which also gives the section numbers describing the implementation of each step in ANSYS Fluent. The rest of this chapter will focus on how to implement the arc model described in Chapter 2 in ANSYS Fluent.

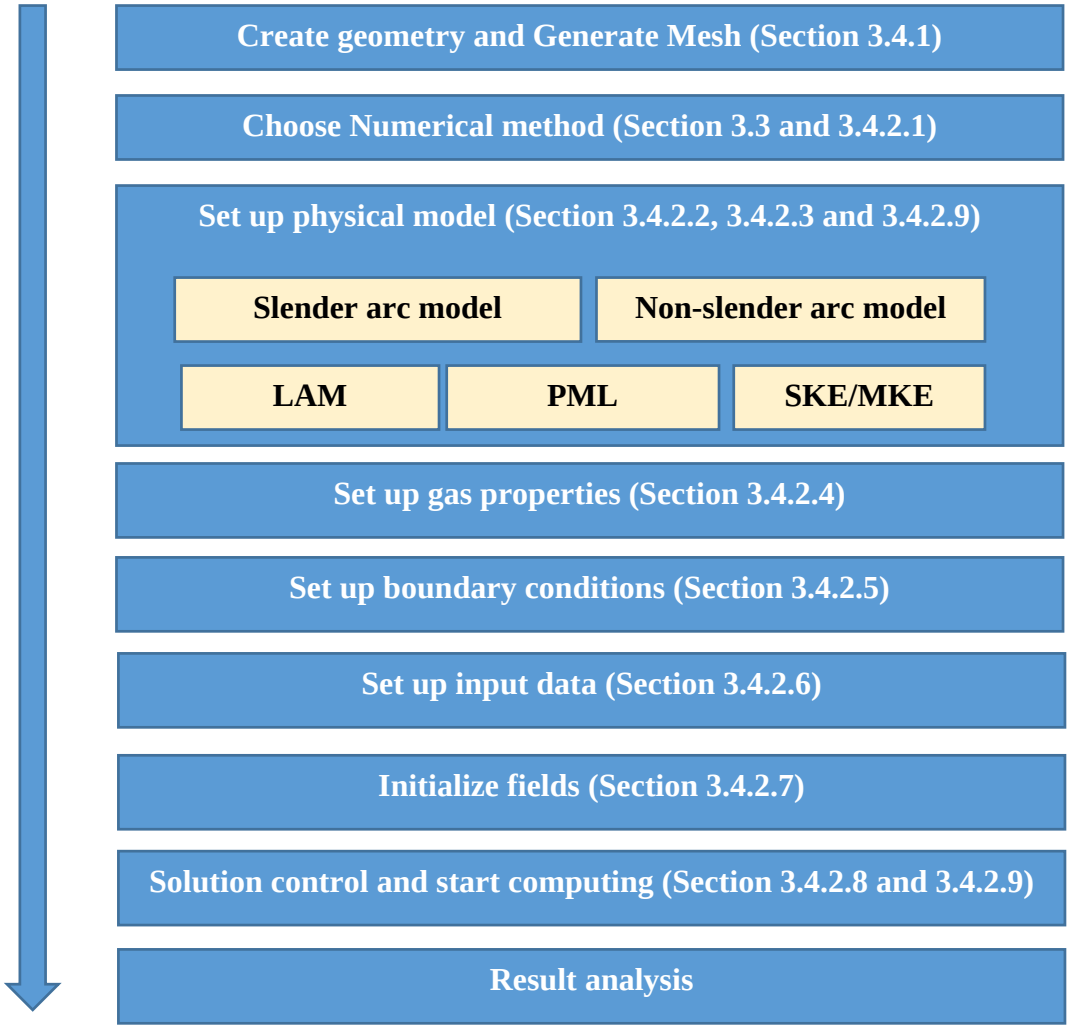

Figure 3-1 The flow chart of the general procedure for setting up a CFD problem/implementing the arc model in any general purpose CFD software package.

3.3. The ANSYS Fluent Solver

ANSYS Fluent is a general purpose CFD solver mainly used for the modelling of fluid flow, heat transfer and chemical reactions between fluids. It can also be used to simulate many other problems in physics, e.g. modelling of electrical field and magnetic field, and also simulations on problems related to magnetohydrodynamics (MHD) [108]. Therefore, the solver is designed to include all corresponding governing equations, e.g. the continuity and momentum conservation equations governing the fluid flow, and the energy equation

governing heat transfer, etc. These governing equations are usually non-linear partial differential equations with their own dependent variables to be solved, e.g. velocity is the dependent variable for momentum conservations and temperature the dependent variable for energy equation. For a particular problem, the user can choose from the list of equations of the solver those governing the problem under investigation by using the GUI of ANSYS Fluent. If the governing equations are not included in the list, the user can construct these equations by defining a User Defined Scalar (UDS) [109]. Details on the implementation of the arc model using GUI and UDS of ANSYS Fluent will be presented in subsequent sections. This section is mainly concerned with a brief introduction to the numerical methods used by ANSYS Fluent for the solution of conservation equations.

3.3.1. **Discretization**

ANSYS Fluent uses finite volume method [44, 103, 107] to discretise a set of partial differential equations to a set of algebraic equations. This is done by integrating a partial differential equation over a finite control volume of a certain shape (e.g. that shown in Figure 3-2), thus yielding a discretized equation that expresses the conservation law on a control volume basis [44, 103, 107]. The general procedure for the discretization of the partial differential equation inside ANSYS Fluent is given below

The conservation equation for a dependent variable (ϕ) is given by

$$\frac{\partial \rho \phi}{\partial t} + \nabla \cdot \left(\rho \phi \vec{v} - \Gamma_{\phi} \nabla \phi \right) = S_{\phi} \tag{3-1}$$

where Γ_{ϕ} is the diffusivity and S_{ϕ} is the source term.

Table 3-1 Conservation equations in general form.

Equation	ϕ	Γ_ϕ	S_ϕ
Continuity	1	0	0
Axial momentum	w	$\mu_l + \mu_t$	$-\frac{\partial p}{\partial z} + \vec{J}X\vec{B}\Big\vert_z$
Radial momentum	v	$\mu_l + \mu_t$	$-\frac{\partial p}{\partial r} + \vec{J}X\vec{B}\Big\vert_r - (\mu_l + \mu_t)\frac{v}{r^2}$
Energy	$\in$	$k_l + k_t$	$\frac{dp}{dt} + \sigma E^2 - q + \ viscous\ heating$
Ke	ke	$\mu_l + \frac{\mu_t}{\sigma_{ke}}$	$G_k - \rho\varepsilon$
Epsilon	ε	$\mu_l + \frac{\mu_t}{\sigma_\varepsilon}$	$C_{1\varepsilon}G_k\frac{\varepsilon}{k} + C_{2\varepsilon}\rho\frac{\varepsilon^2}{k}$

For turbulent flow, Equation (3-1) is the time averaged conservation equation, where φ is the dependent variable and ρ the density. v and w are, respectively, the radial and axial velocity components. The source terms and the diffusion coefficients are listed in Table 3-1 for different conservation equations, in which all notations have their conventional meaning. The subscript l denotes the laminar part of the transport coefficient and t the turbulent part. Laminar (molecular) viscous stresses and turbulent (Reynolds) stresses are taken into account by the diffusion terms on the left hand side of the two momentum equations in Table 3-1. The part of the viscous and turbulent stresses in the radial momentum equation which cannot be written as part of the diffusion term is included in the source term. Ohmic heating and radiation are given in the source term of the energy equation, which also includes the viscous heating due to molecular and turbulent stresses. The Lorentz force generated by the interaction of the arc current with its own magnetic field is accounted for in the source terms of the two momentum equations.

For a finite control volume of arbitrary shape with a volume V, we integrate both sides of Equation (3-1) which yields

$$\int_V \frac{\partial \rho\phi}{\partial t} dV + \oint \rho\phi\vec{v} \cdot d\vec{A} = \oint \Gamma_\phi \nabla\phi \cdot d\vec{A} + \int_V S_\phi dV \qquad (3\text{-}2)$$

where the close surface integral is over the surface of the control volume and $d\vec{A}$ is the elementary area vector of the closed surface. Based on Equation (3-2), the discretized equation on a control volume can be derived which is given by

$$\frac{\partial \rho\phi}{\partial t} V + \sum_f^{N_{faces}} \rho_f \phi_f \vec{v}_f \cdot \vec{A}_f = \sum_f^{N_{faces}} \Gamma_\phi \nabla\phi_f \cdot \vec{A}_f + S_\phi V \qquad (3\text{-}3)$$

where N_{faces} is the number of faces enclosing cell (i.e. N=3 for triangle cell and N=4 for quadrangle cell).

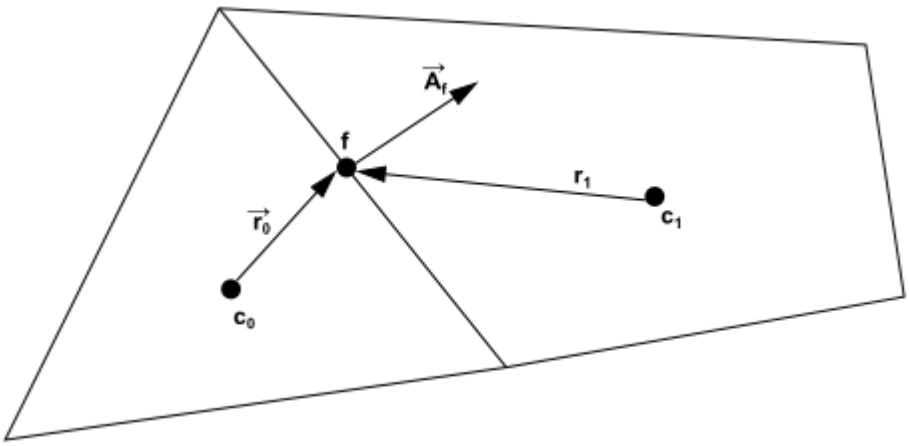

Figure 3-2 Control volume (Cell) used to illustrate discretization of a scalar transport equation

When first-order accuracy is desired, quantities at cell faces are determined by assuming that the cell center values of any field variable represent a cell-average value and hold throughout the entire cell; the face quantities are identical to the cell quantities. Thus when first-order upwinding is selected, the face value ϕ_f is set equal to the cell center value ϕ of in the upstream cell.

Since ANSYS Fluent, like many other CFD solvers (e.g. PHOENICS), solves the discretized equation given by Equation (3-3), we always need to divide the entire volume of the computational domain into a large number of small control volumes. In CFD, a small control volume in a computation domain is usually referred to as a cell. ANSYS Fluent uses both structured and non-structured cells such as triangle cell, quadrangle cell and those mixed for 2 dimensional geometry [107] (e.g. Figure 3-2). The process of dividing the computational domain into a number of cells is commonly known as mesh (grid) generation. Details of mesh generation for nozzle arc simulation will be described later. For every cell in a computational domain there is a set of simultaneous algebraic equations in the form of Equation (3-3).

For the convection term, i.e. the second term on left hand side of Equation (3-3), the first order upwind scheme [44, 103, 107] has been used to evaluate the surface values. For diffusion term, i.e. the first term on right hand side of Equation (3-3), the second order central-differenced has been used. For transient term, the time derivative is discretized using first order backward difference method.

It is noted that Equation (3-3) is generally non-linear with respect to the solved variable. In ANSYS Fluent, Equation (3-3) is linearized which yields the following equation with constant coefficients for each grid

$$a_p \phi = \sum_{nb} a_{nb} \phi_{nb} + b \qquad (3\text{-}4)$$

where a is the linearized coefficient and subscripts *p* and *nb* refer to the target cell and its neighbour cells, respectively.

This results in a system of simultaneous algebraic equations with constant coefficients, the solution of which involves the inversion of a sparse matrix. The elements of this matrix

are the coefficients of ϕ in Equation (3-4). The inversion of this matrix in ANSYS Fluent is done iteratively by either Gauss-Seidel method or incomplete lower upper (ILU) decomposition technique [44, 103, 107] in conjunction with an algebraic multigrid (AMG) method [107].

3.3.2. **Numerical Algorithms Provided by ANSYS Fluent**

The conservation equations are solved by converting the mass conservation equation to a pressure equation [44], the so-called pressure based approach in ANSYS Fluent. For the pressure-based solver, ANSYS Fluent provides two algorithms, i.e. the segregated algorithm and the coupled algorithm [107]. The flow charts of these two algorithms are given in Figure 3-3. For the segregated algorithm, pressure and velocity are solved sequentially, while for the coupled solver, pressure and velocity are solved simultaneously [107]. Of these two approaches, the segregated approach is efficient and can give fast solution, which is therefore the choice for the arc simulations of the present work. Associated the segregated algorithm there are three versions: SIMPLE, SIMPLER and PISO algorithms [107]. For the computer simulation tasks of the present work, we always use SIMPLE as our first choice. However, in some cases, it is difficult to obtain stable or convergent solution using segregated algorithm. For these cases, it has been found that application of pressure-based coupled solver can yield stable and convergent solutions, e.g. for arc simulation based on laminar flow theory the results of which may have steep gradient such as temperature. Thus, for such cases we apply coupled solver, alternatively.

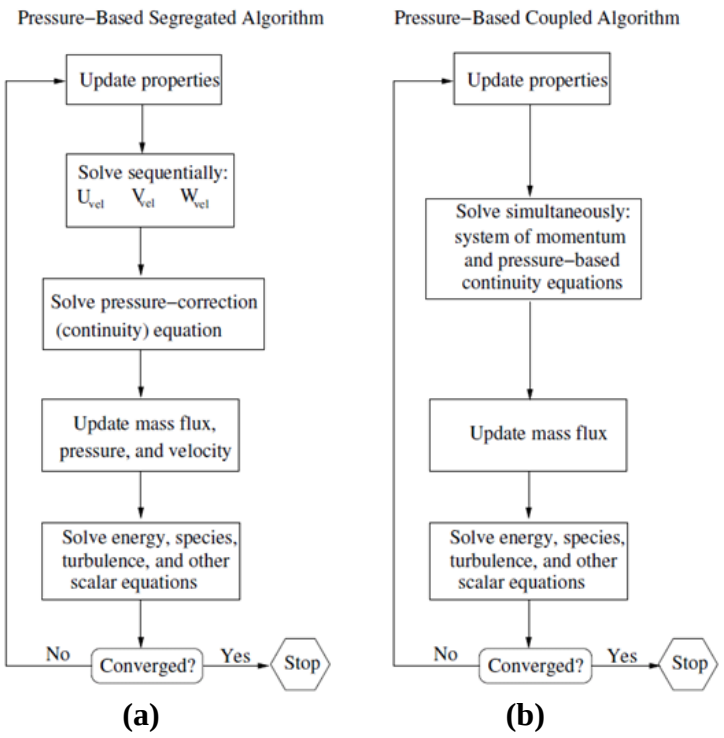

Figure 3-3 Overview of segregated method (a) and coupled method of pressure-based solver (b) in Fluent.

3.3.3. **Solution Convergence Control**

Solution convergence control is an important feature for a CFD software package. It provides stabilities during the iterations to avoid divergence. However, over use of this method would slow down the computing since more iteration is needed to obtain the final solution. ANSYS Fluent provides two solution convergence control methods, the explicit under-relaxation and the pseudo transient under-relaxation [107].

Explicit linear under-relaxation uses a parameter, α, to improve the convergence

$$\phi_{new} = \phi_{old} + \alpha(\phi_{calculated} - \phi_{old}) \qquad (3\text{-}5)$$

where ϕ is the solved variable in question and subscripts new, old and calculated refer respectively to the relaxed value, the value at the last iteration and the recently calculated value. To ensure convergence, the user needs to specify appropriate value of α which

usually found by numerical experiments. Linear relaxation has been found very effective for arc simulation. The values of α used for our arc simulation will be given in section 3.4.2.8.

However, for some cases, e.g. arc simulation based on laminar flow, it is difficult to obtain convergent solutions using linear relaxation. We then use the other convergence control method, the Pseudo transient under-relaxation scheme given below.

$$\rho_p \Delta V \frac{\phi_p - \phi_p^{old}}{\Delta t} + a_p \phi = \sum_{nb} a_{nb} \phi_{nb} + b \qquad (3\text{-}6)$$

where Δt is the pseudo time step, subscript p denotes the cell and ΔV is the cell volume. The value of Δt is again determined by try and error. The values of Δt used for our arc simulation will be given in section 3.4.2.8.

3.4. **Setting up a Problem for Switching Arc Simulation**

The general procedure for the setup of a CFD problem involves the following two aspects [106]:

(1) Create the geometry of computational domain and generate mesh;
(2) Set up the physical models and choose the appropriate solver.

Pre-processors, ANSYS DesignModeler [110] and ANSYS Meshing [111], are used to specify the computation domain and to generate the mesh. The facility, User Defined Functions [109], which is integrated with Application Programming Interface (API) within ANSYS Fluent is used to provide all necessary information required for arc simulation and output results. The following subroutines are integrated with ANSYS Fluent for arc simulation:

(a) The equation of state, thermodynamic properties, transport properties, net radiation coefficients of the arc gases investigated (air and SF_6).

(b) Initial conditions required for arc simulation.
(c) Specification arc discharge conditions (e.g. current, stagnation pressure, rate of change of current before current zero and the rate of rise of voltage after current zero).
(d) Computation of electrical field and arc voltage;
(e) Implementation of the radiation transport model;
(f) All the auxiliary subroutines for storing important computational results as well as for performing further computation on the results to derive the features of the simulated arc discharge (e.g. energy balance)

The details of setting up an arc simulation using ANSYS Fluent are given in the following subsections.

3.4.1. **Create Computational Domain and Generating Mesh**

The geometry of the computational domain (a supersonic nozzle) is created using ANSYS DesignModeler [110]. The process of geometry creation includes:

(a) Definition of important coordinates;
(b) Definition of lines connecting these coordinates to form the shape of the computational domain;
(c) Definition of surfaces which represent different parts of the computational domain where different mesh schemes (e.g. structured or non-structured mesh schemes) may be used.

It is important to note that, for a CFD simulation based on an axisymmetric geometry, the creation of geometry must be based on the first quadrant of X-Y Plane [106]. Otherwise, the simulation cannot be performed in ANSYS Fluent for an axisymmetric geometry.

The completed geometry file is then imported into ANSYS Meshing [111] for mesh generation. Generally, ANSYS Fluent uses the mesh scheme based on unstructured meshes in order to simply the modelling of geometry and generation of mesh, and to enable modelling of more complex geometries than those which can be handled with structured meshes. It, however, also supports mesh schemes based on structure meshes. For our arc simulation, we must apply structured meshes within the arc region, because a number of subroutines, e.g. the one for the radiation model, are designed based on structured mesh systems. We therefore apply a mixed structured and non-structured mesh scheme inside the computation domain of a nozzle (Figure 3-4 (a)), where non-structured mesh is used in the cold flow region.

In addition to mesh generation, a number of line segments, on which the boundary conditions need to be specified, also need to be defined. This is done using ANSYS Meshing. For the nozzles investigated in the present work (e.g. Figure 3-4 (a)), names are given below to the relevant lines together with their properties:

	Name	Properties
(a)	Axis	axisymmetric axis
(b)	Inlet	nozzle flow inlet
(c)	Outlet	nozzle flow outlet
(d)	Wall	the wall (surface) of the nozzle

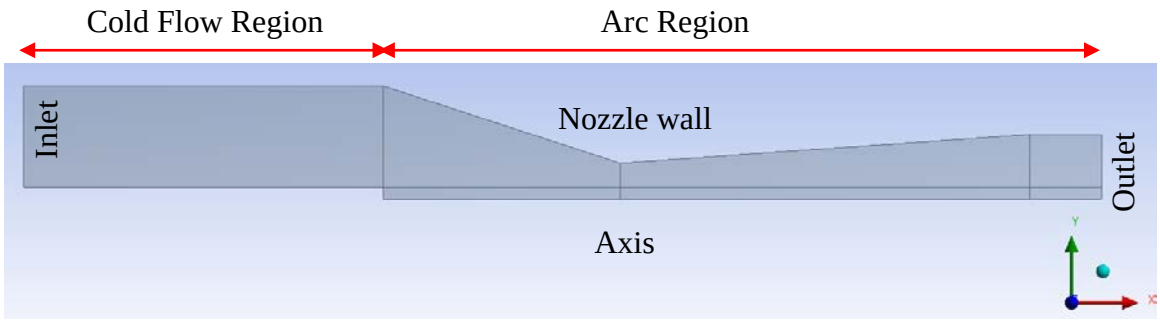

(a)

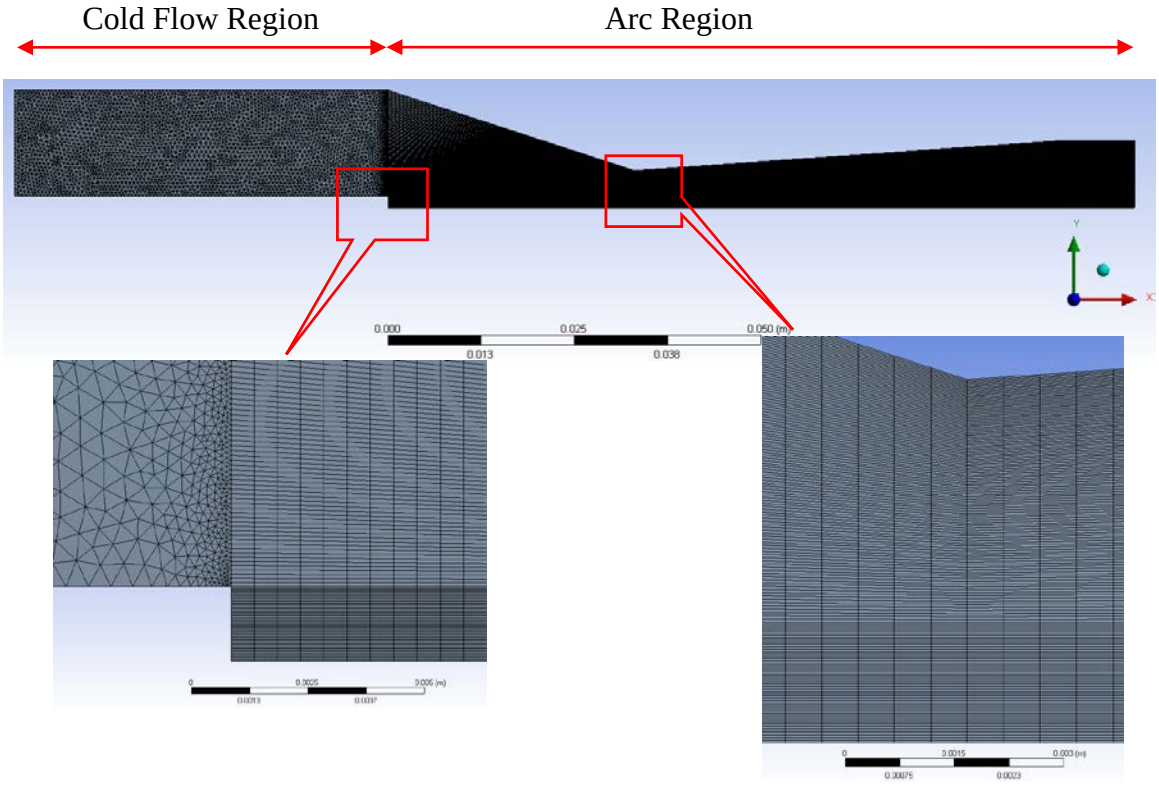

(b)

Figure 3-4 Nozzle geometry and mesh

It is important to note that within ANSYS Fluent the name of a particular line segment cannot be given arbitrarily, which should be assigned according to the convention of ANSYS software, e.g. for the inlet boundary of the computational domain, the name should start with the word “Inlet” [106]. In this way, when defining boundary conditions

at later stages, ANSYS Fluent can automatically recognize it as an inlet boundary and then assign appropriate inlet conditions to this boundary. Otherwise, ANSYS Fluent cannot know what this boundary should be, and the user can only manually assign appropriate boundary conditions, which can increase the time for problem setup.

After the completion of mesh generation and having defined important line segments, we save all these settings as a mesh file which can be imported into ANSYS Fluent solver for computation. The setup of the solver and the physical models for the fluid flow, i.e. the arc and the surrounding gas flow in the present investigation, will be discussed in Section 3.4.2.

3.4.2. The Setting of Physical Model and the Choice of Solver for Arc Simulation

After the completion of the computation mesh we need to define the physical model for the fluid flow to be simulated and to choose the appropriate solver to obtain computational results. For arc simulation detailed information on the establishment the physical model and on the choice of solver is given in the following sections.

3.4.2.1. Choice of the Solver

As discussed in Section 3.2, ANSYS fluent provides two algorithms for numerical computation of fluid flow, i.e. the pressure based solver and the density based solver. We choose pressure based solver in our arc simulation.

3.4.2.2. Choice of Solved Variables

The governing equations of arcs in gas flow are the conservation equations together with those describing electromagnetic fields. The characteristics of an LTE flowing arc at low frequency are fully determined by its velocity, temperature, pressure and electrical

potential (in the case of non-slender arc). We therefore specify these variables as solved variables in ANSYS Fluent.

The azimuthal magnetic flux density is calculated by simplified Ampere's law for an axisymmetric arc. It does not involve the solution of a partial differential equation. It is therefore not necessary to define magnetic flux density as a solved variable.

3.4.2.3. Turbulence Models

Turbulence models described in Chapter 2 need to be implemented in the solver. For the standard k-epsilon model, another two solved variables with the corresponding governing equations need to be specified, one of which for the turbulent kinetic energy and the other for the turbulent dissipation rate. The k-epsilon model is integrated in ANSYS Fluent, which can be implemented by selecting this model using GUI. The Prandtl mixing length model prescribes and algebraic relation to eddy viscosity. This is implemented by using our own subroutine given as a UDF.

3.4.2.4. Input of Real Gas Properties

The switching arc under investigation is a collision dominated plasma in LTE. Its properties are fully determined by two thermodynamic quantities, temperature and pressure. For SF_6 and air at a given temperature enthalpy and transport properties are weakly dependent on pressure. Computational results obtained for air and SF_6 arcs taking into account pressure dependence of these quantities are almost the same as those obtained by using the temperature dependence of these quantities at 10 atm. Therefore we only need to input the dependence of these quantities on temperature at 10 atm. The exceptions are net emission coefficients and gas density which are functions of pressure and temperature. Arc simulation requires the input of the following gas properties:

(a) Enthalpy and temperature relation;
(b) Molecular viscosity as a function of temperature;

(c) Molecular thermal conductivity as a function of temperature;

(d) Electrical conductivity as a function of temperature;

(e) Mach number as a function of temperature;

(f) Equation of state, i.e. density as a function of pressure and temperature. For temperature below 1,000 K, ideal gas law is applied to calculate density.

(g) Net radiation emission coefficients as a function of temperature, pressure and arc radius.

3.4.2.5. Boundary Conditions

The governing equations for the arc model need to be supplemented by necessary boundary conditions before they can be solved. In the present investigation, the required boundary conditions for an arc burning in a supersonic nozzle are given below:

(a) On the nozzle axis, axisymmetric boundary conditions are applied. Thus, all radial derivatives of the dependent variables are set to zero except for the radial velocity which is zero on the axis. These are the default boundary conditions given by ANSYS Fluent for axisymmetric axis of the computational domain [107].

(b) At the nozzle inlet, we use the Pressure Inlet Boundary Conditions [107] supplied by ANSYS Fluent. For the Pressure Inlet Boundary Conditions option, the axial velocity and density are iteratively computed according to the calculated inlet static pressure by assuming that the gas entering the nozzle undergoes an isentropic process [54] from a reservoir with stagnation pressure P_0 and stagnation temperature T_0 (300 K). The Pressure Inlet Boundary Conditions can be set via the corresponding dialogue box in the GUI of ANSYS fluent.

(c) At the nozzle exit, we use the Pressure Outlet boundary Conditions [107] supplied by ANSYS Fluent. For this option, the static pressure P_e needs to be given. During solution procedure, if the flow is supersonic at the flow exit (e.g. in case that P_e has a

very low value), the setting of P_e will be ignored and the gas pressure, velocity and temperature are all interpolated from inside the nozzle according to the relations that the axial gradients of velocity and temperature are equal to zero. If the flow is subsonic at the nozzle exit (e.g. in case that P_e has a high value which causes shock inside the nozzle), the setting of P_e will affect the solution.

(d) At solid surfaces, non-slip boundary condition for velocity is applied through a built-in wall function of ANSYS Fluent. These surfaces are assumed to be adiabatic, for which the heat flux is set to zero. These boundary conditions for solid surfaces are all default boundary conditions supplied by ANSYS Fluent [107].

(e) When applying the standard k-epsilon model and its two variants, relevant boundary conditions need to be specified. The turbulent kinetic energy and dissipation rate at the nozzle inlet are given by [112]

$$ke_{in} = \frac{3}{2}(u_{in}I_t)^2 \tag{3-7}$$

$$\varepsilon_{in} = C_\mu^{3/4}\frac{k_{in}^{3/2}}{l} \tag{3-8}$$

where u_{in} is the nozzle inlet velocity, I_t the turbulent intensity set at 5% as recommended by [112] and l=0.07L. L is the characteristic length of the equipment [103, 112] given by (d_{inlet} - $d_{electrode}$) where d_{inlet} is the diameter of the nozzle inlet and $d_{electrode}$ the electrode diameter. At the nozzle exit, the axial gradients of k and ε are set to zero. These boundary conditions can be set in the relevant dialogue boxes for choice of standard k-epsilon model in ANSYS Fluent GUI [106].

(f) For calculation of electrical field, the relevant settings on boundary conditions are described as follows:

When using the slender arc model, electrical field is calculated by simplified Ohm' law and no boundary conditions are required. When the non-slender arc model is applied, boundary conditions need to be supplied to the current continuity equation. Take the nozzle geometry in Figure 3-4 (a) as an example, the boundary conditions are

(1) At the left end of the upstream electrode, i.e. on the nozzle inlet side, a current density is specified which is denoted as

$$j_z = \sigma \frac{\partial \varphi}{\partial z} = \frac{I}{A_{electrode}} \tag{3-9}$$

where $A_{electrode}$ is the cross-sectional area of the upstream electrode. It is noted that these boundary conditions vary with current which cannot be set directly in ANSYS Fluent GUI. Such varying boundary conditions can be set by applying user-define profile, which is actually a UDF.

(2) At the nozzle exit plane, the electrical potential is set to zero, i.e. $\varphi = 0$.

(3) At all the other boundaries of computational domain, including the axisymmetric axis, the nozzle wall and the nozzle inlet plane, the normal gradients of the electrical potential are set to zero, i.e. $\partial\varphi / \partial n = 0$.

(4) Electrical conductivity in conductors is set to 10^6 S/m.

3.4.2.6. Preparation of an Input Data File

For the simulation of switching arcs, we have created an input data file which provides necessary information for running an arc simulation. The input data file mainly contains two parts which are the gas properties data and the information for model configuration.

Gas properties data are provided by UDFs, which includes the data of thermodynamic and transport properties, the equation of state and radiation data. It is loaded immediately after the state of a solution procedure for a switch arc simulation.

Model configuration defines the settings of arc model, as shown in Figure 3-5. It obeys the format of JSON (JavaScript Object Notation) [113] which is a lightweight data-interchange text format and is easy to read. The content of this configuration file includes:

1. whether or not to enable non-slender arc model {NSA}, if set to true
    a. current continuity equation is calculated,
2. whether or not to enable Lorenz force {JXBENABLE},
3. setting of radiation parameters {RADIATION},
    a. set radiation multiplication factor {RF},
    b. set reabsorption factor {ABF},
    c. set reference temperature {TREF},
    d. set radiation region {REGION} which is automatic determined by program or user specified,
4. setting of the region of Ohmic heating {POWERINPUT/REGION},
5. whether or not to enable post arc {RRRV} to look for the CRRRV, if set to true,
    a. set rate of recover voltage {DVDT},
    b. set start time {StartTime},
6. setting of turbulent Prandtl number for energy equation {TURBULENCE/PRT_ENERGY/CONST},
7. whether or not to enable Prandtl mixing length model {PML}, if set to true,
    a. set parameter c {PMLC},
    b. set active zone {REGION},
8. setting of initialization for a new arc {INIT},
    a. define maximum temperature of the arc column {TMAX},
    b. define the radius of the arc column {RBOUND},
9. setting of the arc current {CURRENT} using linear interpolation which data comes from a key/value map (each pair indicates an arc current at a time instant),
10. setting of the time step {DT} using the data which comes from a key/value map (each pair indicates the time step at a time instant),
11. and setting of the rate of recording the output information such arc voltage, energy balance, etc... {LOG}
    a. set the frequency for generating output data {FREQ},

b. set the name of output file {FILENAME}.

```
{
    "ARC":{
        "NSA":true,
        "JXBENABLE":true,
        "RADIATION":{
            "RF":2,
            "ABF":0.6,
            "TREF":4000,
            "REGION":{
                "ISAUTO":true,
                "XSTART":0,
                "XEND":73.45E-3
            }
        },
        "POWERINPUT":{
            "REGION":{
                "ISAUTO":true,
                "XSTART":0,
                "XEND":73.45E-3
            }
        },
        "RRRV":{
            "ENABLE":false,
            "DVDT":1E9,
            "StartTime":37e-6
        },
        "TURBULENCE":{
            "PRT_ENERGY":{
                "CONST":1
            }
        },
        "PML":{
            "ENABLE":false,
            "PMLC":0.03,
            "REGION": {
                "ISAUTO":true,
                "XSTART":0,
                "XEND":73.45E-3
            }
        },
        "INIT":{
            "TMAX":2.6E4,
            "RBOUND":3E-3
        },
        "CURRENT":{
            "KEY":[
                0,
                1
            ],
            "VAL":[
                1500,
                1500
            ]
        },
        "DT":{
            "KEY":[
                0,
                5e-3,
                27e-3
            ],
            "VAL":[
                500e-6,
                50e-6,
                50e-6
            ]
        },
        "LOG":{
            "FREQ":10,
            "FILENAME":"records.txt"
        }
    },
    "version":"v1"
}
```

Figure 3-5 Model configuration file

3.4.2.7. Initial Conditions

For arc simulation initial conditions need to be provided for a transient arc. For a steady state arc initial conditions are the guessed solution which starts the iterative process to obtain steady state solution.

In the present work, the simulation of an arc in nozzle forms two parts. The first part is the simulation of a DC arc. For steady state arc simulation, we use Hybrid Initialization

Method [107] provided by ANSYS Fluent for initialization of solved variables, e.g. pressure, velocity and temperature outside the arc region. To initiate an arc, we assume an axially uniform cylindrical arc column of radius 3 mm (Figure 3-6) with an axis temperature of 26,000 K which reduces linearly to ambient temperature at a radius of 3 mm.

The second part of the arc simulation is for a transient arc with linearly decaying current (di/dt) from 1 kA DC to zero and a specified linearly increasing recovery voltage after current zero. The initial conditions are therefore the same as the steady state solution for 1 kA DC arc. For the computation of the critical rate of rising of recovery voltage after current zero for a given di/dt, the numerical solution at current zero obtained for the di/dt is as the initial condition.

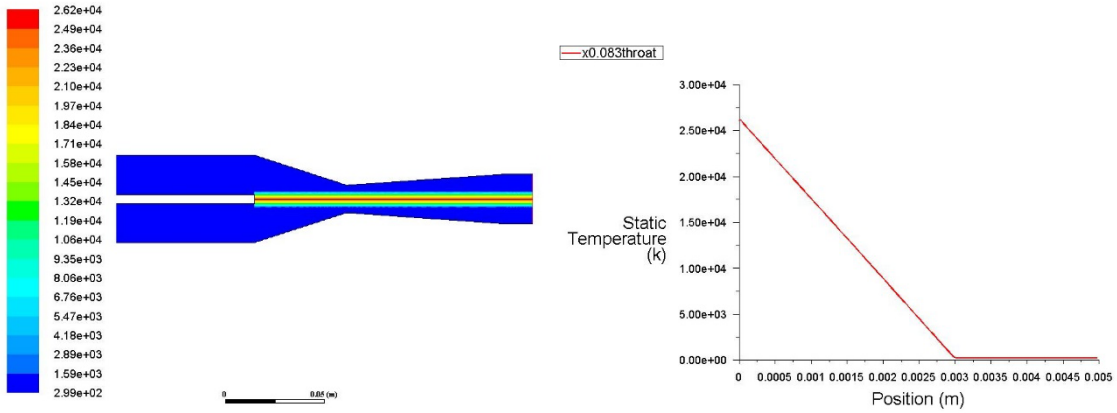

(a) (b)

Figure 3-6 Initialization of the arc temperature. (a) Temperature contour; (b) Radial temperature profile at nozzle throat.

3.4.2.8. Solution Procedures and Convergence Control

In the present work, computer simulations of switching arcs start from the computation of a DC arc. The current is then ramped down towards zero with a specified di/dt after the arc reaches steady state. After current zero, a linearly rising recovery voltage with a specified dV/dt is imposed to find RRRV. Thus, the general procedure of computer

simulation for the arcing process includes three stages, simulation of DC arcs, simulation of transient arcs before current zero and simulation of transient arcs after current zero. For simulation with the scaling nozzle, we only have the first stage. This section presents details of the aforementioned three stages of our computer simulations.

As previously discussed, ANSYS Fluent solves all the conservation equations governing a CFD problem iteratively. The user therefore needs to give sufficient number of iterations and appropriate relaxation factors, and also appropriate size of time step (for transient flow behaviour), to ensure the numerical solutions are well converged (i.e. convergence control). Relevant settings at different stages of our arc simulations will also be given in this section.

A. Computation of DC Nozzle Arcs

Our computer simulations always start from the computations of DC nozzle arcs. For the investigation of Chapter 4, the currents used range from 250 A DC to 3 kA DC, and for the investigation of Chapter 5, we compute the 1 kA DC nozzle arc to obtain the state of arc before the current ramp. Since the simulations here are steady state in nature, the time dependent term in the governing equations are neglected. We do not therefore specify the size of time steps, but only the iteration number and relaxation factors for respective governing equations. Generally, for DC arc simulations, the iteration number of 20,000 is used and the relaxation factors for different equations are: 0.3 for pressure (continuity equation), 0.7 for velocity (radial and axial momentum equations), 0.6 for temperature (energy equation), 0.8 for k-epsilon model equations (if chosen to be solved) and 1 for current continuity equation (if chosen to be solved).

For arc simulation which has difficulty in achieving convergence using linear relaxation, pseudo transient stepping has been used. The typical values of Δt is set to 1 μs.

B. Computation of the Transient Nozzle Arc before Current Zero

As soon as the solutions of the 1 kA DC arc reach steady state, we initiate the simulation from the results of 1 kA DC arc and, in the meantime, ramp down the current with a specified di/dt until the current reaches its zero point. The total computational time required for this state of simulation is uniquely determined by the value of di/dt, e.g. for di/dt=13.5 A/μs, the total time = 1,000 A/13.5 A/μs = 74 μs.

Previous investigations on turbulent SF_6 switching arcs show that the states of arc (e.g. temperature and arc radius) and, subsequently, the arc resistance, change very rapidly shortly before final current zero, for which a very small time step size should be used to catch these features and to ensure the accuracy of the computation. Therefore, in our arc simulations with a current ramp, a time step size of 0.02 μs is used from the instant when the current is below 300 A to that of the current zero. For instants when the current is above 300 A, a relative larger time step size (0.1 μs) is used to save computational time. A sensitivity study for time step sizes was performed and the results showed that, by further reducing time step size, the difference of the results was less than 5%. This means the selection of time step size here is reasonable. The number of iterations for each time step is 50. The settings of linear relaxation factors and/or $\Delta \boldsymbol{t}$ for pseudo transient stepping are the same as those for computations of DC nozzle arcs.

C. Computation of the Nozzle Arc after Current Zero

As soon as the computation before current zero is completed, we initiate the simulation from the results at current zero and, in the meantime, apply a linearly increasing recovery voltage with a specified dV/dt. This stage is simulation aims to find the RRRV of the nozzle arc. It is known that, for gas blast circuit breakers, the characteristic time for thermal extinction and/or reignition is always within 10 μs [16, 47]. Thus, for the present investigation, the total computational time for this stage is specified as 10 μs. Due to rapid variation of arc characteristics during current zero period as previously indicated, the size

of each time step is set to 0.02 μs. The number of iterations for each time step is 50. The settings of linear relaxation factors and/or dt for pseudo transient stepping are the same as those for computations of DC nozzle arcs.

3.4.2.9. User Defined Adjust

Before each iteration, it is necessary to update below quantities which can be done through user-defined adjust function provided by ANSYS Fluent. We apply user-defined adjust functions for the following tasks required in our arc simulation:

A. Update current when it changes with the time
    a. The current is given by a configuration file (Section 3.4.2.6)
    b. After current zero, it is calculated for a given dV/dt
B. Calculate electrical field
    a. For slender arc electrical field would be calculated directly from simplified Ohm's law which is given by

$$E = \mathrm{E}_z = \frac{i}{\int_0^\infty \sigma 2\pi r dr} \tag{3-10}$$

    b. For non-slender arc the electrical field would be obtained from electrical potential.
C. Calculate Ohmic heating (σE^2 in Equation (2-10) of Chapter 2)
D. Calculate net radiation loss
E. Calculate Lorenz force

    For axisymmetric arc the azimuthal magnetic flux density can be calculated by

$$\mathrm{B}_\theta = \frac{\mu_0 \int_0^r j_z 2\pi\xi d\xi}{2\pi r} \tag{3-11}$$

    where the permeability of the arc medium, μ_0, is assumed to be homogenous and equal to $4\pi \times 10^7\ H/m$ and j_z is the axial component of the current density. The two components of Lorentz force are given by

$$f_r = j_z \mathrm{B}_\theta \ and \ f_z = -j_r \mathrm{B}_\theta \tag{3-12}$$

F. If Prandtl mixing length has been used, it would be calculated by Equation (2-25) to (2-28) of Chapter 2
G. Record auxiliary field variables and other global variables for post-processing

3.5. **Parallel Computing**

In order to save computational time, parallel computing technology has been applied when carrying out computer simulations of switching arcs for the present work. Parallel computing for the switching arc simulations has been achieved by activating the parallel module of ANSYS Fluent [109]. The working principle of Parallel ANSYS Fluent is based on distributed memory approach, which enables a simulation task to be performed simultaneously using multiple processes that may be executed on the same machine, or on different machines in a network (Cluster). This requires the computational domain for a simulation task to be split up into multiple partitions. A typical example of partitions for a nozzle arc simulation is given in Figure 3-7, which shows that the computational domain of the nozzle has been divided into 8 partitions. Each partition will be assigned a process. Processes store and perform computations on their own partition while a single layer of overlapping cells along partition boundaries provides communication and continuity across the partition boundaries. The communication and data exchange across the partition boundaries are achieved by applying a set of APIs provided by ANSYS Fluent. These APIs are designed to obey message passing interface (MPI) which is well known as a standard communication protocol for distributed memory approach of parallel computing. With these APIs, ANSYS Fluent can exchange data between processes automatically, for data, e.g. solved variables, across partition boundaries.

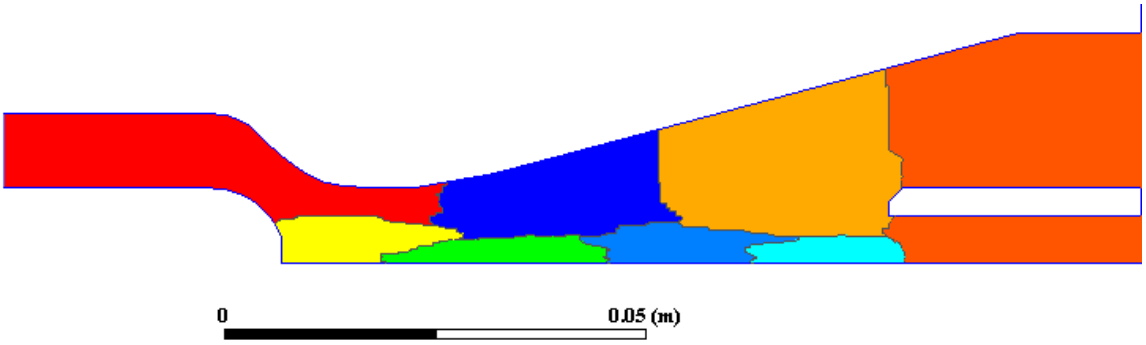

Figure 3-7 An example of domain partitions

For the switching arc simulations, there are a number of subroutines which have operations that require communications between different processes that cannot be done automatically by ANSYS Fluent. Examples of these operations mainly include the following

(a) Radial integration of a variable (e.g. radial integration of net radiation loss in the subroutine for the radiation model) or a certain flux (e.g. radial integration of energy fluxes in the subroutine for energy balance calculations) over the r-direction for a given axial position, which usually needs to be done across partitions.;
(b) Axial integration of a variable or a certain flux over the axial direction, which also needs to be done across partitions;
(c) Search of a certain quantity in the domain, e.g. in the radial direction, may need to be done across partitions. A typical example is the search of the arc's core boundary and/or electrical boundary.

For these cases, the user needs to write corresponding subroutines, using API, to manually carry out necessary communication and data exchanges between processes. The solutions we have used to enable the above mentioned operations are briefly described in the following subsections.

3.5.1. Search of a Quantity in the Radial Direction

To implement the arc model, it is important to compute the variable in each slab. A slab is defined as a group of cells at a given axial position. For instance, we need to calculate the core boundary (83.3%Tmax) of each slab. The following processes describe the way to do this search.

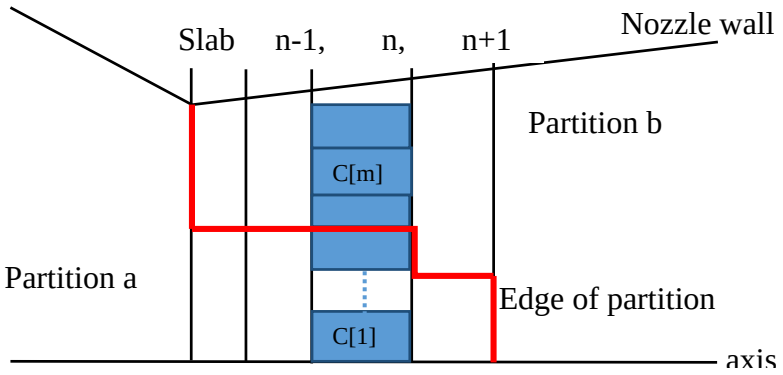

Figure 3-8 Schema of a divided computational domain

1. We assume that the temperature profile of slab n (Figure 3-8) is monotonous which is similar to the profile shown in Figure 2-3 of Chapter 2. Therefore, the arc boundary temperature of slab n is $83.3\%T_{C[1]}$
2. Cell C[1] is located at partition a. We pass the temperature to other partitions by MPI (i.e. partition b in this case).
3. Now all partitions know that the temperature of C[1] and can obtain $83.3\%T_{C[1]}$ which is the arc boundary temperature for slab n. Each partition, then, would look for the cells in slab n and try to find the cell satisfy $T_{C[m-1]}>83.3\%T_{C[1]} \geqslant T_{C[m]}$. There would only one partition contains the location of arc core boundary, R833, and it would be shared across all the partitions by MPI.

3.5.2. Integration in the Radial Direction

To implement our arc model, radial integration has to be performed. For instance, when calculating radiation reabsorption (Equation (2-43) of Chapter 2), the total radiation loss

of each slab need to be integrated up to arc core boundary. It gives a description to implement the radial integration.

1. After R833 has been found, all partitions know that the radius of the arc core boundary for slab n.
2. In each partition, it would search the cells which belong to the slab n and integrate the radiation loss and, then, we would have n numbers of sums across the partitions. The number of n equals to the number of partitions. They are added together and the total sum is shared to all partition by MPI.

3.6. **Concluding Remarks**

The conservation equations governing the behaviour of a switching arc and its surrounding gas flow together with all the supplementary equations, which form the arc model, will be solved by using a general purpose CFD solver, ANSYS Fluent. This chapter is concerned with an introduction to the solver and a detailed discussion on the implementation of the arc model within ANSYS Fluent. Parallel processing is used to obtain computational results. Special subroutines have been incorporated into ANSYS Fluent for computations which require the values of the solved variables of the cells belonging to different partitions.

Chapter 4. DC Arc in an Nozzle Flow

4.1. Introduction

This chapter reports a detailed investigation on the behaviour of an air nozzle arc under different direct currents (DC). The investigation is based on the experimental study of Fang et al [41], the experimental arrangement of which is the closest to a switching arc. Computations are carried out using the arc model based on both the laminar flow (referred to as laminar flow model) and turbulent flow described by two turbulence models given in Chapter 2, i.e. the Prandtl mixing length model and the standard k-epsilon model or its modified version). The role of turbulence is established by comparison between experimentally measured arc voltages reported in [41] and those predicted by laminar flow model. The dominant energy transport processes and the associated material properties in determining the behaviour of air switching arcs are identified.

This chapter is organized as follows. Section 4.2 is concerned with the computational domain and the boundary conditions. In section 4.3, a discussion will be given on the DC arc characteristics, the dominant energy transport processes and the material properties responsible for the arc features. Finally, appropriate conclusions are drawn.

4.2. Computational Domain and Boundary Conditions

Computation has been performed for the Teflon nozzle of Fang et al [41] using the parallel processing facilities of ANSYS Fluent [56]. The computation domain and the grid system are shown in Figure 4-1 where the detailed dimensions and the distribution of grids are given. The arc length is 100 mm with the downstream electrode tip located 10 mm away from the nozzle exit (not shown in the diagram). For all discharge conditions reported in [41] the exit pressure (1 bar) is low enough to ensure that the flow in the nozzle is supersonic and shock free.

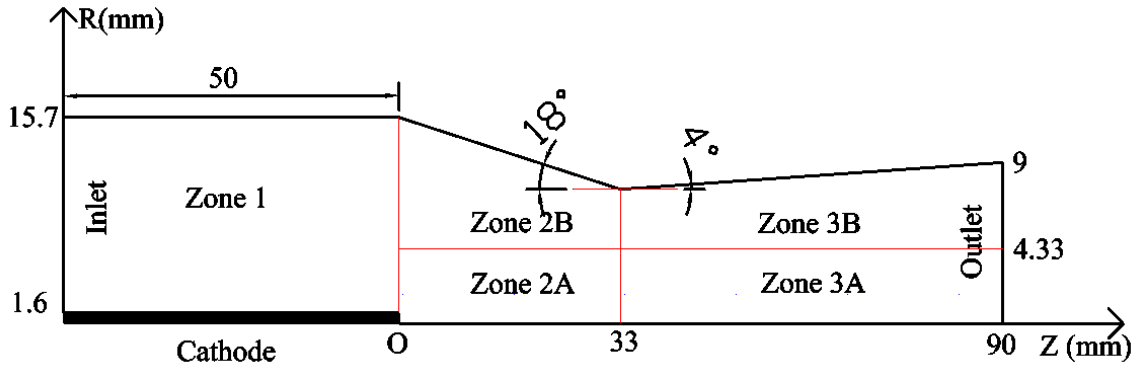

Figure 4-1 Nozzle geometry (not to scale) and grid system. The computation domain is divided into 5 zones: In Zone 1: a non-structured grids consisting of triangle cells with an average edge size of 0.5 mm is used. There are altogether 6872 grids. In Zone 2A uniform rectangular grids are used with a total number of grids of 66 (axial) x 130 (radial). There are 66x30 grids in Zone 2B. A total of 114 x 130 rectangular grids are placed in Zone 3A and 114 x 30 grids in Zone 3B. The radius of upstream electrode is 1.6mm. The radius of nozzle throat is 5mm. The origin of z-axis is at the upstream electrode tip.

Computation has also been done to include the downstream electrode with an open boundary sufficiently far from downstream electrode (known as the extended domain) to simulate the exhaust space for discharging the gas from the nozzle. The results inside the nozzle using the extended domain are the same as the arc computed for the domain given in Figure 4-1. Electrical field between the nozzle exit and the tip of downstream electrode of the extended domain is almost equal to that at the nozzle exit computed by using the domain in Figure 4-1. The only exception is that there is a bow shock very close to the downstream electrode tip which has negligible effects on overall arc voltage. To save computational time the domain of Figure 4-1 is used to obtain the results. Since the distance between the tips of the two electrodes is 100 mm, the electrical field at the nozzle exit is used to calculate the voltage drop between the nozzle exit and the tip of downstream electrode.

The boundary conditions for the arc conservation equations and the governing equations for k-epsilon turbulence model are those of axisymmetry on the axis and no heat flux into the solid parts of the computation domain (3.4.2.5). The boundary conditions for k and ε

are the same as those given in Equation (3-7) and (3-8). When the current is around 2 kA and above at a stagnation pressure of 10 bar the arc fills the nozzle near the exit. We use the non-slender arc model to check if in this region the electrical field can still be calculated by using the slender arc model. The computation domain for electric field is extended in the radial direction to 60 mm from the axis since electrical field is a long range force. The boundary conditions for Equation (2-13) are given below:

(a) The current density entering upstream electrode at the nozzle entrance is assumed uniform as Equation (3-9).
(b) At the nozzle exit plane, the electrical potential is set to zero, i.e. $\varphi = 0$.
(c) At all the other boundaries of the computational domain, including the axisymmetric axis the normal gradients of the electrical potential are set to zero.

4.3. **Results and Discussion**

Computation has been carried out for 3 stagnation pressures (P_0 = 13 bar, 10 bar and 7 bar) and for DC currents from 250 A to 3 kA. The voltage computed by laminar flow arc model is considerably lower than that measured (Figure 2-18 and Figure 4-10). Thus, Prandtl mixing length turbulence model and the k-epsilon model are used to account for the turbulence enhanced momentum and energy transport. The turbulence parameter, *c*, in Prandtl mixing length model (hereafter referred to as PML) is adjusted to give the closest agreement with the measured arc voltage at 1 kA DC and P_0=10 bar. *c* has been found equal to 0.06.

Arc voltages predicted by the k-epsilon model with the default values for the 5 turbulence parameters (hereafter referred to as the standard k-epsilon model) are considerably higher than those measured especially at low current (Figure 4-10). This indicates turbulence effects are too strong. Similar results were obtained when this turbulence model is applied to a round turbulent jet [78]. To reduce the turbulence effects we increase the production of turbulence dissipation by adjusting the value of $C_{1\varepsilon}$ in Equation (2-30) to match the predicted arc voltage with that measured at 1 kA and 10 bar. The value of $C_{1\varepsilon}$ has been

found to be 1.62. $C_{1\varepsilon} = 1.62$ and c = 0.06 have been used to compute the arc voltage for other discharge conditions reported in this chapter. We refer to the k-epsilon model using the modified value of $C_{1\varepsilon}$ as the modified k-epsilon model, or MKE for easy reference.

Computational results are presented for laminar flow model, PML and MKE (known collectively as the flow models for future reference). The inclusion of laminar flow model is to illustrate the different arc characteristics in laminar and turbulent flows. Since the standard k-epsilon model is the most commonly used turbulence model its results will be presented to show its over-prediction of turbulence effects. The qualitative features of the computational results are similar for different stagnation pressures. Unless otherwise specified, the computational results obtained for P_0 = 10 bar are used for discussions.

4.3.1. **Feature of Cold Flow**

Computations of the cold flow have been carried out using laminar flow model and MKE. PML is not used for the computation of cold flow as the internal nozzle flow is not of thin shear layer type, thus turbulence length scale being difficult to define. It has been found that the computational results obtained by laminar flow model and MKE are almost identical. For the cold flow, turbulence effects are negligible. The results obtained by the laminar flow model are therefore used to illustrate the features of the cold flow.

Figure 4-2 shows the temperature field superimposed with the isobars. At the nozzle throat, the variation of nozzle area is not continuous. Point A forms an expansion corner [114], where isobars are bunched and then fanned out. Through the expansion waves at Point A, the flow direction changes from that parallel to the surface of the convergent section of the nozzle to that parallel to the surface of divergent section. Near the nozzle exit, radial pressure gradient is negligible. The axis pressure is shown in Figure 4-3 (a). Rapid pressure drop in the vicinity of the nozzle throat results in strong gas acceleration (Figure 4-3 (b)). However, pressure variation in a large part of the divergent section of the nozzle

is rather gentle (Figure 4-3 (a)), which accompanies a gentle increase in axis velocity (Figure 4-3 (b)). The exit pressure is set to ensure shock free supersonic flow inside the nozzle as shown by the axis Mach number distribution (Figure 4-3 (c)). The mass flow rate at P_0 = 10 bar is 0.187 kg/s.

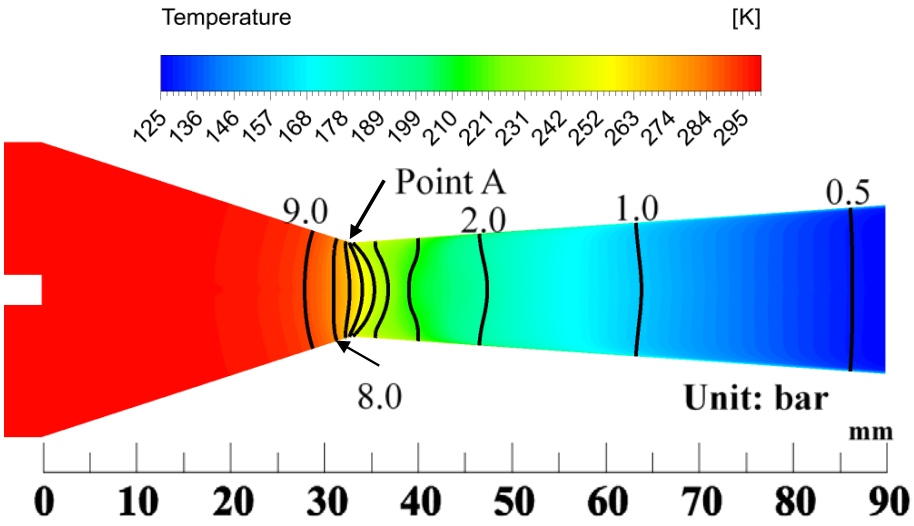

Figure 4-2. Temperature field and pressure distribution for the cold flow at a P_0 = 10 bar computed by the laminar flow model. Pressure difference between two adjacent isobars is 1 bar if not explicitly stated.

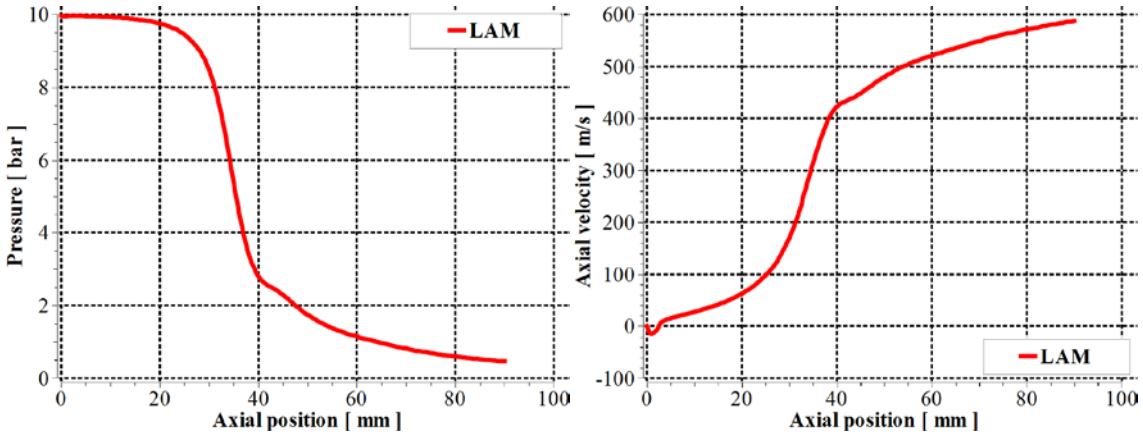

(a) (b)

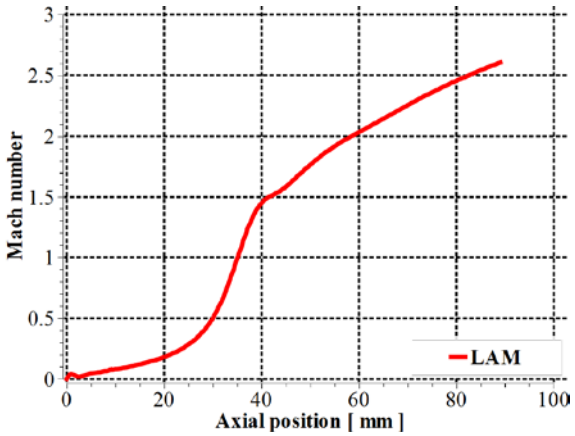

(c)

Figure 4-3 Variations of (a) pressure, (b) axial velocity and (c) Mach number along the nozzle axis for the cold flow at P_0 = 10 bar computed by the laminar flow model.

For air, the equation of state for ideal gas is valid for temperature up to 1,500 K. The density of air is therefore proportional to pressure for a given temperature. The cold flow results indicate that the flow is mainly driven by pressure gradient and viscous stresses are negligible in comparison with pressure gradient. For turbulent flow, Reynolds stress is proportional to the density. Under these conditions, it can easily be shown that the solutions of conservation equations for laminar or turbulent flow are uniquely determined by normalized pressure, P/P_0 [65]. Thus, velocity and Mach number are independent of stagnation pressure and the computed pressure normalized to stagnation pressure is the same for any stagnation pressures.

The pressure distribution of the cold flow inside a nozzle interrupter determines the dielectric strength after the exhaustion of hot gas left by a thermally extinguished arc after current zero.

4.3.2. **Feature of Arc-Flow Interaction**

Ohmic heating inside the arc creates a high temperature and low gas density region within the nozzle. The presence of the arc therefore reduces the effective flow area, thus

modifying the pressure distribution in the nozzle, which in turn affects the arc. Such interaction determines the arc characteristics.

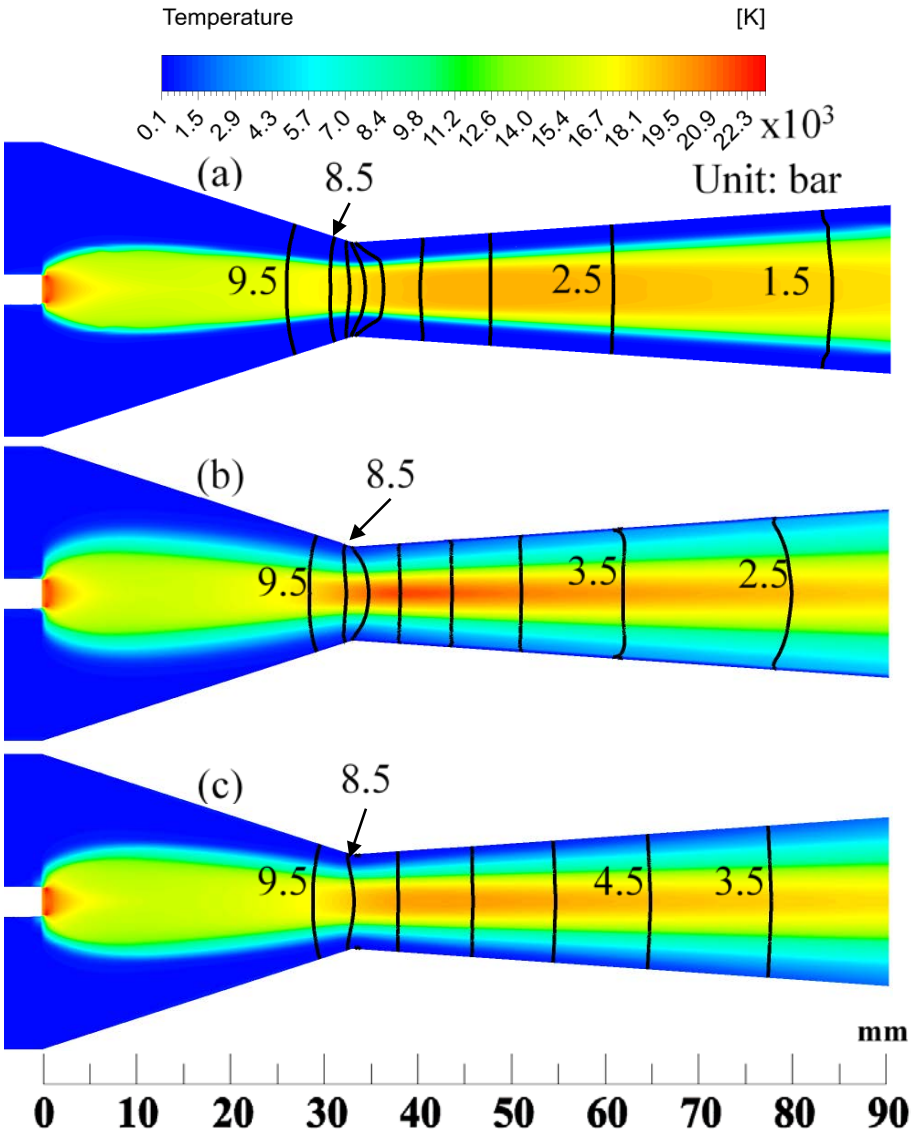

Figure 4-4 Temperature contour together with isobars for a 2 kA DC arc at P_0 = 10 bar. The pressure difference between two adjacent isobars is 1bar. (a) Computed by laminar flow model; (b) Computed by PML; (c) Computed by MKE.

Figure 4-4 shows the temperature field together with isobars for the 2 kA DC arc at a P_0 = 10 bar computed by the three flow models. There is a distinctive core structure, which is surrounded by cold gas (Figure 4-4 (a)), for the arc in laminar flow. The corresponding mass flow rate is about 65% of that of cold flow. The arc size represented by the position

of the 4,000 K isotherm (hereafter referred to as the arc radius) is the smallest for arc in laminar flow and the largest for PML as shown in Figure 4-5. At nozzle exit the surrounding cold gas has almost disappeared for the PML (Curve (2), Figure 4-5). Further increase in current the arc core will touch the Teflon nozzle surface for PML. Under these circumstances nozzle ablation needs to be taken into account. It would be shown later that the estimated power into the nozzle surface in the section where arc touches the nozzle wall will not cause ablation in the time duration during which the experiments were conducted [41]. For MKE there is still a distinctive layer of cold flow surrounding the arc at 2 kA (Curve (3), Figure 4-5). The mass flow rates for PML and MKE are respectively 26% and 32% of the cold flow case. Compared with arc in laminar flow the much reduced mass flow rate for PML and MKE is due to the spread of arc thermal influence region by turbulence effects in the divergent section of the nozzle. Therefore, the presence of an arc reduces the effective flow area inside a nozzle, which results in an increase in pressure but a reduction in its gradient in comparison with that of cold flow (Figure 4-6 (a)). Such features are reflected in the axis pressure distributions of the three flow models. The distributions of axis pressure (Figure 4-6 (a)) and axis velocity (Figure 4-6 (b)) for PML and MKE start to diverge from each other just before the nozzle throat, where flow starts to accelerate rapidly. The turbulence effects produced by MKE are stronger than that of PML, which results in lower flow acceleration, hence a smaller pressure gradient. Thus, the axis pressure of MKE is higher than that of PML. Velocity field is closely coupled with the temperature field, the close interaction of which determines voltage-current (V-I) characteristics. This is discussed in Section 4.3.3.1.

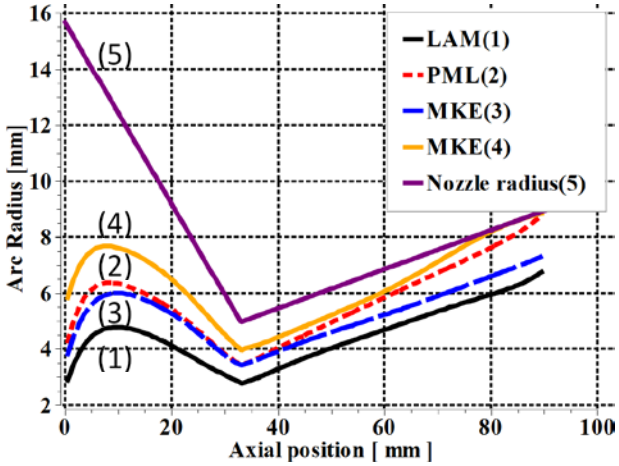

Figure 4-5 Variations of arc radius (radial position of 4,000 K isotherm) for 2 kA computed by (1) laminar flow model; (2) PML and (3) MKE. Curve (4) is the arc radius for 3 kA computed by MKE, which shows that near the nozzle exit hot gas occupies the whole nozzle. Nozzle radius (5) is plotted to show the arc size in relation to the nozzle.

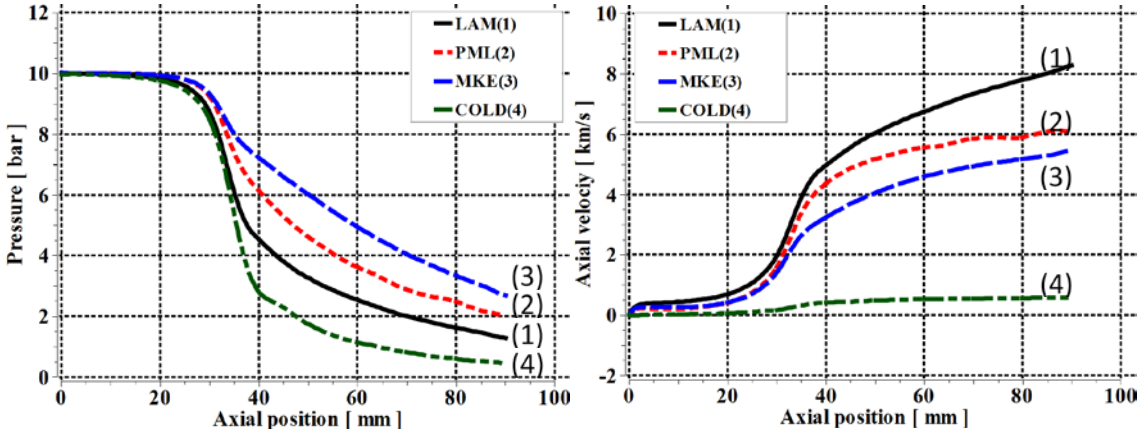

(a) (b)

Figure 4-6 Variations of, (a) pressure and (b) axial velocity, along the nozzle axis for the 2 kA DC arc computed by three flow models. The pressure and axial velocity for the cold flow (Curve (4)) is also plotted to show the effects of the presence of the 2 kA DC arc.

When current is reduced to 1 kA, the qualitative features of the arc predicted by the three flow models are similar to those of the 2 kA arc. Further decrease in current the arc core shrinks and mass flow rate passing the nozzle increases. At 250 A (Figure 4-7), the mass flow rate has attained 93% of the cold flow for the laminar case and 80% for MKE and

PML. There is very little difference between the aerodynamic features in terms of axis pressure (Figure 4-8 (a)) and axis velocity (Figure 4-8 (b)) for the two arcs predicted by MKE and PML. In contrast with the 2 kA case, axis velocity in the divergent section of the nozzle at 250 A no longer increases with distance for both turbulence models. This is due to the increased turbulence intensity when current is reduced and due to the axial development of turbulence along the nozzle length for a given current (Figure 4-9). In the vicinity of the throat where flow is accelerated rapidly turbulent kinetic energy, *k*, reaches a maximum for 250 A. The subsequent decay of *k* is due to a drop in axial velocity component as a consequence of turbulent momentum diffusion. The decrease in axial velocity and the axial expansion of arc size result in a decrease of the rate of turbulence production for 250 A (Equation (2-32)), hence the reduction of *k* towards the nozzle exit. For the 2 kA arc the monotonic increase of *k* is attributed to the continuous flow acceleration (Figure 4-8 (b) and Figure 4-9).

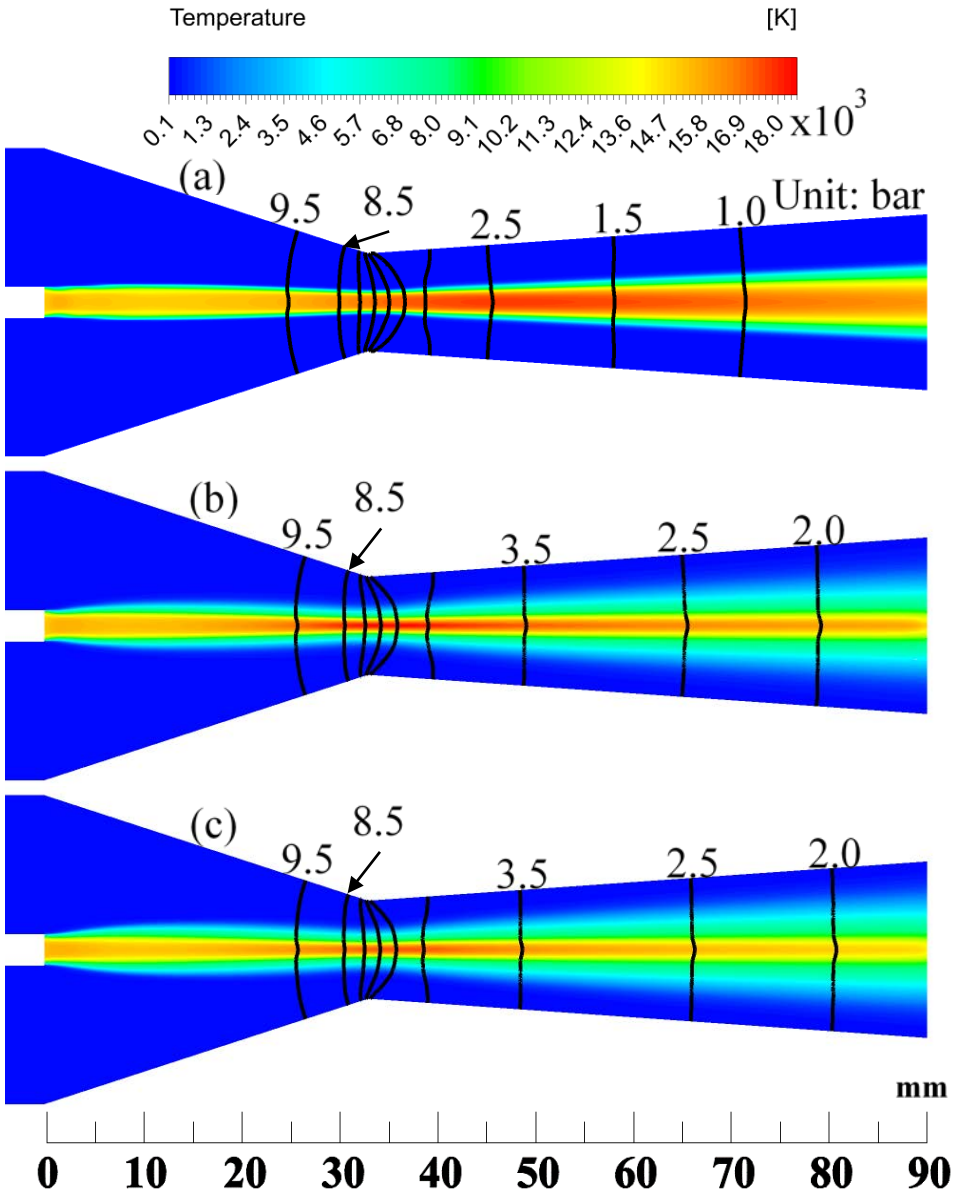

Figure 4-7 Temperature contour together with isobars for a 250 A DC arc at P_0 = 10 bar computed by (a) laminar; (b) PML; (c) MKE. The pressure difference between two adjacent unlabelled isobars after 8.5 bar is 1 bar.

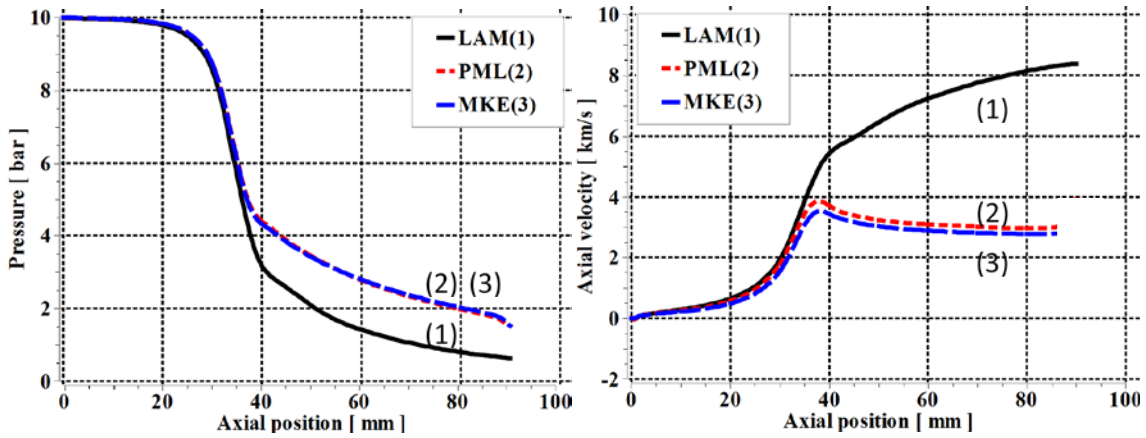

Figure 4-8 Variations of, (a) pressure and (b) axial velocity, along the nozzle axis for the 250 A DC arc computed by three flow models.

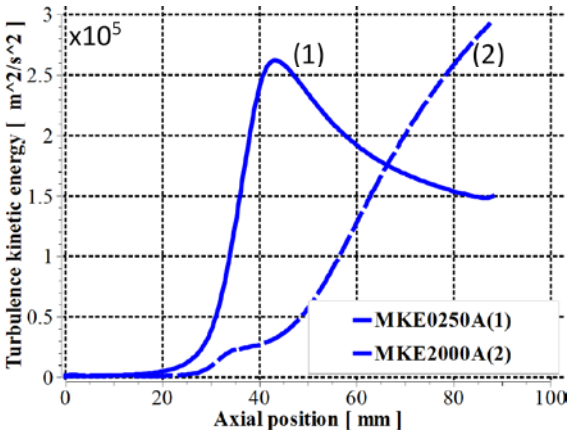

Figure 4-9 Axial distribution of axis turbulence kinetic energy per unit mass: (1) 250 A; (2) 2 kA calculated by MKE.

4.3.3. **Characteristics of DC nozzle arcs**

4.3.3.1. DC Voltage-Current (V-I) Characteristics

The DC V-I characteristics of the air nozzle arcs have been computed using the three flow models. The computed arc voltages are plotted in Figure 4-10 together with the experimental results given in [41] for comparison. The measured and computed arc voltages show a flat part of the V-I characteristic at currents above 2 kA and a negative V-I characteristic for currents below 2 kA. Comparison between measured and computed

arc voltages shows that the arc voltage predicted by the laminar flow model is lower than that measured especially at lower currents. The standard k-epsilon model, PML and MKE give good agreement for currents at 2 kA and above with the standard k-epsilon model grossly over predicting the arc voltage at low currents. Voltage computed by PML is about 10% lower than the corresponding experimental result at 250 A, the lowest current for which experimental results are available for comparison. Such a difference is well within experimental error. Overall MKE gives the best agreement with the measured voltage. The physical processes responsible for such V-I characteristics are discussed in the following two subsections.

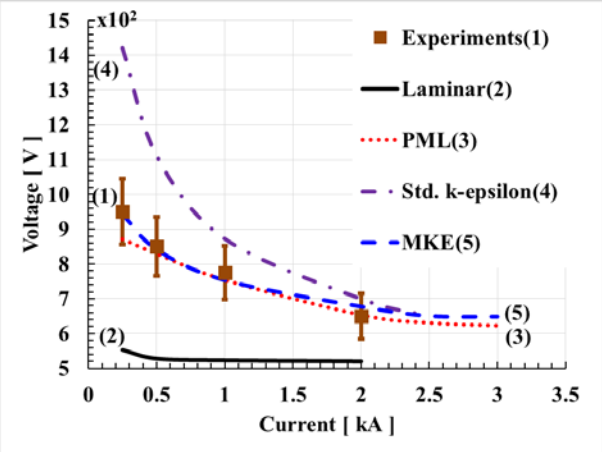

Figure 4-10 V-I characteristics for the DC air nozzle arcs at P_0=10 bar computed by various flow models.

4.3.3.2. Characteristics of Nozzle Air Arc with Radiation Dominated Arc Core

4.3.3.2.1. Overall Features

V-I characteristics are determined by the electrical conductance of the arc which is in turn dependent on the temperature distribution within the arc. Temperature field is the result of the energy balance between power input and various energy transport processes as described by the energy conservation equation. Attention will be paid to identify the dominant energy transport process.

Examination of the computational results for the flat part of the V-I characteristics given by the three flow models shows that the axis temperature for currents of 2 kA and above is not sensitive to the current for a given arc model (Figure 4-11 (a)) and the arc radius is approximately proportional to the square root of current (Figure 4-5) for the part of the nozzle where arc is surrounded by a cold layer of gas flow (Figure 4-5). Thus, the local arc conductance becomes proportional to arc current. Axis electric field distribution is not sensitive to the current for a given arc model (Figure 4-12 (b)) and the arc voltage is almost independent of current (Figure 4-10).

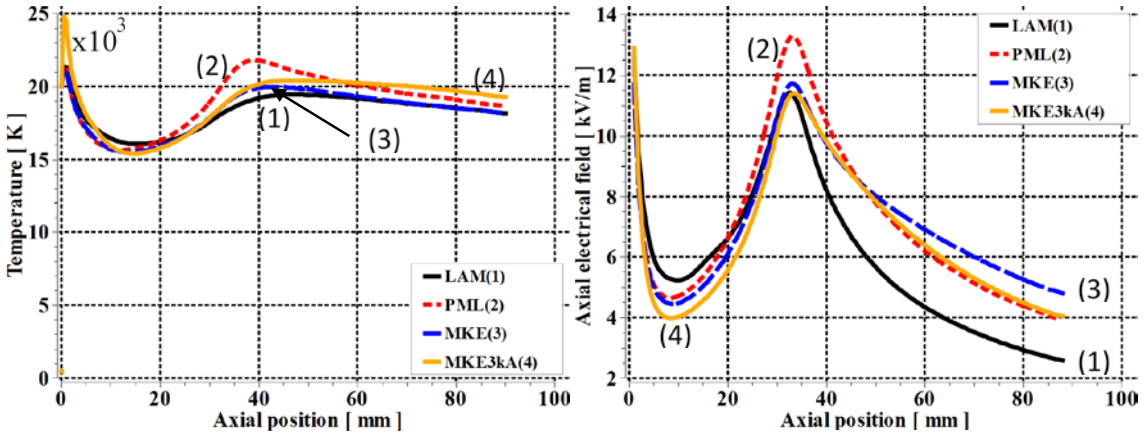

(a) (b)

Figure 4-11 Variations of axis temperature (a) and axial electrical field (b) of 2 kA arc computed by laminar flow model, PML and MKE. The axis temperature (a) and axial electrical field (b) of a 3 kA arc obtained by MKE is also plotted for comparison.

As previously noted the divergent angle of the nozzle in Figure 4-1 is very small. At 3 kA with adiabatic boundary condition for temperature, the temperature near the wall is over 4,000 K in the region within 10 mm to the nozzle exit. Radiation loss near the nozzle exit at 3 kA is less than 15% of local Ohmic input. Radiation induced Teflon ablation is unlikely as at this power level (Figure 4-11 (b)) Teflon will not reach its melting point for the experimental duration of 7 ms [115]. The measured arc voltage at 3 kA (Figure 4-10) remains the same as that of 2 kA within experimental error, which indicates that ablation is unlikely to take place. However, it should be noted that 3 kA should be considered as

the upper current limit for the validity of adiabatic boundary condition for the nozzle in Figure 4-1.

At 2 kA the arc thermal influence region extends close to the wall (Figure 4-4 and 4-5) for the two turbulence models. The arc can no longer be considered as slender. We therefore solve the current continuity equation (Equation (2-13)) for electrical potential with an enlarged computation domain, the results of which are shown in Figure 4-12. Equipotential lines are almost perpendicular to the nozzle axis indicating that radial component of electrical field is negligible and the axial component is uniform across an arc cross section. Thus, simplified Ohm's law (Equation (3-10)) is used to compute the axial electrical field for currents less than 2 kA.

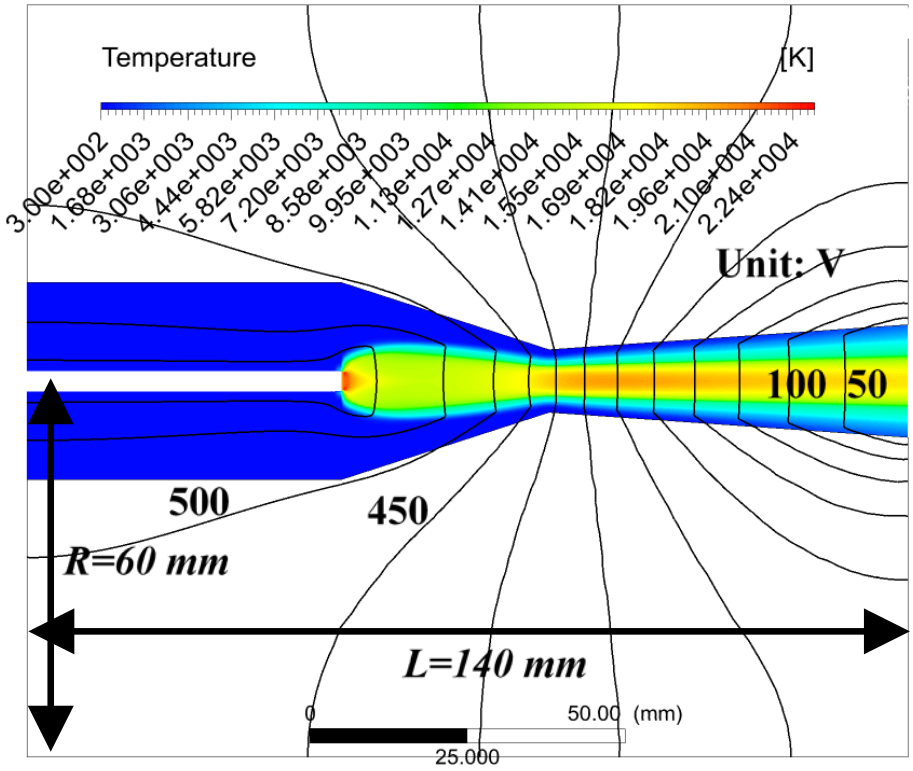

Figure 4-12 Temperature contour together with equipotential distribution for the 2 kA DC arc at P0 = 10 bar using MKE. Potential difference between two adjacent equipotential lines is 50 V. Computation domain has been extended to a radius of 60 mm from the axis to ensure that the potential distribution is no longer affected the size of the computation domain.

4.3.3.2.2. Distinctive Features of Radial Temperature Profiles and the Influence of Material Properties

Of the three flow models, arcs in laminar flow shows a distinctive high temperature core (Figure 4-4) which results in the smallest arc radius. As radial temperature profile determines the local electrical field, it would be interesting to see the features of the radial temperature profiles predicted by the three flow models. In Figure 4-13 the radial temperature at three typical axial stations, the upstream midsection, the nozzle throat and the downstream midsection are plotted.

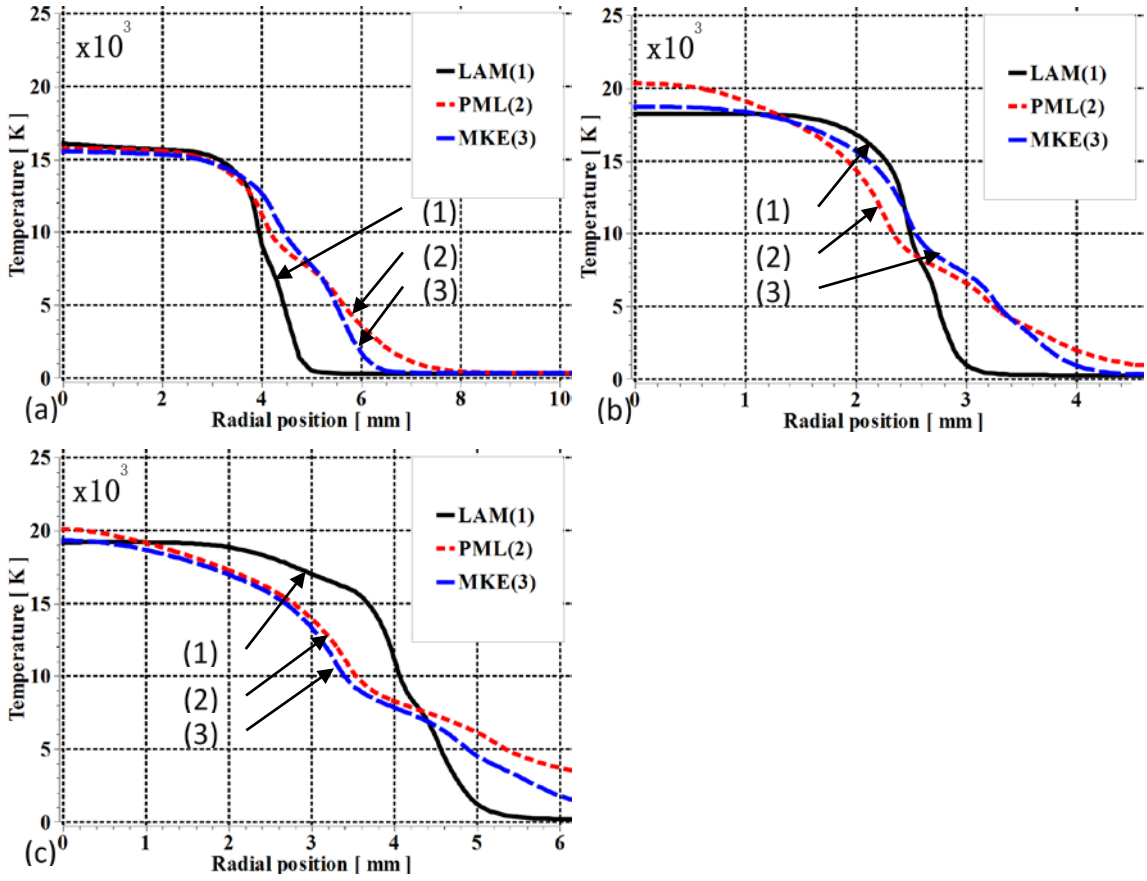

Figure 4-13 Radial temperature profiles computed by the three flow models for the 2 kA DC arc at P0 = 10 bar. (a) upstream midsection z= 15 mm; (b) nozzle throat, z= 33 mm; (c) downstream midsection z= 60 mm.

In the arc core, temperature is almost constant for arc in laminar flow, but for PML and MKE, the effects of turbulence enhanced thermal conduction is clearly shown in the region downstream of nozzle throat (Figure 4-13 (c)). However, for all the three flow models, radiation transport is the dominant energy transport process. In the radiation re-absorption region where 60% of radiation at the core boundary is absorbed, the thickness

of this region and the slope of the temperature profile differ greatly depending on the flow model. There are several inflection points on the radial temperature profiles predicted by PML and MKE which correspond to the peaks of effective thermal conductivity (Figure 4-14). One inflection point is at approximately 7,000 K and the other around 4,000 K. Temperature gradient is mainly determined by thermal conductivity. Molecular thermal conductivity for laminar arc is much smaller than the effective turbulent thermal conductivity (Figure 4-14), which is the sum of molecular and turbulent thermal conductivity. This explains why the temperature gradient in the radiation absorption region of a laminar arc is the largest, thus a thin radiation re-absorption region. Because of the large effective thermal conductivity at the nozzle throat and in the divergent section of the nozzle (Figure 4-14 (b) and (c)) the thickness of the radiation re-absorption region is much bigger than that of the laminar case. The arc is more diffused and has no distinctive core structure for air arc in turbulent flow.

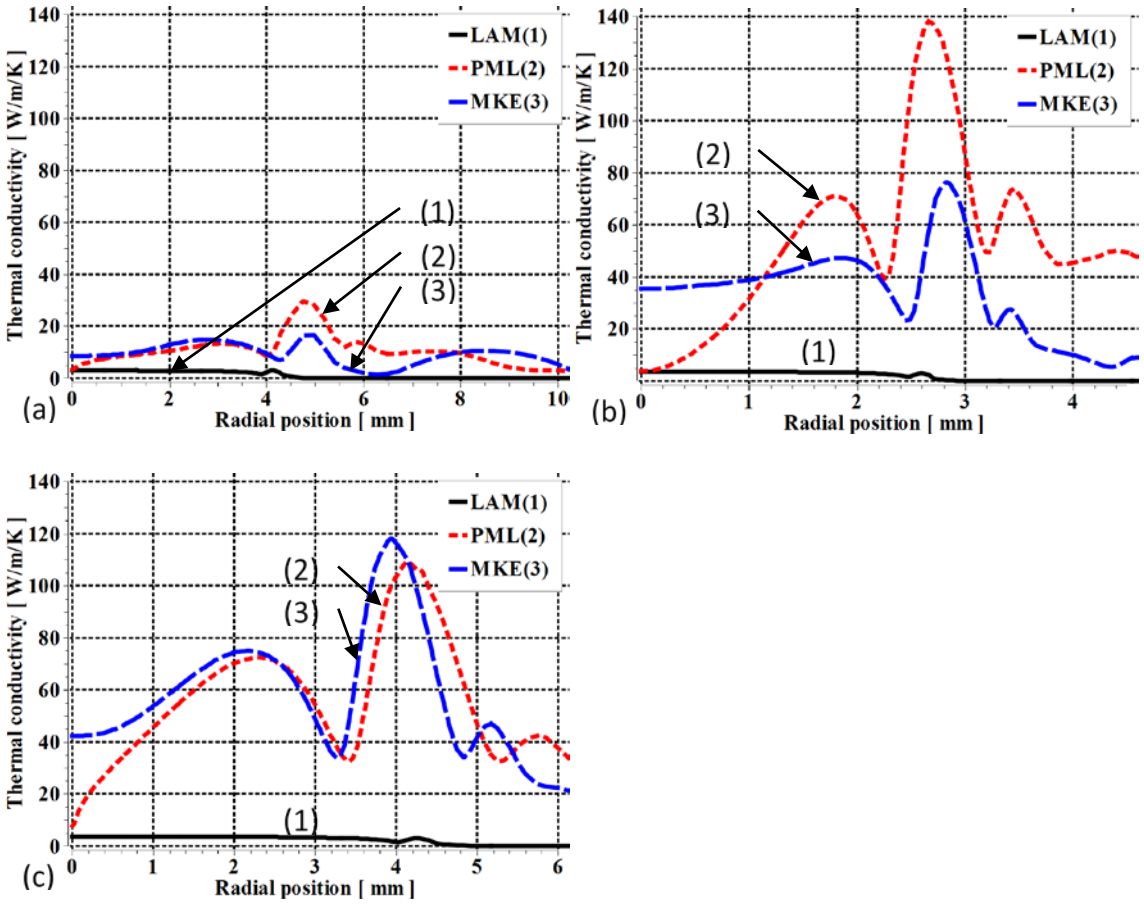

Figure 4-14 Radial profiles of effective thermal conductivity (sum of molecular and turbulent conductivities) computed by the three flow models for the 2 kA DC arc at P0 = 10 bar. (a) upstream midsection z= 15 mm; (b) nozzle throat, z= 33 mm; (c) downstream midsection z= 60 mm. For laminar flow, effective thermal conductivity is simply the molecular part.

Effective thermal conductivity has rather complex features (Figure 4-14). Since turbulent thermal conductivity is the dominant component of effective thermal conductivity, we examine the features of eddy kinematic viscosity. Effective thermal conductivity is the product of effective eddy kinematic viscosity with the material property ρC_P. Radial profiles of effective kinematic viscosity for the 2 kA arc are given in Figure 4-15.

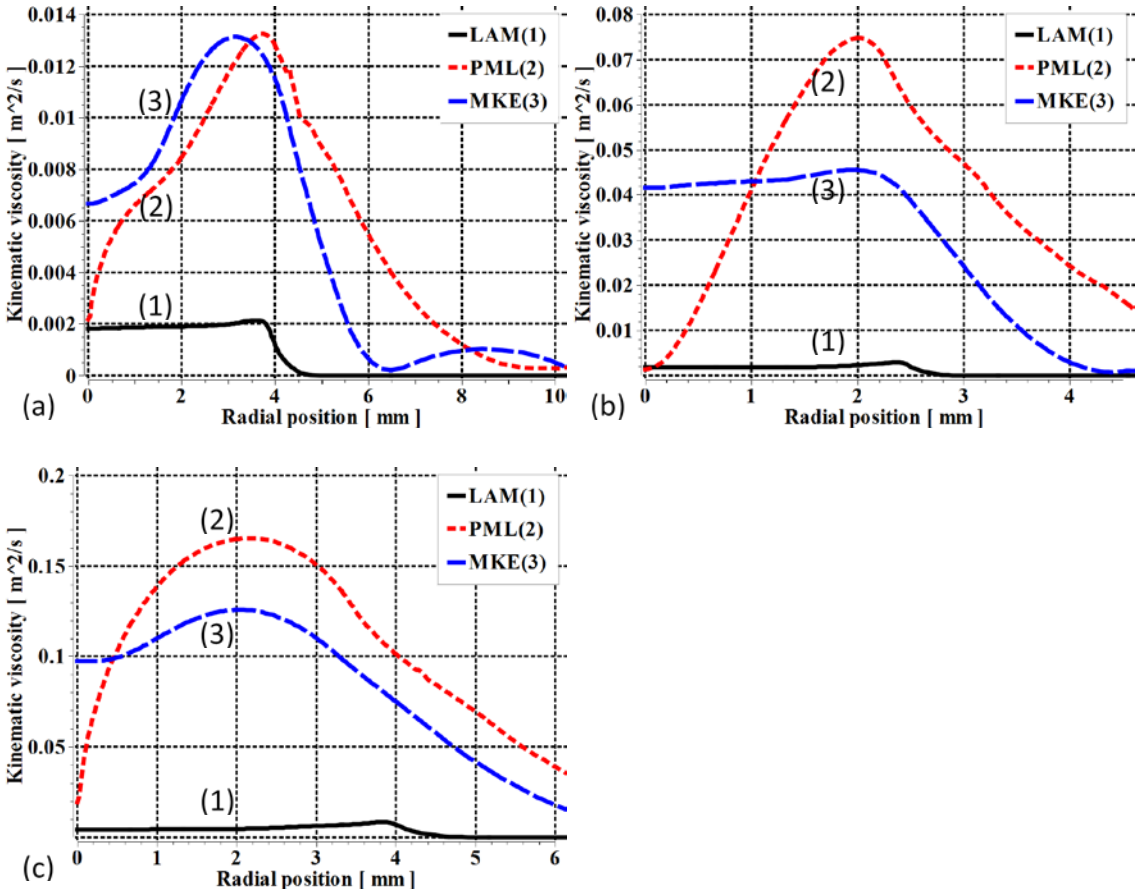

Figure 4-15 Radial profiles of effective kinematic viscosity (sum of molecular and turbulent kinematic viscosity) computed by the three flow models for the 2 kA DC arc at P0 = 10 bar. (a) upstream midsection z= 15 mm; (b) nozzle throat, z= 33 mm; (c) downstream midsection z= 60 mm.

The peak of eddy viscosity for PML in Figure 4-15 is directly related to the radial gradient of axial velocity component (Equation (2-19)). It always exhibits a peak in the region where velocity gradient the largest. For MKE eddy viscosity depends on k^2/ε which is more complex as this ratio is the solution of the transport equations for k and ε, which are also closely coupled with momentum and energy conservation equations. The production of turbulence kinetic energy is related to the velocity gradients (Equation (2-32)). For the MKE model, in the region where the radial gradient of axial velocity component changes slowly due to slow axial acceleration (Figure 4-6 (b)) and the arc expansion (Figure 4-5), eddy kinematic viscosity is nearly a constant (Figure 4-15 (b) and (c)).

For both PML and MKE models the first peak of the radial profile of effective turbulent thermal conductivity (Figure 4-14 (a)) is associated with the peak in eddy kinematic viscosity located in the region with the largest velocity gradient. The two peaks at temperatures around 7,000 K and 4,000 K are respectively caused by the dissociation of nitrogen molecules and by that of oxygen molecules. The dissociations of nitrogen and oxygen molecules produce two peaks in the material property ρC_P as shown in Figure 4-16. These peaks produce two inflection points on the radial temperature profile (Figure 4-13) around 7,000 K and 4,000 K, respectively. Thus, the temperature profiles for PML and MKE in the radiation re-absorption region become very broad. In the divergent section of the nozzle there is no distinctive high temperature core as those observed for SF_6 arc. Such broad radial temperature profile makes the arc radius very big in comparison with SF_6 arc at similar current and pressure [65].

It should be noted that the results obtained by MKE in the upstream midsection show a local peak (Figure 4-15 (a)) in effective kinematic viscosity, which is in the region where the temperature is a constant at its local ambient (Figure 4-13 (a)) and the axial component of velocity is also constant. In such a region there is no mechanism for generating turbulence and k and ε should tend to zero. Numerical results of k and ε are shown in Figure 4-17 which shows that these two quantities are very small in the region for R > 6 mm. This presents much numerical difficulty as the ratio of k^2/ε cannot tend to zero numerically. However, this “artificial” peak in eddy kinematic viscosity and that in effective thermal conductivity will not affect the solution in other regions since the gradients of velocity and temperature are negligible for R > 6 mm in the upstream midsection.

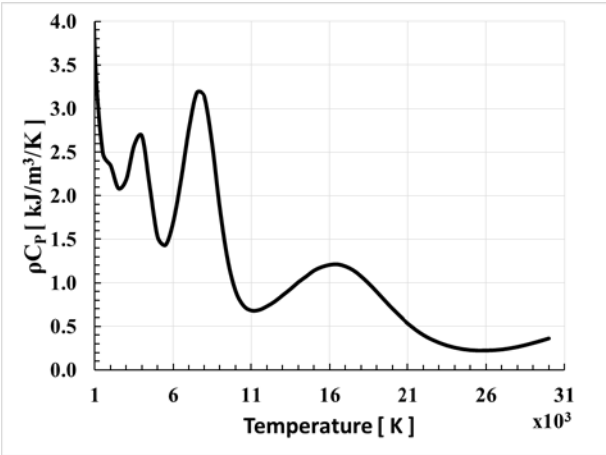

Figure 4-16 ρC_P of air at 10 Bar.

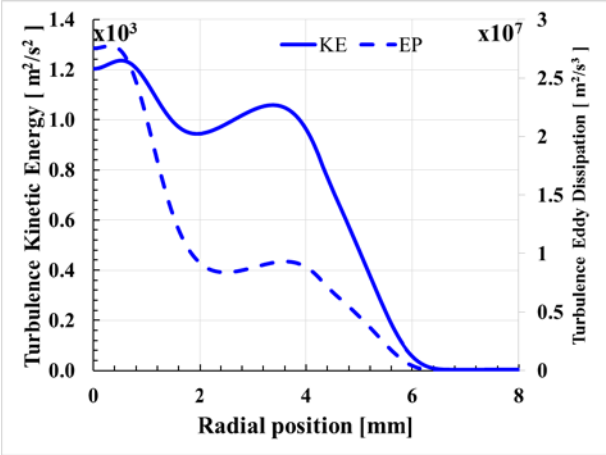

Figure 4-17 Radial profiles of k and ε at upstream midsection z=15 mm for the 2 kA DC arc and P0 = 10 bar.

4.3.3.2.3. Energy Balance

As previously indicated temperature is determined by the balance between electrical power input and various energy transport processes as given in the energy conservation equation. The dominant energy transport processes determine the arc characteristics. It is important to identify the material properties associated with the dominant energy transport processes. The identification of such properties will serve as a guide for the search of a replacement gas for SF_6 as an arcing medium.

Radiation transport is an important energy transfer process in high pressure arcs. With our radiation transport model it is natural that we examine energy balance in the arc volume up to the radial position at which the temperature is equal to 83% of the axis temperature. Following the previous work on SF_6 [65], we call this region as the arc core region although the core structure in air arc for PML and MKE is not clearly defined since outside this region temperature decay is not rapid. This is in contrast with SF_6 arc [65]. The energy balance for the arc core at 2 kA is given in Table 4-1.

Table 4-1 Percentage of electrical power input associated with various energy transport processes for the whole arc length at the core boundary calculated by the three flow models at 2 kA and P0 = 10 bar. Positive means power input and negative power loss.

Model	Power input (10^5 W)	Radiation loss (%)	Radial thermal conduction (%)	Axial enthalpy convection (%)	Radial enthalpy convection (%)
Laminar	9.17	-72.8%	-2.4%	-27.7%	5.8%
PML	7.59	-62.5%	-27.5%	-2.8%	-3.8%
MKE	8.82	-61.3%	-27.6%	-3.9%	-4.5%

Method of calculation: Power input = $\int_{Z1}^{Z2}\int_0^R \sigma E^2 2\pi r dr dz$

Radiation loss (%) = $-\int_{Z1}^{Z2}\int_0^R q 2\pi r dr dz$ / Power input

Radial thermal conduction (%) = $-\int_{Z1}^{Z2}\int_0^R \frac{1}{r}\frac{\partial}{\partial r}\left(rk\frac{\partial T}{\partial r}\right) 2\pi r dr dz$ / Power input

Axial enthalpy convection (%) = $-\int_{Z1}^{Z2}\int_0^R \rho w \frac{\partial h}{\partial z} 2\pi r dr dz$ / Power input

Radial enthalpy convection (%) = $-\int_{Z1}^{Z2}\int_0^R \rho v \frac{\partial h}{\partial r} 2\pi r dr dz$ / Power input

Conventional understanding of heat transfer by convection is based on the non-conservative form of the energy conservation equation expressed in terms of enthalpy [114]. Therefore, arc energy balance calculation is based on this equation. It has been

found that the pressure work in this energy conservation equation accounts for less than 5% of the electrical power input in all results reported in this paper. Pressure work is not given in the tables related to energy balance.

It is shown in Table 4-1 that for the laminar flow case Ohmic input into the core is entirely taken out by radiation and axial enthalpy transport and 86% of the total current is carried by the core. Radiation loss and turbulence enhanced thermal conduction account for over 90% of Ohmic input for PML and MKE. The current carried by the arc core accounts for 59% of the total current for PML and 66% for MKE. It has been found that on the flat part of V-I characteristics where current is larger than 2 kA radiation loss for the two turbulence flow models, PML and MKE, always accounts for no less than 60% of Ohmic input.

To assess the influence of turbulence we need to consider the arc energy balance at the electrical boundary. This is because between the arc core boundary and the electrical boundary nearly 60% of the radiation flux coming out of the arc core is absorbed in this region, thus altering the energy balance. Table 4-2 shows how electrical power input into the electrically conducting core is balanced by various energy transport processes.

Table 4-2 Percentage of electrical power input associated with various energy transport processes for the whole arc length at the electrical boundary calculated by various flow models at 2 kA and P0 = 10 bar. Mathematical expressions for power input and power loss are the same as those in Table 4-1.

Model	Power input (10^6 W)	Radiation loss (%)	Radial thermal conduction (%)	Axial enthalpy convection (%)	Radial enthalpy convection (%)
Laminar	1.07	-25.1%	-1.6%	-106.9%	35.3%
PML	1.29	-14.7%	-19.7%	-85.1%	16.6%
MKE	1.33	-16.3%	-21.7%	-61.3%	-2.5%

Due to radiation absorption the energy balance at the electrical boundary has been greatly altered in comparison with that at the core boundary. For laminar flow radiation loss only accounts for 25% of power input while axial enthalpy transport is the dominant energy removal process. For PML and MKE radiation and thermal conduction account for about 35% power input and the rest is removed by convection. For both turbulence models axial convection is dominant but for PML radial convection acts as a power input mechanism. Although detailed energy balance differs for PML and MKE, arc voltages predicted by these two models are virtually the same when experimental error in measuring the arc voltage (mainly due to short to short variation) is taken into account.

4.3.3.3. Characteristics of with Radiation and Thermal Conduction Dominated Arc Core

When current is reduced from 2 kA, the relative importance of radiation as an energy loss mechanism is reduced while thermal conduction gradually becomes the dominant energy transport process for arcs in turbulent flow. Arc area reduces at a faster rate than current and arc voltage increases with current for turbulent arcs. However, for arcs in laminar flow radiation is still the dominant energy removal process and the arc area is still approximately proportional to current. Arc voltage of a laminar flow arc is hardly increased when the current is reduced to 250 A (Figure 4-10).

The qualitative features of axis temperature (Figure 4-18 (a)), arc radius (Figure 4-18 (b)) and axial electric field (Figure 4-18 (c)) distributions of a 250 A arc are similar to those of 2 kA. Arc radius is the smallest for laminar flow arc but its temperature downstream of throat is the highest. The axis temperature for PML is higher than that of MKE but the latter has a larger arc radius. This results in the electrical field for MKE is slightly higher than that of PML (Figure 4-18 (c)). There is only 3.5% difference in arc voltages predicted by these two turbulence models. Radial temperature profiles at three axial stations for the three flow models are given in Figure 4-19. The features of radial temperature profiles at 250 A are similar to those of 2 kA (Figure 4-13 and 4-19). However, the relative size of the thickness of the radiation re-absorption region to the arc core size is increased compared with that of 2 kA especially in the downstream region of the throat (Figure 4-19 (c)). Such a broad temperature profile at low currents will have detrimental effects for arc thermal extinction during current zero period. The peaks of effective thermal conductivity at 7,000 K and 4,000 K are again responsible for such broad radial temperature profiles.

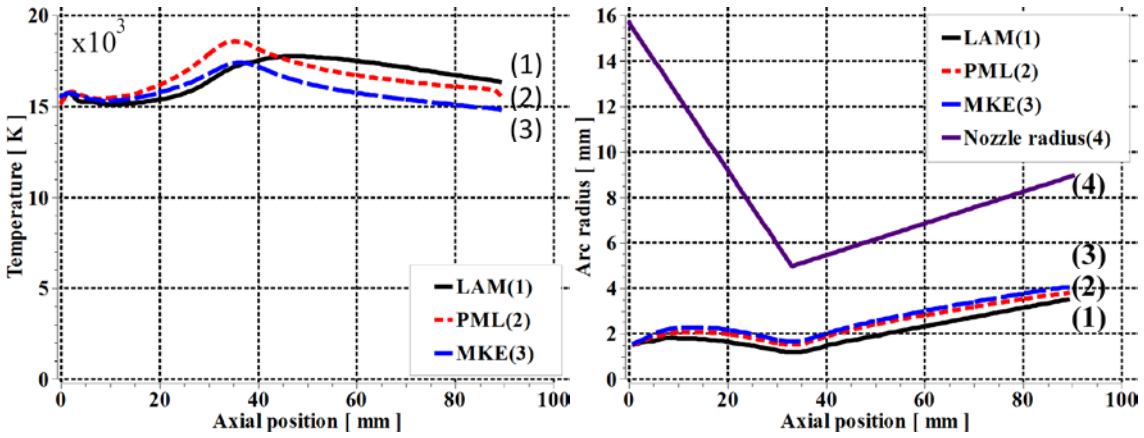

(a) (b)

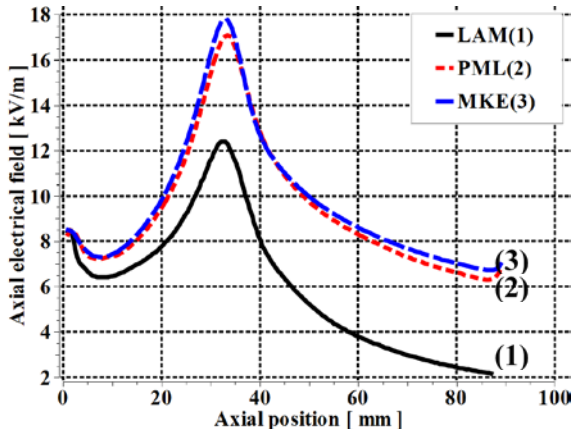

(c)

Figure 4-18 Variations of, (a) temperature, (b) arc radius and (c) electric field, along the nozzle axis for the 250 A DC arc at P0 = 10 bar computed by the three flow models.

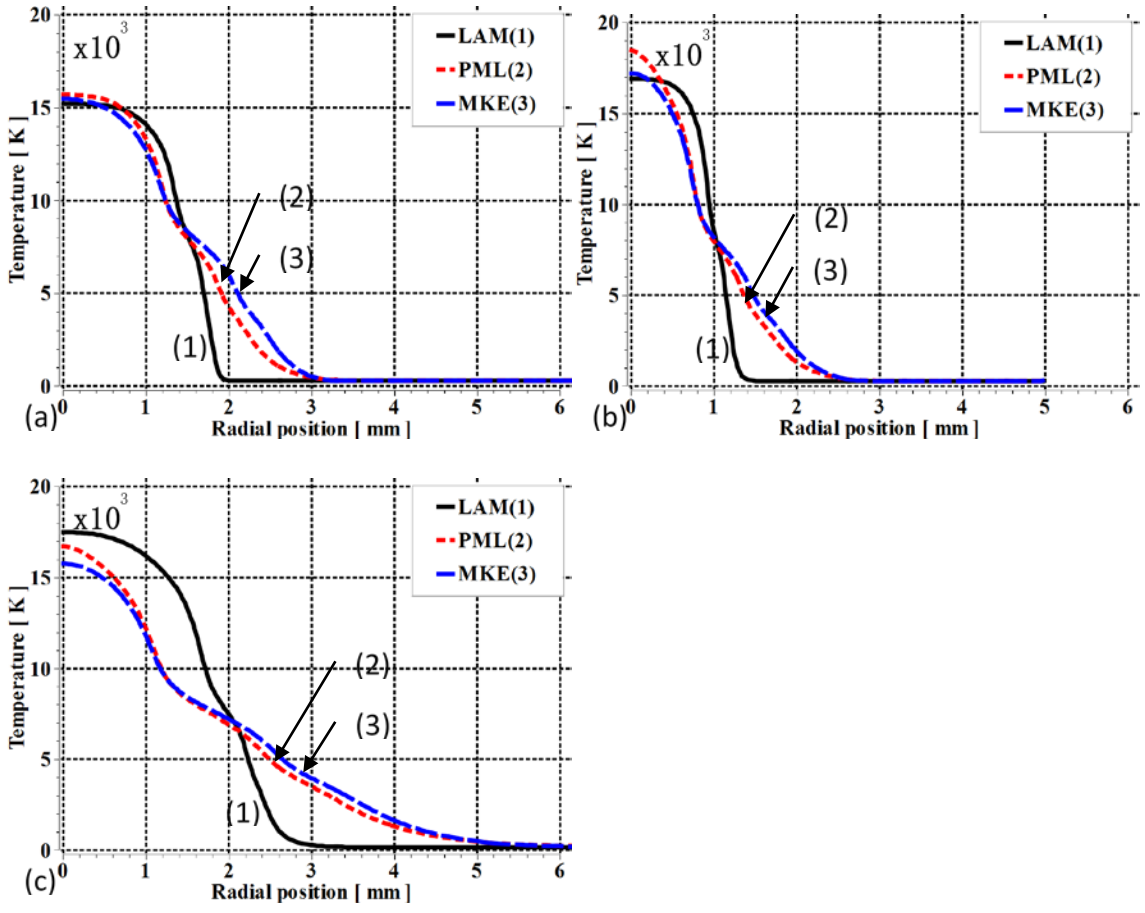

Figure 4-19 Radial temperature profiles computed by the three flow models for the 250 A DC arc at P0 = 10 bar. (a) upstream midsection z= 15 mm; (b) nozzle throat, z= 33 mm; (c) downstream midsection z= 60 mm.

At the core boundary radiation is still dominant for laminar flow but for PML and MKE radiation accounts respectively for 36% and 26% of core Ohmic input (Table 4-3). Energy balance at the electrical boundary for 250 A is given in Table 4-4. Radial and axial enthalpy transport together with radiation loss account for 84% of Ohmic input at the electrical boundary for the laminar case (Table 4-4). For the two turbulence models thermal conduction and axial enthalpy account for 90% of the power input with thermal conduction the most important energy transport process.

Table 4-3 Percentage of electrical power input associated with various energy transport processes for the whole arc length at the core boundary calculated by the three flow models at 250 A and P0 = 10 bar. Mathematical expressions for power input and power loss are the same as those in Table 4-1.

Model	Power input (10^5 W)	Radiation loss (%)	Radial thermal conduction (%)	Axial enthalpy convection (%)	Radial enthalpy convection (%)
Laminar	1.12	-64.6%	-15.3%	-25.2%	7.6%
PML	1.29	-35.9%	-63.2%	2.8%	-2.5%
MKE	1.35	-26.4%	-70.0%	0.9%	-1.6%

Table 4-4 Percentage of electrical power input associated with various energy transport processes for the whole arc length at the electrical boundary calculated by the three flow models at 250 A and P0 = 10 bar. Mathematical expressions for power input and power loss are the same as those in Table 4-1.

Model	Power input (10^5 W)	Radiation loss (%)	Radial thermal conduction (%)	Axial enthalpy convection (%)	Radial enthalpy convection (%)
Laminar	1.39	-20.8%	-7.8%	-134.1%	65.5%
PML	2.27	-8.2%	-54.8%	-45.5%	9.9%
MKE	2.34	-6.1%	-54.6%	-49.0%	11.1%

4.3.3.4. The Effects of Stagnation Pressure

Computation of arc voltage has also been done using PML and MKE for 7 bar and 13 bar. Laminar flow arc model is not used as it cannot give a satisfactory account of energy loss mechanism. Qualitative arc features at P_0 = 7 bar and 13 bar are similar to the arc at P_0 = 10 bar. Table 4-5 summarizes the arc voltages computed for the three pressures together with the corresponding experimental results, which were given in [41].

Table 4-5 Arc voltages by the three flow models for different values of P0 and the currents ranging from 250 A to 3 kA.

U(V)	13 bar			10 bar			7 bar		
I (A)	PML	MEK	Exp	PML	MEK	Exp	PML	MEK	Exp
250				906	937	930			
500				830	842	850	688	737	789
1000	876	1071	1075	754	746	750	612	636	667
1500		937	924	690	677	700		588	626
2000	760	846	848	645	665	650	533	552	606
2500		777	803	630	650	650			
3000	696	715	773	622	648	660			

Computations have only been done for those cases where experimental results are available for comparison with the predicted voltage. For 7 bar the arc in the divergent section near the nozzle exit already fills the nozzle for currents around 2 kA, which renders the adiabatic boundary condition invalid. Thus, no computational results are given for currents above 2 kA at 7 bar. The experimental results given in the table are derived from the non-dimensional VI characteristics of [41] which are subject to an error of $\pm$15% around the value given in Table 4-5.

Table 4-5 indicates that voltages predicted by PML and MKE at 10 bar fall within the error bar (Figure 4-10). That means that there is no preference as regards which turbulence model should be used for P_0 = 10 bar. However, arc voltage predicted by MKE for P_0 = 7 bar and 13 bar is closer to the experimental results than that by PML. This indicates that MKE gives a better description of the length and velocity scales of the eddies responsible for turbulent energy transfer at P_0 = 7 and 13 bar. For the accuracy of prediction under a wide range of gas discharge conditions, MKE is a preferred turbulence model for air nozzle arcs although computational cost is higher than that of PML.

If we use the voltages predicted by MKE at P_0 = 10 bar and 13 bar with the voltage at P_0 = 10 bar as the base to derive the voltage dependence on pressure, we find that the voltages at these two pressures are proportional to the stagnation pressure to the power of 1.2, but between P_0 = 10 bar and 7 bar, arc voltages are proportional to the stagnation pressure to the power of 0.4. This is in contrast with the voltage of DC SF_6 arcs which is proportional to the square root of stagnation pressure [65]. For air nozzle arc in the nozzle of Figure 4-1 with a very small divergent angle it appears that there is no simple relationship between arc voltage and stagnation pressure. However, this could be a direct consequence of an arc burning in a very narrow divergent section of the nozzle. When current is sufficiently high for a given stagnation pressure (for example at 2 kA and P_0 = 7 bar), the arc in this section is no longer surrounded by a cold flow as in the case for SF_6 nozzle arc [65]. The behaviour of an arc which fills the nozzle could be very different from the one with a surrounding cold gas. The investigation of such a nozzle arc is beyond the scope of the present investigation as nozzle ablation and a change of wall boundary condition for temperature need to be considered.

4.4. **Summary**

A detailed computational investigation into the behaviour of an air arc burning in the nozzle of Fang et al [41] has been carried out using three flow models, the laminar flow model, the Prandtl mixing length model (PML) and the modified k-epsilon model (MKE).

Arc voltage predicted by the laminar flow arc model is considerably lower than the measured arc voltage while the standard k-epsilon model grossly over predicted the arc voltage in comparison with experimental results. A modified k-epsilon turbulence model is then introduced to reduce the turbulence effects by adjusting one of the five turbulence parameters ($C_{1\varepsilon}$) to increase the turbulence dissipation rate. The value of $C_{1\varepsilon}$ and that of the turbulence parameter in PML, *c*, have been found respectively to be 1.62 and 0.06 by matching the predicted arc voltage with that measured arc voltage at 1 kA and P_0 = 10 bar. These values have been used to predict the arc voltage at other current and pressure.

When the dominant energy transport is radiation loss at the arc core boundary arc voltage is almost independent of current. This is the case for laminar flow arcs and for PML and MKE when current is 2 kA and above for the nozzle of [41]. For arcs in laminar flow axial enthalpy transport and radiation loss are the two most important energy transport processes for all currents investigated in this chapter. On the flat part of the V-I characteristics, the results of overall energy balance at the electrical boundary obtained by PML and MKE show that axial enthalpy transport and turbulence enhanced thermal conduction nearly account for all electrical power input.

For PML and MKE when current is reduced from 2 kA at P_0 = 10 bar arc voltage starts to rise. At the arc core boundary thermal conduction gradually becomes the dominant energy transport process. At 250 A and P_0 = 10 bar it accounts for over 60% of the electrical power input into the core. At the electrical boundary thermal conduction and axial enthalpy balance the electrical input with thermal conduction being the dominant energy loss mechanism.

Qualitative arc features at different stagnation pressures are similar. However, in contrast with DC SF_6 arcs [65] there is no simple relationship between arc voltage and stagnation pressure. Overall, MKE gives the best agreement with experimentally measured arc

voltage for the three stagnation pressures investigated. Therefore, MKE is the preferred arc model for air nozzle arcs.

A distinct feature of air arcs is the shape of its radial temperature profile. For air arcs under turbulent flow there is no distinctive high temperature core. Radial temperature is very broad with the thickness of the radiation re-absorption bigger than the core. The radial extent of the arc's thermal influence region for air arcs is much bigger than SF_6 under similar discharge conditions. Such broad radial temperature profile is due to the material property, ρC_P, which produces the peaks in turbulent thermal conductivity at 4,000 K and 7,000 K due to respectively the dissociation of oxygen molecules and nitrogen molecules. Such peaks will have detrimental effects on arc thermal recovery. To seek replacement gas for SF_6 one should aim at finding a gas its ρC_P does not have peaks above 4,000 K at which electrical conductivity due to thermal ionization is negligible. Yet, a peak in ρC_P is desirable just below 4,000 K to force a sharp drop in temperature above 4,000 K and a gentle temperature tail below 4,000 K. This ensures a core formation and a small arc size. ρC_P of SF_6 has such properties, hence superior arc quenching capability.

Chapter 5. Current Zero Behaviour of an Air Nozzle Arc Burning in a Supersonic Nozzle

5.1. Introduction

A detailed computational study on the behaviour of the DC air nozzle arcs has been discussed in Chapter 4. It has been shown that compared with the experimentally measured arc voltage the voltage predicted by an arc model based on laminar flow is too low. Prandtl mixing length model and a modified k-epsilon model are used to take into account of turbulence enhanced momentum and energy transport. It has been found that the material property of air, the product of density and specific heat, ρCp, determines the radial temperature profile, hence the electrical behaviour of the arc.

This chapter is a continuation of Chapter 4, which is concerned with the transient behaviour of a switching air arc burning in a supersonic nozzle (hereafter referred to as the nozzle arc). The arc is subjected to a current ramp with a rate of current decay, di/dt, towards current zero and a voltage ramp with the rate of increasing, dV/dt, after current zero. The current ramp and voltage ramp are used to simulate the discharge conditions of an arc in a circuit breaker in which the peak of a fault current does not have influence on the arc behaviour in the vicinity of a natural AC current zero (the so-called current zero period). For air switching arcs during current zero period, Frind and Rich have reported the experimental investigation of air nozzle arc based on a two-pressure system, and the measurements of the critical rate of rise of recovery voltage (RRRV) [66]. The discharge conditions of [66] will be used for the present investigation. The role of turbulence and the material properties determining the interruption capability of air as a switching medium will be further investigated for a rapidly changing arc during current zero period. The same turbulence models as in Chapter 4 will again be used to study the arc behaviour under the discharge conditions specified in [66]. In order to demonstrate the role of turbulence, the laminar flow model will be included in the present investigation. For ease of discussion, the arc models based on laminar and turbulent flow will be referred to collectively as flow models hereafter. The computed values of RRRV will be compared

with those reported in [66]. Based on such comparison, together with the investigation of Chapter 4, the role of turbulence and material properties in determining the behaviour of air switching arcs will be identified. A discussion on the relative merits of the turbulence models employed will also be given.

It is noted that, with the experimental conditions of Frind and Rich [66], a shock will be generated inside the nozzle, which affects the arc characteristics as compared with the nozzle arc without the shock [64]. Attention will therefore also be paid to the shock structure and the flow features behind the shock as indicated by computational results. The differences between flow features computed by different flow models, and their effects on predictions of the interruption capability of nozzle interrupter, are discussed.

This chapter is organized as follows. Section 5.2 gives a discussion of computational results and comparison with experiments where a detailed analysis of the physical mechanisms encompassed in each flow model will be given to show its adequacy in describing the rapidly varying arc during current zero period. Physical mechanisms responsible for the dependence of RRRV on stagnation pressure and di/dt are discussed in Section 5.3. Relative merits of flow models are discussed in Section 5.4. Finally, appropriate conclusions are drawn.

5.2. **Results and Discussion**

Version 17.0 of ANSYS Fluent [105] has been used to solve the governing equations. Parallel processing facility of ANSYS Fluent [105] has been used for all computations of the present work. Computations have been performed on the nozzle-electrode configuration used in the experiments of Frind and Rich [66]. The computational domain, which includes the geometry of the nozzle-electrode configuration, is shown in Figure 5-1. The diameter of the nozzle inlet is 25 mm and that of the outlet 38.4 mm. The nozzle throat is 31.3 mm away from the nozzle inlet and its diameter is 12.5 mm. The nozzle has

a 15 degree expansion half angle for the diverging part downstream of the nozzle throat. The distance between two electrodes is 50.3 mm. The upstream electrode has a round tip and the downstream electrode is hollow, both of which have an outer diameter identical to the diameter of the nozzle throat. The inner diameter of the hollow contact is 4 mm. The nozzle exit is connected to a cylindrical dumping tank which is represented by an open boundary with fixed pressure as shown in Figure 5-4. This is consistent with the experimental conditions of [66].

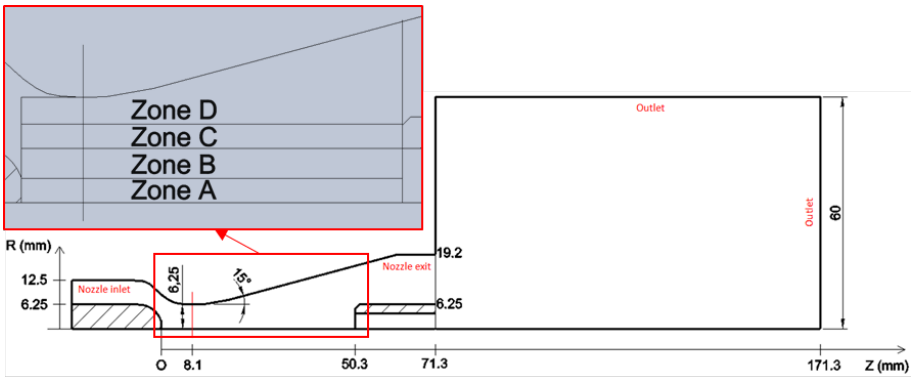

Figure 5-1 Nozzle geometry and grid system. The arc is formed in Zone A-D which are meshed with structured grids. Zone A contains 201 (axial) x 60 (radial) grids. There are 201 x 30 grids in Zone B. Zone C and Zone D contains 201x15 grids per each Zone. All other computation domains are meshed with non-structured grids with an average edge size of 1 mm. There are totally 21105 structured grids and 9829 non-structured grids.

In the experiments of [66], the dumping tank is very large (600 L), but the detailed dimensions of which are however not given in [66]. In order to save computational time, we do not consider such a large dumping tank with closed boundaries, but use an open boundary downstream of the nozzle exit (Figure 5-1) to simulate the role of the dumping tank. Since the amount of gas discharged into the dumping tank during experiment is much smaller than that in the dumping tank it is expected that the region in the dumping tank which will be affected by the mass flow out of nozzle is limited in the vicinity of nozzle exit. Numerical experiments show that at the outlet in Figure 5-1 the gas is still and the pressure remains at the value specified in the experiments of [66]. Thus, a pressure outlet boundary condition of ANSYS Fluent [106] is applied for which the static pressure is 0.25 of the upstream stagnation pressure and the gas stagnation temperature is 300 K. In case that the gas is sucked into the nozzle, the thermodynamic state of the sucked in gas at the

outlet is computed in the same way as that at the nozzle inlet in Chapter 4 by using the static pressure as the stagnation pressure.

The boundary conditions for solution of the arc conservation equations are the same as those reported in Chapter 4. At the nozzle inlet, three upstream stagnation pressures, P_0 = 13.6, 27.2 and 37.5 atm, have been applied. At the outlets (Figure 5-1), the static pressure, P_e, is set to 0.25 of the upstream stagnation pressure which is consistent with the experimental conditions of [66]. As previously mentioned, when flow is sucked into the nozzle, the gas crossing the outlet is of a stagnation pressure of 0.25 of the upstream stagnation pressure and a stagnation temperature of 300 K. With such setting of P_e at the nozzle exit, a shock will be generated inside the nozzle which will be shown by the computational results in subsequent sections.

The current is ramped down towards current zero with a fixed value of di/dt, from a DC plateau of 1 kA. Three values of di/dt, 6, 13.5 and 27 A/μs, have been investigated. The choice of 1 kA as plateau ensures quasi-steady state of the arc at this current for which the solutions at current zero is independent of the plateau current, i.e. the peak current of a sinusoidal current does not affect the arc at current zero [116].

For the Prandtl mixing length model, the value of turbulence parameter, *c*, is adjusted to give the closest agreement with the measured RRRV for P_0=37.5 atm and di/dt = 27 A/μs. The value of *c* is found to be 0.03, which is used for all the other discharge conditions. It is however found that the computed RRRV with *c*=0.03 is generally lower than measurements for all the other values of di/dt and P_0. We believe that, for air switching arcs, there exists a certain relation between *c* and di/dt. Attempts are therefore made to increase the value of c in order to achieve a better agreement between computed and measured RRRV for lower values of di/dt. This, however, results in unrealistic flow features behind the shock, whilst the numerical solution cannot converge with *c* greater than 0.03. Therefore 0.03 has been used.

For the standard k-epsilon model, previous investigation (Chapter 4) indicates an over-estimation of turbulence effects with the default values of the 5 turbulence parameters of this model. For the transient air nozzle arc of the present investigation, this model again over predicts the RRRV as compared with the experiments. We therefore apply the same approach as in the investigation of Chapter 4 by increasing the value of one turbulence parameter, $C_{1\varepsilon}$, of the standard k-epsilon model to increase the turbulence dissipation rate, thus reducing the turbulence effects. The value of $C_{1\varepsilon}$ is adjusted to give the closest agreement with measured RRRV for P_0=37.5 atm and di/dt=13.5 A/μs, which is found to be 1.65 and will be used for all the other discharges considered in the present investigation.

In order to illustrate the difference between the arc characteristics under laminar and turbulent flow conditions, the computational results obtained by the laminar flow model are also included. For convenience of discussion in the following sections, the laminar flow model, the Prandtl mixing length model and the standard k-epsilon model with $C_{1\varepsilon}$=1.65 are referred to as LAM, PML and MKE, respectively.

5.2.1. Cold Flow Features

Computations of the cold flow have been performed using LAM and MKE. PML is not used for computation of cold flow due to the reason given in 4.3.1. A shock is formulated in the divergent nozzle section which is similar to a normal shock. It has been found that computational results obtained by the two flow models are almost identical before the shock. After the shock, however, the flow features differs widely depending on the flow models.

Figure 5-2 shows computed results obtained by LAM, for the pressure distribution superimposed with pressure isobars, and the Mach number distribution of the nozzle. Points B and C in the region close to the nozzle throat (known as the transonic region of

the nozzle) can be considered as expansion corners where the pressure isobars are bunched, thus forming the expansion wave zones (Figure 5-2 (a)). Through the expansion wave zone at Point B, the flow direction is gradually turned to align with the surface of the transonic region and at Point C to the surface of the divergent nozzle section. The qualitative flow features in the transonic region is quite similar to those reported in [65] for the region around the flat throat of the nozzle. However, for the nozzle investigated in [65], the nozzle area in the throat region changes discontinuously. Due to such discontinuity of nozzle contour together with large convergence angle of the nozzle inlet section, a small low pressure region is formulated right after point B. Such low pressure will result in low gas density which can have adverse effects on the dielectric strength of the nozzle. For the nozzle of the present investigation, the nozzle contour of the transonic region changes continuously. Hence, the pressure close to the nozzle wall also changes continuously and there is no such low pressure region as discovered for the nozzle of [65]. Such continuous change of the nozzle contour is therefore preferred when designing the nozzle geometry. As previously, the flow features predicted by MKE is the same as those predicted by LAM before the shock including those in the transonic region.

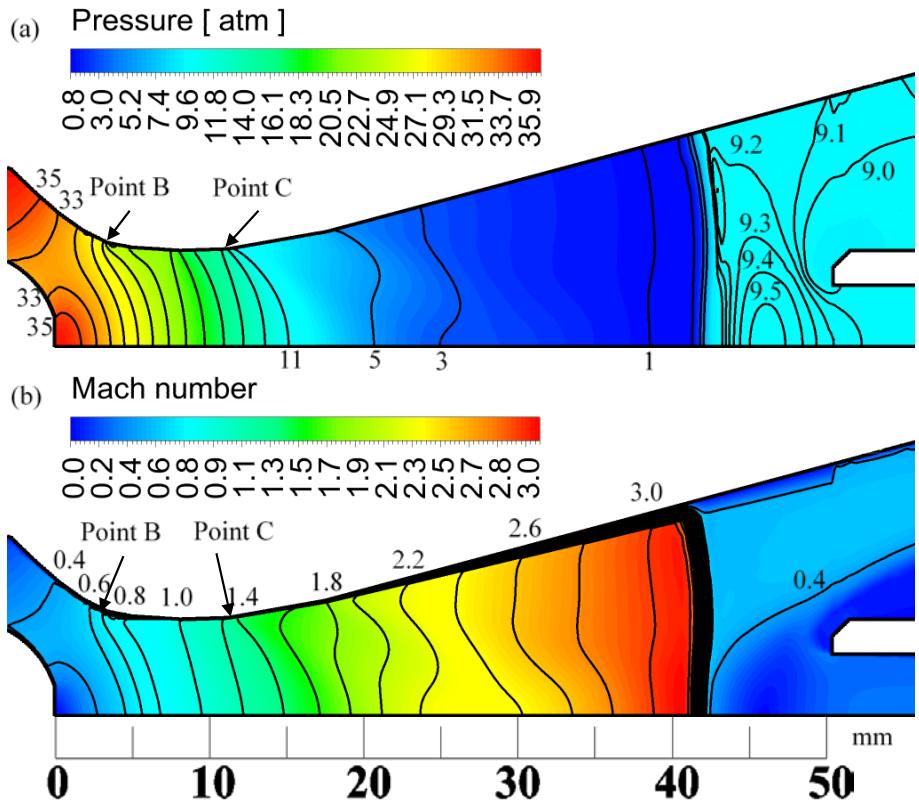

Figure 5-2. Temperature contour together with pressure isobars (a), and, the Mach number contour (b) for the cold nozzle flow at P_0=37.5 atm computed by LAM. The pressure difference between two isobars are 2 atm if not explictly stated.

In the transonic region of the nozzle, the rapid pressure drop results in strong acceleration of the gas. The gas becomes supersonic after the nozzle throat until it meets the standing shock which is characterized by a concentration of isobars at an axial position of 42 mm as shown in Figure 5-2. Due to adverse pressure gradient produced by the shock, gas flow decelerates quickly after the shock. The axis pressure and velocity distributions after the shock are shown in Figure 5-3. Figure 5-4 is an enlarged diagram showing the difference in axis pressures calculated by LAM and MKE. The pressure peak for the laminar flow (Figure 5-4) corresponds to the flow stagnation point on the axis. Near the nozzle exit, pressure is lower than that in the dumping tank (9.38 atm) (Figure 5-5 (a)) and the gas in the dumping tank is sucked into the nozzle forming a very complex flow pattern (Figure 5-5 (b)). The flow near nozzle axis passing through the shock collides with that sucked in from the dumping tank thus forming a flow stagnation point. Part of the flow sucked into

the hollow electrode circulates the downstream electrode, thus forming the largest vortex. Another part of the sucked in flow returns to the dumping tank. Altogether 4 vortices are formed within the largest vortex. The gas flow from upstream passing through the shock is deflected by the largest vortex and is then discharged into the dumping tank.

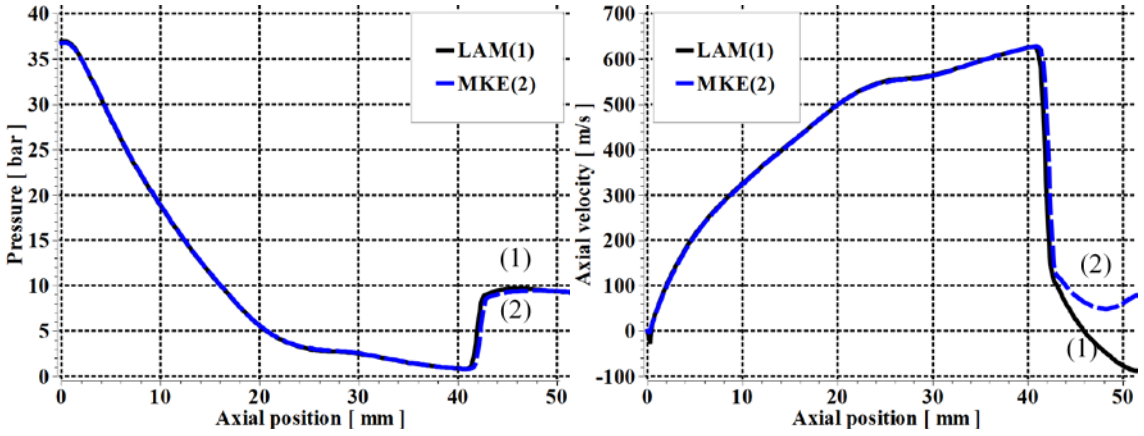

(a) (b)

Figure 5-3. Axis pressure and axis velocity as a function of axial position for the cold nozzle flow computed by the two flow models at P_0=37.5 atm. (a) Axis pressure and (b) Axis velocity.

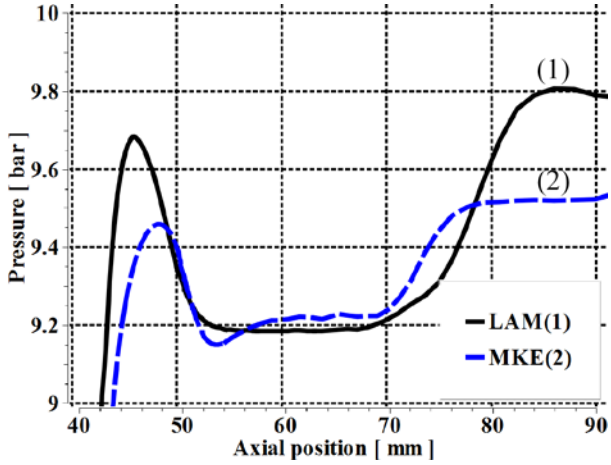

Figure 5-4. Enlarged diagram for axis pressure distributions calculated by LAM and MKE for the region 50mm<z<70mm. This region is inside the hollow downstream electrode. For z>70mm, it is inside the dumping tank.

Pressure distribution near the downstream electrode and the flow pattern computed by MKE are given in Figure 5-6 (b). Although the pressure within the nozzle is lower than that in the dumping tank, there is no gas sucked into the nozzle from the dumping tank via hollow electrode. The flow immediately after the shock manages to surmount the pressure rise in front of the tip of downstream electrode, thus there being no reverse flow (Figure 5-6 (b)). However, there is a flow separation region at the wall near the nozzle exit caused by the adverse pressure gradient in that region. Flow from upstream of the separation region is deflected, thus reducing the effective area for the nozzle flow. The pressure distributions on the surface 3-4 and near the corner of 2 of the downstream electrode tip (Figure 5-5 and Figure 5-6) ensure the flow passing the tip to be aligned with surfaces 1-2 and 4-5.

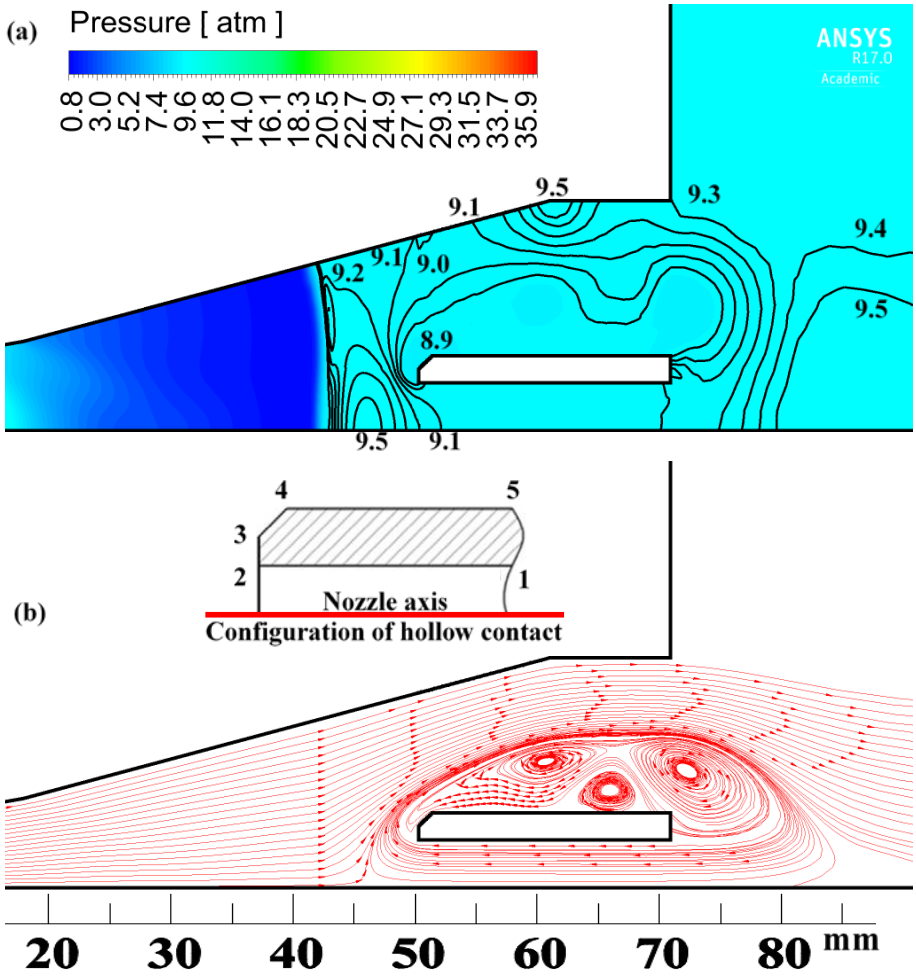

Figure 5-5 (a) Pressure distribution after the shock. (Pressure difference between two isobars is 0.1 atm) (b) The flow pattern in this region at 37.5 atm computed by LAM. Some of the streamlines seem to pass through the

electrode. This is due to the software for streamlines caused by rather coarse non-structured grids. Nonetheless (b) captures the features of the flow pattern.

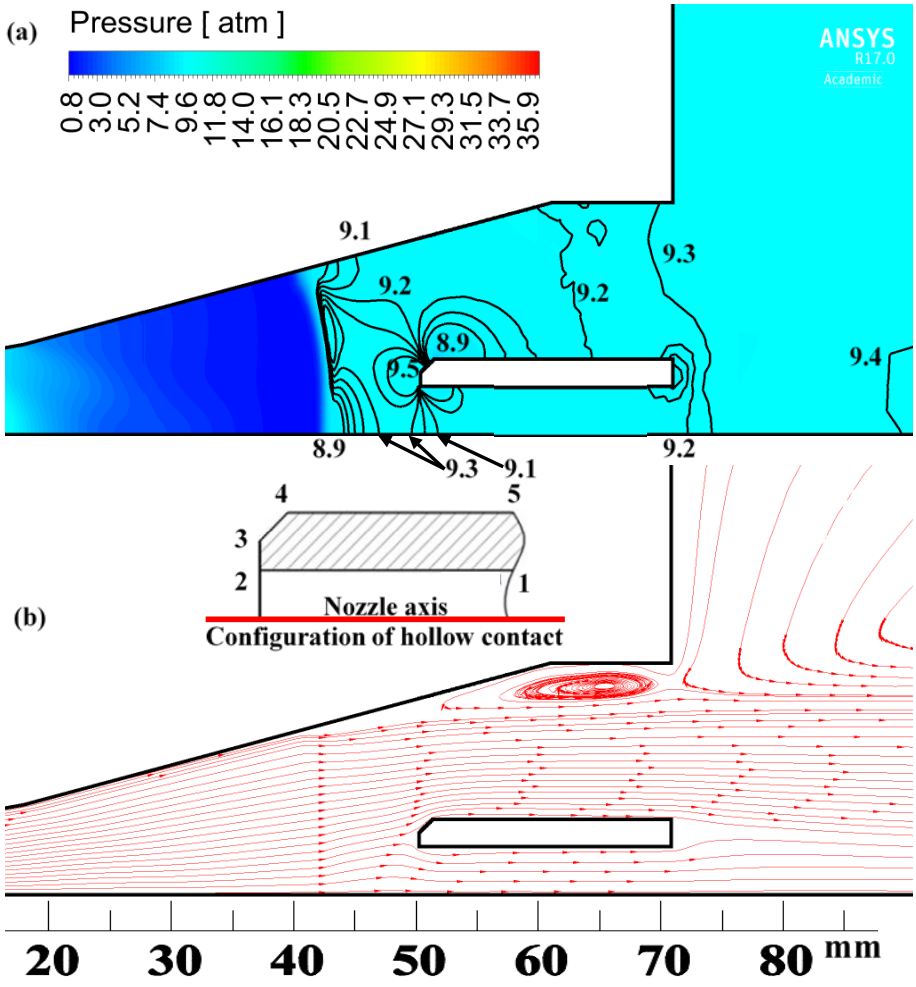

Figure 5-6 Flow pattern behind the shock computed by MKE at P_0=37.5 atm. (a) Pressure distribution together with isobars and (b) The flow pattern in this region.

In front of the upstream electrode tip, flow separation occurs which results in the creation of a wake where the pressure is almost constant and the flow circulates. This is very similar to that reported in [64]. However, the sizes of the wake are flow model dependent.

It has readily been shown that the detailed pressure distribution and velocity field of the gas in the near electrode regions, as well as those behind the shock, differ widely

depending on the flow model. As no experimental results are reported in [66] for the cold flow, no conclusions can be drawn regarding the accuracy of the predictions given by the two flow models. However, since the results of the two flow models in the region before the shock are almost identical, we believe that the flow features after the shock and those near the electrodes predicted by the laminar flow model are closer to the reality since turbulence is not important for the cold flow.

In addition, for the cold flow inside the nozzle, the gas velocity and Mach number are independent on the stagnation pressure, the reasons of which are discussed in Chapter 4.

The computational results presented in this section regarding the cold flow features do give an indication on the dielectric strength of the nozzle. With an arc, the flow features inside the nozzle will be substantially altered, which will be shown in 5.2.2.1.

5.2.2. Arc Behaviour Before Current Zero

Ohmic heating inside the arc creates a high temperature and low gas density region within the nozzle. The presence of the arc therefore reduces the effective flow area, thus modifying the pressure distribution in the nozzle including the shock structure, which in turn affects the arc. Such interaction determines the arc characteristics. It has been found from the computational results that the qualitative features of the arc are similar for different values of P_0 and di/dt. Unless otherwise specified, the computational results for P_0=37.5 atm and di/dt=13.5 A/μs are used to show the typical arc features predicted by different flow models.

5.2.2.1. Features of the Arc-flow Interaction

The temperature distributions together with the pressure isobars predicted by LAM, PML and MKE are given in Figure 5-7 for the arc at 1 kA DC. Computational results obtained by all the three flow models show a distinctive layer of cold flow surrounding the arc. A

shock is generated in the cold flow region due to the high pressure ratio, which interacts strongly with the arc. Compared with the flow behaviour in the absence of the arc, the features of the shock and the gas flow behind the shock have been substantially altered. With an arc, the shock centre moves upstream and the shock is broadened which cannot be considered as a normal shock. The qualitative features of the arc and the gas flow predicted by the three flow models are similar before the shock, while after the shock, these features show strong dependence on the flow models (Figure 5-7).

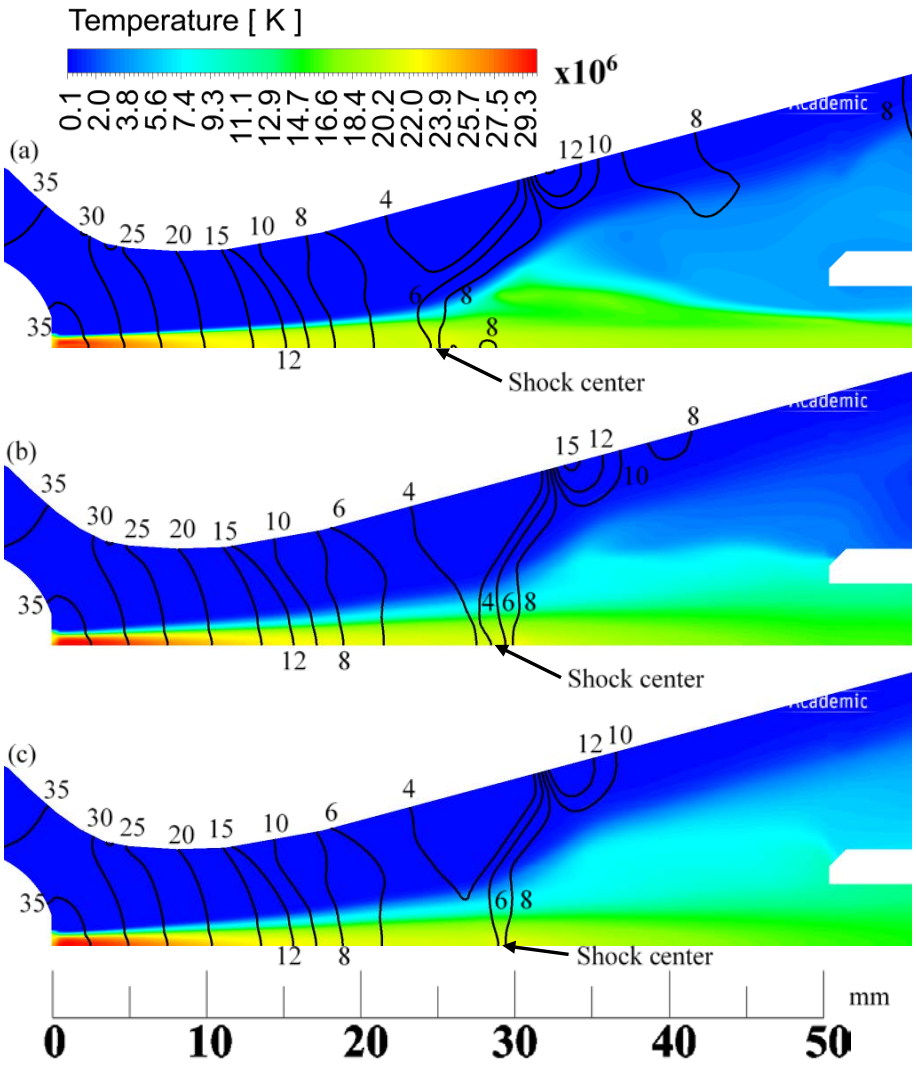

Figure 5-7 Temperature contour together with pressure isobars in the nozzle at 1 kA DC and at P_0=37.5 atm. Results are obtained by (a) LAM, (b) PML and (b) MKE.

Figure 5-8, Figure 5-9 and Figure 5-10 show the detailed temperature and pressure distributions behind the shock (hereafter referred to as the arc-shock interaction region) obtained by the three flow models. For the discussion of arc-shock interaction, it is convenient to separate the nozzle arc system into three regions: a high-temperature core which carries a larger part of the arc current with a boundary temperature of approximately 10,000 K (this is different from the arc core defined for radiation transport which is the isotherm of 83.3% of the axis temperature), a thin layer (commonly known as the thermal layer) surrounding the arc core in which the temperature rapidly decays to that of the surrounding cold flow, and the cold flow region (see Figure 5-7, the arc section before the shock). When the shock interacts with the arc, the shock centre in the cold flow and that in the arc core differ because of the deflection of the cold flow by the arc and the pressure waves originated from the shock centre in the clod flow being refracted when propagating into a region in which temperature rises [117]. Compared with the cold flow the shock centre in the cold flow region is shifted upstream as shown in Figure 5-8 (a). The shock centre in the arc is further shifted upstream due to refraction of pressure waves (Figure 5-8 (b)). The shock strength in the arc is also weaker as some of isobars in the shock of the cold flow cannot penetrate the arc (Figure 5-7).

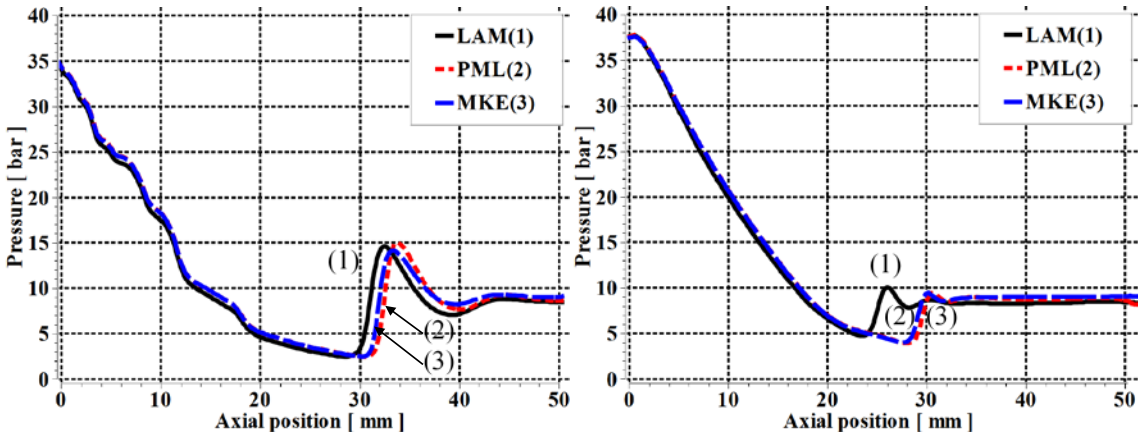

Figure 5-8 Pressure distribution for 1 kA at 37.5 atm computed by three flow models. (a) Pressure along the nozzle wall. The curves are not smooth due to non-uniform grids. (b) Pressure on the nozzle axis.

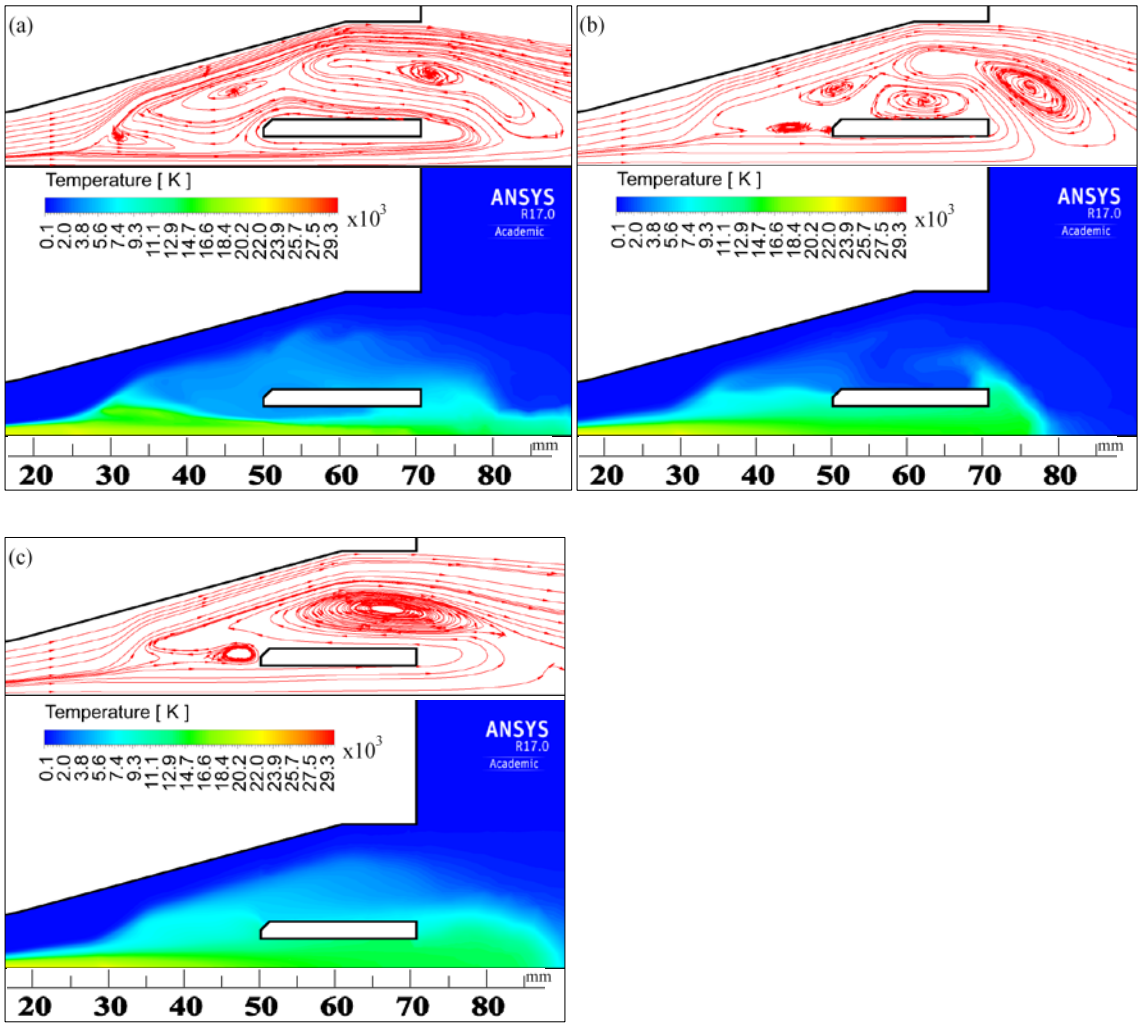

Figure 5-9 The streamlines and temperature contours at 1 kA, 37.5 atm (a) computed by LAM. (b) by PML and (c) by MKR.

The flow pattern in the region between the shock and nozzle exit is extremely complex (Figure 5-9). The qualitative behaviour of the flow pattern is similar for all three flow models. The axis velocity before the shock can reach over 8,000 m/s. The high velocity core near the axis can surmount the pressure rise through the shock region and is then exhausted through the nozzle exit to the dumping tank. However, the plasma away from the axis inside the hollow electrode has a reduced velocity which is turned back by the high pressure in the dumping tank. The paths of the turned back flow depend on the flow model, thus forming different flow patterns characterized by the number, sizes and locations of the vortices. The shape of the arc in this region is shaped by the vortices. Part

of the flow after passing through the shock is deflected by the rapid radial expansion of the arc associated with the vortices thus deflected into the low temperature region closed to the nozzle wall. If these vortices, especially the one close to the downstream electrode tip, in which high temperature gas circulates, do not disappear at current zero, dielectric recovery will be seriously affected.

It will be shown later that RRRV predicted by MKE has achieved best agreement with experiments. We use the results by MKE to discuss the evolution of flow features when current is linearly ramped down towards current zero. For di/dt = 13.5 A/μs, it takes 74 μs to reach current zero from 1 kA DC plateau. When current is reduced towards current zero the pressure distributions along the axis and the nozzle wall hardly change (Figure 5-10) but the axis velocity (Figure 5-11) does decrease due to the reduced temperature towards current zero.

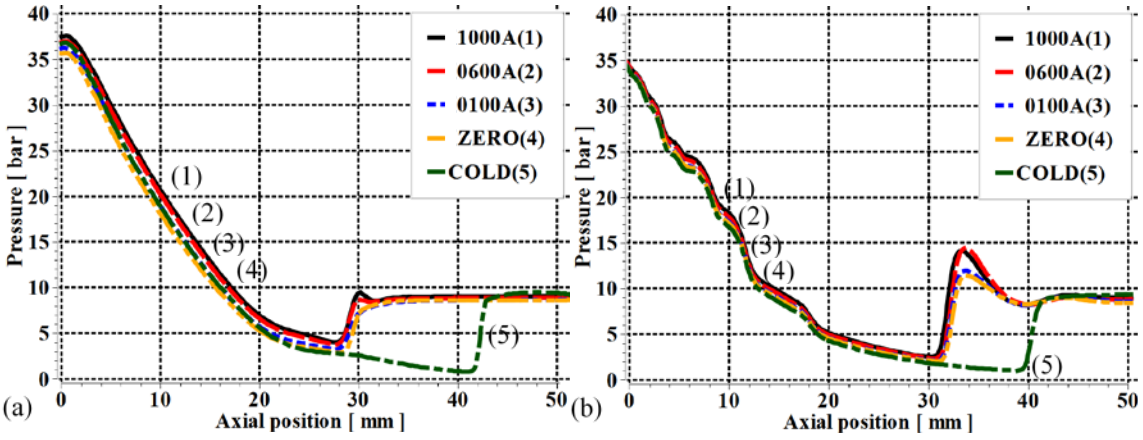

Figure 5-10 Pressure distribution corresponding to different instant currents as indicated in the diagram for di/dt= 13.5 A/μs and P_0= 37.5 atm. (a) On the nozzle axis. (b) Along the nozzle wall. Results are obtained by MKE.

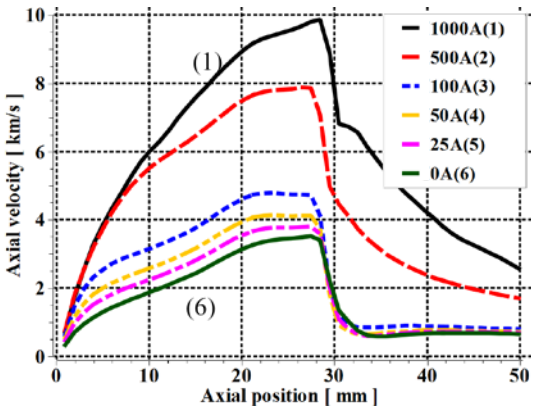

Figure 5-11 Axis velocity at different instant currents as indicated in the diagram for di/dt= 13.5 A/μS and P_0= 37.5 atm. Results are obtained by MKE.

When current decays towards zero, the streamlines at an instant current 500A and those at current zero are given in Figure 5-12. In principle, these streamlines change from one instant to the next and it would be difficult to ascertain a definite flow pattern from a snap shot. However, the two instantaneous streamlines show similar features. We can therefore conclude that the qualitative features of the flow pattern remain largely the same when the current is reduced to zero. The flow entering the hollow electrode at an instant current 500 A (Figure 5-12 (a)) is entirely returned to the nozzle. Part of this returned flow circulates the upper vortex and is exhausted into the dumping tank. The flow pattern at current zero is similar. The sizes of the vortices do not vary much when current decays from 500 A to zero although the upper vortex has reduced its size from 1 kA to 500 A.

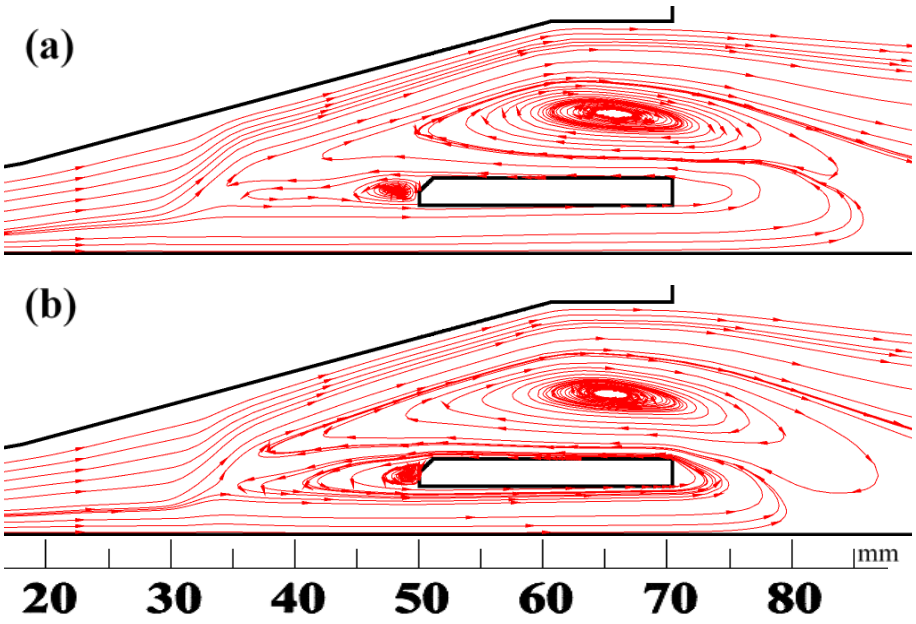

Figure 5-12 Instant streamline patterns for di/dt= 13.5 A/μs and P0= 37.5 atm. (a) instant current= 500 A. (b) Current zero. Results are obtained by MKE.

5.2.2.2. Characteristics of the Nozzle Arcs

5.2.2.2.1. General Features

The choice of 1 kA DC as the plateau of the current ramp ensures that the arc can maintain quasi-steady state for the chosen flow models immediately after the current is ramped down. This ensures the computational results at current zero being independent of the choice of the plateau current. The voltage-current (V-I) characteristics in this period show a flat part with the voltage close to the DC voltage for the same current. For the three flow models, quasi-steady state can be maintained up to an instantaneous current of 500 A. After 500 A, the arc voltage computed by these models deviates greatly from the corresponding DC voltage (Figure 5-13). It should be noted that in contrast with the results in Chapter 4 DC voltages for currents above 500 A computed by different flow models are almost the same. This is due to that the arc almost fills the divergent part of the nozzle in Chapter 4 while the arc in Frind and Rich nozzle is always surrounded by a cold flow.

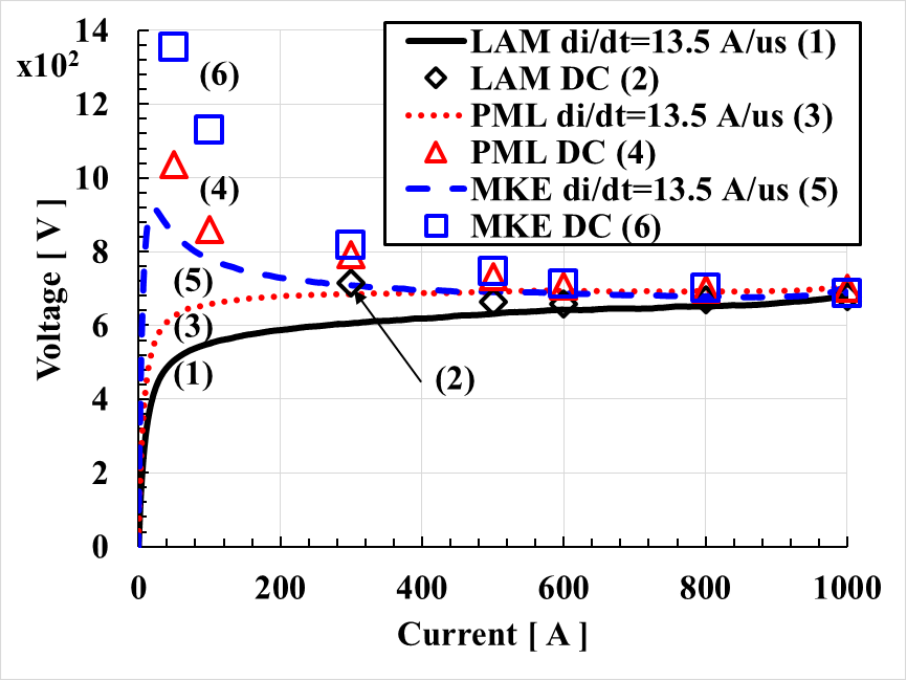

Figure 5-13 The V-I characteristics for the nozzle arc computed by the three flow models during the current ramp for P0=37.5 atm and di/dt=13.5 A/μs, together with DC arc voltages for comparison.

The variations of axis temperature, arc radius and electric field at a few instants before current zero are given respectively in Figure 5-14, Figure 5-15 and Figure 5-16, for those computed by the three flow models. Results show that, after the shock, the axis temperature decays slowly with current, and the arc radius, which is very large as compared with that before the shock, hardly changes for currents below 100 A. Such behaviour is due to very stagnant nature of the flow in the arc-shock interaction as previously discussed in Section 5.2.2. Consequently, the arc section after the shock only takes a small proportion of arc voltage during the current ramp as indicated by the electric field. Careful examination of the computational results indicates that the voltage taken up by this section of the arc is less than 15% of the total arc voltage at 1 kA and it reduces to less than 1% at 0.5 μs before current zero. The role of this arc section in arc extinction is therefore considered negligible, and it is the arc section before the shock that is the most important in the determination of RRRV of the nozzle arc. For this reason, we only concentrate on the arc section before the shock for discussion of the transient air arc behaviour hereafter unless otherwise specified.

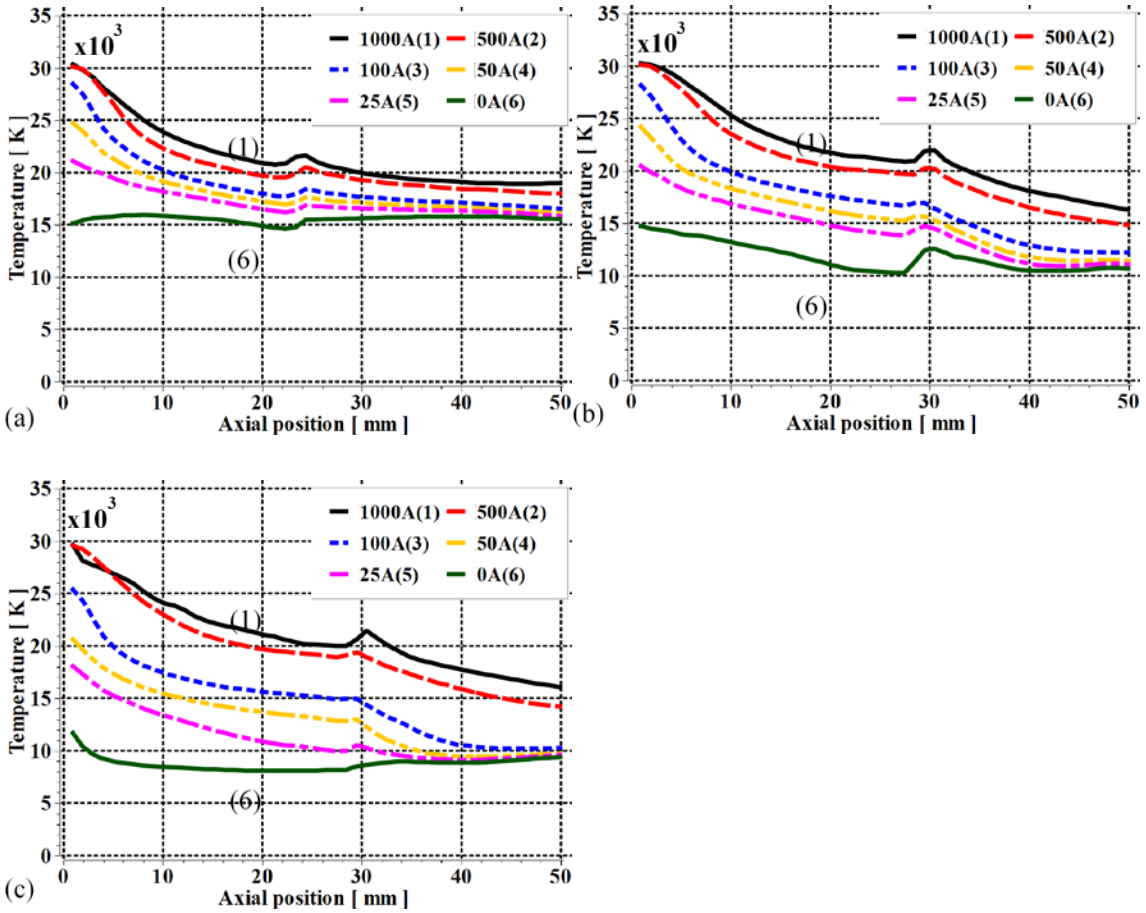

Figure 5-14 Variations of axis temperature with axial position at different instantaneous current before current zero. P0=37.5 atm and di/dt=13.5 A/μs. Results are obtained by (a) LAM, (b) PML and (c) MKE.

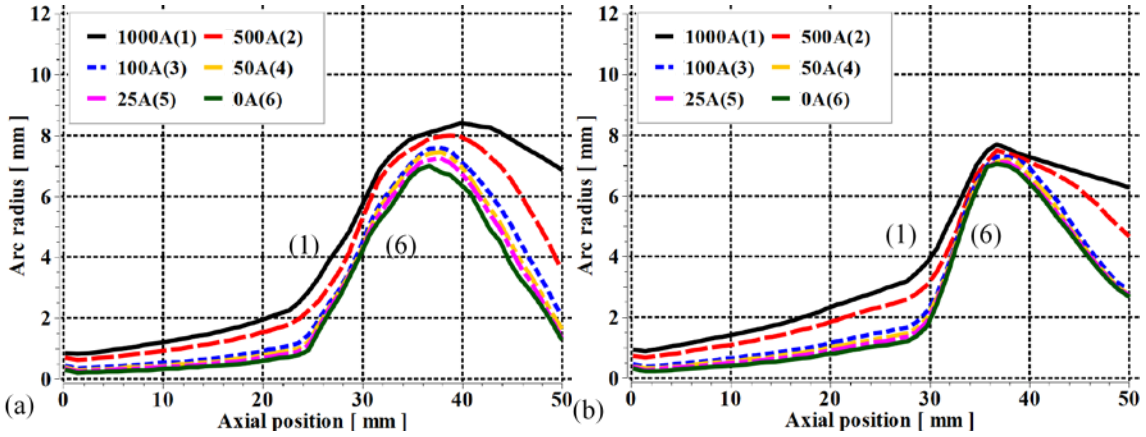

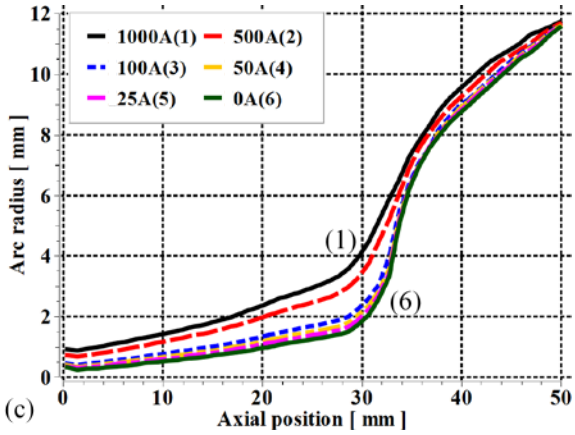

Figure 5-15 Variations of arc radius with axial position at different instantaneous current before current zero. P0=37.5 atm and di/dt=13.5 A/μs. Results are obtained by (a) LAM, (b) PML and (c) MKE.

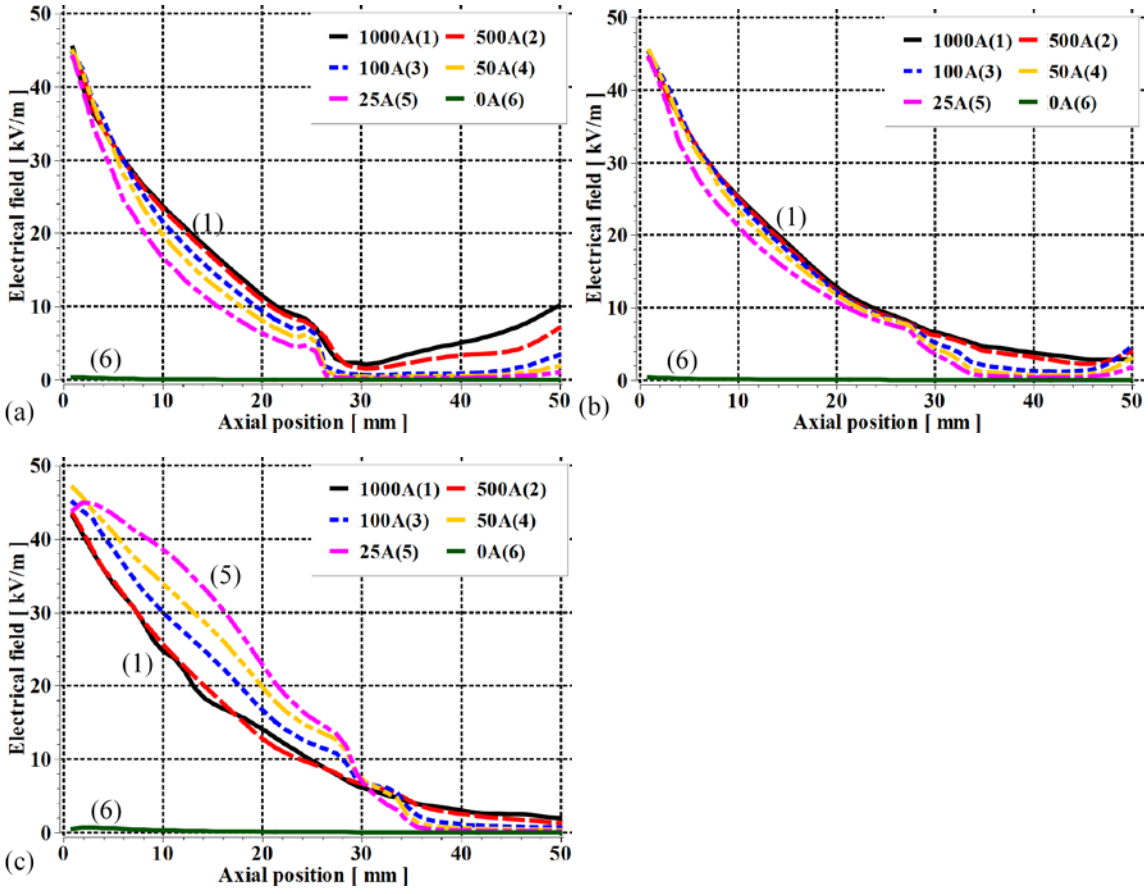

Figure 5-16 Variations of electric field with axial position at different instantaneous current before current zero. P0=37.5 atm and di/dt=13.5 A/μs. Results are obtained by (a) LAM, (b) PML and (c) MKE.

Before the shock, the axis temperature (Figure 5-14) is not sensitive to the current and the arc radius (Figure 5-15) is approximately proportional to the square root of current for currents down to 500 A. The arc can maintain quasi-steady state from 1 kA to 500 A. Electric field is therefore not sensitive to the current for which the V-I characteristics show a flat part (Figure 5-13). Such relation between the arc behaviour and the currents are the same as that reported in [118] for the SF_6 arc in quasi-steady state, which appears to be always true as long as the arc is surrounded by a cold layer of gas inside the nozzle interrupter. In addition, the results show that the variations of electric field and the resulting arc voltages computed by the three models are virtually the same for currents above 500 A, while the variations of the axis temperature and arc radius do have dependence on the flow models as shown by Figure 5-14 and Figure 5-15. Regarding such behaviour, it should be noted that the local electric field is determined by not only the axis temperature and arc radius, but more importantly, the radial temperature distributions at given axial position. A more detailed discussion will be given in Section 5.2.2.2.2.

When the current is below 500 A, the axis temperature and arc radius decrease rapidly with current decay. Results show that the rates of decay of temperature and arc radius predicted by MKE are both greater than those predicted by PML and LAM, which results in different trends in the variations of electric field with current and, subsequently, the deviation of arc voltages computed by the two flow models (Figure 5-13). For MKE, the electric field increases with current decay which results in a negative V-I characteristic for currents below 400 A followed by a voltage extinction peak shortly before current zero. For PML and LAM, the electric field shows a reverse trend as compared with that computed by MKE, for which the arc voltage continues to drop with current decay and shows no voltage extinction peak. The most rapid drop of arc temperature at low currents computed by MKE is due to strong turbulence effects predicted by MKE. PML however predicts much weaker effects of turbulence as compared with MKE. The time variation of arc temperature and its decay rate during current zero period depend on the energy transport processes predicted by different flow models and the material properties of air,

i.e. ρC_P, associated with these energy transport processes, the detailed discussion of which will be followed in Section 5.2.2.2.2.

5.2.2.2.2. Distinctive Features of Radial Temperature Profiles and the Dominant Energy Transport Process

As previously indicated, the arc temperature distribution is determined by the balance between electrical power input, various energy transport processes and the rate of change of energy storage, which in turn determine the arc characteristics. Attempts are therefore made to identify the dominant energy transport processes, as well as the material properties affecting these processes, for the rapidly changing arc during current zero period. The identification of such properties will serve as a guide for the search of a replacement gas for SF_6 as an arcing medium.

For LAM, predicted results on the variations of radial temperature profiles with current are given in Figure 5-17 (a) and Figure 5-18 (a) for the nozzle throat at Z=8 mm and a typical axial position in the divergent nozzle section at Z=25 mm, respectively. Temperature profiles show a distinctive high temperature core when the current is above 500 A. It is this arc core that carries 80% of the current, which therefore determines the arc voltage. Inside the arc core, the temperature profile is rather flat which indicates the dominance of radiation transport. This is confirmed by energy balance calculations at 800 A (Table 5-1), which shows that, at the core boundary, radiation transport accounts for 85% of the electric power input, where the effects of other energy transport mechanisms, i.e. axial and radial thermal convection and radial thermal conduction, altogether accounts for only 11.2% of the electric power input. In the radiation re-absorption region where 60% of the radiation from the arc core is absorbed, the temperature gradient is very steep resulting in a thin radiation re-absorption region. Energy balance calculation at the electrical boundary at 800A (Table 5-2) shows that axial convection (accounts for 87.3% of the electric power input) is the dominant energy loss mechanism, while radiation loss accounts for less than 30% of the electric power input. At the electric boundary, radial thermal convection acts as an energy input mechanism.

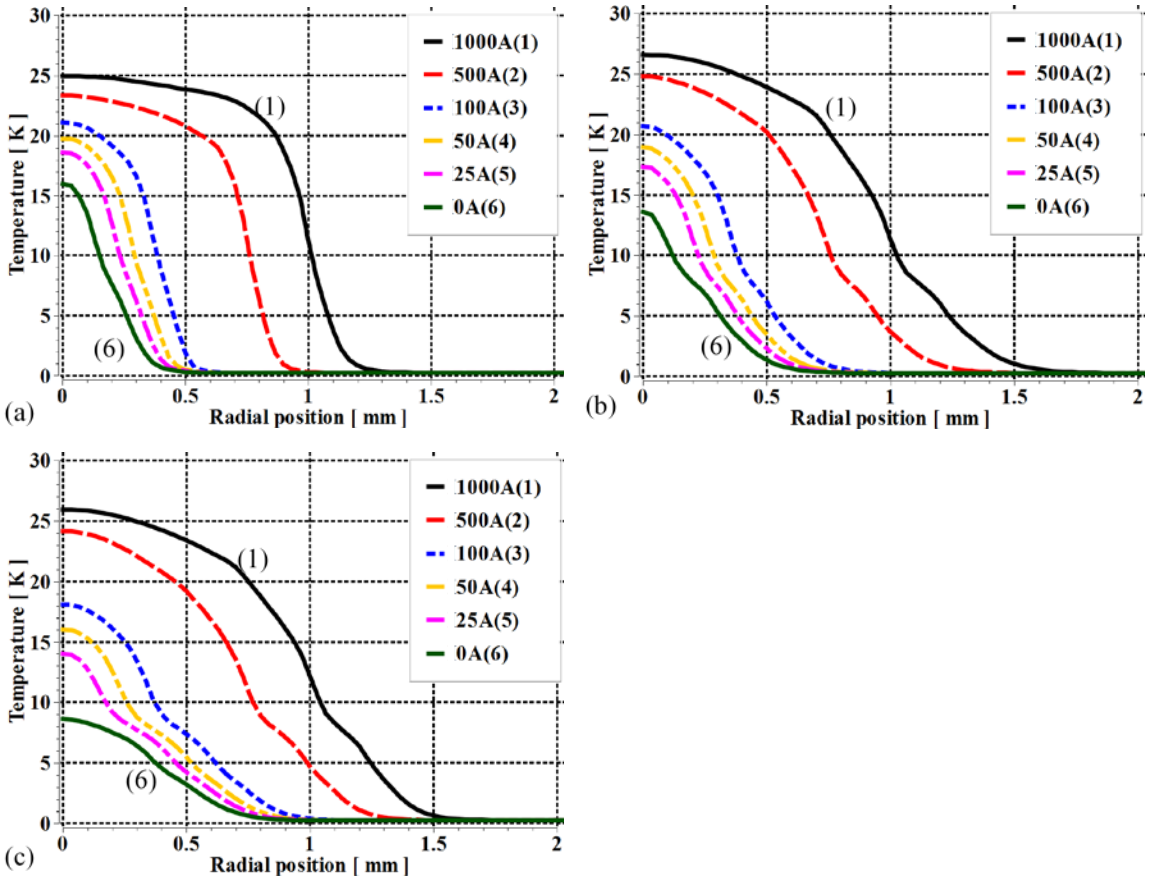

Figure 5-17 Radial temperature profiles at the nozzle throat, Z=8 mm, for a few instantaneous currents before current zero. P0=37.5 atm and di/dt=13.5 A/µs. Results are obtained by (a) LAM, (b) PML and (c) MKE.

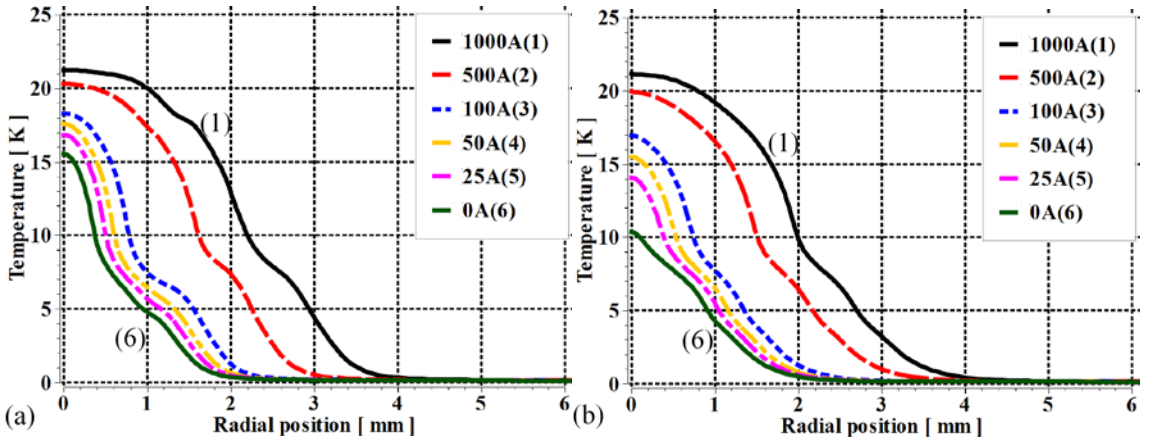

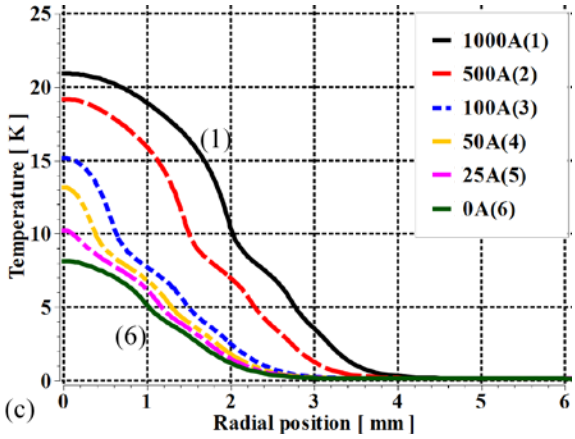

Figure 5-18 Radial temperature profiles at Z=25 mm for a few instantaneous currents before current zero. P0=37.5 atm and di/dt=13.5 A/µs. Results are obtained by (a) LAM, (b) PML and (c) MKE.

Table 5-1 Percentage of electric power input associated with various energy transport processes at the core boundary for the arc section before the shock computed by the three flow models at an instantaneous current of 800 A. P_0=37.5 atm and di/dt=13.5 A/μs. Energy balance calculation only considers the arc section before the shock due to the reason given at the beginning of Section 5.2.2.2.1. Positive sign means power input and negative sign power loss. This applies to all tables for energy balance calculations.

Model	Electric power input (10^5 W)	Radiation loss (%)	Radial thermal conduction (%)	Axial thermal convection (%)	Radial thermal convection (%)	Expansion cooling (%)	Rate of change of energy storage (%)
LAM	3.20	-85.0	-3.4	-10.6	2.8	-11.3	1.9
PML	2.61	-80.8	-13.9	-0.8	1.0	-9.0	0.8
MKE	2.49	-79.1	-17.1	-0.0	1.1	-8.8	1.2

Method of calculation: Expansion cooling (%) = $\int_{Z1}^{Z2}\int_0^R \frac{dP}{dt} 2\pi r dr dz$

Rate of change of energy storage (%) = $-\int_{Z1}^{Z2}\int_0^R \rho \frac{\partial h}{\partial t} 2\pi r dr dz$ / Power input

Mathematical expressions for the rest energy transport processes are the same as those given in Chapter 4.

Table 5-2 Percentage of electric power input associated with various energy transport processes at the electric boundary for the arc section before the shock computed by the three flow models at an instantaneous current of 800 A. P_0=37.5 atm and di/dt=13.5 A/μs. Mathematical expressions for power input and power loss are the same as those in Table 5-1..

Model	Electric power input (10^5 W)	Radiation loss (%)	Radial thermal conduction (%)	Axial thermal convection (%)	Radial thermal convection (%)	Expansion cooling (%)	Rate of change of energy storage (%)
LAM	3.96	-27.8	-1.5	-87.3	15.8	-11.3	13.5
PML	4.19	-20.2	-11.9	-91.9	25.5	-11.6	11.9
MKE	4.16	-19.0	-11.8	-95.2	26.4	-11.9	12.0

Temperature profiles computed by the two turbulence models, i.e. PML and MKE, are very different from those by LAM, which shows a very diffusive profile without a distinctive arc core but with a very broad radiation re-absorption layer. The radial temperature gradient computed by the two turbulence models is thus much smaller than that by LAM. This is mainly because turbulence thermal conductivity is much greater than molecular thermal conductivity for the laminar flow with two peaks around 7,000 K and 4,000 K as shown in Chapter 4. Thus, for the two turbulence models, the arc core carries around 60% of the total current which is less than the prediction given by LAM.

Despite such large differences in radial temperature profiles between LAM and the two turbulence models, thus the portion of the total current carried by the arc core, the dominant energy transport processes computed by PML and MKE are similar to those computed by LAM at both the core boundary and the electric boundary for currents of 500 A and above. For both PML and MKE, energy balance calculation at 800 A shows that, at the core boundary (Table 5-1), radiation loss is the dominant energy transport mechanism (accounts for 80% of the electric power input). Turbulence enhanced radial thermal conduction only accounts for 13.9% and 17.1% of the electric power input respectively for PML and MKE. At the electric boundary (Table 5-2), energy balance results at 800 A computed by the two turbulence models both show that axial thermal convection is again the dominant energy transport mechanism, while turbulence enhanced radial thermal conduction accounts for only around 12% of the electric power input.

Table 5-1 indicates that the rate of change of energy storage in the arc core accounts for less than 2% of the electric power input, and thus the arc core is in quasi-steady state. However, at the electric boundary, the rate of change of energy storage is already over 10% of the electric power input, meaning the radiation re-absorption region starts to deviate from quasi-steady state. The effects of such deviation of quasi-steady state in the radiation re-absorption region are not reflected by the arc voltage as the current is mainly carried in the core region (over 80% for LAM, and over 60% for PML and MKE, of the current are carried inside the high temperature core). Such behaviour holds and the arc can maintain quasi-steady state for currents down to 500 A.

When the current decreases towards current zero, the arc temperature further decreases, and radiation as an energy loss mechanism gradually becomes less important. Qualitative features of radial temperature profiles computed by the three flow models are still similar to those at higher currents. For LAM, at the core boundary radiation is still the dominant energy transport mechanism as shown in the energy balance calculation for 50 A (Table 5-3). The qualitative trend of energy balance at the electric boundary is virtually the same as those at higher currents with axial enthalpy transport being the dominant energy loss mechanism. For the two turbulence models, at the core boundary, turbulence enhanced radial thermal conduction becomes the dominant energy loss mechanism, whilst radiation loss only plays a secondary role (Table 5-3). At the electric boundary (Table 5-4), axial thermal convection is still the dominant energy transport mechanism which is similar to the case at high currents, although turbulent enhanced thermal conduction becomes more important as compared with that at high currents. In other words, for transient air arc, turbulence enhanced thermal conduction never becomes the most important energy loss mechanism at the electrically conducting core. However, turbulent energy transport through enhanced thermal conductivity has a decisive effect on the radial temperature profile, which in turn affects convection processes. It has been shown that MKE predicts much stronger turbulence effects in comparison with PML, as indicated by the percentage of electric power input accounted for by turbulence enhanced radial thermal conduction at 50 A. Predictions on turbulence effects by different turbulence models are affected by

predictions on the length and velocity scales of turbulence, further details of which are presented in Section 5.2.2.2.3. It is also noted that, unlike for higher currents, radial thermal convection becomes energy loss mechanism, which is associated with radial inflow due to the rapidly decreasing temperature in the vicinity of current zero.

For air arcs, results of energy balance up to the electrical boundary show that, axial convection is always the dominant energy transport mechanism during the whole period of current ramp. Even for the arcs predicted by turbulent flow theory, PML and MKE, this is also the case. However, the temperature inside the core boundary just before current zero and at current zero (Table 5-5) is controlled by turbulent thermal conduction. At current zero, for all three flow models axial and radial convection are dominant for energy balance up to the electrical boundary (Table 5-6). A radial in flow of cold gas goes into the electrically conducting region. Turbulent enhanced radial thermal conduction is not important at high currents but it still plays a secondary role at the vicinity of current zero. For SF_6 nozzle arc turbulence enhanced thermal conduction becomes dominant energy loss mechanism in the vicinity of current zero while axial thermal convection is less important [118]. One cause resulting in this difference in dominant energy transport processes between arcs in air and SF_6 is due to the material property, the product of density and enthalpy, ρh, which determines thermal convection. It is known that ρh of air is higher than that for SF_6 for temperature greater than 7,000 K (1.4). Since air density is lower than that of SF_6 velocity in air arc reaches a higher value than in SF_6 for the same pressure difference across the nozzle. Thus, for air arcs axial thermal convection is strong and dominates arc behaviour. The other reason for the differences between air and SF_6 arcs is associated with the turbulence enhanced thermal conduction inside air arcs. Although it never becomes the most important energy transport process for the electrically conducting region it makes the radial temperature very broad with large arc radius in comparison with an SF_6 arc under similar discharge conditions. This in turn makes axial enthalpy transport dominant. The broadened radial temperature profile is the result of the material property, ρC_P, as discussed in Chapter 4.

Table 5-3 Percentage of electric power input associated with various energy transport processes at the core boundary for the arc section before the shock computed by the three flow models at an instantaneous current of 50 A. P_0=37.5 atm and di/dt=13.5 A/μs. Mathematical expressions for power input and power loss are the same as those in Table 5-1.

Model	Electric power input (10^4 W)	Radiation loss (%)	Radial thermal conduction (%)	Axial thermal convection (%)	Radial thermal convection (%)	Expansion cooling (%)	Rate of change of energy storage (%)
LAM	1.63	-66.9	-27.1	-35.7	-3.0	-13.6	50.7
PML	1.58	-41.1	-75.3	-4.5	-6.9	-10.3	40.4
MKE	2.09	-14.3	-89.5	-12.5	-9.2	-4.7	32.2

Table 5-4 Percentage of electric power input associated with various energy transport processes at the electric boundary for the arc section before the shock computed by the three flow models at an instantaneous current of 50 A. P_0=37.5 atm and di/dt=13.5 A/μs. Mathematical expressions for power input and power loss are the same as those in Table 5-1.

.Model	Electric power input (10^4 W)	Radiation loss (%)	Radial thermal conduction (%)	Axial thermal convection (%)	Radial thermal convection (%)	Expansion cooling (%)	Rate of change of energy storage (%)
LAM	2.17	-20.4	-6.8	-277	-32.9	-19.2	262
PML	2.45	-10.7	-32.8	-220	-31.3	-27.1	226
MKE	3.26	-3.7	-56.7	-162	-32.8	-23.9	182

Table 5-5 Percentage of electric power input associated with various energy transport processes at the core boundary for the arc section before the shock computed by the three flow models at current zero. P_0=37.5 atm and di/dt=13.5 A/μs. Mathematical expressions for power input and power loss are the same as those in Table 5-1 but the denominator is changed to rate of change of energy storage since electrical power input equals zero at current zero.

Model	Electric power input (10^5 W)	Radiation loss (%)	Radial thermal conduction (%)	Axial thermal convection (%)	Radial thermal convection (%)	Expansion cooling (%)	Rate of change of energy storage (W)
LAM	0	-8.7	-16.7	-30.0	-14.0	-6.6	8.77E3
PML	0	-2.6	-45.7	-29.6	-17.6	-1.9	6.64E3
MKE	0	-0.1	-57.2	-20.8	-15.7	-3.3	2.29E4

Table 5-6 Percentage of electric power input associated with various energy transport processes at the electric boundary for the arc section before the shock computed by the three flow models at current zero. P_0=37.5 atm and di/dt=13.5 A/μs. Mathematical expressions for power input and power loss are the same as those in Table 5-1 but the denominator is changed to rate of change of energy storage since electrical power input equals zero at current zero.

Model	Electric power input (10^5 W)	Radiation loss (%)	Radial thermal conduction (%)	Axial thermal convection (%)	Radial thermal convection (%)	Expansion cooling (%)	Rate of change of energy storage (W)
LAM	0	-0.6	-12.0	-50.1	-29.7	-4.4	4.98E4
PML	0	-0.1	-16.6	-47.4	-29.5	-4.4	5.21E4
MKE	0	-0.0	-22.7	-43.2	-27.8	-4.1	5.82E4

Regarding the detailed features of the radial temperature profiles computed by the three flow models, results show that they all have two inflection points at the temperature of 7,000 K and 4,000 K, respectively. For the laminar flow model, this is due to the molecular

thermal conductivity which has two peaks at 7,000 K and 4,000 K due to dissociation of nitrogen and oxygen molecules. For the arcs computed by the two turbulence models, it is known that turbulent thermal conductivity is the dominant part of the effective thermal conductivity. The presence of two inflection points of the radial temperature profile computed by PML and MKE is due to the two peaks of ρC_P at 7,000 K and 4,000 K. In addition there is a third inflection point around 9,000 K which is due to the peak in kinematic eddy viscosity associated with the maximum in the radial gradient of axial velocity that gives rise to the peak in turbulent thermal conductivity. Details for this will be given in Section 5.2.2.2.3.

5.2.2.2.3. The Performance of the Two Turbulence Models in Predicting Turbulence Effects

The two turbulence models used in the present work are based on eddy viscosity (we refer this to kinematic eddy viscosity, ν_t, in the present work) which characterizes the turbulence effects. As previously indicated, MKE predicts much stronger turbulence effects than PML, which depends on the evolution of ν_t with current decay. It is therefore necessary to discuss the evolution of ν_t which is determined by the turbulence length scale, λ_c, and velocity scale, V_c, computed by the two turbulence models. Since the turbulence effects are the most pronounced in the downstream of the nozzle throat, we choose the axial position of Z=25 mm to illustrate the variation of λ_c, V_c and the resulting ν_t towards current zero.

For PML, λ_c is directly related to arc thermal radius through the turbulence parameter c=0.03. λ_c, is a constant across the arc cross section for a given axial position and current, which is reduced as the arc size shrinks towards current zero (Figure 5-19 (a)). V_c, on the other hand, is related to local velocity gradients as well as λ_c. Variation of V_c is complex due to highly non-linear nature of the governing equations (Figure 5-19 (b)). The resultant ν_t is shown in Figure 5-20. The peak of ν_t is due to the peak in V_c which is directly related to the radial gradient of axial velocity.

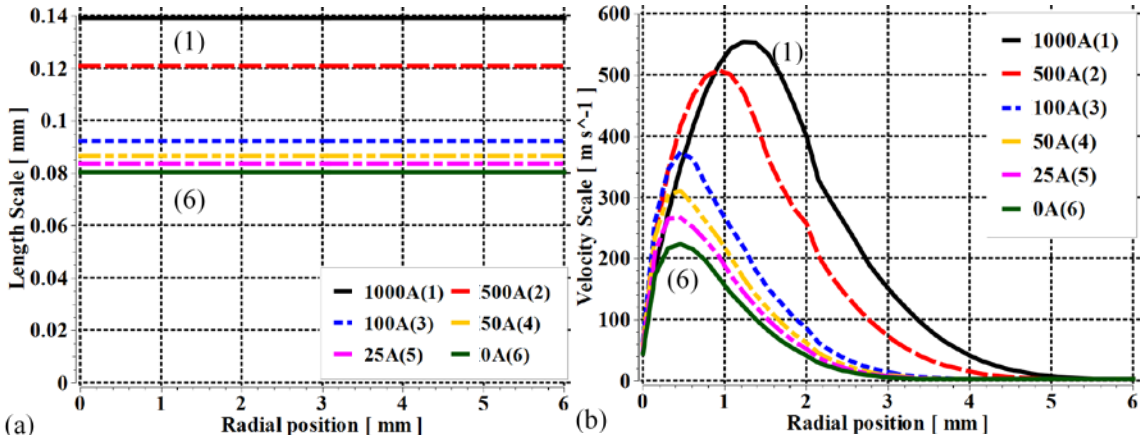

Figure 5-19 Variations of λ_c and V_c at Z=25 mm with current decay predicted by PML with c=0.03. P_0=37.5 atm and di/dt=13.5 A/μs. (a) λ_c and (b) V_c.

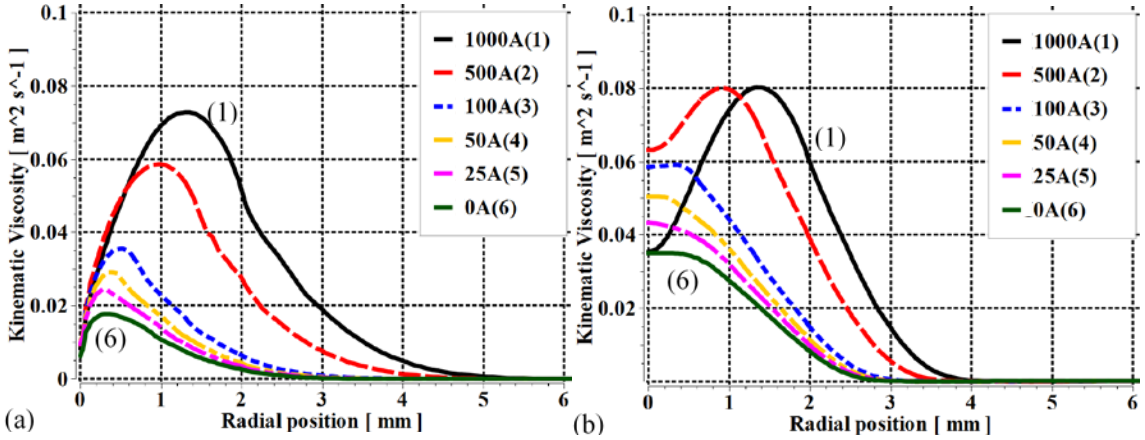

Figure 5-20 Radial profiles of eddy kinematic viscosity, ν_t at Z=25 mm computed by the two turbulence models before and at current zero. (a) by PML, and (b) by MKE.

For MKE, λ_c is related to the turbulent kinetic energy, k, and dissipation rate, ε, the variations of which are governed by corresponding transport equations. Their profiles are shown in Figure 5-21 for Z=25 mm, both of which show a peak where the radial gradient of axial velocity is the largest. With the current decay, the peaks for both k and ε shifts towards the axis due to radial diffusion of these two quantities. As compared with the prediction given by PML, the relation between λ_c and the current is more complicated, and the average values of λ_c (Figure 5-22 (a)) at a given axial position are smaller than those of PML. V_c computed by MKE is defined as the square root of k the variation of which is therefore coincide with the variation of k with current decay. The value of V_c (Figure 5-22

(b)) is generally larger than that computed by PML. Although λ_c is smaller, the resultant v_t is greater (Figure 5-19 (b)), due to larger V_c obtained by the MKE in comparison with that given by PML. This results in much faster rate of decay of arc temperature, and thus a voltage extinction peak, predicted by MKE, whilst the arc voltage of PML does not have extinction peak due to much weaker turbulence effects predicted by this model.

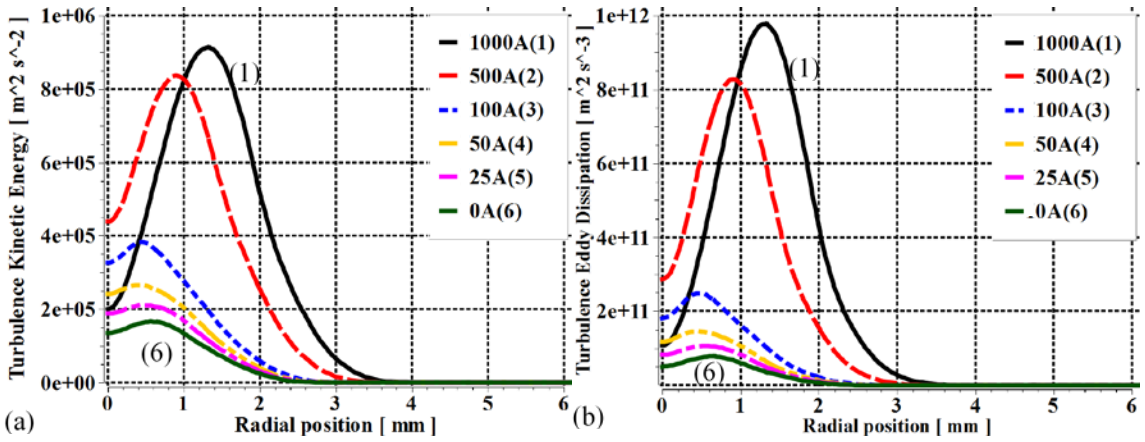

Figure 5-21 Variation of k and ε at Z=25 mm with current decay computed by MKE. P_0=37.5 atm and di/dt=13.5 A/μs. (a) k and (b) ε.

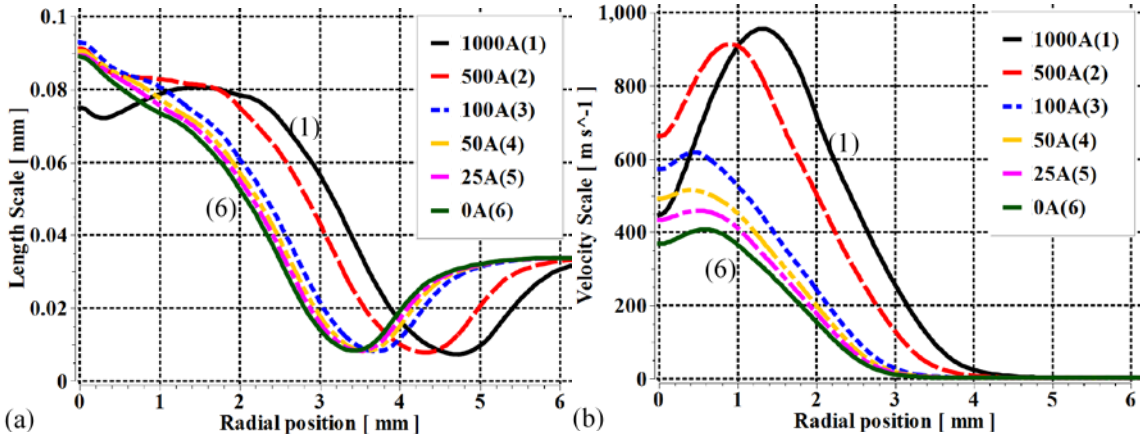

Figure 5-22 Variations of λ_c and V_c at Z=25 mm with current decay predicted by MKE. P_0=37.5 atm and di/dt=13.5 A/μs. (a) λ_c and (b) V_c.

5.2.2.2.4. Arc Conditions in the Vicinity of Current Zero

Thermal interruption of an arc in a nozzle interrupter is determined by the arc temperature in the vicinity of current zero. For LAM, radiation and axial convection are important and the radial convection determines the radial extent of the arc. For PML and MKE, turbulent thermal conduction becomes the most important at the core boundary for which the axis temperature drops quickly a few microseconds before current zero, whereas at the electrical boundary, thermal conduction is not important which cannot effectively take the energy out of the arc's electrically conducting core due to the effects of ρC_P as discussed in Chapter 4. As a result, the decay in temperature of an arc is much slower than that of SF_6.

Axis temperature and arc radius at current zero are given in Figure 5-14 and Figure 5-15. Thermal interruption capability depends on the rates of decay of temperature and arc radius. The time variations of axis temperature and arc radius at the nozzle throat are given in Figure 5-23. The decay of axis temperature at throat is the lowest for LAM and the fastest for MKE. Figure 5-23 (a) shows that there are two temperature decay rates with an approximate demarcation at 3 μs before current zero. Since axial convection is the most important energy transport mechanism the arc radius is controlled by convection. At current zero the characteristic time for the time variation of arc radius at throat, the absolute value of [R/(dr/dt)], at current zero is approximately 20 μs for all three flow models. This is consistent with the transit time taken by an arc element to travel from the upstream electrode tip to the tip of downstream electrode with an average axis velocity of 2,000 m/s (Figure 5-11). For MKE the characteristic time for axis temperature variation is about 50 μs at an instant current of 140 A (approximately 10 μs before current zero). In the last 3 μs before current zero this characteristic time is reduced to 2 μs, which is consistent with the characteristic time for a radial thermal conduction dominated core (Table 5-5).

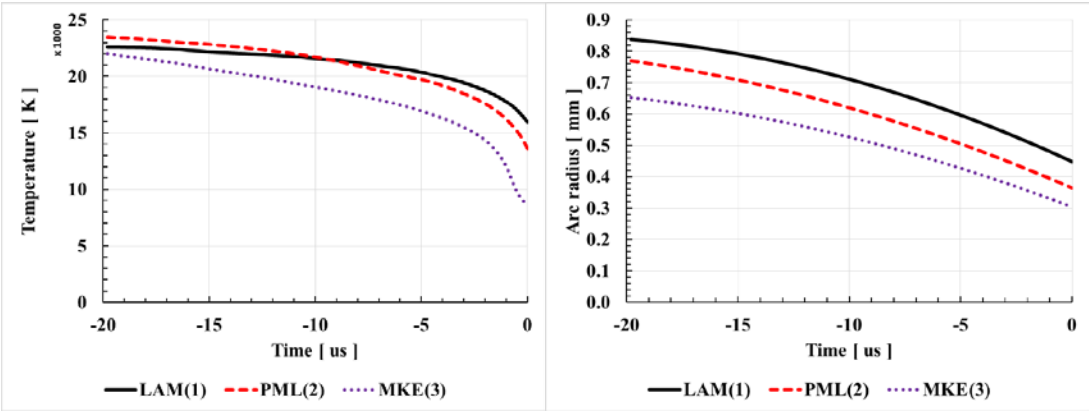

(a) (b)

Figure 5-23 The time variation of axis temperature (a) and arc radius (b) computed by 3 flow models at nozzle throat for 13.5 A/μs and P_0= 37.5 atm.

Of the three flow models MKE gives the lowest axis temperature and the smallest arc radius, thus the highest RRRV. It should be noted that at current zero the radius of the electrical boundary is about 50% of the radius characterizing arc's thermal influence (Figure 5-18 (c)). This is in contrast with the radial temperature profile of SF_6 which shows steep radial temperature gradient around 4,000 K below which electrical conductivity is negligible. Thus, SF_6 arc has a distinctive core structure. Since axial convection is the most important power loss mechanism for air arcs this results in a slower rate of reduction of temperature and arc radius in comparison with SF_6 switching arc for which thermal conduction is dominant near current zero [64]. It is therefore expected that RRRV of air will be lower than that of SF_6.

5.2.3. **The Behaviour of the Transient Arc After Current Zero**

A linearly increasing voltage at a given rate of rise (dV/dt, known as the rate of rise of recovery voltage) is used after current zero to investigate the thermal interruption capability of the nozzle interrupter. The value of dV/dt, at which the arc will just be extinguished, is commonly known as the RRRV. This will be found computationally by applying the three flow models. The qualitative features of the arc behaviour after current

zero are similar for different values of P_0 and di/dt. Unless otherwise specified, results are presented for P_0=37.5 atm and di/dt=13.5 A/μs.

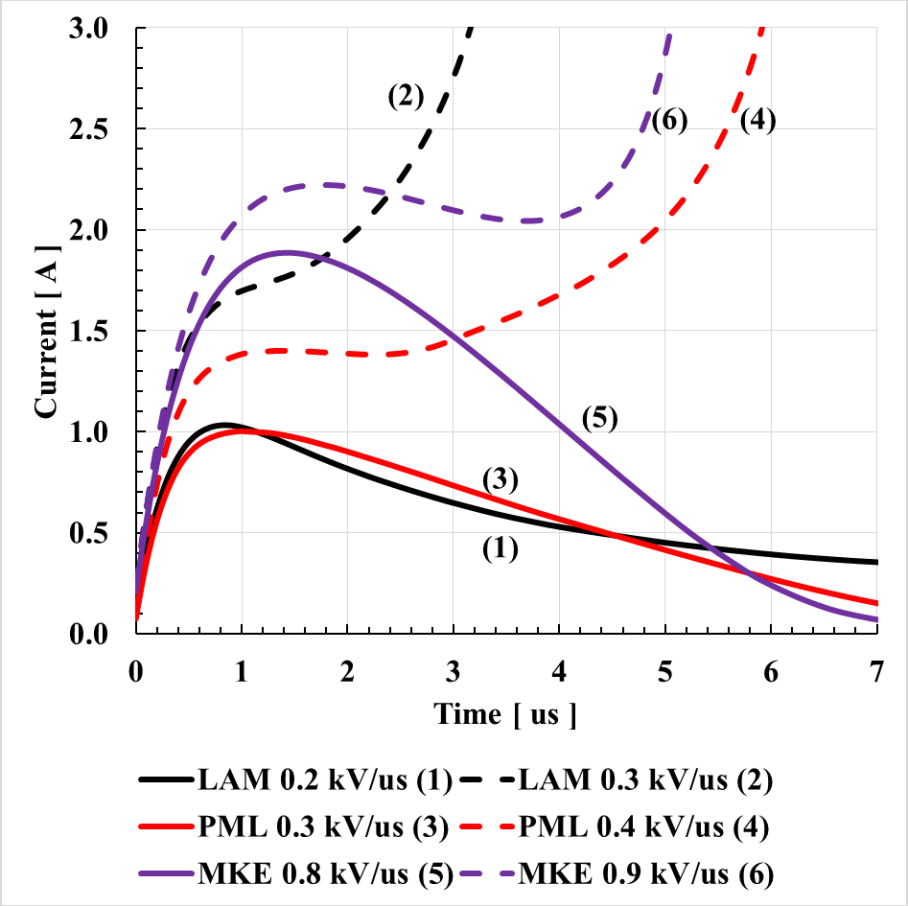

Figure 5-24 Post-arc current predicted by the three flow models for P_0=37.5 atm and di/dt=13.5 A/μs.

Typical results of post-arc currents predicted by the three flow models are given in Figure 5-24. For LAM, the predicted post-arc currents given in Figure 5-24 indicate the RRRV of around 0.25 kV/μs. The values of RRRV predicted by the two turbulence models are respectively 0.35 kV/μs for PML and 0.85 kV/μs for MKE. In contrast with SF_6 RRRV predicted by LAM and those by PML and MKE are of the same order of magnitude.

Computed axis temperature and electric field distributions at different instants after current zero are given in Figure 5-25 to Figure 5-30 for PML, MKE and LAM,

respectively. Qualitative features of the results obtained by PML and MKE are almost the same. When the arc is thermally extinguished, axis temperature decays within 7 μs to below 4,000 K after current zero in the arc section before the shock. In the region after the shock the arc temperature hardly changes within such a short period due to the stagnant flow feature as previously discussed, for which the recovery voltage taken by the arc section in this region is negligible. According to Figure 5-25 and Figure 5-27 the recovery voltage is taken up by the arc section before the shock. For this arc section, during thermal recovery the electric field increases with time due to temperature decay and the shrinkage of arc size caused by radial conduction and axial convection cooling effects. When arc is reignited (Figure 5-26 and Figure 5-28) the temperature rises rapidly first upstream electrode while the temperature in the rest part of the arc still decreases due to thermal inertia. The peak of electrical field moves downstream, which subsequently arrests the temperature decay and eventually, the temperature and the current increase rapidly.

Results obtained by LAM are still qualitatively quite similar (Figure 5-29 and Figure 5-30) to those computed by the two turbulence models. The differences are all quantitative in nature, e.g. slightly longer characteristic time for thermal extinction/reigniting, higher temperature and thus lower electric field.

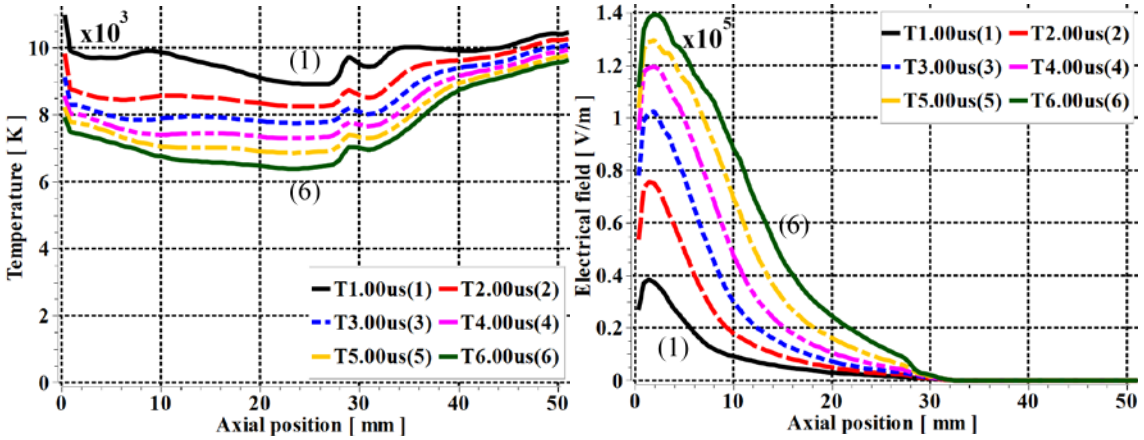

(a) (b)

Figure 5-25 Axis temperature (a) and electrical field (b) computed by PML when arc is extinguished. dV/dt=0.3 kV/us and P_0= 37.5 atm.

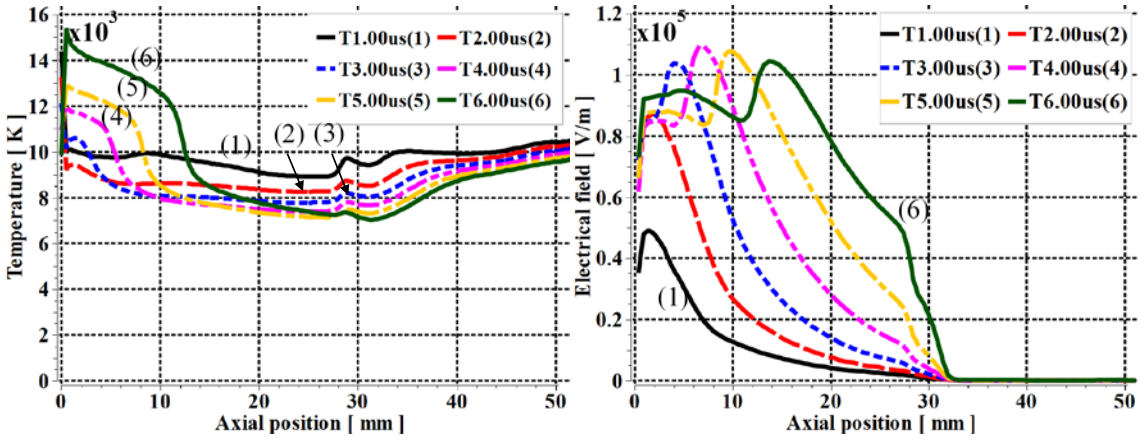

(a) (b)

Figure 5-26 Axis temperature (a) and electrical field (b) computed by PML when arc is reignited. dV/dt=0.4 kV/us and P_0= 37.5 atm.

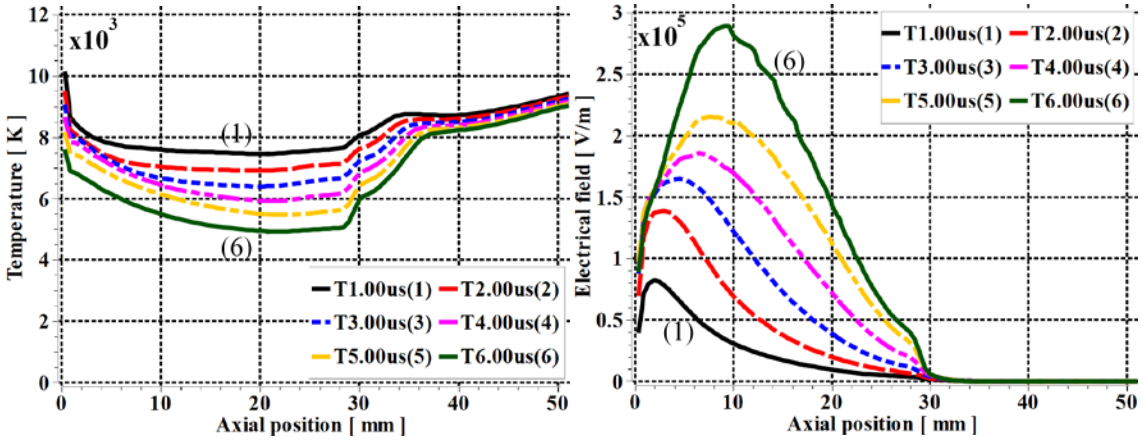

(a) (b)

Figure 5-27 Axis temperature (a) and electrical field (b) computed by MKE when arc is extinguished. dV/dt=0.8 kV/us and P_0= 37.5 atm.

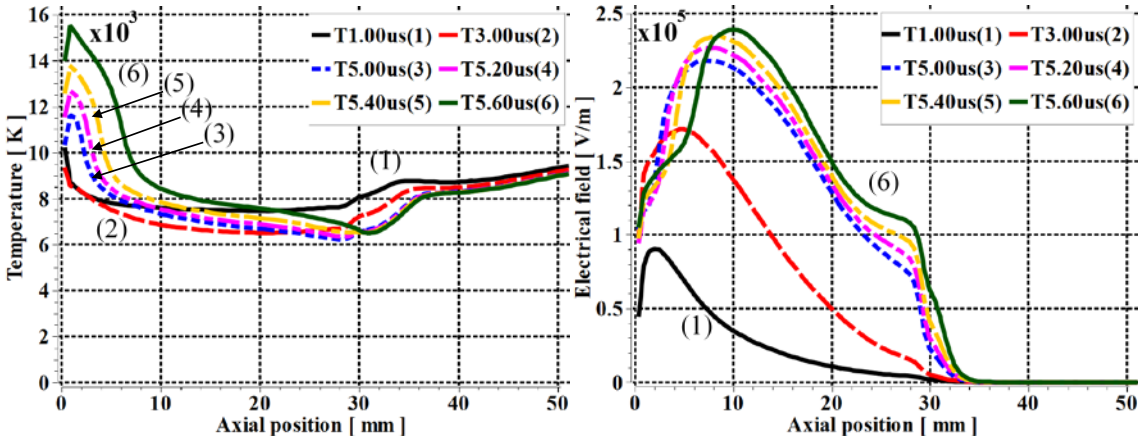

(a) (b)

Figure 5-28 Axis temperature (a) and electrical field (b) computed by MKE when arc is reignited. dV/dt=0.9 kV/us and P_0= 37.5 atm.

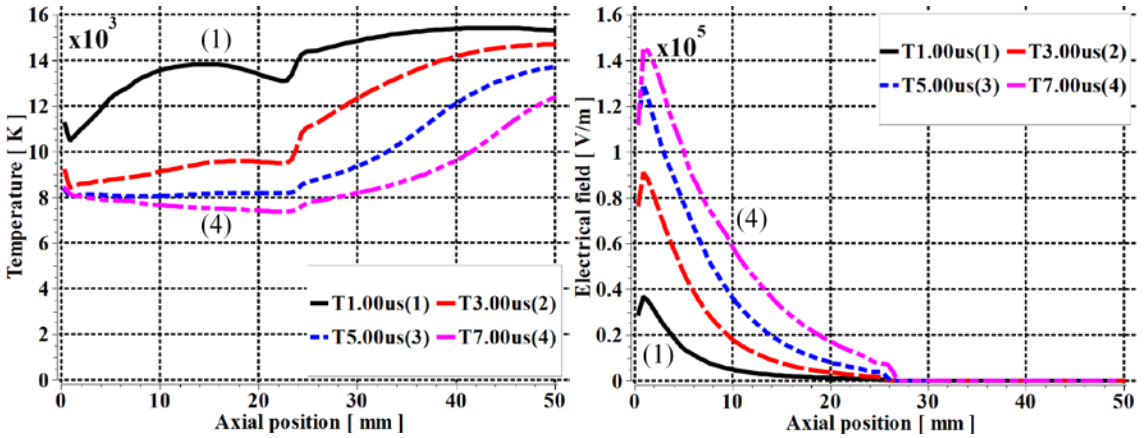

(a) (b)

Figure 5-29 Axis temperature (a) and electrical field (b) computed by LAM after current zero when arc is extinguished. dV/dt=0.2 kV/us and P_0= 37.5 atm.

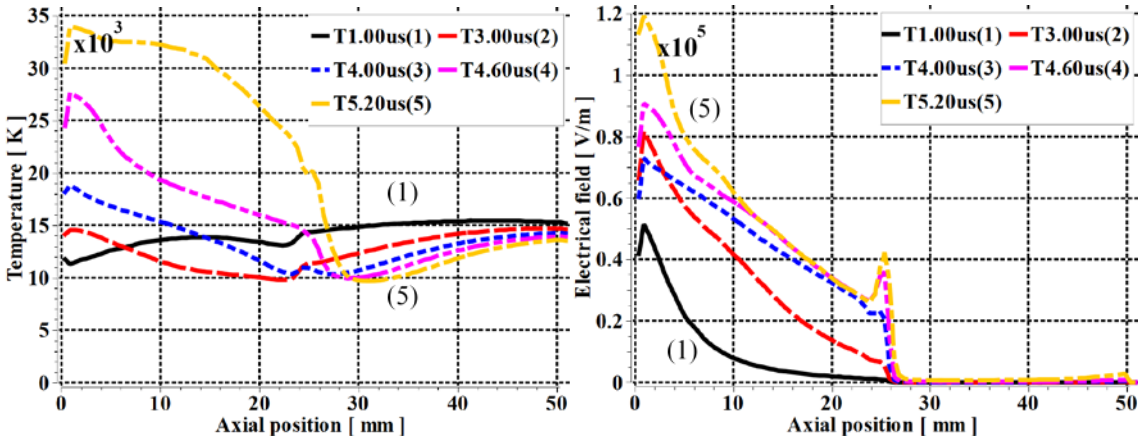

(a) (b)

Figure 5-30 Axis temperature (a) and electrical field (b) computed by LAM after current zero when arc is reignited for dV/dt=0.3 kV/us and P_0= 37.5 atm.

5.2.4. **Comparison with Experiments**

For the computation of RRRV in the present investigation, we have applied not only LAM, PML and MKE but also the standard k-epsilon model with default turbulence parameters. The standard k-epsilon model is still widely used for predicting RRRV ([62, 80]). The

computational results of RRRV as a function of di/dt for P_0 = 37.5 atm for the 4 flow models are summarized in Figure 5-31 together with the experimental results given in [66] for comparison.

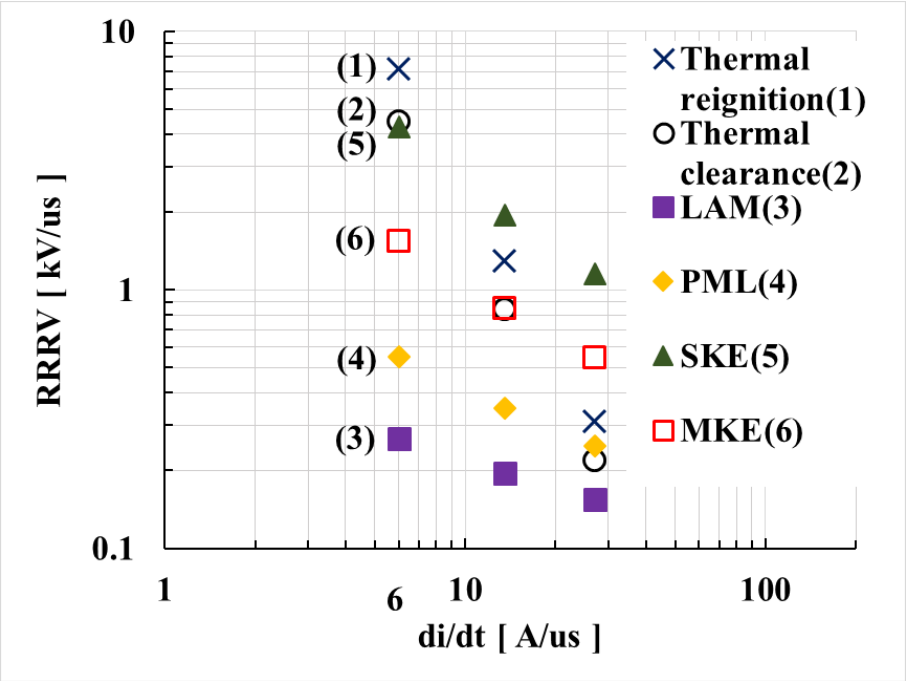

Figure 5-31 Comparison between measured and computed RRRV obtained by LAM, PML and MKE as well as the standard k-epsilon model for P_0= 37.5 atm and different values of di/dt.

The RRRV computed by LAM is the lowest, which is on average an order of magnitude lower than the measured RRRV. This indicates the importance of turbulence in the determination of arc behaviour which is consistent with the conclusions drawn from the investigation on DC air arcs [Chapter 4].

By applying PML, we have chosen the turbulence parameter c=0.03 to match the computed RRRV with that measured RRRV at P_0=37.5 atm and di/dt=27 A/μs. The computed RRRV with c=0.03, however, cannot agree with the measurements at other values of di/dt for the same P_0, which means that for air arcs there exists certain relation between c and di/dt. Attempts are therefore made to increase the value of c, in the hope of achieving a better agreement between computed and measured RRRV for lower values of

di/dt, especially for di/dt=13.5 A/μs. This is because the experimentally measured RRRV [66] at di/dt=13.5 A/μs covers a range of stagnation pressure, which can be beneficially used to assess the range of applicability of PML. Such an attempt however results in unrealistic flow features behind the shock due to sudden increase in turbulence length scale by arc expansion behind the shock. It is not possible to obtain a numerically convergent solution at 1 kA plateau of the current ramp.

Similar to the findings reported in Chapter 4, the standard k-epsilon model over estimates the turbulence effects, which results in a higher RRRV than the experimentally measured RRRV except at P_0=37.5 atm and di/dt=6 A/μs. This suggests that the turbulence parameters of the standard k-epsilon model should vary with different values of di/dt. We therefore use the same approach as that in Chapter 4 by adjusting $C_{1\varepsilon}$ to match the experimental results at di/dt=13.5 A/us for a stagnation pressure of 37.5 atm. Such an attempt has been successful and we obtain $C_{1\varepsilon}$= 1.65 for MKE. However, the predicted RRRV at other di/dt (Figure 5-31) gives large discrepancy with the experimental results. None of the turbulence models investigated can predict satisfactorily the dependence of RRRV on di/dt at a given stagnation pressure.

5.3. **The Dependence of RRRV on Stagnation Pressure, P_0, at a given di/dt**

It is well known that, for a given nozzle, the DC arc voltage is proportional to the square root of P_0, while the RRRV always appears to show a much stronger dependence on P_0. Reasons for a stronger pressure dependence of RRRV than that of the DC voltages have been investigated for the SF_6 nozzle arc [118]. The investigation in [118] indicates that the strong dependence of RRRV on P_0 is due to the combined influence of turbulence enhanced thermal conduction and the radial inflow of the cold flow that causes rapid decay of arc temperature and shrinkage of arc size just before current zero. It is however pointed out in [118] that such strong pressure dependence is the nonlinear behaviour of the arc

which cannot be attributed to a particular gas property or a physical process explicitly dependent on pressure.

For the air arcs burning in the nozzle of Figure 5-1, the experimentally measured RRRV and those computed by MKE only show slightly stronger pressure dependence than the square root of P_0. This is different from the SF_6 arc the RRRV of which show much stronger pressure dependence [118]. We therefore examine the computational results of MKE (due to the best performance of this model in predicting RRRV as shown later) to see how the arc behaviour is dependent upon pressure and whether any difference exists between air and SF_6 arcs regarding the causes of such pressure dependence. It is also noted that our earlier investigation indicates no simple relationship between arc voltage and P_0 for the DC nozzle arcs in air (Chapter 4). However, the arc in the nozzle used in Chapter 4 has a very small cross section downstream of the nozzle throat. For moderate currents the arc is no longer surrounded by a cold flow downstream of the nozzle throat. We will investigate the DC voltage dependence on stagnation pressure first and then followed by an examination of the dependence of RRRV on pressure.

For DC air arcs burning in the nozzle of Figure 5-1, the computed DC arc voltages are summarized in Table 5-7 for 13.6 atm and 37.5 atm with currents ranging from 1 kA to 100 A. We have found that, the DC arc voltages are proportional to the square root of P_0 within the current range investigated for the nozzle of Figure 5-1. Detailed computational results show there is always a cold flow surrounding the arc and the nozzle is not thermally blocked by the arc even for the highest current (1 kA) at 13.6 atm. In the case where the nozzle is not blocked, computational results always suggest that the axis temperature is not sensitive to P_0 for a given current, and the arc radius is approximately proportional to $(P_0)^{0.25}$. These features are the same as SF_6 nozzle arc surrounded by cold flow [65]. For the earlier investigation of DC air arcs (Chapter 4), the arc blocks the nozzle for currents above 2 kA at P_0=10 bar, and nozzle blockage takes place at 1 kA at P_0=7 bar. It is believed that the nozzle blockage in the divergent section of the nozzle is the main reason why arc voltage is no longer proportional to the square root of pressure. This means that DC air

arc voltage is proportional to the square root of P_0 provided that the arc is surrounded by a cold gas flow.

Table 5-7 DC arc voltages for different values of P_0 at four currents computed by MKE.

Current (A DC)	Voltage (V) at P_0=13.6 atm	Voltage (V) at P_0=37.5 atm
1000	419	693
800	422	698
600	429	709
300	481	806

When the current is ramped down from 1 kA DC, for a given di/dt, the cross-section is inversely proportional to the square root of P_0 for the arc in quasi-steady state. A smaller size arc can respond to the current variation more quickly. The arc at a higher stagnation pressure can therefore maintain quasi-steady state longer than an arc at a lower stagnation pressure for the same di/dt. After the breakdown of quasi-steady state of the arc at lower pressure while the one at high pressure is still in quasi-steady state, the voltage ratio of the two arcs at the same instant current will be higher than the square root of pressure ratio. However, the results shown in Figure 5-32 indicate that the voltage ratio of the two arcs at 13.6 atm and 37.5 atm is still equal to the square root of the pressure ratio at 20A (less than 2μs before current zero) for di/dt= 13.5 A/μs. Just before current zero axis temperature decays at a much faster rate the voltage ratio of arcs at different pressures is no longer proportional the square root of the pressure ratio. There are many rapidly changing physical processes involved which interact with each other in a non-linear fashion. The outstanding feature of turbulent air switching arc is the very broad radial temperature profile caused by the material property ρC_P and the dominance of convection for the overall arc energy balance at the electrical core boundary. Convection is associated with gas motion which has a characteristic time much longer than that of turbulent thermal conduction. Arc radius decays at a much slower rate than that of axis temperature, the decay rate of which is determined by turbulent thermal conduction just before current zero

(Figure 5-23). Because of this the rate of rise of arc conductance is only accelerated in the last 2 μs before current zero (Figure 5-33). The arc resistance ratio for the two arcs at 13.6 atm and 37.5 atm is proportional to the pressure ratio to the power of 0.6, which indicates that the pressure dependence of RRRV would be approximately the same ([112]).

Computational results of RRRV obtained by the 3 flow models and those by the standard k-epsilon model are given in Figure 5-34 together with the experimental results as a function of stagnation pressure for di/dt= 13.5 A/μs. It is well known that there is large uncertainty in experimentally measured RRRV due to shot to shot variation. The experimental uncertainty is not mentioned in [66]. Nevertheless, according to the experimental points plotted in Figure 5-34 for thermal extinction and reignition, this uncertainty is estimated to be 35% of the RRRV corresponding to thermal clearance. Due to such experimental uncertainty, the exponent of the dependence of RRRV on P_0 (i.e. y in $\mathrm{RRRV} \propto P_0^y$) ranges from 0.5 to 1 for di/dt=13.5 A/μs. The computed RRRV by MKE suggest that y = 0.7, which is considered satisfactory in the view of 35% of uncertainty in measured RRRV.

Figure 5-34 indicates that in comparison with experimental results the standard k-epsilon model grossly over predicts RRRV and LAM under estimates. With c=0.03 PML also predicts RRRV much lower than experiments. The value of c is chosen by matching the computed RRRV for di/dt= 27 A/μs at 37.5 atm with the measured RRRV. Numerical difficulties in the region behind the shock caused by sudden increase in the mixing length scale due to arc expansion prevents optimizing the value of c for di/dt= 13.5A/μs. Such numerical difficulties encountered by PML in dealing with the shock region restrict the use of PML in the presence of the shock. With the chosen value of $C_{1\varepsilon}$= 1.65 MKE gives the best agreement with experimental results. However, when the same value of $C_{1\varepsilon}$ is used for di/dt other than 13.5 A/μs results are not satisfactory. This implies that di/dt has a strong influence on the turbulence length and velocity scales.

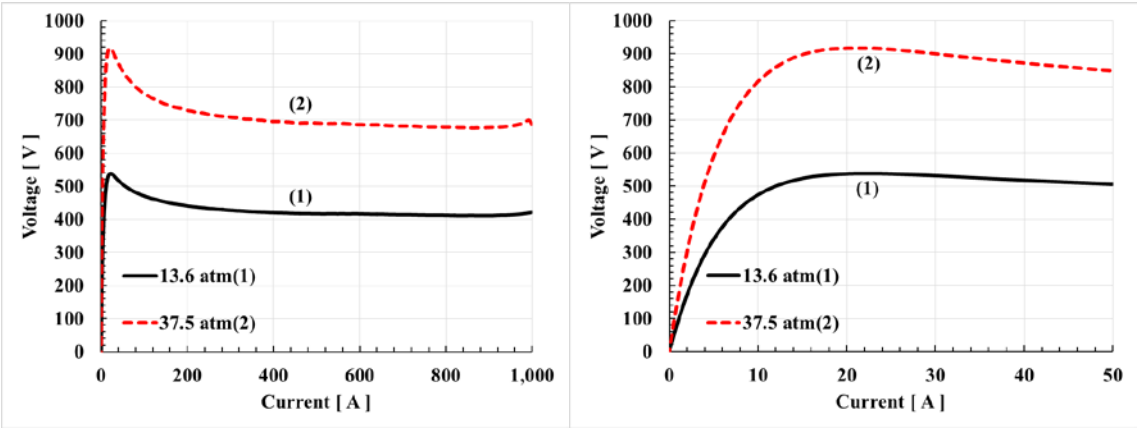

Figure 5-32 The voltage-current (V-I) characteristics for the nozzle arcs computed by MKE corresponding to the current ramp, for P_0=13.6 atm and 37.5 atm, and, di/dt=13.5 A/μs. (a) V-I characteristics and (b) enlarged V-I characteristics shortly before current zero.

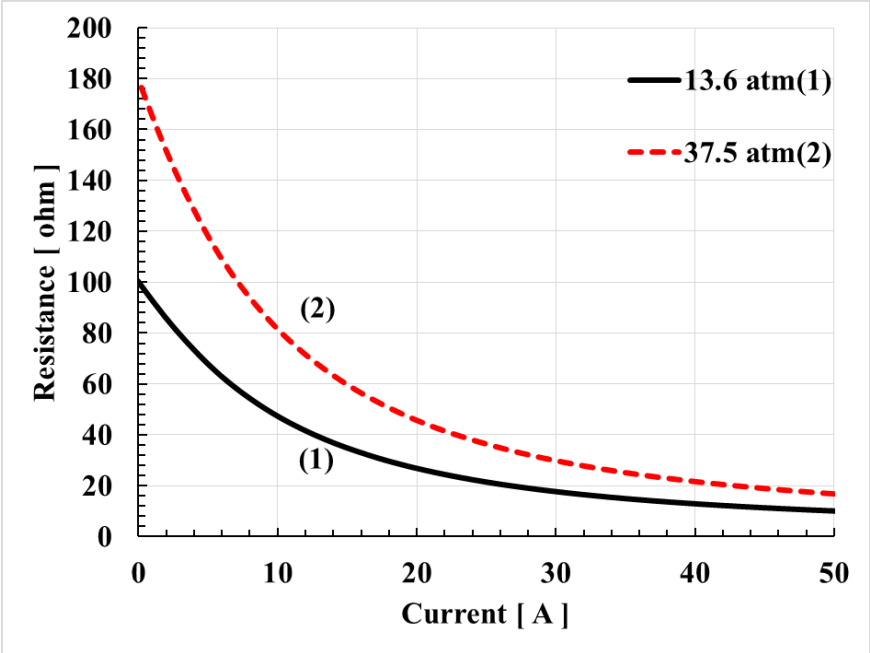

Figure 5-33 Variation of arc resistance as a function of current shortly before current zero computed by MKE, for P_0=13.6 atm and 37.5 atm, and, di/dt=13.5 A/μs.

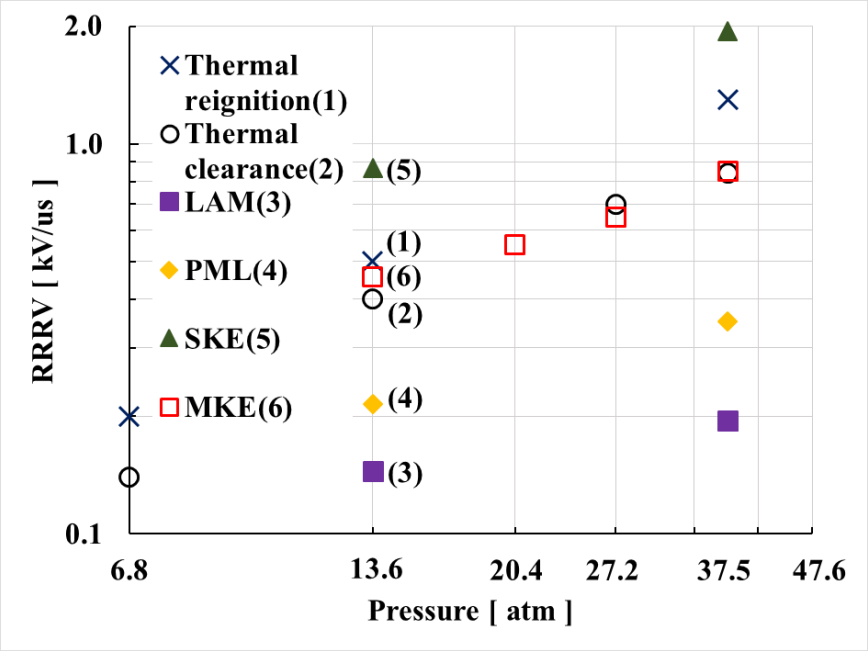

Figure 5-34 RRRV computed by LAM, PML, MKE and the standard k-epsilon model together with experimental results plotted as a function of stagnation pressure for di/dt= 13.5A/μs.

5.4. **Summary**

The behaviour of the transient air arc burning in the nozzle of Frind and Rich [66] has been numerically investigated using the three flow models employed in Chapter 4, namely the laminar flow model (LAM), the Prandtl mixing length model (PML) and the modified k-epsilon model (MKE).

Computational results have been analysed to reveal the detailed flow features for the cold flow and in the presence of the arc at a stagnation pressure of 37.5 atm and di/dt= 13.5A/μs. With the exit pressure set at 0.25 of the upstream stagnation pressure, a shock is generated in the nozzle. In the absence of the arc, the shock is similar to a normal shock. The presence of the upstream and downstream electrodes alters the local flow behaviour with a wake near the upstream electrode tip and compression waves near the downstream electrode tip. Detailed flow features regarding the shock and compression waves and the wake differ widely between flow models. The implication of such flow features on

dielectric strength of the nozzle has been discussed. Apart from the regions near electrode and after the shock, different flow models give almost the same results for the cold nozzle flow. With an arc in the nozzle, the nozzle flow features have been greatly altered as compared with those of the cold flow. There is strong interaction between the arc and the shock, resulting in the shock centre being moved upstream and the gas from the dumping tank being sucked into the nozzle. The complex interaction between the gas flow emerging from the shock and that produced by sucked-in gas from the dumping tank generates complex flow features characterized by vortices. When the current is ramped down to zero these vortices remain. Temperature decay in the regions occupied by the vortices is extremely slow due to the circulating flow inside vortices. However, the arc behind the shock takes a low percentage of total arc voltage. Therefore RRRV is determined by the arc section upstream of the shock. After the arc is thermally extinguished the region occupied by the vortices will have low dielectric strength.

A detailed numerical study on the transient air arc behaviour and a comparative study of different flow models have been conducted for P_0=37.5 atm and di/dt=13.5 A/μs. For currents down to 500 A and for all flow models, radiation loss and axial thermal convection are the dominant energy transport processes at the high temperature core and the electric boundary, respectively. Thermal conduction is not significant for which the arc voltage is not sensitive to flow models during this period. It is also found that the arc at currents of 200 A and above can remain approximately in quasi-steady state. When the current is ramped down towards zero, thermal conduction gradually becomes significant for which the arc voltages computed by different flows become different. At the core boundary, thermal conduction becomes the dominant energy loss mechanism in the vicinity of current zero. However, at the electric boundary, even at the vicinity of current zero, thermal conduction still plays a secondary role, and it is the axial thermal convection that is the dominant energy transport process in the determination of the arc behaviour. The dominance of axial thermal convection is mainly due to the very broad radial temperature profile caused by the peaks of turbulent thermal conductivity in the temperature region around 7,000 K and 4,000 K as discussed in Chapter 4. This is in

contrast with the SF_6 arc investigated in [118] for which thermal conduction is dominant both at the core boundary and the electric boundary at the vicinity of current zero.

Computational results of RRRV have been obtained using the three flow models together with the standard k-epsilon model. These results are compared with the measurements of Frind and Rich [66]. It has been shown that MKE with $C_{1\varepsilon}$=1.65 can give satisfactory predictions of RRRV for di/dt=13.5 A/μs at different stagnation pressures. For a given P_0 with different values of di/dt, there appears to have certain relation between the turbulence parameters and di/dt, since a single chosen value of a particular turbulence parameter cannot match all the experimental results for the range of values of di/dt studied. PML with c=0.03 chosen by matching computed RRRV with that measured at 27 A/μs and P_0= 37.5 atm fails to make a single satisfactory prediction of RRRV. Numerical difficulties encountered by PML in the region behind the shock prevent the application of PML to air arcs with shocks. The same is also true for the predicted RRRV obtained by LAM. The standard k-epsilon model gives satisfactory agreement with experiment at di/dt=6 A/μs and P_0=37.5 atm but over predicts RRRV for other discharge conditions.

The pressure dependence of the measured RRRV and those predicted by MKE are only slightly stronger than the square root of P_0, i.e. similar to the pressure dependence of arc voltages for arcs in quasi-steady state. This is in contrast with the SF_6 arc investigated in [118], the RRRV of which shows very strong dependence on stagnation pressure. The main reason for such weak pressure dependence is due to the very broad radial temperature profile which results in axial convection being the most important energy transport process up to the electrical boundary. Turbulence enhanced thermal conduction never becomes the most important energy loss mechanism at the electric boundary due to the effects of peaks of turbulent thermal conductivity produced by the material property, ρC_P. This results in a slow rate of shrinkage of arc radius. Arc resistance only shows a pressure dependence to a power of 0.6 at current zero.

Chapter 6. Comparative Study on the Behaviour of the Switching Arcs in Air and SF_6

6.1. Introduction

In Chapters 4 and 5, a detailed investigation has been carried out for the behaviour of the switching arc in air under both steady (DC) and transient current conditions. This investigation has confirmed that turbulence plays an important role in determining the behaviour of switching arcs in air. Apart from the confirmation on the role of turbulence, the material properties which are critical in the determination of the thermal interruption capability of air as a switching medium have also been identified, i.e. ρCp and ρh: these material properties are associated with the dominant energy transport mechanisms of switching arcs which determines the temperature distribution of the arc and the surrounding flow. It is therefore important to examine the information regarding these material properties when choosing a switching medium (as a replacement of SF_6) for a gas-blast circuit breaker, as indicated in the previous two chapters.

Through the investigation, it has been noted that the behaviour of switching arcs in air is very different from those in SF_6 as previously studied [64, 65, 118]. Such difference is of course due to differences in material properties, including ρCp and ρh, between air and SF_6. SF_6 is currently the most widely used switching medium for high voltage gas-blast circuit breakers above 110 kV which has superior interruption capability than air. In order to establish a guideline in search of replacement of SF_6, it is important to identify the difference in material properties between a gas candidate and SF_6, and how such differences in material properties affect the dominant energy transport processes. However, no such investigation has so far been done, which has prompt the present investigation for a detailed comparative study on the behaviour of the switching arcs in air and SF_6. The aim of the investigation is to find out the reasons for the superior interruption capability of SF_6 by looking into differences in dominant energy transport mechanisms and the material properties associated with these processes, between air and SF_6. Through the investigation, it is expected that a general guidance can be established

regarding how to search for a replacement of SF_6 as a switching medium for gas-blast circuit breakers.

The computational investigation is based on the experimental study reported by Frind and Rich for the transient switching arcs typical of the current zero period of arcing [66]. The experimental results available in [66] for both the air and the SF_6 arcs are the measurements the critical rate of rise of recovery voltage (RRRV) obtained at the stagnation pressures (P_0) ranging from 13.6 atm to 37.5 atm, and the rate of current decay, di/dt=13.5 A/μs. The effects of turbulence for both the air and the SF_6 arcs are accounted for by the standard k-epsilon model with one of its turbulence parameter ($C_{1\varepsilon}$) adjusted to match the experimental results. The standard k-epsilon model with adjusted $C_{1\varepsilon}$ is referred to as MKE hereafter. The computational results together with the measured RRRV will be used to analyse the difference on the behaviour of the arc in air and SF_6 and the material properties responsible for such differences.

6.2. **Results and Discussion**

Computations have been carried out using a current ramp with a plateau of 1 kA and a rate of current decay before current zero, and a voltage ramp after current zero to determine RRRV. The computational domain is the same as that for the investigation in Chapter 5. MKE is used to model the effects of turbulence. The boundary conditions for the arc conservation equations and those of the k-epsilon model equations are the same as those reported in Chapter 3. The present work considers values of P_0 ranging from 13.8 to 37.5 atm at one value of di/dt, 13.5 A/us. The exit pressure is $0.25P_0$ which is consistent with the experimental conditions of [66]. For MKE, the value of one turbulence parameter, $C_{1\varepsilon}$, is adjusted to give the closest agreement between computed and measured RRRV for P_0= 37.5 atm and di/dt=13.5 A/μs. The value of $C_{1\varepsilon}$ is 1.65 for the arc in air and 1.72 for the arc in SF_6.

The qualitative features of the arc behaviour are similar for different values of P_0. Unless otherwise specified, the predicted results at P_0=37.5 atm and di/dt=13.5 A/μs will be used to illustrate the typical arc behaviour and the difference in arc behaviour for air and SF_6.

6.2.1. Features of the Cold Flow

Computations of the cold flow have been performed using MKE for both air and SF_6 inside the nozzle. Figure 6-1 shows the computational results regarding the pressure distribution superimposed with pressure isobars, and the Mach number distribution of the nozzle. Results show that the qualitative flow features inside the nozzle for both air and SF_6 are similar, with a shock formulated in the divergent nozzle section due to corresponding to the exit pressure applied. The qualitative flow features have been discussed in Chapter 5 which is not repeated here. However, detailed flow features are sensitive to the gas medium in the following aspects:

(a) For SF_6, the location of the shock is slightly closer to the tip of the downstream electrode in comparison with air (Figure 6-2 and Figure 6-3). It is known from Chapter 5 and [64] that, when the shock is in presence, the voltage taken by the arc section after the shock is negligible, for which the effective arc length that can carry the recovery voltage is shortened. The location of the shock being closer to the downstream electrode means the effective arc length is longer, and thus a better thermal interruption capability. The strength of the shock, on the other hand, is similar for both air and SF_6.

(b) Qualitative flow features after the shock are different for air and SF_6 as shown by Figure 6-4.

(c) Regarding the flow behaviour before the shock, results show that air attains much higher velocity and stronger acceleration of the gas than SF_6, which is in favour of enhancing thermal convection cooling effects. Such behaviour is due to lower density of

air, which however results in the mass flow rate for air (1.08 kg/s) to be only half of that for SF_6 (2.27 kg/s). It should however be noted that, a larger mass flow rate does not necessarily mean the thermal convection cooling effects should be stronger. With an arc inside the nozzle, the thermal convection cooling effects actually depends on the material property, ρh, the gas velocity and the radial temperature profiles determined by the material property, ρCp. All these quantities show very complicated correlations between each other, and it will be shown in the subsequent sections how they affect thermal convection.

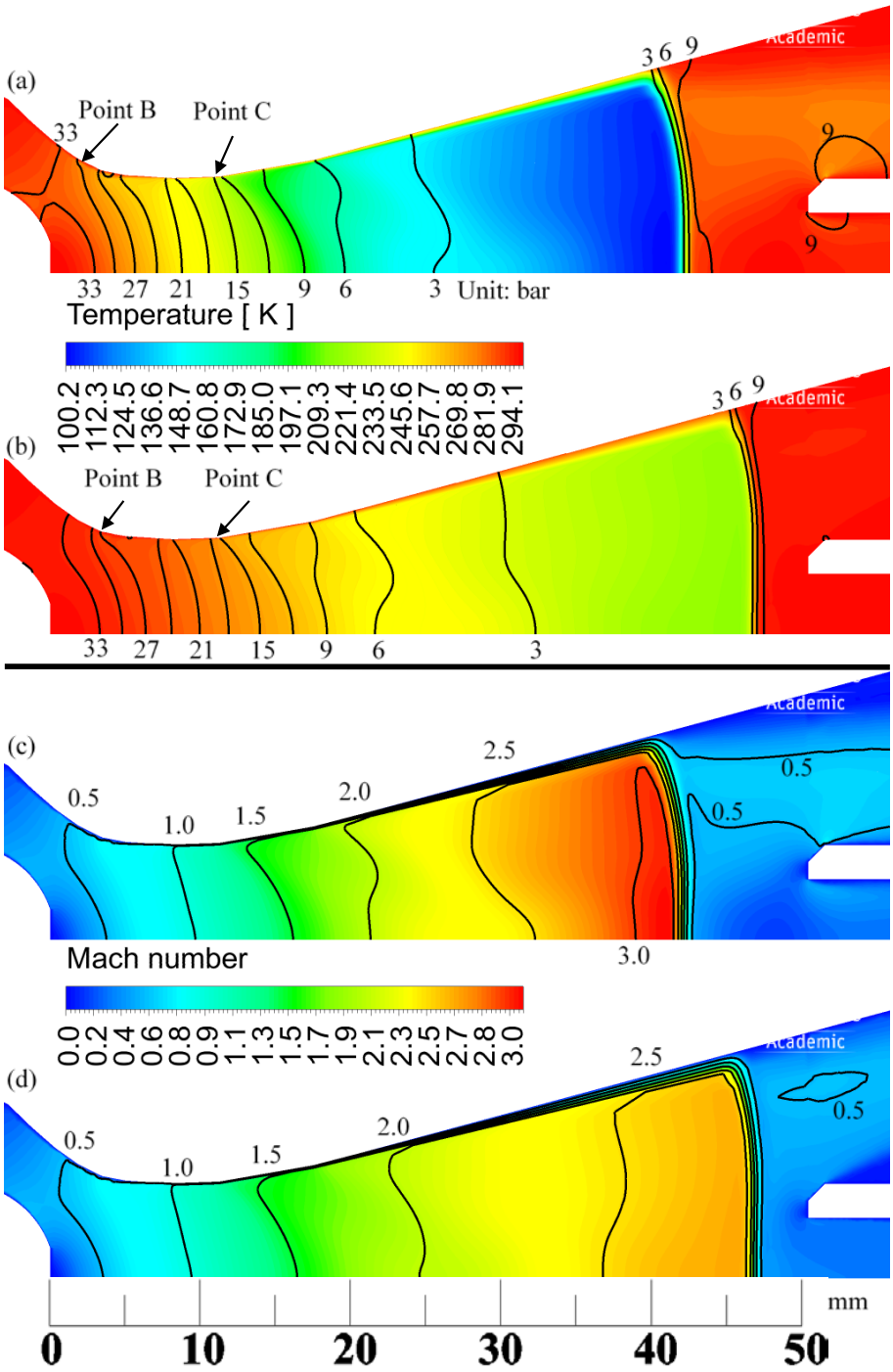

Figure 6-1 Temperature contour together with pressure isobars, and, the Mach number contour for the cold nozzle flow at P_0=37.5 atm. Results are obtained by MKE. (a),(b) Temperature contour together with pressure isobars for Air and SF_6 respectively and (c),(d) Mach number distribution for Air and SF_6 respectively.

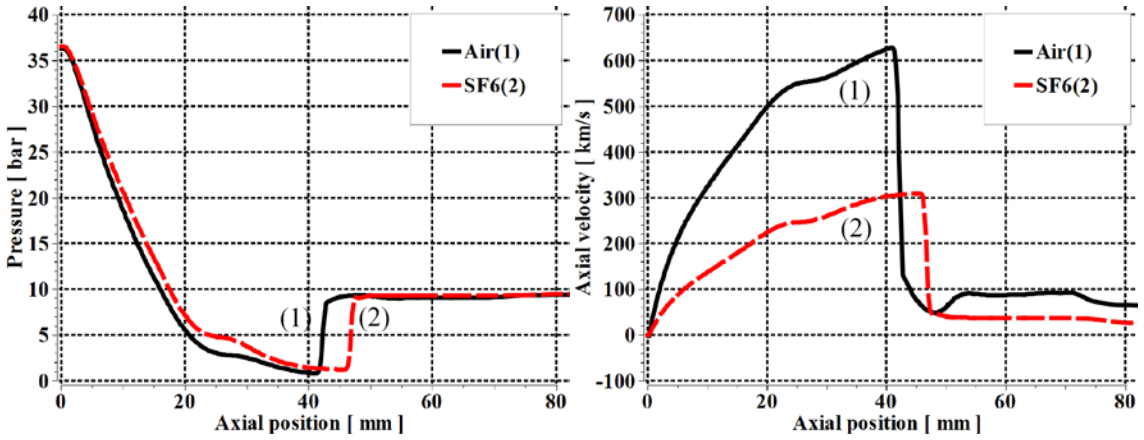

(a) (b)

Figure 6-2 Axis pressure and axis velocity as a function of axial position for the cold nozzle flow at P_0=37.5 atm for both air and SF_6. (a) Axis pressure and (b) Axis velocity.

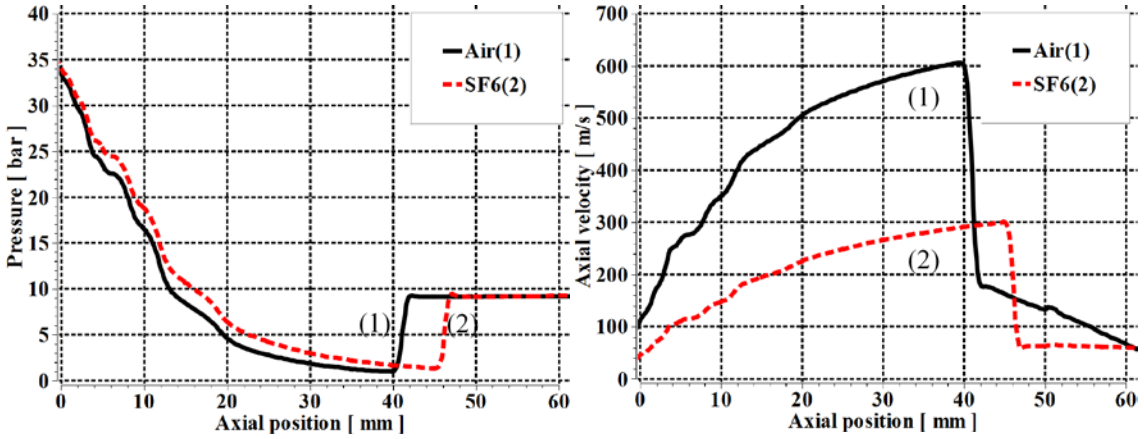

(a) (b)

Figure 6-3 Pressure and axial velocity near the nozzle wall as a function of axial position for the cold nozzle flow at P_0=37.5 atm for both air and SF_6. (a) Pressure and (b) Axial velocity.

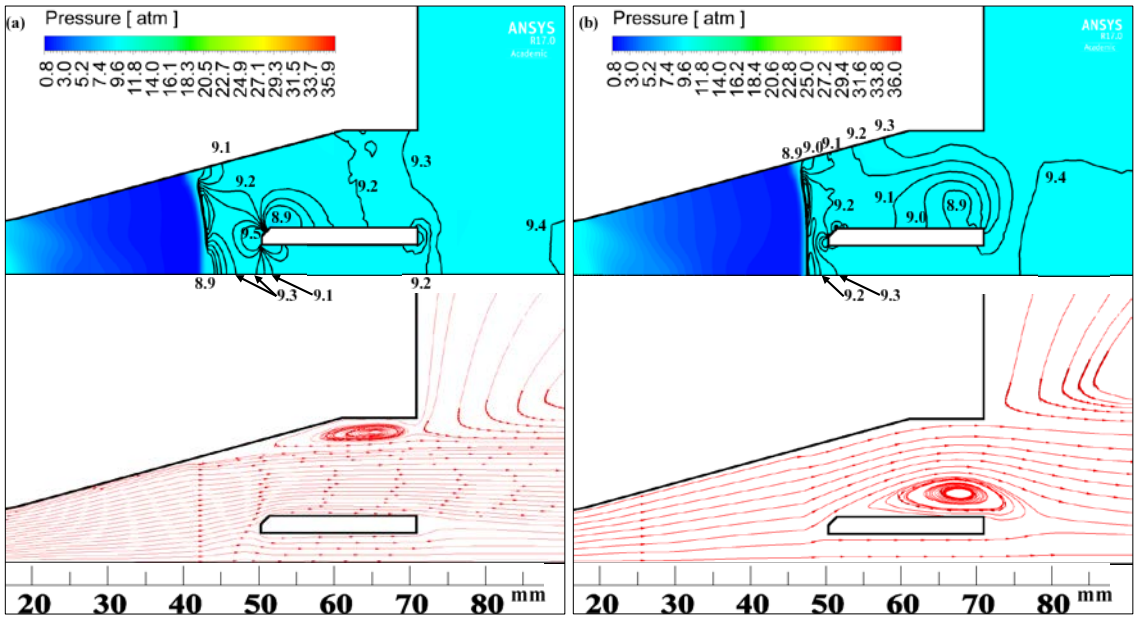

(a) (b)

Figure 6-4 Pressure distribution and flow streamline pattern behind the shock computed by MKE at P_0=37.5 atm. (a) Air and (b) SF_6.

6.2.2. Arc Behaviour before Current Zero

6.2.2.1. Features of the Arc-flow Interaction

Ohmic heating inside the arc creates a high temperature and low gas density region within the nozzle. The presence of the arc therefore reduces the effective flow area, thus modifying the pressure distribution in the nozzle including the shock structure, which in turn affects the arc. Such interaction determines the arc characteristics. With an arc, the shock centre moves upstream and the shock is broadened which cannot be considered as a normal shock. The temperature and the streamline patterns of the gas flow after the shock are given in Figure 6-5 and Figure 6-6 respectively for air and SF_6 at a few instants before current zero. For air, the arc and flow features behind the shock have been discussed in Chapter 5 and those for SF_6 are the same as those discussed in [64]. Results in Figure 6-5 and Figure 6-6 show that the flow features behind the shock are dependent on the gas medium inside the nozzle. Regardless of differences in the flow features, for both air and SF_6, the common features for the arc and flow behaviour behind the shock are the

generation of vortices which gives rise to broadened arc size and very slow rate of temperature decay during current ramp due to very stagnant local flow features. The arc voltage taken by this arc section is small at higher currents (at 1 kA, the percentage of arc voltage taken by the arc section after the shock is 11% for both the air arc and SF_6 arc) which even becomes negligible at the vicinity of current zero. This results in reduced effective arc length as already discussed in Chapter 5 and [64]. The pressure distributions (Figure 6-7 (a) and Figure 6-8 (a)) indicate that, with an arc in the nozzle, the location of the shock and the shock strength is not sensitive to gas medium. This means, for the nozzle of the present investigation and for both air and SF_6, the effective arc length is the same. Since the arc section after the shock can hardly take any voltage at the vicinity of current zero, we focus our discussion on the arc section before the shock.

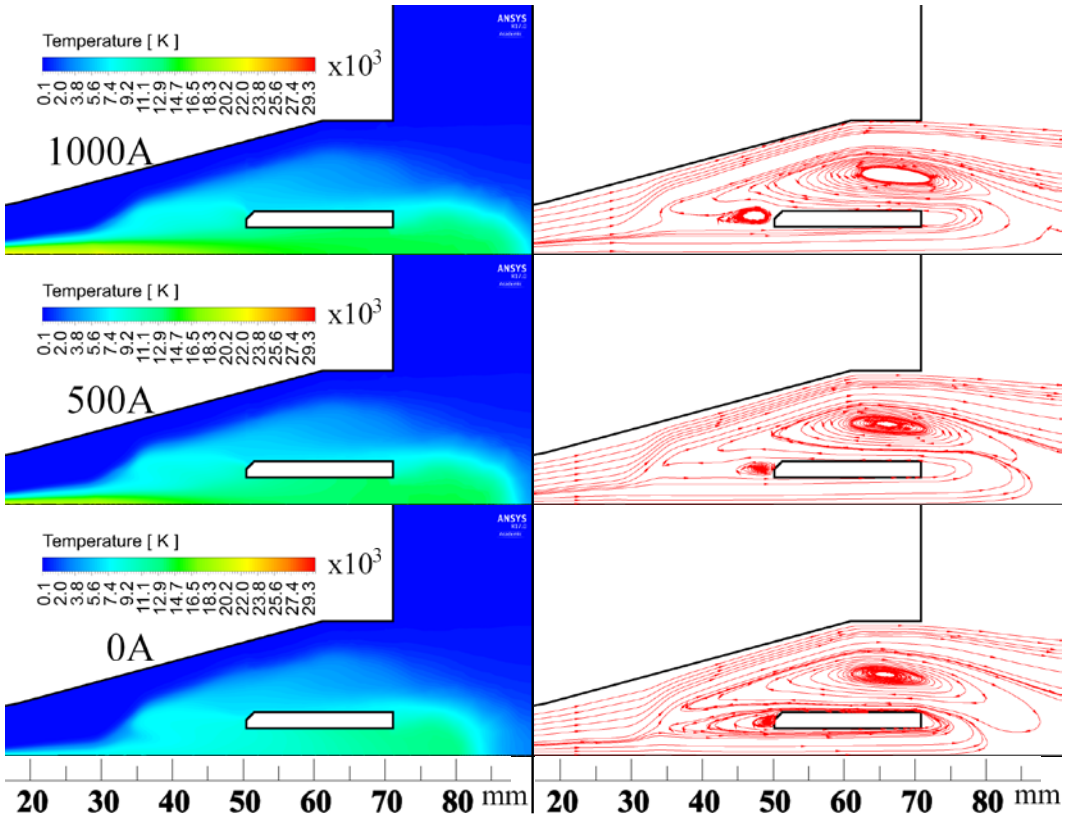

Figure 6-5 Temperature distributions and streamline patterns of air at a few instants before current zeros for P_0=37.5 atm and di/dt=13.5 A/us. Results are obtained by MKE.

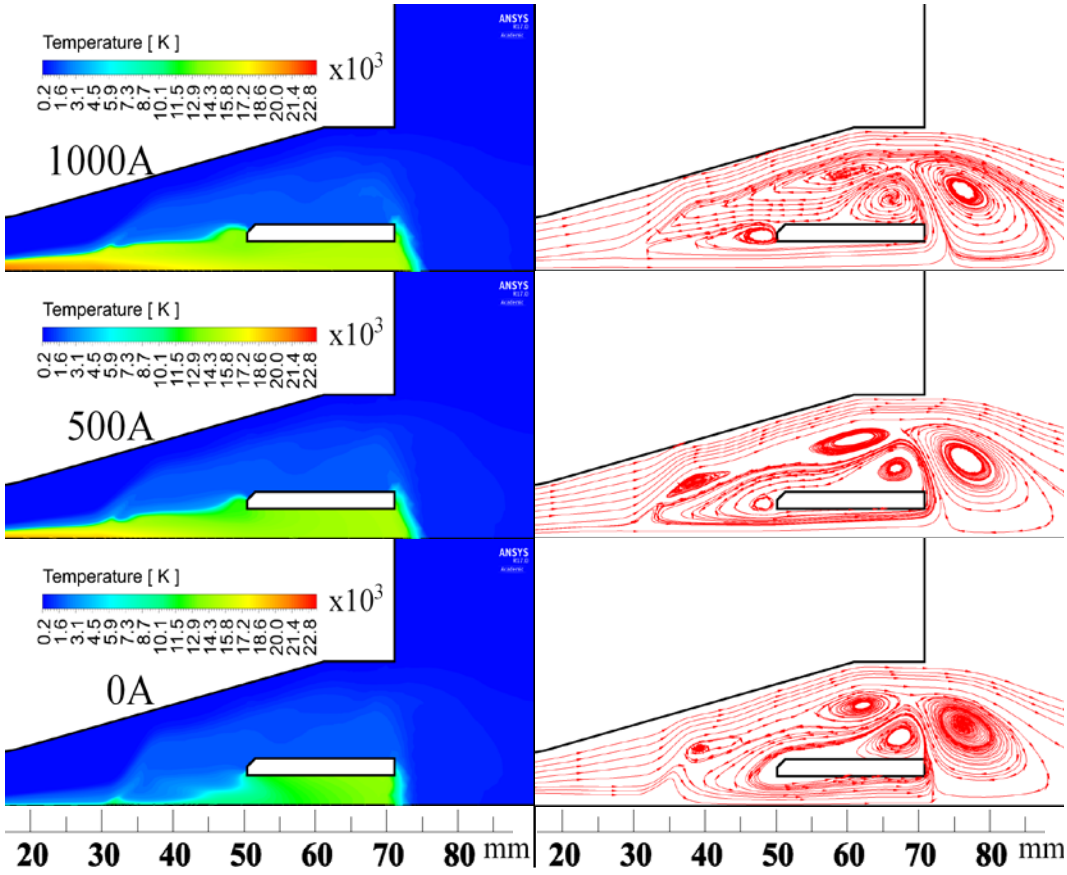

Figure 6-6 Temperature distributions and streamline patterns of SF_6 at a few instants before current zeros for P_0=37.5 atm and di/dt=13.5 A/us. Results are obtained by MKE.

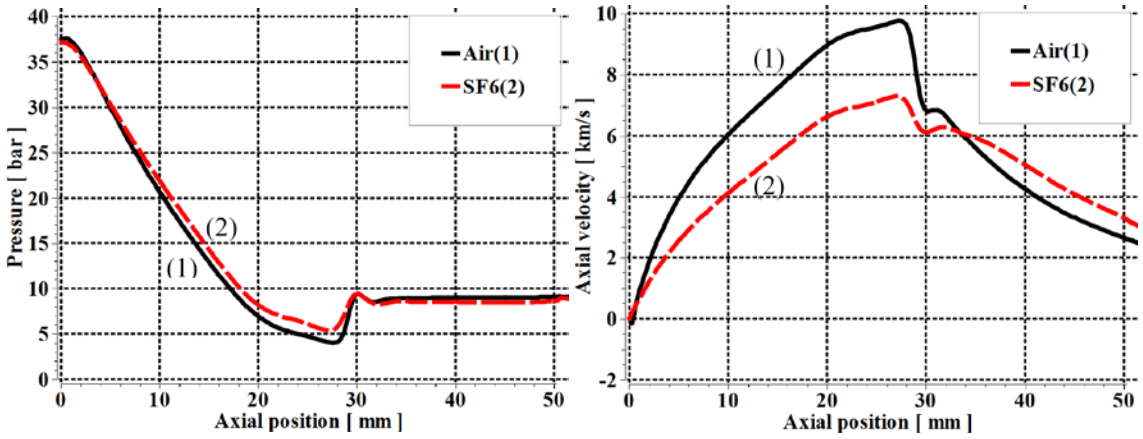

(a) (b)

Figure 6-7 Axis pressure and axis velocity at 1 kA DC for air and SF_6 at P_0=37.5 atm. (a) Axis pressure and (b) Axis velocity.

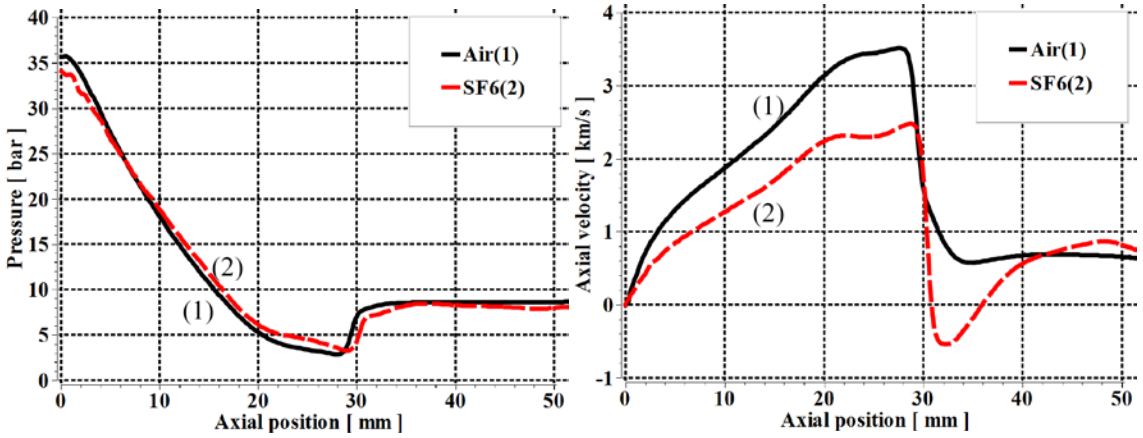

(a) (b)

Figure 6-8 Axis pressure and axis velocity at current zero for air and SF_6 at P_0=37.5 atm and di/dt=13.5 A/µs. (a) Axis pressure and (b) Axial velocity.

6.2.2.2. General Arc Features

The variations of axis temperature, arc radius and electric field at a few instants before current zero are given respectively in Figure 6-9, Figure 6-10 and Figure 6-11, for the air and the SF_6 arcs. The air arc has a higher axis temperature until in the last 2 µs before current zero, and larger arc radius, in comparison with the SF_6 arc during the current ramp. However, the electric field for the air arc is higher than that for the SF_6 arc, and thus a

higher arc voltage, until in the last 2 μs before current zero (Figure 6-12). Actually, it is known that the local electric field depends not only on the axis temperature and arc radius, but also the detailed radial temperature profiles. Attention is therefore paid to the differences in radial temperature profiles between the air and the SF_6 arcs, and the energy transport processes responsible for the arc's temperature distributions.

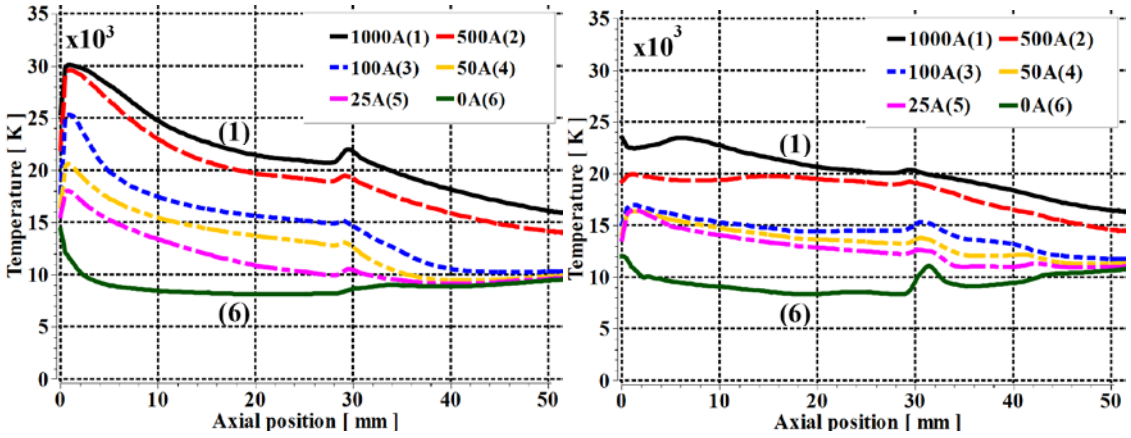

Figure 6-9 Variations of axis temperature with axial position at different instantaneous currents before current zero for P_0=37.5 atm and di/dt=13.5 A/μs. (a) Air and (b) SF_6.

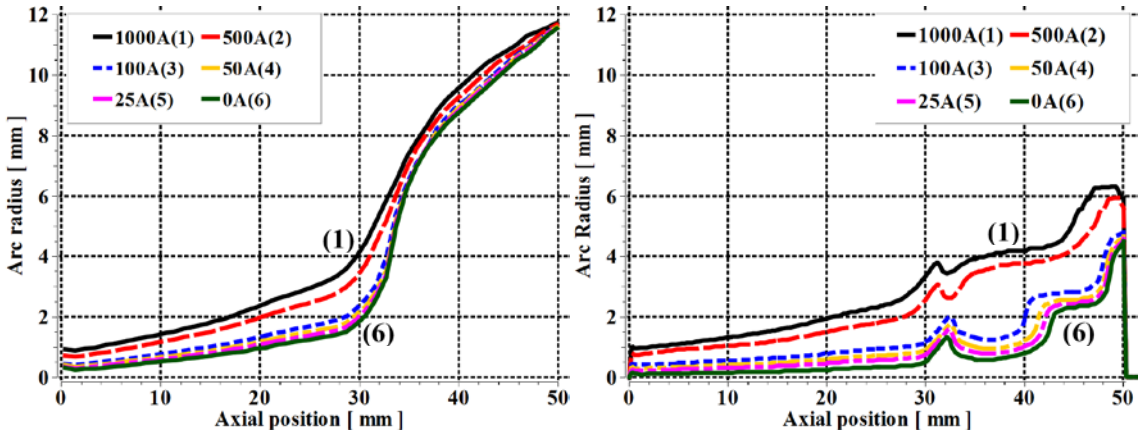

Figure 6-10 Variations of arc radius with axial position at different instantaneous currents before current zero for P_0=37.5 atm and di/dt=13.5 A/μs. (a) Air and (b) SF_6.

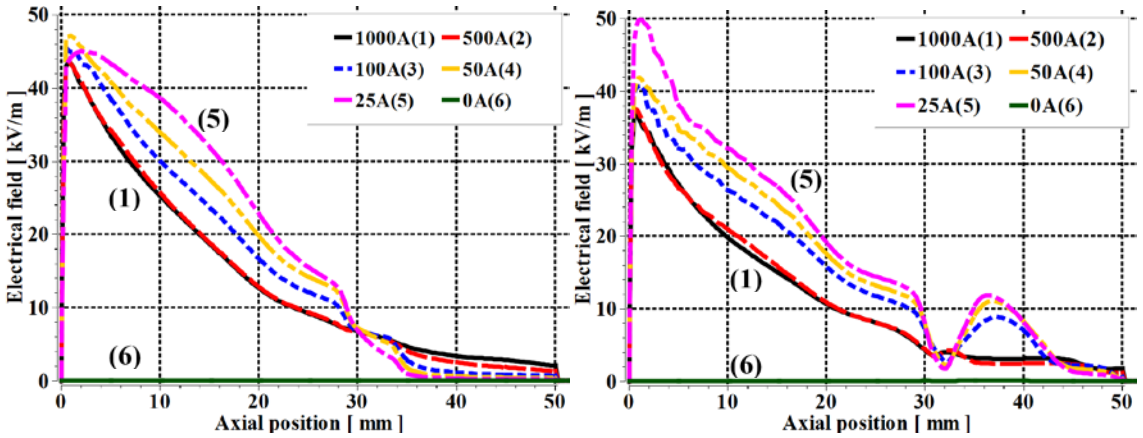

Figure 6-11 Variations of electric field with axial position at different instantaneous currents before current zero for P_0=37.5 atm and di/dt=13.5 A/μs. (a) Air and (b) SF_6.

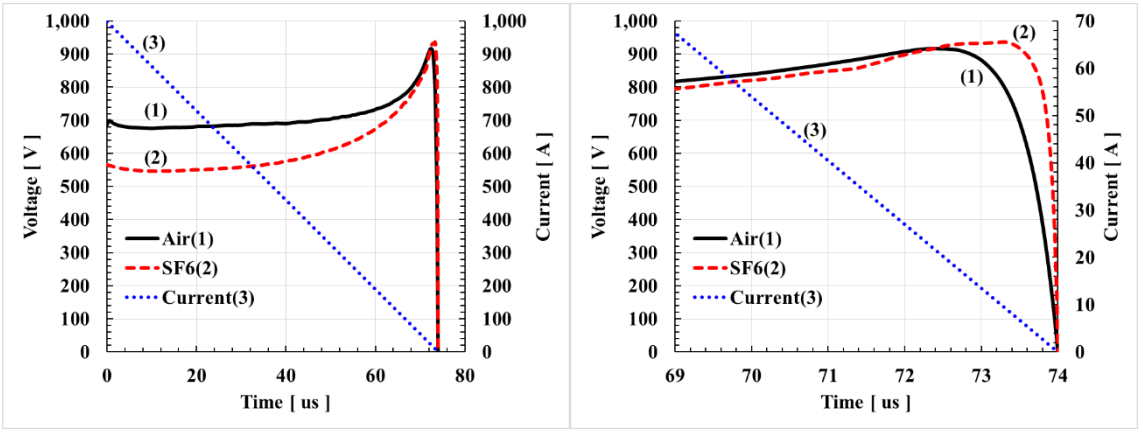

Figure 6-12 Voltage-current (V-I) characteristics for the air and the SF_6 arcs before current zero. (a) V-I characteristics before current zero and (b) enlarged V-I characteristics in the last 5 μs before current zero.

Variations of radial temperature profiles of the air and the SF_6 arcs at a few instants before current zero are given in Figure 6-13 and Figure 6-14 respectively for two typical axial positions. It has clearly been shown that the detailed radial temperature profiles for the air and the SF_6 arcs differ widely during the current ramp. Such a difference in the radial temperature profiles are of course due to the dominant energy transport processes and the material properties associated with these processes. A detailed discussion is given below.

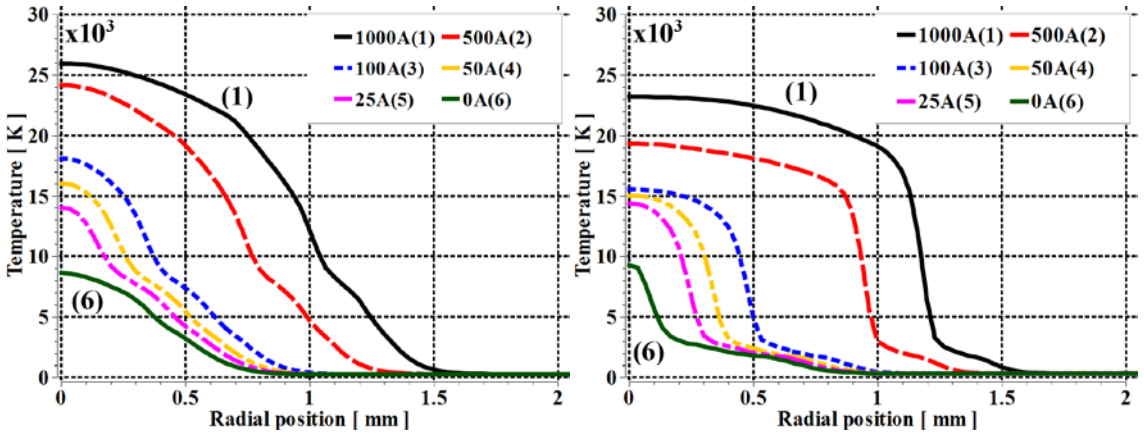

Figure 6-13 Radial temperature profiles at the nozzle throat, Z = 8 mm, for air and SF6 at a few instants before current zero. P_0=37.5 atm and di/dt=13.5 A/µs. (a) Air and (b) SF6.

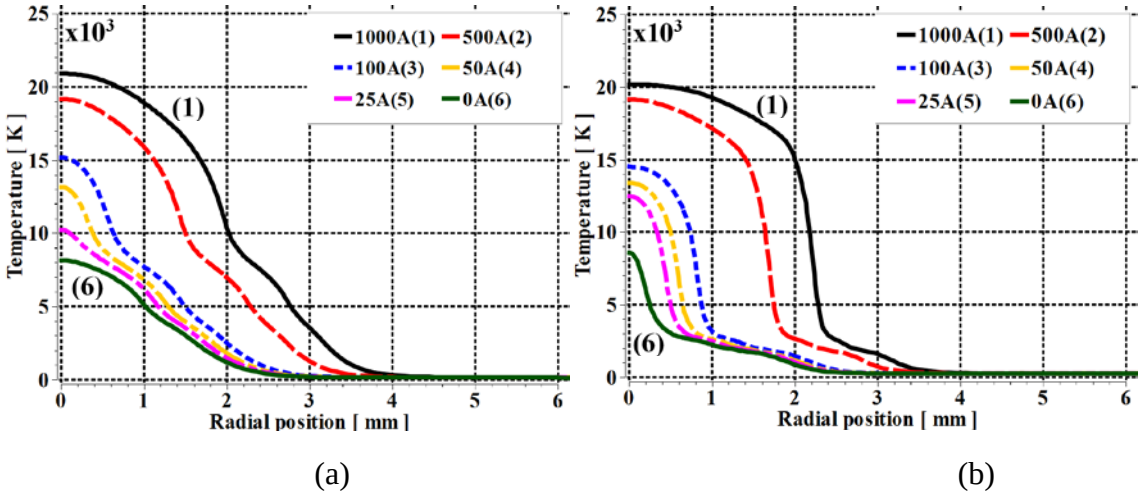

Figure 6-14 Radial temperature profiles at Z = 25 mm for air and SF_6 at a few instants before current zero. P_0=37.5 atm and di/dt=13.5 A/µs. (a) Air and (b) SF_6.

At the currents down to 500 A, radial temperature profiles for the SF_6 arc have a distinctive and very broad arc core but a very thin radiation re-absorption layer (Figure 6-13 (b) and Figure 6-14 (b)). For the air arc at the same currents, the radial temperature profiles have a very broad radiation re-absorption region but no distinctive core structure (Figure 6-13 (a) and Figure 6-14 (a)). The reasons for such a very diffusive radial temperature profile

of the air arc is due to the effects of ρC_P for air having two peaks at the temperature of 7,000 K and 4,000 K (Figure 6-15), which has been discussed in detail in the Chapters 4 and 5. For the SF_6 arc, ρC_P has no peak for temperature above 4,000 K and is also much smaller than that for air in the temperature range of 4,000 K to 17,000 K. In addition, results show that the SF_6 arc attains lower gas velocity (Figure 6-7 (b) and Figure 6-8 (b)), i.e. lower axial velocity together with the radial gradient of axial velocity than the air arc, for which eddy kinematic viscosity for the SF_6 arc is generally smaller than that for the air arc during current ramp (Figure 6-16 and Figure 6-17). Consequently, turbulent thermal conductivity for the SF_6 arc is smaller than that for the air arc especially in the radiation re-absorption layer where no peak is available for turbulent thermal conductivity for the SF_6 arc (Figure 6-18 and Figure 6-19). It is also noted that ρC_P for SF_6 has a peak, resulting in a peak in turbulent thermal conductivity for SF_6 at temperature just below 4,000 K (Figure 6-18 and Figure 6-19), which forces a sharp drop in temperature above 4,000 K and a gentle temperature tail below 4,000 K. Such behaviour of ρC_P for SF_6 results in a very constricted radial temperature profile in the radiation re-absorption layer for the SF_6 arc (Figure 6-13 (b) and Figure 6-14 (b)).

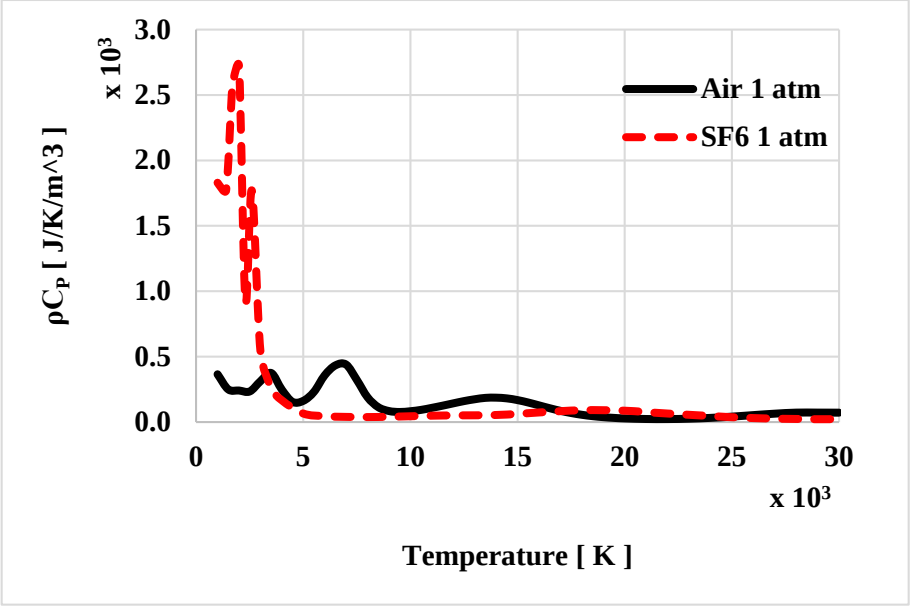

Figure 6-15 Comparison of the material property, ρC_P, between air and SF_6.

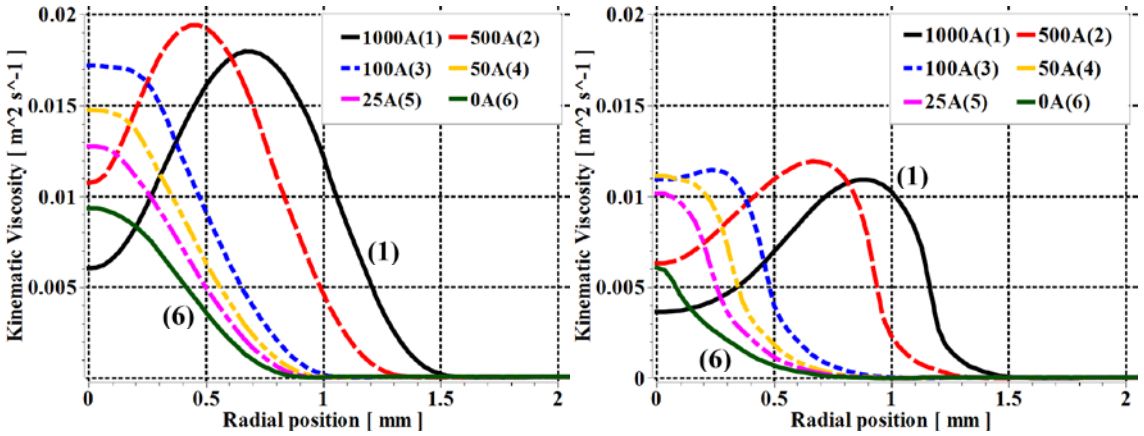

(a) (b)

Figure 6-16 Eddy kinematic viscosity of air and SF_6 at the nozzle throat, Z = 8 mm, at a few instants before current zero for P_0=37.5 atm and di/dt=13.5 A/µs. (a) Air and (b) SF_6.

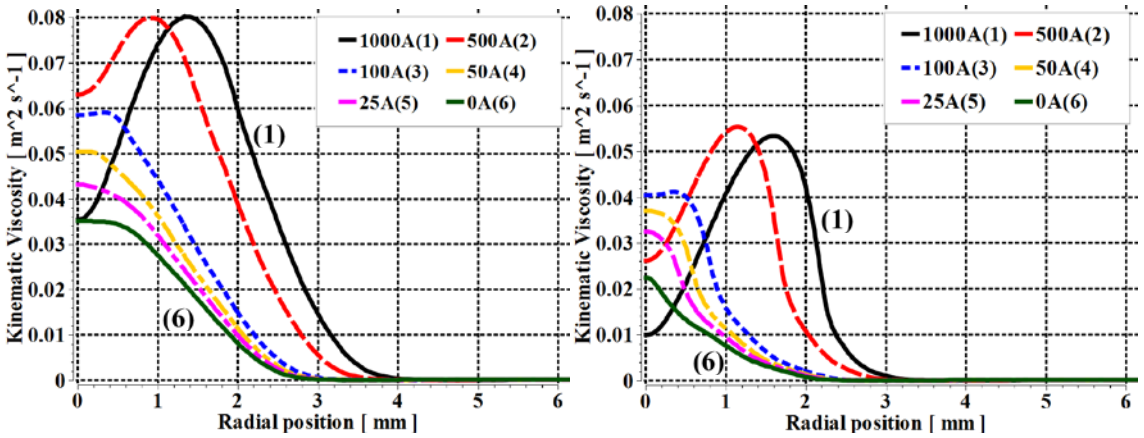

(a) (b)

Figure 6-17 Eddy kinematic viscosity of air and SF_6 at Z = 25 mm at a few instants before current zero for P_0=37.5 atm and di/dt=13.5 A/µs. (a) Air and (b) SF_6.

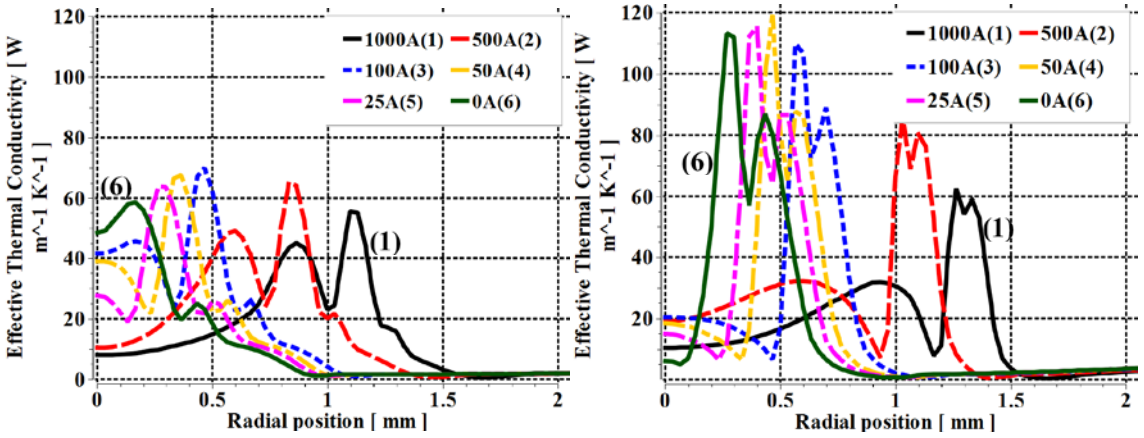

Figure 6-18 Turbulent thermal conductivity of air and SF_6 at the nozzle throat, Z = 8 mm, at a few instants before current zero for P_0=37.5 atm and di/dt=13.5 A/μs. (a) Air and (b) SF_6.

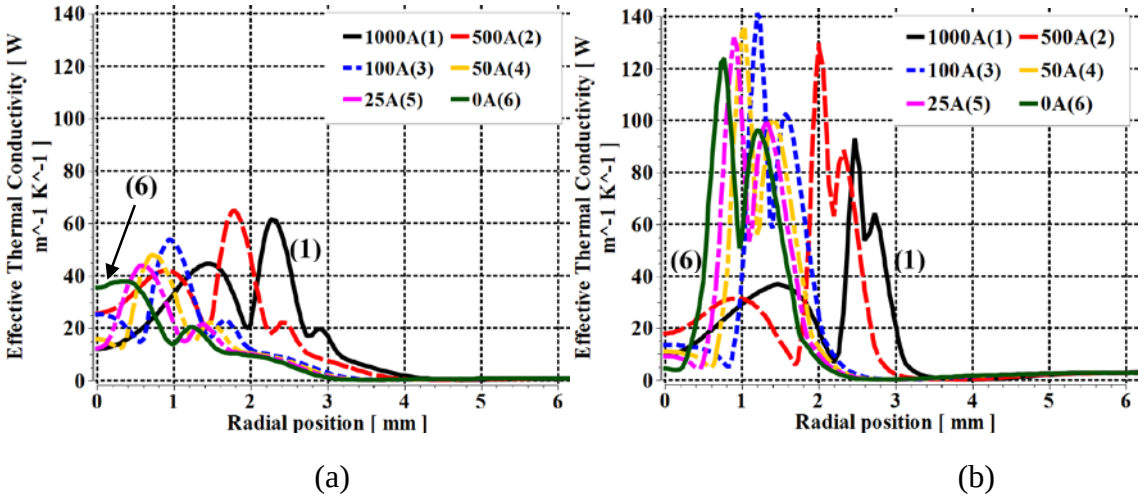

Figure 6-19 Turbulent thermal conductivity of air and SF_6 at Z = 25 mm at a few instants before current zero for P_0=37.5 atm and di/dt=13.5 A/μs. (a) Air and (b) SF_6.

Energy balance calculation for the SF_6 arc shows that, for currents down to 500 A, radiation loss is the dominant energy transport mechanism (Table 6-1), which gives rise to very uniform temperature profile inside the arc core for the SF_6 arc. It is found that 80% of the current is carried by the arc core, and therefore radiation loss is the dominant energy transport mechanism that determines the arc characteristics for the SF_6 arc at current down to 500 A. At the electric boundary (Table 6-2), axial thermal convection is the most

important energy transport mechanism and turbulent thermal conduction plays a secondary but still significant role. However, for currents down to 500 A, turbulent thermal conduction does not have much effect on the arc voltage, since the radiation re-absorption layer is very thin for the SF_6 arc.

For the air arc, radiation is also dominant inside the arc core (Table 6-1), which renders a quite uniform temperature distribution inside the arc core, at currents down to 500 A. As previously mentioned, there is no distinctive core structure for the air arc and the arc core is of course very thin in comparison with the radiation re-absorption region. It is found that less than 60% of the current is carried inside the core for the air arc, and therefore the arc voltage is also determined by the radiation re-absorption layer. Inside the radiation re-absorption layer, turbulent thermal conduction is responsible for the diffusive radial temperature profile due to two peaks of ρC_P and the resulting turbulent thermal conduction. However, at the electric boundary, turbulent thermal conduction is not important (Table 6-2) while axial thermal convection is the dominant energy transport mechanism. Turbulent thermal conduction being less important at the electric boundary is due to the diffusive profile of radiation re-absorption layer with very mild temperature gradient caused by the peaks in turbulent thermal conductivity due to ρC_P. As discussed in Chapter 5, the dominance of axial thermal convection is mainly due to the very broad temperature profile of the air arc. In contrast with the air arc, for the SF_6 arc, turbulence thermal conduction is significant while the axial thermal convection is not as significant as that for the air arc at the electric boundary. One reason for the stronger axial thermal convection for the air arc is of course due to much broader radial temperature profile of the air arc in comparison with that of the SF_6 arc, due to the effect of ρC_P. Another reason is that, air has larger ρh than SF_6 within the temperature range of 7,000 K to 20,000 K (Figure 6-20), and the air arc attains higher velocity than the SF_6 arc. These factors are also responsible for stronger axial thermal convection of the air arc in comparison with that of the SF_6 arc at the electric boundary. It will be shown later that, for the air arc, axial thermal convection is always dominant, which is therefore the actual energy transport mechanism controlling the arc's temperature decay at the vicinity of current zero. For the

air arc, turbulent thermal conduction will never become the most important even around current zero. For the SF_6 arc, turbulent thermal conduction will become the dominant energy transport mechanism in the vicinity of current zero, which controls the arc's temperature decay as well as arc radius.

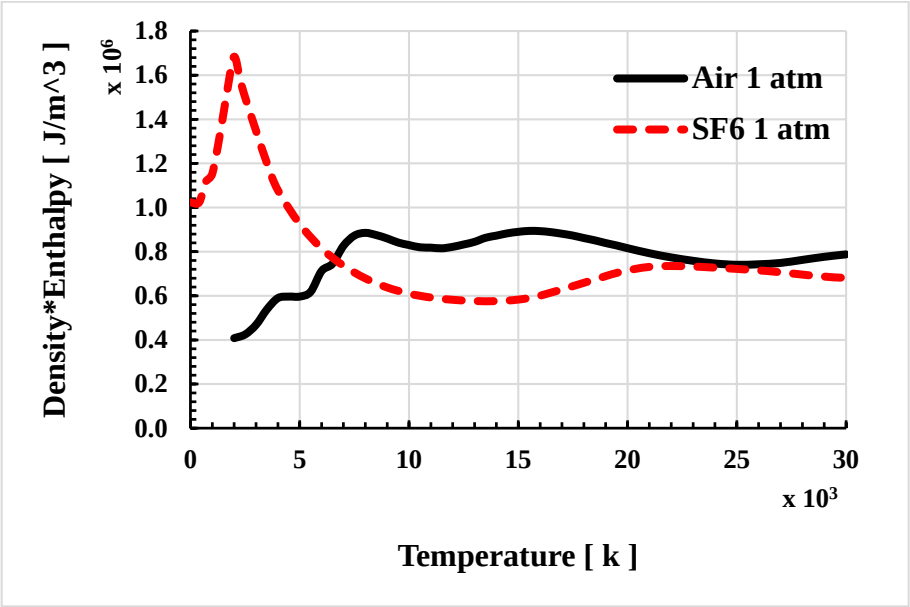

Figure 6-20 Comparison of the material property, ρh, between air and SF_6.

Table 6-1 Electric power input associated with various energy transport processes at the core boundary for the arc section before the shock at a few instants before current zero. P_0=37.5 atm and di/dt=13.5 A/μs. The mathmatic expressions of varies energy tranport are given in Chapter 4 and 5.

Gas	Power input	Radiation loss	Radial thermal conduction	Axial convection	Radial convection	Pressure work	Rate of change of energy storage
1 kA DC							
Air	**3.20E+05**	**-80.6%**	**-12.9%**	**-1.0%**	**1.3%**	**-5.7%**	**0.0%**
SF_6	**3.54E+05**	**-69.2%**	**-12.4%**	**-9.9%**	**-5.5%**	**-7.6%**	**0.0%**
500 A							
Air	**1.48E+05**	**-72.3%**	**-27.5%**	**3.4%**	**1.9%**	**-4.5%**	**1.9%**
SF_6	**1.87E+05**	**-62.8%**	**-19.3%**	**-19.0%**	**-3.3%**	**-6.3%**	**9.2%**
100 A							
Air	**3.62E+04**	**-27.3%**	**-83.1%**	**7.3%**	**-2.5%**	**-2.1%**	**10.6%**
SF_6	**4.63E+04**	**-61.1%**	**-39.8%**	**-3.4%**	**-5.1%**	**-3.1%**	**15.3%**
50 A							
Air	**2.09E+04**	**-14.3%**	**-89.5%**	**-12.5%**	**-9.2%**	**-4.7%**	**32.2%**
SF_6	**2.44E+04**	**-50.2%**	**-63.5%**	**-2.2%**	**-4.4%**	**-1.9%**	**24.9%**
25 A							
Air	**1.04E+04**	**-7.4%**	**-145.6%**	**7.1%**	**-14.1%**	**-1.3%**	**65.7%**
SF_6	**1.39E+04**	**-37.2%**	**-79.7%**	**-1.8%**	**-6.4%**	**-1.1%**	**29.0%**

Table 6-2 Electric power input associated with various energy transport processes at the electric boundary for the arc section before the shock at a few instants before current zero. P_0=37.5 atm and di/dt=13.5 A/μs. The mathmatic expressions of various energy tranport are given in Chapter 4 and 5. At current zero, the denominator is replaced with rate of change of energy storage term since the power input is equal to zero.

Gas	Power input	Radiation loss	Radial thermal conduction	Axial convection	Radial convection	Pressure work	Rate of change of energy storage
1 kA DC							
Air	5.22E+05	-19.7%	-9.6%	-91.7%	29.7%	-7.5%	0.0%
SF_6	4.23E+05	-11.7%	-27.4%	-56.7%	2.7%	-7.6%	0.0%
500 A							
Air	2.65E+05	-16.2%	-16.2%	-102.8%	26.5%	-7.7%	18.6%
SF_6	2.17E+05	-11.1%	-38.7%	-54.4%	-0.2%	-6.5%	13.9%
100 A							
Air	6.10E+04	-6.5%	-37.7%	-137.1%	-0.1%	-9.5%	92.2%
SF_6	5.40E+04	-10.8%	-64.5%	-46.7%	-22.2%	-2.9%	46.7%
50 A							
Air	3.26E+04	-3.7%	-56.7%	-162.0%	-32.8%	-23.9%	182.0%
SF_6	2.86E+04	-8.8%	-82.5%	-37.6%	-50.0%	-1.2%	83.4%
25 A							
Air	1.77E+04	-1.7%	-91.0%	-206.2%	-85.3%	-25.2%	310.0%
SF_6	1.59E+04	-13.6%	-99.4%	-27.7%	-77.3%	0.6%	120.1%
Current zero							
Air	0.0%	0.0%	-22.7%	-43.2%	-27.8%	-4.1%	5.8E+04
SF_6	0.0%	-0.2%	-40.8%	-5.9%	-54.0%	1.5%	1.4E+04

The differences in the dominant energy transport mechanisms between the air and the SF_6 arcs determine the respective radial temperature profiles for the air and the SF_6 arcs. At currents down to 500 A, results show that the arc radii are similar for both the air and the SF_6 arcs. Due to very thin radiation re-absorption region, SF_6 arc has a much broader arc core region than the air arc. Such radial temperature profile gives a lower arc voltage of the SF_6 arc as compared with the air arc for currents down to 500 A (Figure 6-12).

When the current further decays towards zero, the arc temperature is reduced because of reduced Ohmic input. Therefore, for both the air and the SF_6 arcs, the radiation loss becomes less important. Computational results show that, for the air arc, the qualitative features of the radial temperature profiles are similar to those at currents of 500 A and above (Figure 6-13 (a) and Figure 6-14 (a)). It is however noted that, at currents below 500 A, the axis temperature drops rapidly while the arc radius shrinks at a slow rate. Energy balance calculation shows that turbulence thermal conduction gradually becomes the most significant at the core boundary (Table 6-1) which is responsible for rapid rate of decay of axis temperature. At the electric boundary, axial thermal convection is always the dominant energy loss mechanism while turbulent thermal conduction only plays a secondary role (Table 6-2). As previously discussed, the behaviour of turbulent thermal conduction is due to ρC_P. The two peaks of ρC_P for air results in the very diffusive re-absorption region and slow shrinkage of arc size. For the SF_6 arc, turbulent thermal conduction becomes the dominant energy loss mechanism although radiation is still significant for currents above 50 A (Table 6-1 and Table 6-2). At the core boundary, radiation is still significant for currents down to 50 A, although turbulent thermal conduction becomes more important. This explains the slower rate of decay of axis temperature in comparison with that of the air arc for currents above 50 A (Figure 6-21 (a) and Figure 6-22 (a)). In the last 2 μs before current zero, turbulence thermal conduction also becomes the dominant energy loss mechanism inside the arc core, for which the axial temperature drops at a very rapid rate, for the SF_6 arc (Figure 6-21 (b) and Figure 6-22 (b)). As compared with the air arc, at the electric boundary, for the SF_6 arc axial thermal convection is much less significant, which is even not important at the vicinity of current

zero (Table 6-2). This is again due to much more constricted radial temperature profile of the SF_6 arc, and also the value of ρh of SF_6 which is smaller than air together slower gas velocity attained in the SF_6 arc. Turbulence thermal conduction as a dominant energy loss mechanism gives rise to more rapid temperature decay of SF_6 arc at currents below 500 A (Figure 6-9). It is also noted that for the SF_6 arc, when the current is below 500 A, at the electric boundary radial thermal convection starts to act as a temperature cooling mechanism (i.e. energy loss mechanism) because of the radial inflow of cold gas to maintain mass balance due to rapid temperature decay. The strong cooling effects due to combined effects of turbulent thermal conduction and radial thermal convection associated with radial inflow give rise to very rapid arc temperature decay and rapid shrinkage of the arc size for the SF_6 arc. For the air arc, energy inside the radiation re-absorption region cannot effectively be taken out due to weak turbulent thermal conduction at the electric boundary, for which the temperature decay inside the radiation re-absorption region and arc size shrinkage are slow. Therefore, radial thermal convection never becomes an energy loss mechanism until the current is around 100 A. The weaker turbulent thermal conduction and the resulting late occurrence of the radial thermal convection as a cooling mechanism as well as the dominance of axial thermal convection at the electric boundary all result in the fact that the temperature decay in the radiation re-absorption region and arc size shrinkage for the air arc are much slower than those of the SF_6 arc for currents below 500 A. Therefore, the voltage of the SF_6 arc increases in a more rapid rate for currents below 500 A which becomes higher than that of the air arc in the last 2 μs before current zero.

6.2.2.3. Arc Conditions at the Vicinity of Current Zero

Thermal interruption of the nozzle arc is determined by the arc temperature in the vicinity of current zero. As previously discussed, for the air arc, turbulent thermal conduction becomes the most important at the core boundary for which the axis temperature drops quickly a few microseconds before current zero, whereas at the electric boundary, turbulent thermal conduction is not important which cannot effectively take the energy out of the arc's electrically conducting core due to the effects of ρC_P as discussed in

Chapters 4 and 5. At the electric boundary axial thermal convection is the dominant energy transport mechanism which controls the arc size for the air arc. For the SF_6 arc, turbulence thermal conduction is the dominant energy transport mechanism at the vicinity of current zero. This also gives rise to the fact that, for the SF_6 arc, radial thermal conduction associated with radial inflow becomes the energy loss mechanism in an instant (the instant of 500 A) much earlier than that of the air arc (the instant of 100 A). At the vicinity of current zero, the combined effects of turbulent thermal conduction and radial thermal convection control the arc size for the SF_6 arc. All these reasons can explain the results of Figure 6-21 and Figure 6-22 showing much faster rates of decay of axis temperature and arc radius for the SF_6 arc than those for the air arc in the last 2 μs before current zero.

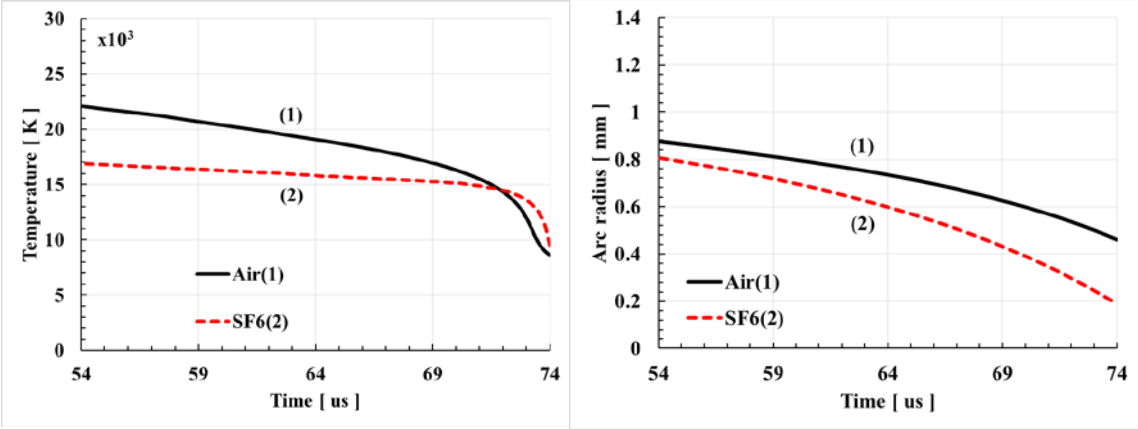

(a) (b)

Figure 6-21 The time variation of axis temperature and arc radius at the nozzle throat, Z=8 mm, for the air and the SF6 arc at P_0=37.5 atm and di/dt=13.5 A/μs. (a) Axis temperature and (b) Arc radius.

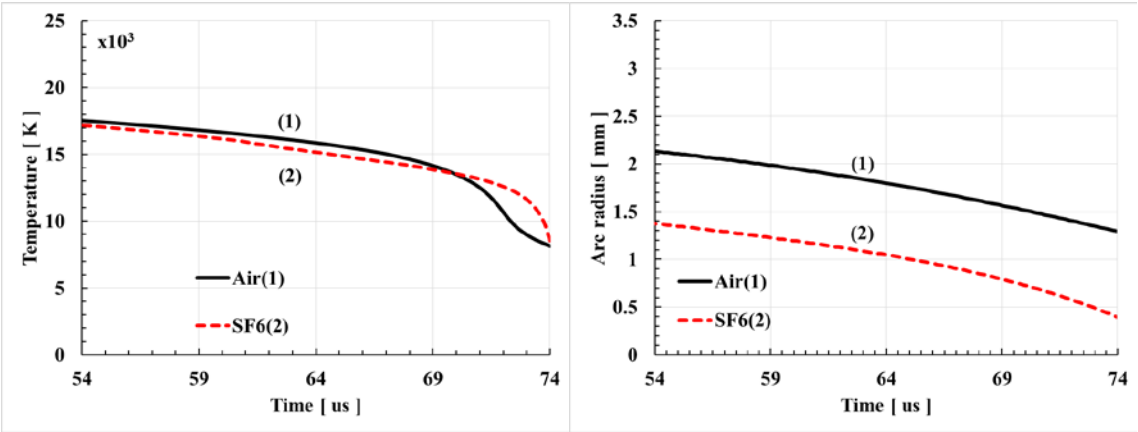

(a) (b)

Figure 6-22 The time variation of axis temperature and arc radius at Z=25 mm for the air and the SF6 arc at P_0=37.5 atm and di/dt=13.5 A/μs. (a) Axis temperature and (b) Arc radius.

Axis temperature and arc radius at current zero are given in Figure 6-21 and Figure 6-22. Thermal interruption capability depends on the rates of decay of temperature and arc radius. Figure 6-21 (a) and Figure 6-22 (a) show that, for the air arc, there are two temperature decay rates with an approximate demarcation at 3 μs before current zero. Since axial thermal convection is the most important energy transport mechanism, the arc radius is controlled by convection for the air arc. At current zero, the characteristic time for the time variation of arc radius (the absolute value of [R/(dr/dt)]) is in the order of 10-20 μs for the air arc (Table 6-3). The characteristic time for axis temperature variation is about 50 μs at an instant current of 140 A (approximately 10 μs before current zero). In the last 3 μs before current zero this characteristic time is reduced to 2 μs. For the SF_6 arc, turbulent thermal conduction controls the variations of temperature and arc radius in the vicinity of current zero. The characteristic times for the variations of arc radius and axis temperature for the SF_6 arc are given in Table 6-3. It has been shown that the characteristic time of arc radius variation for the SF_6 arc is only 0.25 of that of the air arc. As regards the characteristic time for the axis temperature variation, for the SF_6 arc it is longer than that for the air arc at 10 μs before current zero. The reason for this is indicated by the energy balance at the core boundary (Table 6-1) showing that, for the air arc, turbulent thermal conduction is dominant inside the arc core, while for the SF_6 arc, radiation is still

significant, for currents above 100 A. For currents below 50 A, energy balance at the core boundary shows that, for both the air and the SF_6 arc, turbulent thermal conduction is dominant. In the last 2 μs before current zero, axis temperature decay for the SF_6 arc is much faster than that for the air arc as indicated by Table 6-3.

Table 6-3 Characteristic time for the variations of arc radius and axis temperature at two typical axial positions for both the air and the SF_6 arcs at P_0=37.5 atm and di/dt=13.5 A/μs.

[R/(dR/dt)]			
		Z=8 mm	Z=25 mm
Current zero	Air	11.2 μs	17.8 μs
	SF6	3.2 μs	4 μs
[T/(dT/dt)]			
		Z=8 mm	Z=25 mm
10 μs before current zero	Air	57.6 μs	70.4 μs
	SF6	125 μs	60 μs
Current zero	Air	4.9 μs	11.4 μs
	SF6	1 μs	1.5 μs

6.2.3. Arc Behaviour after Current Zero

The RRRV of nozzle arcs in both air and SF_6 have been determined by applying a linearly increasing voltage at a given rate of rise (dV/dt) after current zero. Typical results of post-arc currents for the air and the SF_6 arcs at P_0=37.5 atm and di/dt=13.5 A/μs are given in Figure 6-23. The computed values of RRRV for the air and the SF_6 arcs are respectively 0.85 kV/μs and 9.85 kV/μs at P_0=37.5 atm and di/dt=13.5 A/μs.

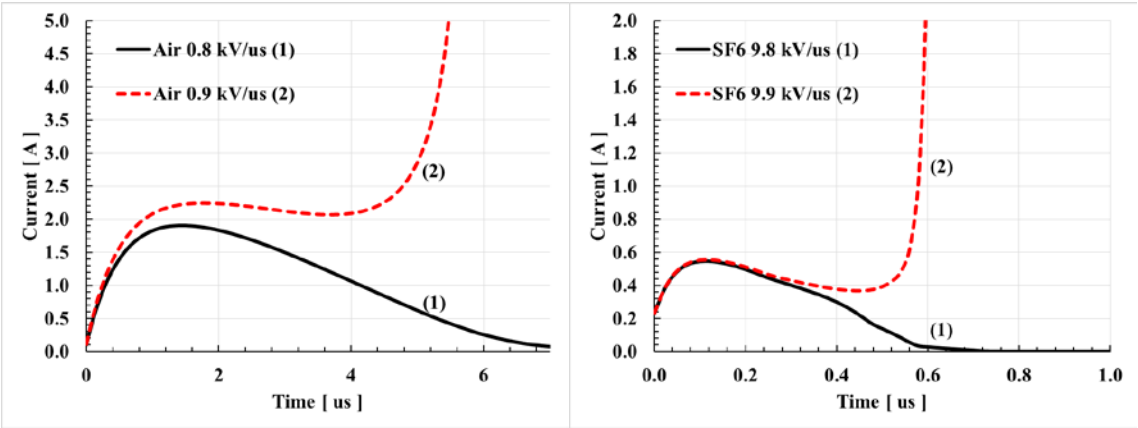

(a) (b)

Figure 6-23 Post-arc current for the air and the SF_6 arc for P_0=37.5 atm and di/dt=13.5 A/μs.

Computed axis temperature and electric field distributions at different instants after current zero are given in Figure 6-24 and Figure 6-25 for the air arc, and Figure 6-26 and Figure 6-27 for the SF_6 arc. For the air arc, when the arc is thermally extinguished, axis temperature decays within 6 μs to about 5,000 K after current zero in the arc section before the shock. In the region after the shock the arc temperature hardly changes within such a short period due to the stagnant flow feature as previously discussed, for which the recovery voltage taken by the arc section in this region is negligible. According to Figure 6-24 and Figure 6-25 the recovery voltage is taken up by the arc section before the shock. For this arc section, during thermal recovery the electric field increases with time due to temperature decay and the shrinkage of arc size caused by radial conduction and axial convection cooling effects. When arc is reignited (Figure 6-25) the temperature rises rapidly first upstream electrode while the temperature in the rest part of the arc still decreases due to thermal inertia. The peak of electrical field moves downstream, which subsequently arrests the temperature decay and eventually, the temperature and the current increase rapidly.

For the SF_6, qualitative features regarding the variations of axis temperature and electric field after current zero are similar to those for the air arc, but these results show that the

characteristic time for the thermal recovery and/or reignition is an order of magnitude smaller than that of the air arc, indicating a much faster thermal recovery for SF_6. For SF_6 arc, turbulent thermal conduction is the dominant energy loss mechanism during thermal recovery process.

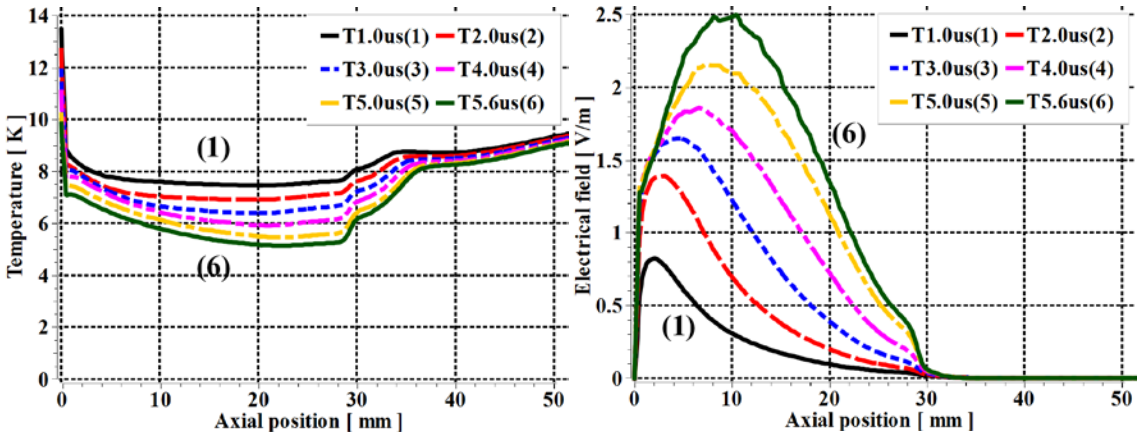

(a) (b)

Figure 6-24 Axis temperature (a) and electrical field (b) computed for air when arc is extinguished. dV/dt=0.8 kV/μs and P_0= 37.5 atm.

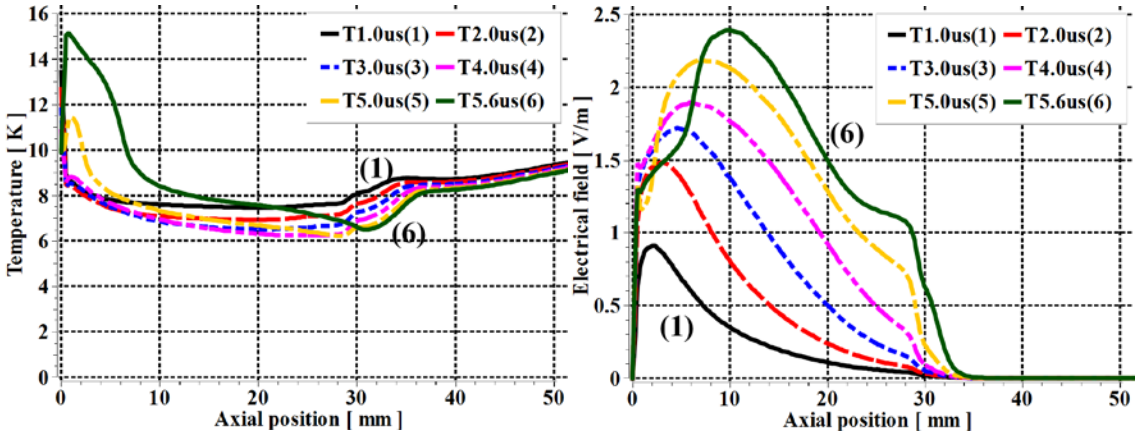

(a) (b)

Figure 6-25 Axis temperature (a) and electrical field (b) for air when arc is reignited. dV/dt=0.9 kV/μs and P_0= 37.5 atm.

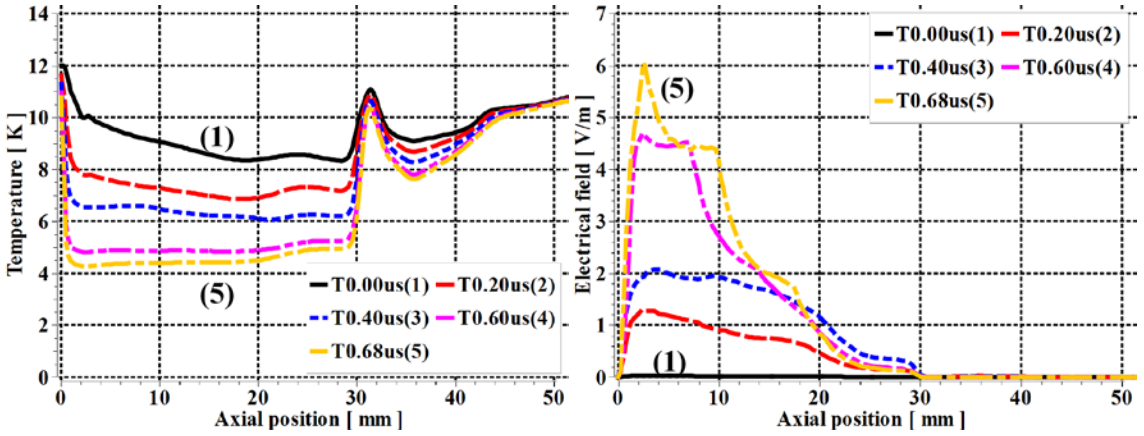

(a) (b)

Figure 6-26 Axis temperature (a) and electrical field (b) computed for air when arc is extinguished. dV/dt=9.8 kV/μs and P_0= 37.5 atm.

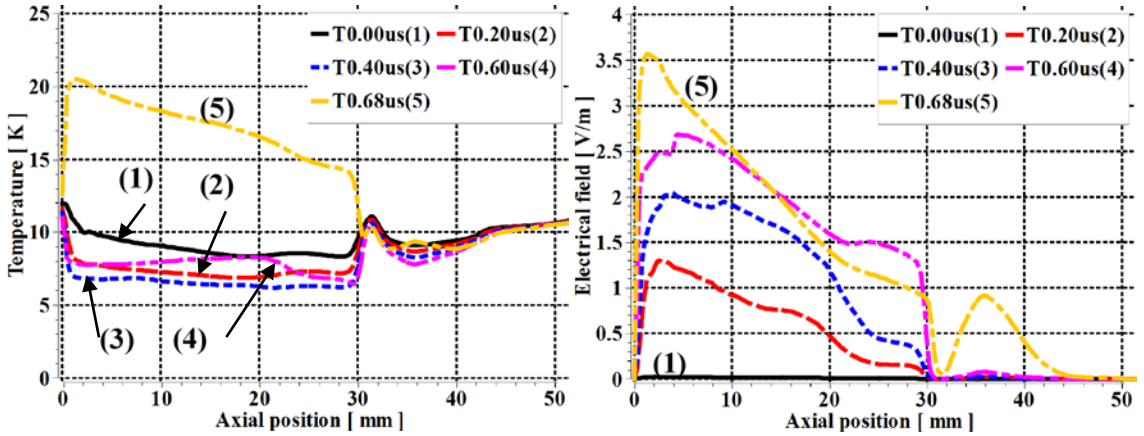

(a) (b)

Figure 6-27 Axis temperature (a) and electrical field (b) for air when arc is reignited. dV/dt=9.9 kV/μs and P_0= 37.5 atm.

For both the air and the SF_6 arcs, the computed RRRV as a function of P_0 at di/dt=13.5 A/us are plotted in Figure 6-28 together with experimental results for comparison. By applying MKE, the computed RRRV generally agrees well with the measured RRRV for both the air and the SF_6 arcs. Due to the difference in energy transport processes and the

material properties responsible to these processes, RRRV for SF_6 is an order of magnitude higher than that of air.

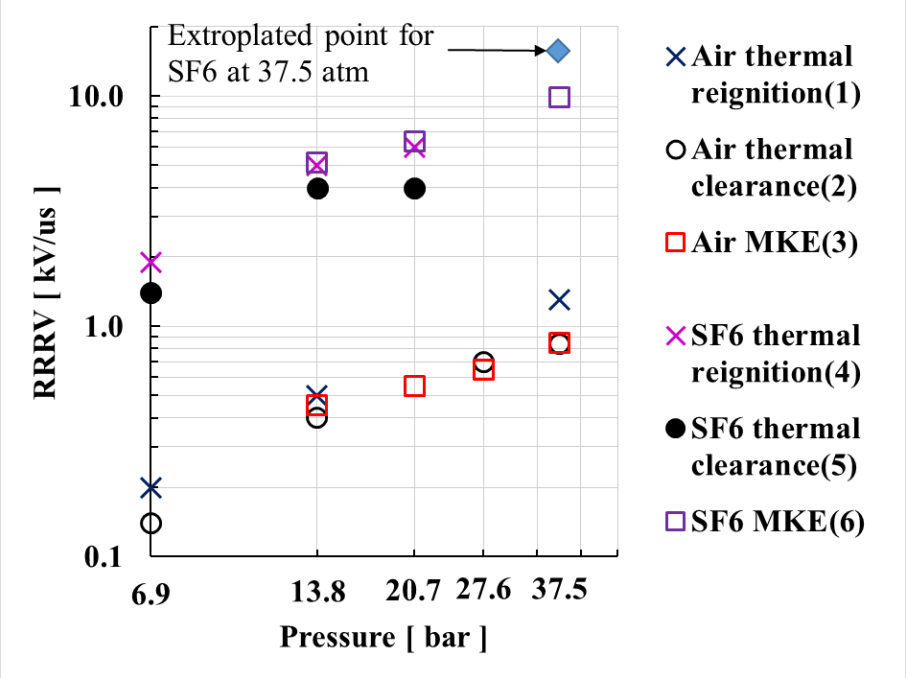

Figure 6-28 Computed RRRV for the air and the SF6 arcs together with measured RRRV for comparison.

6.3. **Summary**

A detailed comparative study on the behaviour of the switching arcs in air and SF_6 has been carried out based on the experimental conditions of Frind and Rich [66]. The effects of turbulence are computed by using MKE with one turbulence parameter, $C_{1\varepsilon}$, to be 1.65 for the air arc and 1.72 for the SF_6 arc, both of which are found by matching the predicted RRRV with the measured RRRV at P_0=37.5 atm and di/dt=13.5 A/us.

Computational results show that the differences in the electrical behaviour of the air and the SF_6 are due to differences in their respective radial temperature profiles and the variations of these profiles (i.e. rates of decay of temperature and the arc radius) with

current decay. The features of radial temperature profiles of an arc are of course determined by the dominant energy transport processes and, more importantly, the material properties of the arcing gas (i.e. air and SF_6) associated with these processes, i.e. ρC_P and ρh. ρC_P for air has two peaks at temperatures of 7,000 K and 4,000 K which gives rise to very diffusive radial temperature profiles with broad radiation re-absorption region but without a distinctive arc core. This in turn results in the dominance of axial thermal convection at the electric boundary which actually the arc radius, while turbulent thermal conduction is not important at the electric boundary. The arc radius for the air arc therefore shrinks in a slow rate. ρC_P for SF_6 does not have peaks for temperatures above 4,000 K but there is a peak at temperature just below 4,000 K, which results in very constricted radial temperature profile for the SF_6 arc. Such constricted radial temperature profile results in the dominance of turbulent thermal conduction at the electric boundary which brings in strong cooling effects, thus causing rapid shrinkage of the arc radius and temperature decay for the SF_6 arc at the vicinity of current zero. The more rapid shrinkage of the arc radius and temperature decay at the vicinity of current zero result in stronger thermal interruption capability of the nozzle arc in SF_6 than that in air. Apart from the effects of ρC_P, another material property, ρh, also affects thermal convection. Results show that the dominance of axial thermal convection for the air arc is due to ρh and gas velocity, both of which are higher than those for the SF_6 arc.

Through the present investigation, a general guidance in the search of a gas replacement for SF_6 as a switching medium may be established which are given below:

(a) ρC_P of the gas should not have peaks above 4,000 K at which electric conductivity due to thermal ionization is negligible. However, a peak in ρC_P is desirable just below 4,000 K to force sharp drop in temperature above 4,000 K and a gentle temperature tail below 4,000 K.

(b) The gas should have large values of ρh, which can favour the increase of the thermal convection cooling effects.

Chapter 7. Conclusion and Future Work

7.1. Conclusion

This thesis is solely concerned with the physical processes occurring in an arc inside a high voltage circuit breaker. Modern high voltage circuit breakers mostly use SF_6 which is however a well known greenhouse gas, thus resulting in much interest in searching for the more environmentally friendly substitutes. The search for a replacement gas to SF_6 is however hindered by a lack of knowledge as regards the gas property which determines the arc interruption capability. Air was widely used as the switching medium in high voltage circuit breakers before the introduction of SF_6 [119], yet our understanding of the physical processes occurring in air switching arcs at the time was limited, due to the limitation of computer power and a lack of experimental results under well specified discharge conditions. Since air is an important industrial gas and can often be mixed with other gases in the pursuit of finding a replacement gas for SF_6, there have now been renewed interests in using air as a switching medium. With the advancement of computer technology and our understanding of arc physics, it is now possible to carry out more rigorous theoretical modelling of air switching arcs, which forms the subject matter of this thesis.

This thesis aims at establishing a satisfactory arc model to predict switching arcs in air under DC and transient conditions. The conservation equations of a switching arc in LTE are similar to those of an ordinary fluid but modified to include the Lorentz force in momentum conservation equation and Ohmic input and radiation transport in the energy conservation equation. For SF_6 arcs, there is now consensus that the arc is in turbulent state. The modelling of turbulent arcs is based on Reynolds time average of the arc conservation equations which gives the time averaged conservation equations. The closure of these equations requires additional relations known as the turbulence models. Turbulence models are always problem specific and need to be verified by experimental results.

Much work has been done on the modelling of turbulent SF_6 arcs, which confirms the importance of turbulence in determining the SF_6 arc behaviour. However, there is very little work on air arcs in gas flow, and thus it is not known if turbulence is important for such arcs in air. This prompts a detail investigation on the behaviour of air switching arcs especially the role of turbulence. Computations are therefore carried out using the arc models based on both laminar flow (i.e. the laminar flow model, LAM) and turbulent flow with appropriate turbulence models. Of the turbulence models used in switching arc applications, the Prandtl mixing length model (PML) has been shown to be most successful, and the standard k-epsilon model is almost the industrial standard for the modelling of turbulent shear flow. We therefore apply these two turbulence models in our investigation. For the work of this thesis, computations are all performed using the parallel processing facilities of ANSYS Fluent.

Verification of arc models requires reproducible experimental results covering a wide range of discharge conditions. Extensive test results in the form of DC arc voltage [41] and in the form of RRRV [66] have been reported for an air arc in a supersonic nozzle interrupter with fixed upstream and downstream pressures. Such a two-pressure system eliminates pressure transients caused by reflections within a circuit breaker which inevitably affects the arc in the nozzle interrupter. Thus, the test results given in [41, 66] are well suited for the verifications of arc models for air. Through the comparison between experimental results and the results predicted by the laminar arc model the role of turbulence in air arcs can be determined.

The characteristics of an air arc under direct currents in the nozzle of Fang et al [41] are investigated in the current range from 3 kA to 250 A and at three stagnation pressures. Arc voltage predicted by the LAM is considerably lower than the measured arc voltage which confirms the importance of turbulence in determining the air arc behaviour. Of the two turbulence models applied, PML can give satisfactory predictions on the arc voltage with a single optimized value of turbulence parameter, while the standard k-epsilon model grossly over predicts the arc voltage. A modified k-epsilon model (MKE) is then

introduced by adjusting one of its 5 turbulence parameters, $C_{1\varepsilon}$, by matching the predicted arc voltage with the corresponding measurement at 1 kA and 10 bar. $C_{1\varepsilon}$ has been found to be 1.62. Overall, MKE is found to give the best agreement with experimentally measured arc voltage. The predicted voltage-current characteristics of the air arc show a flat part at currents above 2 kA and a rising arc voltage for currents below 2 kA. On the flat part of V-I characteristics, radiation loss is the dominant energy transport mechanism at the arc core boundary, whilst at the electric boundary axial thermal transport and turbulence enhanced thermal conduction nearly account for all the power input with axial thermal convection the most important mechanism. For currents below 2 kA, turbulence enhanced thermal conduction gradually becomes the dominant energy transport process at the core boundary. At the electric boundary thermal conduction and axial thermal convection balance the power input with thermal conduction becomes the most important at currents of 250 A and below.

A distinct feature of air arcs is the shape of its radial temperature profile as shown by the computational results. For air arcs under turbulent flow there is no distinctive high temperature core. Radial temperature is very broad with the thickness of the radiation re-absorption bigger than the core. Such broad radial temperature profile is due to the material property, ρC_P, which produces the peaks in turbulent thermal conductivity at 4,000 K and 7,000 K due to respectively the dissociation of oxygen molecules and nitrogen molecules. Such peaks will have detrimental effects on arc thermal recovery.

Computational investigation on the current zero period for an air arc has been carried out based on the experimental conditions of Frind and Rich [66]. A detailed numerical study on the transient air arc behaviour and a comparative study of different flow models have been conducted for P_0=37.5 atm and di/dt=13.5 A/μs. The arc features and the dominant energy transport mechanisms are similar to the DC air arcs in the nozzle of Fang et al [41]. Computational results of RRRV have been compared with the measurements of Frind and Rich [66]. It has been shown that MKE with $C_{1\varepsilon}$=1.65 can give satisfactory predictions of RRRV for di/dt=13.5 A/us at different stagnation pressures. For a given P_0 with different

values of di/dt, there appears to have certain relation between the turbulence parameters and di/dt, since a single chosen value of a particular turbulence parameter cannot match all the experimental results for the range of values of di/dt studied. PML with c=0.03 chosen by matching computed RRRV with that measured at 27 A/μs and P_0= 37.5 atm fails to make a single satisfactory prediction of RRRV. Numerical difficulties encountered by PML in the region behind the shock prevent the application of PML to air arcs with shocks. RRRV predicted by LAM is much below that measured. The standard k-epsilon model gives satisfactory agreement with experiment at di/dt=6 A/μs and P_0=37.5 atm but over predicts RRRV for other discharge conditions.

The pressure dependence of the measured RRRV and those predicted by MKE are only slightly stronger than the square root of P_0, i.e. similar to the pressure dependence of arc voltages for arcs in quasi-steady state. This is in contrast with the SF_6 arc, the RRRV of which shows very strong dependence on stagnation pressure. The main reason for such weak pressure dependence is due to the very broad radial temperature profile which results in axial convection being the most important energy transport process up to the electrical boundary. Turbulence enhanced thermal conduction never becomes the most important energy loss mechanism at the electric boundary due to the effects of peaks of turbulent thermal conductivity produced by the material property, ρC_P. This results in a slow rate of shrinkage of arc radius. Arc resistance only shows a pressure dependence to a power of 0.6 at current zero.

MKE can give good predictions of the arc voltage under DC conditions and of RRRV at a fixed di/dt for different stagnation pressures. It appears that the value of the turbulence parameter, $C_{1\varepsilon}$, depends on di/dt. Such a dependence needs to be established in future.

It is not known what material properties determine the characteristics of arcs in different gases especially if turbulence is important. The identification of such material properties is important in the search of a replacement switching gas for SF_6 as this is urgently required for environment protection. A comparative study of air and SF_6 arcs under

identical test conditions is therefore conducted, which reveals that ρC_P is the material property mainly responsible for the vastly different interruption capabilities of these two gases. The two peaks of ρC_P for air at 7,000 K and 4,000 K result in very diffusive radial temperature profile and very slow rate of shrink of arc size in the vicinity of current zero. Computational results show that the radial extent of the arc's thermal influence region for air arcs is much bigger than SF_6 under similar discharge conditions. For SF6, ρC_P does not have peaks above 4,000 K at which the electric conductivity due to thermal ionization is negligible, but there is a peak just below 4,000 K. This forces a sharp drop in temperature above 4,000 K and a gentle temperature tail below 4,000 K, thus ensuring a core formation and a small arc size, and also much faster rate of shrinkage of arc size at the vicinity of current zero, for the SF_6 arc.

7.2. **Proposed Future Work**

A satisfactory switching arc model is the key to achieve predictive design of high voltage circuit breakers. The difficulty in achieving predictive design lies with a lack of reliable test data for the verification of computer simulated results and with the deficiencies in the modelling of the effects of turbulence on switching arc behaviour. Therefore, much work still needs to be considered in future on both the modelling side and the experiments. The work proposed below is for immediate future.

7.2.1. **Theoretical Work on Turbulence Modelling**

Although it is commonly recognized that the physics of turbulence is contained within the conservation equations for arcs, direct numerical solution of arc conservation equations is neither practical in terms of the computational cost nor is necessary as the majority of engineering design only requires the statistical information about a system. That means in the foreseeable future that theoretical investigation of turbulent switching arcs will be based on statistical treatment (e.g. Reynolds time average) to conservation equations, which gives rise to the so-called closure problem, i.e. making the number of equations equal to the number of unknowns. The closure of the equations involves making

assumptions which results in the introduction of parameters (commonly known as turbulence parameters) the values cannot be determined by a consideration of basic physics. These turbulence parameters are optimised for a class of flow problems. Thus, turbulence models are application specific. The performance of a turbulence model is judged by the range of applicability of the chosen values of the turbulence parameters. Ideally, the values of the turbulence parameters can be optimised with the least experimental effort.

MKE has limited success in predicting the air switching arc behaviour during current zero period. The value of $C_{1\varepsilon}$ should be dependent on di/dt. Such dependence should take place only after the breakdown of quasi-steady state. Much work in this area remains to be done.

The dependence of the value of $C_{1\varepsilon}$ on di/dt implies that the size and characteristic time of the dominant eddy for enhanced momentum and energy transfer in a turbulent air arc change with di/dt. This is the influence of time varying temperature field on the flow produced by the varying electrical power input associated with di/dt. At present the characteristic time of turbulent temperature fluctuation is assumed to be the same as turbulent kinetic energy by assuming unity turbulent Prandtl number. The rate of decay of arc temperature depends on di/dt especially in the time duration of a few microseconds before current zero. It is therefore highly desirable to introduce an equation which can describe the characteristic time for turbulent temperature variation. In the arc context, temperature variation also results in density variation, which has not be considered in the turbulence models used in this thesis.

A fruitful approach to the problem indicated above is to use the mass averaged arc conservation equations in LTE, which has been applied to modelling of turbulent combustion systems [120, 121]. It is therefore proposed to use Favre average to derive the mass averaged conservation equations, thus taking care of density fluctuation due to that of temperature and compressible effects. Characteristic time for temperature variation is

determined by the introduction of two additional equations, the temperature variance equation and the dissipation rate of temperature variance. The turbulent kinetic energy equation and its dissipation rate equation of the k-epsilon model are included, which enable eddy viscosity to be calculated. Gradient transport will be used to link the corresponding unknown turbulent fluxes involving the correlation of the time or mass averaged product of two fluctuating quantities [121]. The comparison of the predicted temperature with experimental results requires the conversion of mass averaged temperature to time averaged temperature, which can be done by adopting of Lee [122] using a probability density distribution function.

In addition to arc modelling it is proposed to look for potential replacement for SF_6 as an arc interruption medium by gases/ gas mixtures which are environmentally friendly with the desired temperature dependence of ρC_P. An extensive computational programme needs to be initiated to compute the thermodynamic properties of high temperature gas/ gas mixtures.

7.2.2. Experimental Work for the Nozzle Arcs Burning in Different Gases

The availability of reliable test data under a wide range of discharge conditions is of critical importance in establishing a satisfactory mathematical model for turbulent switching arcs. Such experimental data is extremely scarce, especially for gases other than SF_6. In addition, the greenhouse effects of SF_6 make it highly desirable to search for replacements by other environmental friendly gases, which requires experimental work on a range of possible candidates for a replacement for SF_6.

In order to achieve reliability and reproducibility of experimental results, the experiments should always be performed under strictly controlled gas discharge conditions and one should always avoid very complicated flow behaviour caused by wave reflection taking

place in the complex structure of a circuit breaker. It is therefore suggested to use a two-pressure system.

The proposed experimental work essential to the verification of arc modelling is summarised below:

(a) Perform arc experiments in supersonic nozzle with fixed pressures at the nozzle inlet and exit under DC arc conditions for air, SF6 and other potential gases/gas mixtures. Establish, if possible, the on-set conditions for arc instability. For specified DC current measure arc voltage and temperature. The pressure range should cover the generation of shock within the nozzle.

(b) Repeat the same experiments for the current zero period as in (a) but with the time resolved measurements for arc voltage, post arc current and arc temperature covering a range of di/dt relevant to circuit breakers. This includes the measurement of RRRV.

Appendix (List of publications)

1. Liu J, Zhang Q, Yan J D, J Zhong and Fang M T C, “Characteristics of DC Nozzle Arcs in Air”, under review (J. Phys. D).

2. Zhang Q, Liu J, Yan J D and Fang M T C,“The Modelling of an SF6 Arc in a Supersonic Nozzle: II. Current Zero Behaviour of the Nozzle Arc”, proved to publish soon (J. Phys. D).

3. Zhang Q, Liu J and Yan J D, “Flow structure near downstream electrode of a gas-blast circuit breaker”, 2014. Paper submitted to the 7th Triennial Special Issue of the IEEE Transactions on Plasma Science “Images in Plasma Science (August 2014)”, published online, DOI: 10.1109/TPS.2014.2309174.

4. Liu J, Zhang Q, Yan J D and Fang M T C,“AIR ARCS BURNING IN TURBULENT ROUND JET”, In：The XXth International Conference on Gas Discharges and Their Applications,The University of Orleans. (2014)

5. Yuan D L, Wang H Y, Liu J and Yan J D, “Prediction of Temperature Rise in MV Switching Cabinet”, IEICE Tech. Rep.,vol. 113,no. 298,EMD2013-126,pp. 213-216,Nov. 2013

References

[1] S. Sivanagaraju, Electric power transmission and distribution.

[2] R. T. Lythall, The J & P Switchgear Book, 7th Edition, Newnes-Butterworths, London, 1972.

[3] Bhel, Bharat Heavy Electricals Limited, Handbook of switchgears, 2005.

[4] M. Zuhaib, M. S. Alam and J. Ahmed, "Gas insulated substation," [Online]. Available: http://www.slideshare.net/sharique_64/gas-insulated-substation-14315261.

[5] J. Kuffel and P. Kuffel, High voltage engineering fundamentals.

[6] "UK ELECTRICITY NETWORKS," [Online]. Available: http://www.parliament.uk/documents/post/pn163.pdf.

[7] "Ultra-high-voltage electricity transmission in China," [Online]. Available: https://en.wikipedia.org/wiki/Ultra-high-voltage_electricity_transmission_in_China.

[8] C. H. Flurscheim, Power Circuit Breaker Theory and Design, IEE Power Engineering Series, Peter Peregrinus Ltd., 1982.

[9] M. Kapetanovic, “High Voltage Circuit Breakers (KEMA),” 2011.

[10] Blower, Distribution switchgear, London: William Collins Sons & Co. Ltd..

[11] Z. Liu, J. Wang, S. Xiao, Z. Wang, S. Yuan, J. Jin, H. Zhou and R. Yan, “Development of high voltage vacuum circuit breakers in China,” *IEEE Trans on Plasma Science*, vol. 35, pp. 856-65, 2007.

[12] H. J. Lingall, A. P. Strom and T. E. Browne, “An investigation of the arc quenching behaviour of sulphur hexafluoride,” *AIEE Trans.*, vol. 77, pp. 242- 246, 1953.

[13] R. E. Friedrich and R. N. Yeckley, “A new design in power circuit breaker design utlising SF6,” *AIEE Trans.,* Vols. PAS-78, pp. 695- 706, 1959.

[14] B. J. Calvino and P. Pezzi, “Interruption characteristics of an SF6 self-extinguishing circuit breaker,” *Int Conference on Large High Tension Electrical System*, 1968.

[15] G. Bernard, P. Malkin and W. Legros, “An SF6 ccircuit breaker using auto-expansion principle,” *IEEE Trans on Power Delivery*, vol. 3, pp. 1739- 1744, 1988.

[16] J. D. Yan, M. T. C. Fang and W. Hall, “The development of PC Based CAD tools for auto-expansion circuit breaker design,” *IEEE Trans on power delivery*, vol. 14, pp. 176-181, 1999.

[17] L. G. Christophorou, J. K. Olthoff and D. S. Green, “Gases for electrcial insulation and arc interruption:possible present and future alternatives to SF6,” *NIST Technical Note 1425, US Department of Commerce*, November 1997.

[18] “SF6 recycling guide, CIGRE Task Force 23.10.01,” August 1997.

[19] A. Lee and L. S. Frost, “Interruption capability of gases and gas mixtures in a puffer-type interrupter,” *IEEE Trans on Plasma Science*, vol. 8, pp. 362- 367, 1980.

[20] H. Ayrton, The electric arc, The Electrician Printing and Publishing Co (New York: D Van Nostrand), 1902.

[21] M. I. Boulos, P. Fauchais and E. Pfender, Thermal Plasmas Fundamentals and Applications, New York: Plenum Press, 1994.

[22] J. Slepian, “Extinction of an arc,” *AIEE Trans.*, vol. 47, pp. 1398-1402, 1928.

[23] A. M. Cassie, “Arc rupture and circuit severity: a new theory,” *CIGRE, Rep. 102*, pp. 1-14, 1939.

[24] T. E. Browne Jr, “A study of ac arc behaviour near current zero by means of mathematical models,” *AIEE Trans.*, vol. 67, pp. 147-153, 1948.

[25] O. Mayr, “Beitrage zur theorie des ststischen und des dynamischen lichbogens (contribution to the theory of static and dynamic arcs),” *Arch. Elect.*, vol. 37, pp. 588-608, 1943.

[26] R. P. P. Smeets and V. Kertesz, “Evaluation of high-voltage circuit breaker performance with a validated arc model,” *IEE Proc., Gener. Transm. Distrib.*, vol. 147, pp. 12-125, 2000.

[27] B. W. Swanson and R. M. Roidt, “Boundary layer analysis of an SF6 circuit breaker arc,” *IEEE Trans. Power App. Syst.*, Vols. PAS-90, pp. 1086-1093, 1971.

[28] B. W. Swanson and R. M. Roidt, “Arc cooling and short line fault interruption,” *IEEE Trans. Power App. Syst.*, Vols. PAS-90, pp. 1094-1102, 1971.

[29] B. W. Swanson and R. M. Roidt, “Some numerical solutions of the boundary layer equations,” *Proc. IEEE*, vol. 59, pp. 493-501, 1971.

[30] B. W. Swanson, R. M. Roidt and T. E. Brown, Jr., “A thermal arc model for short line fault interruption,” *ETZ-A*, vol. 93, pp. 375-380, 1972.

[31] B. W. Swanson and R. M. Roidt, “Thermal analysis of an SF6 circuit breaker arc,” *IEEE Trans. Power App. Syst.*, Vols. PAS-91, pp. 381-389, 1972.

[32] B. W. Swanson, “Nozzle arc interruption in supersonic flow,” *IEEE Trans. Power App. Syst.*, Vols. PA[41S-96, pp. 1697-1706, 1977.

[33] D. T. Topham, “The electric arc in constant pressure axial gas flow,” *J. Phys. D.*, vol. 4, pp. 1114-1125, 1971.

[34] W. Hermann and K. Ragaller, “Theoretical description of the current interruption in HV gas blast breakers,” *IEEE Trans. Power App. Syst.*, Vols. PAS-96, pp. 1546-1555, 1977.

[35] M. T. C. Fang and D. Brannen, “A Current-Zero Arc Model Based on Forced Convection,” *IEEE TRANSACTIONS ON PLASMA SCIENCE,* Vols. PS-7, no. 4, DECEMBER 1979.

[36] L. Neimeyer, K. Ragaller, W. Hermann, U. Kogelschatz and E. Schade, “Experimental and theoretical investigation high current arcs in a supersonic nozzle,” *J Phys D: Appl. Phys,* vol. 7, pp. 1703-22, 1974.

[37] J. J. Lowke and H. C. Ludwig, “A simple method for high current arcs stabilized by forced convection,” *J Appl Phys,* vol. 46, pp. 3361-67, 1975.

[38] D. T. Tuma and J. J. Lowke, “Prediction of properties of arcs stabilized by forced convection,” *J Appl Phys,* vol. 46, pp. 3352-60, 1975.

[39] M. D. Cowley, “Integral methods of analysing electric arcs: I. Formulation,” *J. Phys. D: Appl. Phys.,* vol. 7, pp. 2218-31.

[40] S. K. Chan, M. D. Cowley and M. T. C. Fang, “Integral methods of analysing electric arcs. III. Shape-factor correlation for low radiation and laminar flow,” *J. Phys. D: Appl. Phys.,* vol. 9, pp. 1085-99, 1976.

[41] M. T. C. Fang, S. Ramakrishnan and H. K. Messerle, “Scaling Laws for Gas-Blast Circuit-Breaker Arcs During the High Current Phase,” *IEEE Transactions on plasma science,* Vols. PS-8, no. 4, pp. 357-62, 1980.

[42] R. W. Liebermann and J. J. Lowke, “Radiation emission coefficients for sulfur hexafluoride arc plasmas,” *J. Quant. Spectrosc. Radiat. Transf.,* vol. 17, pp. 253-64, 1976.

[43] J. F. Zhang, M. T. C. Fang and D. B. Newland, “Theoretical investigation of a 2kA arc in a supersonic nozzle,” *J. Phys. D: Appl. Phys.,* vol. 20, pp. 368-79, 1987.

[44] S. V. Pantankar, Numerical Heat Transfer in Fluid Flow, New York: Hemisphere Publishing Corporation, 1980.

[45] M. T. C. Fang and W. Y. Lin, “Current zero behaviour of a gas blast arc, Pt.1:Nitrogen,” *Proc. IEE,* vol. 137, pp. 175-183, 1990.

[46] M. T. C. Fang and Q. Zhuang, “Current Zero Behaviour of an SF6 Gas Blast Arc, Pt.I: Laminar Flow,” *J.Phys.D.: Appl. Phys.*, vol. 25, pp. 1197-1204, 1992.

[47] M. T. C. Fang, Q. Zhuang and X. Guo, “Current Zero Behaviour of an SF6 Gas Blast Arc, pt II. Turbulent Flow,” *J. Phys. D: Appl. Phys.*, vol. 27, pp. 74-83, 1994.

[48] *PHOENICS is the name of a commercial CFD package supplied by CHAM which is based at Bakery House, 40 High Street, Wimbledon Village, London, SW19 5AU, UK.*.

[49] U. Rutten, “Simulation of switching arc-gas interaction in SF6 breakers,” *Proc. Of 10th Int. Conference on Gas Discharges and their Applications,* pp. 140-143, 1992.

[50] M. T. C. Fang and J. D. Yan, “Common problem encountered in computer simulation of gas blast arcs,” *Proc of the third int. conf. on electrical contacts, arcs, apparatus and their applications,* vol. 1, pp. 1-7, 1997.

[51] S. Kwan, M. T. C. Fang and W. Hall, “Arc-shock interaction inside a supersonic nozzle,” *IEEE Trans Plasma Science,* vol. 24, pp. 85-86, 1996.

[52] M. T. C. Fang, J. D. Yan and C. Jones, “Electrical and aerodynamic behaviour of arc under shock conditions,” *IEEE Trans Plasma Sci.*, vol. 24, pp. 840-845, 1997.

[53] S. Kwan, PhD Thesis, University of Liverpool, United Kingdom, 1996.

[54] J. D. Yan, PhD Thesis, University of Liverpool, United Kingdom, 1997.

[55] J. L. Zhang, J. D. Yan, A. B. Murphy, W. Hall and M. T. C. Fang, “Computational investigation of arc behaviur in an auto-expansion circuit breaker contaminated by ablated nozzle vapor,” *IEEE Trans. on Plasma Science*, pp. 706 - 719, 2002.

[56] *ANSYS Fluent is the name of a commercial CFD package supplied by ANSYS which is based at Southpointe, 2600 ANSYS Drive, Canonsburg, PA 15317, USA.*

[57] F. Lago, J. J. Gonzalez, P. Freton and A. Gleizes, “A numerical modelling of an electric arc and its interaction with the anode: Part I. The two-dimensional model,” *Journal of Physics D: Applied Physics*, vol. 37, no. 6, p. 883–897, 2004.

[58] R. Bini, N. T. Basse and M. Seeger, “Arc induced turbulent mixing in an SF6 circuit breaker model,” *J. Phys. D: Appl. Phys.*, vol. 44, 2011.

[59] F. Reichert, J. J. Gonzalez and P. Freton, “Modelling and simulation of radiative energy transfer in high-voltage circuit breakers,” *Journal of Physics D: Applied Physics*, vol. 45, no. 37, 2012.

[60] Q. Zhou, H. Li, X. Xu, F. Liu, S. Guo, X. Chang, W. Guo and P. Xu, “Comparative study of turbulence models on highly constricted plasma cutting arc,” *J. Phys. D: Appl. Phys.*, vol. 42, no. 1, 2009.

[61] M. Seeger, M. Schwinne, R. Bini, N. Mahdizadeh and T. Votteler, “Dielectric recovery in a high-voltage circuit breaker in SF6,” *J. Phys. D: Appl. Phys.*, vol. 45, no. 39, 2012.

[62] D. C. Wilcox, Turbulence Modeling for CFD (La Cañada, CA: DCW Industries), 2006.

[63] J. D. Yan, K. I. Nuttall and M. T. C. Fang, “A comparative study of turbulence models for SF6 arcs in a supersonic nozzle,” *J. Phys. D: Appl. Phys.*, vol. 32, p. 1401–6, 1999.

[64] Q. Zhang, J. D. Yan and M. T. C. Fang, “Current Zero Behaviour of an SF6 Nozzle Arc under Shock Conditions,” *J. Phys. D: Appl. Phys.*, vol. 46, 165203, 2013.

[65] Q. Zhang, J. D. Yan and M. T. C. Fang, “Modelling of SF6 arc in a supersonic nozzle. Part I: Cold flow features and DC arc characteristics,” *J. Phys. D: Appl. Phys.*, vol. 47, 215201, 2014.

[66] G. Frind and J. A. Rich, “Recovery speed of axial flow gas blast interrupter: Dependence on pressure and dI/dt for Air and SF6,” *Power Apparatus and Systems, IEEE Transactions,* Vols. PAS-93, 1974.

[67] H. R. Griem, Plasma Spectroscopy, New York, McGraw- Hill, 1964.

[68] E. Lewis, A. N. Prasad and G. R. Jones, “Current zero spectroscopy of a high power SF6 circuit breaker arc,” *Proc. Of gas discharge and their applications, Oxford,* pp. 31-34, 1985.

[69] W. Hermann, U. Kogelschatz, L. Niemeyer, K. Ragaller and E. Schade, “Experimental and theoretical study of a stationary high-current arc in a supersonic nozzle flow,” *J. Phys. D: Appl. Phys.,* vol. 7, pp. 1703-1722, 1974.

[70] P. J. Shayler and M. T. C. Fang, “The transport and thermodynamic properties of a copper-nitrogen mixture,” *J. Phys.D.: Appl. Phys.,* vol. 10, pp. 1659-1669, 1977.

[71] J. M. Yos, Tranport properties of Nitrogen, Hydrogen, Oxygen and Air to 30000K, 1963.

[72] J. A. Shercliff, A textbook of magnetohydrodynamics, Pergamon Press, 1965.

[73] J. J. Gonzalez, R. Girard and A. Gleizes, “Decay and post-arc phases of a SF6 arc plasma: a thermal and chemical non-equilibrium model,” *J. Phys. D: Appl. Phys.,* vol. 33, pp. 2759- 68, 2000.

[74] J. J. Gonzalez, A. Gleizes and P. Kerenek, “SF6 circuit breaker arc modelling: influence of the electric field on the electrical conductivity,” *J. Phys. D: Appl. Physics.,* vol. 27, pp. 985-993, 1994.

[75] J. B. Belhaouari, J. J. Gonzalez and A. Gleizes, “Simulation of a decaying SF6 arc plasma: Hydrodynamic and kinetic coupling,” *Phys. D: Appl. Physics,* vol. 31, pp. 1219-1232, 1998.

[76] N. Peters, Turbulent Combustion, Cambridge University Press, 2000.

[77] W. Hermann, U. Kogelschatz, L. Niemeyer, K. Ragaller and E. Schade, “Investigation on the physical phenomena around current zero in HV gas-blast breakers,” *IEEE Trans. Power Appar. Syst. 96*, pp. 1165-76, 1977.

[78] P. A. Davidson, Turbulence: An Introduction for Scientists and Engineers (Oxford: Oxford University Press), 2004.

[79] H. Schlichting, Boundary Layer Theory 7th edn (New York: McGraw Hill), 1979.

[80] B. E. Launder and D. B. Spalding, “The numerical computation of turbulent flows,” *Comput. Methods Appl. Mech. Eng.*, vol. 3, p. 269–89, 1974.

[81] P. J. Shayler and M. T. C. Fang, “Radiation transport in wall-stabilised nitrogen arcs,” *J. Phys. D: Appl. Phys.*, vol. 11, no. 1743-56, 1978.

[82] V. Aubrecht and M. Bartlova, “Net Emission Coefficients of Radiation in Air and SF6 Thermal Plasmas Plasma,” *Chem. Plasma. Process.*, vol. 29, pp. 131-47, 2009.

[83] S. D. Eby, J. Y. Trepanier and X. D. Zhang, “Modelling radiative transfer in SF6 circuit-breaker arcs with the P-1 approximation,” *J. Phys. D: Appl. Phys.*, vol. 31, pp. 1578-88, 1998.

[84] V. Aubrecht and J. J. Lowke, “Calculations of radiation transfer in SF6 plasmas using method of partial characteristics,” *J. Phys. D: Appl. Phys.*, vol. 27, pp. 2066-73, 1994.

[85] C. M. Dixon, J. D. Yan and M. T. C. Fang, “A comparison of three radiation models for the calculation of nozzle arcs,” *J. Phys. D: Appl. Phys.*, vol. 37, pp. 3309-18, 2004.

[86] K. A. Ernst, J. G. Kopainsky and H. H. Maecker, “The energy transport, including emission and absorption, in N2-arcs of different radii,” 1973.

[87] V. Aubrecht and M. Bartlova, “Radiation transfer in thermal plasmas of air, N2 and CO2”.

[88] A. Gleizes, B. Rahmani, J. J. Gonzalez and B. Liani, “Calculation of net emission coefficient in N2, SF6 and SF6-N2 arc plasmas,” *J. Phys. D: Appl. Phys.*, vol. 24, pp. 1300-9, 1991.

[89] A. Gleizes, J. J. Gonzalez, B. Liani and G. Raynal, “Calculation of net emission coefficient of thermal plasmas in mixtures of gas with metallic vapour,” *J. Phys. D: Appl. Phys.*, vol. 26, pp. 1921-27, 1993.

[90] T. Billoux, Y. Cressault, P. Teulet and A. Gleizes, “Calculation of the net emission coefficient of an air thermal plasma at very high pressure,” *12th High-Tech Plasma Processes Conference (HTPP-12), J. Phys.*, 2012.

[91] Y. Naghizadeh-Kashani, Y. Cressault and A. Gleizes, “Net emission coefficient of air thermal plasmas,” *J. Phys. D: Appl. Phys.*, vol. 35, pp. 2925-34, 2002.

[92] B. Peyrou, L. Chermartin, P. Lalande, B. G. Cheron, P. Riviere, M.-Y. Perrin and A. Soufiani, “Radiative properties and radiative transfer in high pressure thermal air plasmas,” *J. Phys. D: Appl. Phys.*, vol. 45, no. 45, 2012.

[93] J. M. Yos, “Revised transport properties for high temperature air and its components,” *AVCO-RAD*, 1967.

[94] R. S. Devoto, “Electron transport properties in high-temperature air,” *Phys of Fluids*, vol. 19, pp. 22-24, 1976.

[95] A. B. Murphy, “Transport Coefficients of Air, Argon-Air, Nitrogen-Air, and Oxygen-Air Plasma,” *Plasma Chemistry and Plasma Processing*, vol. 15, no. 2, 1995.

[96] M. Capitelli, G. Colonna, C. Gorse and A. Angola, “Transport properties of high temperature air in local thermodynamic equilibrium,” 1999.

[97] A. D'Angola, G. Colonna, C. Gorse and M. Capitelli, “Thermodynamic and transport properties in equilibrium air plasmas in wide pressure and temperature range,” *Eur. Phys. J. D*, vol. 46, pp. 129-150, 2008.

[98] W. Z. Wang, Y. Wu, M. Z. Rong and F. Yang, “Theoretical computation studies for transport properties of air plasmas,” 2011.

[99] J. C. Morris, R. P. Kudis and J. M. Yos, “Measurements of electrical and thermal conductivity of hydrogen, nitrogen and argon at high temperatures,” *Phys of Fluid,* vol. 13, pp. 608-617, 1970.

[100] R. S. Devoto, U. H. Bauder, J. Cailleteau and E. Shire, “Air transport coefficients from electric arc measurements,” *Phys of Fluids,* vol. 21, pp. 552-558.

[101] E. I. Asinovsky, A. V. Kirillin, E. P. Pakhomov and V. E. Shabaskov, "Experimental investigation of transport properties of low-temperature plasma by means of electric arc," vol. Proceedings of the IEEE, no. 4, 1971.

[102] P. W. Schreiber, A. M. Hunter and K. R. Benedetto, “Electrical conductivity and total emission coefficient of air plasma,” *AIAA Journal,* vol. 11, no. 6, 1973.

[103] H. K. Versteeg and W. Malalasekera, An Introduction of Computational Fluid Dynamics: The Finite Volume Method 2nd edn (Harlow: Prentice-Hall), 2007.

[104] T. M. Wong, Computer Simulation and Visualisation of Complex Systems: Arcs and Hot Gas Flow in Auto-expansion Circuit Breakers (PhD thesis: University of Liverpool), 2008.

[105] “ANSYS software,” [Online]. Available: http://www.ansys.com/ ,http://www.ansys.com/Products/Fluids/ANSYS-Fluent.

[106] “ANSYS Fluent Users Guide,” [Online]. Available: https://support.ansys.com.

[107] “ANSYS Fluent Theory Guide,” [Online]. Available: https://support.ansys.com.

[108] “ANSYS Fluent Advanced Add-On Modules,” [Online]. Available: https://support.ansys.com.

[109] “ANSYS Fluent UDF Manual,” [Online]. Available: https://support.ansys.com.

[110] “ANSYS DesignModeler Users Guide,” [Online]. Available: https://support.ansys.com.

[111] “ANSYS Meshing Users Guide,” [Online]. Available: https://support.ansys.com.

[112] Q. Zhang, Modelling of Turbulent SF6 Switching Arcs (PhD thesis: University of Liverpool), 2014.

[113] *JSON is described by RFC7159 which is a product of the Internet Engineering Task Force(IETF).*

[114] J. D. Anderson, Modern Compressible Flow (New York: McGraw-Hill), 1982.

[115] M. T. C. Fang and D. B. Newland, “DC nozzle arcs with mild wall ablation,” *J. Phys. D: Appl. Phys.*, vol. 16, no. 5, pp. 793-810, 1983.

[116] G. Frind, R. E. Kinsinger, R. D. Miller, H. T. Nagamatsu and H. O. Noeske, “Fundamental investigation of arc interruption in gas flows,” *EPRI EL-284 (Project 246-1)*, 1977.

[117] R. W. B. Stephens and A. E. Bate, Acoustics and vibration physics, Arnold, London, 1966.

[118] Q. Zhang, J. Liu, J. D. Yan and M. T. C. Fang, “Modelling of SF6 arc in a supersonic nozzle: II. Current zero behaviour of the nozzle arc,” *J. Phys. D: Appl. Phys. Under review.*.

[119] T. Poinsot and D. Veynante, Theoretical and Numerical Combustion 2nd edn, Philadelphia: Edwards, 2005.

[120] P. A. Libby and F. A. Williams, Turbulent Reacting Flow, Berlin: Spring-Verlag, 1980.

[121] S. Sarkar and L. Balakrishnan, “Application of a Reynolds Stress Turbulence Model to the Compressible Shear Layer,” *ICASE Report*, no. 90-18, 1990.

[122] Y. C. Lee, Modelling Work in Thermal Plasma Processing (PhD thesis: University of Minnesota), 1984.